THE UNIVERSITY *of* EDINBURGH

Numerical modelling of geophysical monitoring techniques for CCS

Rami Eid

Thesis presented for the degree

Doctor of Philosophy

THE UNIVERSITY
of EDINBURGH

School of GeoSciences

2016

Abstract

I assess the potential of seismic and time-domain controlled-source electromagnetic (CSEM) methods to monitor carbon dioxide (CO_2) migration through the application of a monitorability workflow. The monitorability workflow describes a numerical modelling approach to model variations in the synthetic time-lapse response due to CO_2 migration. The workflow consists of fluid-flow modelling, rock-physics modelling and synthetic seismic or CSEM forward modelling. I model CO_2 injected into a simple, homogeneous reservoir model before applying the workflow to a heterogeneous model of the Bunter Sandstone reservoir, a potential CO_2 storage reservoir in the UK sector of the North Sea. The aim of this thesis is to model the ability of seismic and time-domain CSEM methods to detect CO_2 plume growth, migration and evolution within a reservoir, as well as the ability to image a migrating front of CO_2.

The ability to image CO_2 plume growth and migration within a reservoir has not been demonstrated in the field of CSEM monitoring. To address this, I conduct a feasibility study, simulating the time-lapse CSEM time-domain response of CO_2 injected into a saline reservoir following the multi-transient electromagnetic (MTEM) method. The MTEM method measures the full bandwidth response. First, I model the response to a simple homogeneous 3D CO_2 body, gradually increasing the width and depth of the CO_2. This is an analogue to vertical and lateral CO_2 migration in a reservoir. I then assess the ability of CSEM to detect CO_2 plume growth and evolution within the heterogeneous Bunter Sandstone reservoir model. I demonstrate the potential to detect stored and migrating CO_2 and present the synthetic results as time-lapse common-offset time sections. The CO_2 plume is imaged clearly and in the right coordinates.

The ability to image seismically a migrating front of CO_2 remains challenging due to uncertainties regarding the pore-scale saturation distribution of fluids within the reservoir and, in turn, the most appropriate rock-physics model to simulate this: uniform or patchy saturation. I account for this by modelling both saturation models, to calculate the possible range of expected seismic velocities prior to generating and interpreting the seismic response. I demonstrate the ability of seismic methods to image CO_2 plume growth and evolution in the Bunter Sandstone saline reservoir model and highlight clear differences between the two rock-physics models. I then modify the Bunter Sandstone reservoir to depict a depleted gas field by including 20% residual gas saturation. I assess the importance and implication of patchy saturation and present results which suggest that seismic techniques may be able to detect CO_2 injected into depleted hydrocarbon fields.

Lay summary

For carbon capture and storage (CCS) to become widely accepted, it has to be demonstrably safe and effective from an emissions reduction perspective. For this to occur, containment of stored CO_2 needs to be monitored with sufficient confidence and, with a large emphasis on leakage detection and quantification.

Seismic and controlled-source electromagnetic (CSEM) time-lapse methods, through the acquisition of repeated datasets over time, can allow for observed changes in physical parameters in the reservoir to be imaged caused by the displacement of brine by less dense, more compressible and more resistive CO_2. Reservoir simulation to synthetic geophysical numerical modelling workflows can be used to model the potential of seismic and CSEM methods to detect leakage and migration within the reservoir. These workflows are typically used before, during and after CO_2 injection to determine what a given sensor would measure in a given environment. This is the process through which a subsurface geological model is injected with CO_2 and then used to generate a synthetic seismic section or synthetic EM response. However, current best practice application of such workflows for CO_2 storage monitoring vary considerably due to practical experience and field deployment.

For seismic monitoring, the ability to image accurately a migrating CO_2 plume remains challenging due to uncertainties regarding the pore-scale distribution of fluids in the reservoir, and in turn, the most appropriate rock-physics fluid-saturation model to simulate this. For CSEM monitoring, the ability to image CO_2 plume growth and migration within a reservoir has not been demonstrated. Furthermore, there have been no feasibility studies or workflows published for the application and deployment of CSEM techniques at CCS sites.

To address this, I present a monitorability workflow which can be used to assess the potential of seismic and CSEM to monitor CO_2 migration. The monitorability workflow describes a numerical modelling approach to model variations in the synthetic time-lapse response due to CO_2 migration. The workflow consists of fluid-flow modelling, rock-physics modelling and synthetic seismic or CSEM forward modelling. I demonstrate the application of the workflow to model the ability of seismic and CSEM to detect CO_2 plume growth, migration and evolution within a reservoir, as well as the ability to image a migrating front of CO_2.

Declaration

I declare that this thesis has been composed solely by myself and that it has not been submitted, either in whole or in part, in any previous application for a degree. Except where otherwise acknowledged, the work presented is entirely my own.

Rami Eid

April 2016

Acknowledgements

I would like to thank my supervisors Anton Ziolkowski, Mark Naylor and Gillian Pickup for all their support, guidance and advice. They have always had an open-door policy and without their help, this project would never have reached this stage. I would also like to thank David Wright, for all his help and assistance with the EM modelling, Mark Chapman, for all the rock-physics discussions and Carlos da Costa Filho for sharing his coding expertise.

This project would never have been possible without the funding and support of E.ON and ETP, which I am truly grateful for. I would specially like to thank Tim Hill and his group for all the interesting discussions, Barrie Shepherd and ETP for increasing my grant to cover my knee operation and Stuart Simmons who worked so hard to get this project up and running. I would also like to thank PGS for providing access to Nucleus+ and PEMrad. In particular, to Johnathan Linfoot and Silke Bude for all the training and support.

To all my friends in Adelaide, especially the 'High school group', thank you for making my move to Edinburgh as smooth as possible. The surprise packages throughout the years gave me so much joy and always reminded me of home. In particular to Rachel Hill, Sampretha Babu and Tim Hatfield, I could never have asked for better friends. Even though we are on opposite sides of the world, you were always just a phone call away.

To all my friends in Edinburgh, thank you for all the great times. In particular, to my pod buddy 'Gus' (Andrew) Fraser-Harris for putting up with me over the years and constantly providing great advice. To my 'Three Shades of Upper Gray' flatmates Axel Laurel Tcheheumeni Djanni and Nicola Rigonat for making the flat feel like home and to my Edinburgh Bloods Scottish AFL premiership teammates, thank you for welcoming me to the team and for all the great times. Last but not least, to Darren Bisset, Alice Macente, Johannes Miocic, David Monaghan and Siôn Gardner. I will never forget your friendship, kindness and support during my operation and recovery.

Finally, to my family. Thank you for everything. I am so lucky to be surrounded by such a kind, loving and supportive family. Especially to Ghada and Samir Eid who sacrificed so much and dropped everything to help me when I needed it most.

Contents

List of figures

List of Tables

Symbols and Abbreviations

SI units are used throughout the thesis as specified in the following list. In addition to the symbols listed here, the symbols x, y and z have been used throughout to denote the cartesian coordinate axes.

Symbol	Description	Units
A	sectional area	m^2
a	tortuosity factor	-
d	size of saturation heterogeneity, or saturation 'patch'	m
f	frequency	Hz
g	earth impulse response	Ω/m^2
k	permeability	m^2
K_{air}	bulk modulus of the pore-filling gas	Pa
K_{dry}	dry frame bulk modulus	Pa
K_{fl}	pore-fluid bulk modulus	Pa
K_{HM}	Hertz-Mindlin dry rock bulk modulus	Pa
K_m	matrix bulk modulus	Pa
K_{min}	mineral bulk modulus	Pa
K_{sat}	bulk modulus of a saturated rock	Pa
kr	relative-permeability	-
L	length	m
L_c	critical length scale	m
m	cementation factor	-
n_c	coordination number	-
n	saturation exponent	-
N	uncorrelated noise	V
P	pressure	Pa
Pc	capillary pressure	Pa
Pth	threshold pressure	kPa
q	flow rate	m^3/s
R	resistivity	Ω/m
R_{CO2}	residual saturation	-

r_{off}	source-receiver offset	m
S	saturation	-
S_{wir}	irreducible water saturation	-
Sr	MTEM system response	$A\ m^2$
T	temperature	°C
t	time	s
U_{HM}	Hertz-Mindlin dry rock shear modulus	Pa
v	poisson's ratio	Pa
V_{clay}	volume of clay	-
Vp	P-wave velocity	m/s
V_l	measured voltage response	V
η	viscosity	$Pa.s$
μ	shear modulus	Pa
ρ	density	g/cm^3
σ	conductivity	$\Omega.m$
ϕ	porosity	-
ϕ_c	critical porosity	-

Abbreviations	
IPCC	Intergovernmental Panel on Climate Change
CCS	Carbon Capture and Storage
CMP	Common mid-point
CO_2	Carbon dioxide
CSEM	Controlled-source electromagnetic
EM	Electromagnetic
EU CCS	European Storage CCS Directive
GCCSI	Global Carbon Capture and Storage Institute
HED	Horizontal electric dipole
IEA	International Energy Agency
GHG	Greenhouse Gas
MMV	Monitoring, measurement and verification
MTEM	Multi-transient electromagnetic
NMO	Normal moveout
PSPI	Phase-shift plus interpretation
RGWC	Residual gas-water contact
ROAD	Rotterdam CCS Demonstration Project

Thesis

1. Introduction

1.1 Review

1.1.1 Climate change and the importance of CCS

According to the Intergovernmental Panel on Climate Change (IPCC), the rise in atmospheric concentrations of CO_2 has resulted in an average increase in global temperature of around 0.74°C during the 20th century (IPCC, 2007, IPCC, 2013). Recent forecasts by the International Energy Agency (IEA) and IPCC have shown that by 2100, average global temperatures could increase by 6°C (IPCC, 2007, IEA, 2011, IPCC, 2013). An increase in temperature of that scale could have catastrophic effects on the climate, resulting in increased occurrences of natural disasters, such as heat waves, rising sea levels, and flood events (GCCSI, 2012).

Through the continued burning of fossil fuels, large amounts of CO_2 will continue to be released into the atmosphere, gradually increasing CO_2 concentrations, which relate to approximately 60% of total global anthropogenic greenhouse gas (GHG) emissions (GCCSI, 2012).

Carbon Capture and Storage (CCS) can reduce the overall GHG emissions from industry and power stations that use fossil fuels, while also easing the transition from current fossil fuel based energy systems to future low-carbon energy systems (Chadwick et al., 2009). CCS involves capturing carbon dioxide produced by the burning of fossil fuels and storing it in deep geological formations (Baines and Worden, 2004, Benson, 2005, Cook, 2012). This technology involves the adaptation of existing, proven technologies used by several industries which can be used as analogues for underground geological storage, none more so than improved oil recovery with CO_2 and underground storage of natural gas.

CCS projects such as Sleipner (Norway), Snøhvit (Norway), Weyburn (Canada), Otway (Australia), In Salah (Algeria) and Ketzin (Germany) have increased understanding of the physical and chemical impacts of CO_2 migration in a reservoir as well as providing insight into reservoir monitoring, measurement and verification (MMV) technologies.

1.1.2 Geophysical monitorability

For CCS to become widely accepted, it has to be demonstrably safe and effective from an emissions reduction perspective. For this to occur, containment of stored CO_2 in the intended formation needs to be monitored with an emphasis on leakage detection and quantification.

Monitorability of CO_2 storage sites is a site-specific problem which involves the measuring, monitoring and verification (MMV) of injected CO_2 in the subsurface. The purpose of MMV is to identify and quantify the movement of CO_2 in the reservoir and to ensure the safe and reliable operation of a CCS project.

Although several methods have been proposed for the subsurface monitoring of CO_2, surface geophysical techniques provide the most accurate and accessible methods as they are non-invasive and are able to detect and map distinctive physical parameters related to the distribution of rock layers and structures in the subsurface. In particular, the application of seismic and controlled-source electromagnetic (CSEM) time-lapse methods, through the acquisition of repeated datasets over time, potentially allow for observed changes in physical parameters in the reservoir to be imaged caused by the displacement of brine by less dense, more compressible and more resistive CO_2.

Modelling the potential of seismic and CSEM techniques to detect leakage and migration involves the application of reservoir simulation to synthetic geophysical numerical modelling workflows. These workflows are typically used before, during and after CO_2 injection to determine what a given sensor would measure in a given environment. This is the process through which a simulation of CO_2 injection into a subsurface geological model is performed and then used to generate a synthetic seismic section or synthetic EM response. This tool is used during initial storage-site assessment stages to determine whether the injected CO_2 will generate an interpretable change in the processed seismic or CSEM data. Current best practice application of such workflows for CO_2 storage monitoring using seismic and EM methods vary considerably due to practical experience and field deployment.

1.1.3 Seismic monitoring of CO_2 storage

Seismic monitoring techniques have been used successfully to match the simulated growth of the CO_2 plume against site monitoring observations at the Sleipner CCS storage site (Chadwick et al., 2006a, Singh et al., 2010, Boait et al., 2012). The monitoring focuses mainly on the detection of structurally trapped CO_2; that is, CO_2 at high concentrations trapped below an impermeable seal. However, the ability to image accurately a free-phase migrating CO_2 plume – defined as CO_2 which is not immobilized by residual or structural trapping – remains challenging due to uncertainties regarding the pore-scale distribution of fluids in the reservoir, and in turn, the most appropriate rock-physics fluid-saturation model to simulate this: uniform or patchy saturation.

Typically, a uniform saturation distribution model is assumed. That is, immiscible phases are assumed to be homogeneously distributed throughout the pore space. This is typical for virgin homogenous reservoirs. However, the injection and migration of CO_2 disrupts this equilibrium, resulting in a non-uniform, partially saturated, phase distribution: a patchy saturation distribution. This dictates the formation and evolution of fluid patches resulting from two-phase flow (CO_2 and water) through porous rocks. Uniform and patchy saturation represent the lower and upper bounds of calculated seismic velocities as a function of CO_2 saturation Mavko and Mukerji (1998).

The application and importance of patchy saturation for CO_2 monitoring is a relatively new field and hence only moderately understood. This is reflected in the current literature. Key publications modelling CO_2 monitorability include Chadwick et al., (2004), Chadwick et al., (2005), Arts et al., (2007), Arts et al., (2009), Kazemeini et al., (2010), Mukhopadhyay et al., (2010), Cairns et al., (2012), Nader et al., (2012), Pevzner et al., (2013), White (2013b), Grude et al., (2014), Padhi et al., (2014), Chadwick et al., (2014) and Si et al., (2015).

With regard to the application of the most appropriate rock-physics model, a summary can be made that most of the research currently undertaken in the field of CO_2 seismic monitoring:

1. Only assume uniform saturation (Chadwick et al., 2005, Arts et al., 2007, Arts et al., 2009, Mukhopadhyay et al., 2010, Nader et al., 2012, Pevzner et al., 2013, White, 2013b, Grude et al., 2014, Chadwick et al., 2014);
2. Mention patchy saturation with no application (Chadwick et al., 2004);
3. Model and compare patchy and uniform saturation in very simple scenarios which don't highlight the key differences between the two end-member models (Kazemeini et al., 2010, Cairns et al., 2012, Si et al., 2015).

Furthermore, the modelled scenarios in each publication simulate CO_2 injection into homogeneous reservoirs only. In most cases, the CO_2 plume is modelled as a single, constant saturation. This does not represent the complex nature of the subsurface. This uncertainty demonstrates the need for a serious study of the application of the rock-physics end-member models.

1.1.4 CSEM monitoring of CO_2 storage

EM techniques for CO_2 storage monitoring have been proposed by several researchers, including Ramirez et al., (2003), Um & Alumbaugh (2007), Christensen et al., (2006), Kiessling et al., (2010) and Bourgeois & Girard (2010). However, the deployment of CSEM monitoring for CCS is relatively untested in the field. Currently, it has only been deployed at the Sleipner CCS site, yielding inconclusive results.

The feasibility of CSEM monitoring of offshore oil and gas reservoirs has been studied extensively (Lien and Mannseth, 2008, Orange et al., 2009, Black and Zhdanov, 2009, Andréis and MacGregor, 2011, Kang et al., 2012, Bhuyian et al., 2012). The authors successfully model the ability of CSEM techniques to detect fluid changes in the reservoir due to oil or gas production. However, in each study, the generated synthetic time-lapse responses were modelled in the frequency domain only and using either 1D models (Ellis and Sinha, 2010), 2D models (Lien and Mannseth, 2008,

Orange et al., 2009, Black and Zhdanov, 2009, Kang et al., 2012), or very simple 3D models (Andréis and MacGregor, 2011, Bhuyian et al., 2011, Bhuyian et al., 2012).

Frequency-domain CSEM is only one approach to modelling a synthetic EM response. Another approach is modelling a synthetic EM response in the time-domain through the application of the multi-transient electromagnetic (MTEM) method. Frequency-domain CSEM measures the amplitude and phase for certain defined frequencies only, as opposed to MTEM which measures the transient change of the received signal containing the full frequency spectrum. This has a clear advantage over frequency-domain CSEM. Other advantages include the ability to image a clear airwave response which can then be muted easily, and when analysed in time-lapse, clear arrival times associated with only the subsurface anomaly can be imaged.

There have been no feasibility studies or monitorability workflows published for the application and deployment of CSEM techniques at CCS sites, especially in the time-domain. However, the potential application of CSEM for CCS monitoring has been presented at two SEG meetings: Ellis and Sinha (2010) in Denver, 2010 and Bhuyian et al., (2011) in San Antonio, 2011. Both presentations demonstrate the ability for CSEM method to detect CO_2 in the subsurface. However, the modelled scenarios in both presentations were of a single block of CO_2 of constant saturation, performed in the frequency domain only.

The advantages of analysing the CSEM response in the time-domain has been demonstrated by Wright et al., (2002) and Ziolkowski et al., (2007). Wright et al., (2002) demonstrate the potential for monitoring the movement of subsurface fluids with time while Ziolkowski et al., (2007) demonstrates the ability to visualise CSEM data as common-offset sections. This is a key advantage which shouldn't be underestimated, as it allows for a direct comparison to seismic data, allowing for possible integration of both seismic and CSEM techniques. This has not been demonstrated for CO_2 storage monitoring.

1.2 Claim

This thesis assesses the CO_2 monitorability of both seismic and CSEM techniques. This is achieved through the development of a monitorability workflow. The workflow is flexible and can be adapted for both seismic and CSEM to model variations in the time-lapse signal through the application of fluid-flow modelling, rock physics modelling and geophysical forward modelling.

For seismic monitoring, to account for the uncertainties regarding the most appropriate rock-physics fluid saturation distributions, I model both end-member models - patchy saturation and uniform saturation – and apply the workflow to three storage scenarios: a homogeneous saline reservoir, a heterogeneous saline reservoir and a depleted gas field. This is the first study which models the effect of the rock-physics end-member models on CO_2 injected into heterogeneous virgin saline reservoirs and depleted gas fields. Current research in the field of CCS detectability generate synthetic seismic sections of CO_2 injected into homogeneous reservoirs only. This does not provide an accurate representation of the complexity which is often experienced in the subsurface, as CO_2 is always injected into heterogeneous reservoirs. Injection into heterogeneous reservoirs results in a range of CO_2 saturations, and hence calculated velocities, which are not constant in the plume body and result in seismic signatures which are more complex when compared to homogeneous reservoir settings. Therefore, modelling both end-members allows for a more accurate representation of the level of complexity which could be encountered in the subsurface. This predicts the largest possible range of expected velocities prior to generating and interpreting the seismic response. This is important, as the seismic response depends not only on the fluid type - liquid or gas - but also on the spatial distribution of the phases (White, 1975, Mavko and Mukerji, 1998). This allows for improved matching of plume activity in the storage reservoir, as well as potentially improving current quantification techniques.

For CSEM monitoring, I build on the work presented by Wright et al., (2002) and Ziolkowski et al., (2010) and model the time-domain EM response to CO_2 injection

and storage in a saline reservoir using the MTEM method. The depth and width of the CO_2 plume will be varied and the resultant response noted. This will provide an analogue to vertical and lateral migration. I then model the EM response over a potential CO_2 storage site. This is the first study which models: 1) the time-lapse EM response to injected CO_2 in the time-domain, 2) the expected change in measured amplitude due to lateral and vertical migration, and 3) the synthetic time-domain EM responses of CO_2 injected into a 3D heterogeneous reservoir.

For the first time I also model a loss of containment, in particular a free-phase migrating front of CO_2. This has not been assessed in the field of CSEM monitorability, while current research in the field of seismic monitorability assess the detectability of small, structurally trapped, highly saturated accumulations of CO_2 only (for example Chadwick et al., (2006a), Pevzner et al., (2013) and Chadwick et al., (2014)). This places more importance on the geometry of the accumulation than on the saturation. Instead, I assess the ability of seismic and CSEM techniques to detect a loss of containment by simulating a free-phase migrating front of CO_2 of lower saturations, typically ranging from 5 to 20%. Lower saturations allow for an accurate assessment as to whether the required change in seismic velocity or resistivity is great enough to result in a resolvable change on time-lapse seismic sections or time-lapse EM responses. This allows for an assessment as to whether the monitorability of a migrating front is sensitive to the saturation of the CO_2, and hence the change in velocity or resistivity, or whether factors such as the geometry of the plume play a more crucial role.

1.3 Agenda

Chapter 2 is a discussion of the CO_2 storage and monitoring regulation and objectives.

Chapter 3 is a review of the surface seismic and CSEM monitoring techniques currently being deployed at the two operational European offshore CCS sites: Sleipner and Snøhvit.

Chapter 4 describes the flexible monitorability workflow developed specifically for this thesis in order to model the level of complexity which could be encountered in the subsurface more accurately. The workflow can be adapted to generate synthetic seismic sections or synthetic EM responses to model variations in the time-lapse signal. The workflow is demonstrated in Chapters 5, 6, 7 and 8.

In Chapter 5, I assess the ability of seismic techniques to monitor four key stages during a CCS project: Stage 1) migrating plume during injection; Stage 2) contact with primary seal; Stage 3) first instance of a breach; and Stage 4) contact with secondary seal. This is achieved by building a 3D homogeneous reservoir model of an ideal storage complex consisting of two reservoir-seal pairs. A zone of weakness is included in the intraformational seal to encourage a loss of containment and the migration of CO_2 from the primary to the secondary reservoir. Analysis of the results corroborates the known ability of seismic technique to detect structurally trapped CO_2. However free-phase migrating CO_2 is shown to be more difficult to image.

Once I have assessed the ability to monitor CO_2 injected into homogeneous reservoirs, I then apply the workflow to a heterogeneous saline reservoir in Chapter 6. This reservoir is of the Bunter Sandstone Formation in the UK sector of the North Sea. I assess the ability of seismic methods to image plume growth, evolution, and migration by simulating the injection of 2 MT of CO_2 over 20 years. I highlight the clear differences between the rock-physics models and comment on the importance of the spatial geometry of a migrating front when monitoring a loss of containment.

In Chapter 7, I modify the Bunter Sandstone model and model two injection scenarios: 1) CO_2 injection into a depleted gas cap; and 2) CO_2 injection into a depleted gas field.

I then assess the ability to image the CO_2 plume in each scenario with a focus on the role and importance of patchy saturation. I present results which suggest that seismic techniques may be able to detect CO_2 injected into depleted gas fields.

I then shift my focus to CSEM monitorability. In Chapter 8 I perform a feasibility study on the potential for CSEM to monitor and detect injected CO_2. The synthetic response is modelled in the time-domain through the application of the multi-transient electromagnetic (MTEM) method. First, I summarise the MTEM method and model the earth impulse response to a simple CO_2 layer in 1D and 3D. Second, I model the response to a 3D CO_2 plume, gradually increasing the width and depth of the CO_2, noting the expected change in amplitude for each scenario. Third, I apply the monitorability workflow on the heterogeneous Bunter Sandstone model, assessing the ability of MTEM to image and detect plume growth, evolution, and migration by simulating the injection of 2 MT of CO_2 over 20 years.

In Chapter 9, I discuss the main findings and implications of my research with a focus on the interplay between CO_2 saturation, the geophysical signal and geological heterogeneity. I present two proposals for future research.

The Appendix contains some added information. Appendix A continues from the rock-physics modelling presented in Chapter 4 by investigating the effect of the Gassmann variables on seismic velocity. Appendix B verifies the PEMrad modelling code used in Chapter 8 with the 1D MTEM forward modelling code, EX1D. The last appendix, Appendix C, contains explanations regarding reproducibility and data. The input files required to run PEMrad are detailed and the Java scripts and Matlab codes are included to reproduce the rock-physics modelling and seismic processing.

The workflow presented in Chapter 4, and results presented in Chapter 6, have been published in Eid et al., (2015a). Additionally, I gave oral presentations of the progress of my research at the Greenhouse Gas Control Technologies (GHGT) conference 2014 (Eid et al., 2014) and the European Association of Geoscientists & Engineers (EAGE) conference 2015 (Eid et al., 2015b).

2. CO_2 storage and monitoring regulation and objectives

I summarise the two key sources of legislation for the geological storage and successful monitoring of CO_2 in the subsurface. The key terms, monitoring objectives and minimum requirements are outlined and the importance of the storage complex defined. I finish by expanding on the two main monitoring objectives: containment and conformance assurance.

2.1 Offshore monitoring regulation

There are two key sources of legislation regulating the offshore storage of CO_2 within the EU. They are the OSPAR Guidelines (OSPAR, 2007) and the European Storage (EU CCS) Directive (EC, 2009).

For the purpose of clarity, I define a small number of key terms in Table 2.1 which are used throughout. The terms are defined in the EU CCS directive (EC, 2009):

Table 2.1. Key terms as defined by the EU CCS Directive (EC, 2009).

Key terms and definitions	
Storage of CO_2	Injection accompanied by storage of CO_2 in underground geological formations;
Geological formation	A lithostratigraphical subdivision within which distinct rock layers can be found and mapped;
Operator	Any natural or legal, private or public person who operates or controls the storage site or to whom decisive economic power over the technical functioning of the storage site has been delegated according to national legislation;
Storage site	A defined volume area within a geological formation used for the geological storage of CO_2 and associated surface and injection facilities;
Storage complex	The storage site and surrounding geological domain which can have an effect on overall storage integrity and security: that is, secondary containment formation;
Migration	Movement of CO_2 within the storage complex;
Leakage	Unintended subsurface migration of CO_2, specifically release of CO_2 from the storage complex;
CO_2 plume	The dispersing volume of CO_2 in the geological formation;
Substantial change	Any change not provided for in the storage permit, which may have significant effects on the environment or human health;
Corrective measures	Any measures taken to correct significant irregularities or to close leakages in order to prevent or store the release of CO_2 from the storage complex;
Closure	Of a storage site means the definitive cessation of CO_2 injection into that storage site;
Post-closure	The period after the closure of a storage site, including the period after the transfer of responsibility to the competent authority;

Table 2.2 provides a summary of the monitoring objectives for both pieces of legislation. The OSPAR guidelines are primarily focussed on detecting and avoiding leakage. The guidelines place emphasis on monitoring throughout all stages of a storage project for the purpose of detecting a potential leak. Monitoring is expected to continue until there is confirmation that the probability of any environmental effects are reduced to insignificant levels.

Table 2.2. Summary of the monitoring objectives as set out in the OSPAR guidelines (OSPAR, 2007) and the EU CCS Directive (EC, 2009).

Monitoring objectives	
OSPAR guidelines	Performance confirmation.
	Detect possible leakage.
	Local environmental impacts on ecosystems.
	Effectiveness of CO_2 storage as a greenhouse gas mitigation technology.
EU CCS Directive	Compare actual and modelled behaviour of CO_2 in storage site.
	Detect significant irregularities.
	Detect migration of CO_2.
	Detect leakage of CO_2.
	Detect significant adverse effects for surrounding environment.
	Assess effectiveness of correct measures taken.
	Update assessment of the safety and integrity of the storage complex.

The EU CCS Directive takes the OSPAR principles and further develops them to provide more detail, as well as placing specific requirements, throughout the monitoring process. Monitoring, as required by the EU CCS Directive, plays a fundamental part in providing confidence to the regulators and community that the project is operating according to plan, therefore confirming that the injected CO_2 is remaining within the geological storage complex. Monitoring must be based on a monitoring plan which is proposed by the operator when applying for the storage permit. The monitoring plan should provide details of the monitoring to be

undertaken during the main stages of the project; baseline, operational and post-closure. The plan is required to be updated every five years to take into account changes in assessed risk of leakage, changes to assessed risk to the environment and human health, new scientific knowledge, and improvements in best available technology.

The Directive does not specifically state the use of any particular monitoring technique but rather provides guidelines on the desired monitoring requirements, summarised in Table 2.3.

Table 2.3. Monitoring guideline requirements as set out set out in the EU CCS Directive (EC, 2009)

Monitoring guideline requirements
Detect the presence, location and migration paths of CO_2 in the subsurface.
Provide information about pressure-volume behaviour.
Provide information about the spatial distribution of the CO_2 plume to refine numerical simulations.
Provide wide aerial spread in order to capture information on previously undetected potential leakage pathways.

Throughout the operational phase, monitoring at a minimum frequency of once per year is required to be completed by the operator and submitted to the competent authority. In the case where leakage out of the storage complex occurs, the operator is expected to notify the competent authority and take necessary corrective measures. Monitoring will be intensified as required to assess the scale of the leak and the effectiveness of the corrective measures.

During closure of a storage site, the operator is required to demonstrate complete and permanent containment of the stored CO_2 by providing evidence which: indicates conformity of injected CO_2 with modelled behaviour; an absence of any detectable leakage; and that the storage site is evolving towards long-term stability. If proven, monitoring is reduced to a level which allows for the identification of leakage. The directive applies to the storage of CO_2 in the territory of the Member States.

2.2 The storage complex

The EU CCS Directive (EC, 2009) defines the 'storage complex' as:

- *'the storage site and surrounding geological domain which can have an effect on overall storage integrity and security: that is, secondary containment formations'*

The definition of the storage complex is crucial as it includes a secondary containment reservoir. Movement of CO_2 from the primary to secondary reservoir is termed migration. Leakage is defined as the release of CO_2 from the storage complex itself. Figure 2.1 is a schematic indicating the different terms.

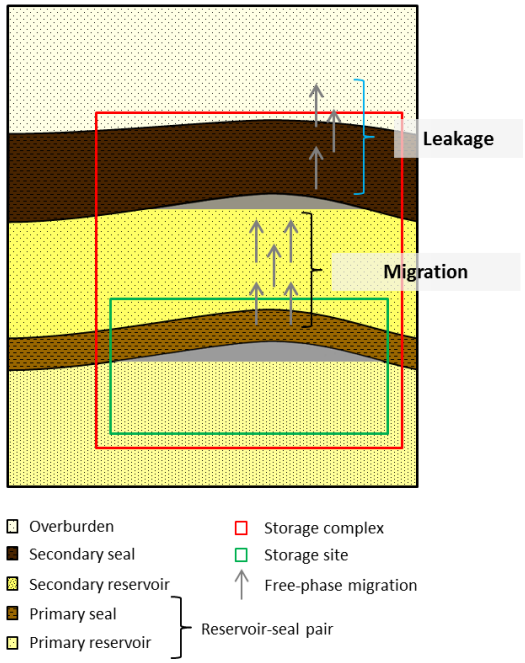

Figure 2.1. Schematic of a storage complex as defined by the EU CCS Directive (EC, 2009).

The definition of the storage complex includes:

- Primary reservoir-seal pair into which the CO_2 is physically injected and is expected to migrate and be stored;
- Secondary reservoir-seal pair that may contain the CO_2 in case the plume migrates beyond the primary seal.

The operator is required to assess the safety and integrity of the entire storage complex in both the short term the and long term.

2.3 Monitoring objectives

The International Energy Agency Greenhouse Gas R&D Programme (IEAGHG) conducted a review of offshore monitoring for CCS projects (IEAGHG, 2015) and suggested two key monitoring themes which can be extracted from the objectives outlined in the OSPAR Guidelines (OSPAR, 2007) and the European Storage Directive (EC, 2009) (Table 2.1). They are:

- The requirement to demonstrate that the storage site is currently performing effectively and safely,
- Ensure that it will continue to do so via provision of information supporting and calibrating prediction of future performance.

From this, the authors concluded two main monitoring objectives:

1) Containment assurance,
2) Conformance assurance.

Containment assurance aims to prove storage performance and to demonstrate that the stored CO_2 is securely retained within the storage complex. To achieve this, monitoring is divided into two zones: deep and shallow. Deep monitoring requires the identification of unexpected CO_2 migration from the primary to secondary storage site as well as the possible movement of CO_2 outside the storage complex, resulting in a leak. Identification of CO_2 migration is key as it provides operators with an early warning system of potential movement of CO_2 to the surface. Shallow-focussed monitoring requires the detection of CO_2 migration in the shallow subsurface by identifying physical or chemical changes in the seawater column or in the surrounding sediment. A minimum requirement for deep-focused monitoring systems is that it can reliably detect any leakage, with no gaps in spatial coverage, and to a specified detection threshold. Such detection thresholds have not been defined. Shallow monitoring systems should be capable of detecting emissions at the surface.

Conformance monitoring aims to demonstrate a high level of agreement between modelled simulations of the site behaviour and site monitoring observations. This enables testing and calibrating of models of current site behaviour, forming the basis for prediction of future behaviour and long term secure storage. Successful conformance monitoring allows for successful site closure. Non-conformance is achieved when observed site behaviour deviates from the predicted. Conformance monitoring is primarily deep focused and is aimed at imaging and characterising processes in and around the storage reservoir.

Should an event occur where containment and/or conformance requirements are not met, the authors recommend the application of a third category, contingency monitoring. This requires additional monitoring in order to track and assess the deviation from the planned performance, and design corrective measures if necessary.

Summary

In this chapter I provide a summary of the current regulation and monitoring objectives for large-scale offshore CO_2 storage projects. First I defined the key terms, monitoring objectives and minimum requirements as stipulated in the OSPAR Guidelines and the European Storage Directive, detailing what is expected of the operator. I then described the two main monitoring objectives: containment and conformance assurance.

3. Current deep-focused EU offshore monitoring for CO_2 storage

I review the monitoring objectives and techniques currently being deployed at the two operational European offshore CO_2 storage projects: Sleipner and Snøhvit. I summarise their main findings and subsequent limitations of both surface seismic and CSEM techniques.

3.1 Current & operational European CO_2 storage sites

There are currently two operational offshore CO_2 storage sites in Europe which deploy deep-focused, surface geophysical techniques: Sleipner and Snøhvit. Table 3.1 provides a summary of their main features as well as the deployed monitoring tools.

I now describe each of the storage sites and provide an overview of their deep-focused geophysical monitoring programs and objectives.

Table 3.1. Summary of current operational offshore EU CCS sites and the deployed deep-focused geophysical monitoring tools. Modified from IEAGHG (2015).

	Sleipner	Snøhvit
Location	Norwegian North Sea	Norwegian Barents Sea
Water depth	90 m	250-330 m
Injection start	1996	2008
Injection rate	1 Mt/year	0.77 Mt/year
Amount injected	15 Mt	2.3 Mt
Total intended	20 Mt	23 Mt
Injection depth	1012 m	2600 m
Type of reservoir	Mio-Pliocene, sandstone saline reservoir	Heterogeneous Mesozoic interbedded sandstone-shale
Deployed monitoring tools		
3D/4D seismic	✓	✓
2D seismic	✓	✓
Gravity (surface)	✓	
CSEM (seabed)	✓	

3.1.1 Sleipner

Sleipner is the world's longest running industry-scale CO_2 storage project, having commenced in 1996. CO_2 is separated from natural gas produced from the neighbouring Sleipner West field and is then reinjected into the Utsira Sand, a major saline reservoir of late Cenozoic age (Chadwick et al., 2008). Injection is via a deviated well at a depth of 1012m. The average injection rate is 1 Mt/year with close to 15 Mt of CO_2 injected by 2014 (IEAGHG, 2015).

The Utsira sand is an ideal reservoir for CO_2 storage. The reservoir is 250m thick and comprises uncemented and weakly consolidated sand of the late Cenozoic age. Porosities range from 35 to 40% with permeabilities ranging from 1 to 8 Darcy (Zweigel et al., 2004).

The monitoring objectives at Sleipner focus on the identification of storage risk, namely:

- Migration through geological seals,
- Lateral migration into wellbores,
- Lateral migration of CO_2 outside the Sleipner license area.

The monitoring program is based around containment and conformance assurance. A major focus is to track the growth and migration of the CO_2 plume within the reservoir in order to predict future behaviour. A significant time-lapse monitoring program has been deployed since 1994. The deployed surface geophysical techniques are outlined in Table 3.2.

Containment assurance

Using seismic techniques, the CO_2 plume at Sleipner has been successfully mapped due to bright amplitude reflections within the reservoir, as well as prominent velocity push-down effects at the base of the reservoir. Time-lapse seismic images have been able to image successfully the clear progressive growth of the plume at the top reservoir since injection started in 1996 (Figure 3.1). Interpretation of the time-lapse images has identified nine separate accumulations of CO_2 within the reservoir. These

have been attributed to thin seismically-unresolvable intra-reservoir mudstones. To date, there have been no indications of a loss of containment outside the Utsira reservoir. However, there is still some uncertainty as to whether migration out of the reservoir will be visible on seismic sections. Changes in the seismic time-lapse images outside the storage reservoir have been identified throughout the monitoring process, but have been attributed to variable amounts of repeatability error or noise. Chadwick and Noy (2010) estimated that the Sleipner datasets can detect accumulations of CO_2 corresponding to 2800 tonnes at the top reservoir. However, this value assumes full CO_2 saturation as well as a uniform saturation distribution. Lower saturations, and hence, lower velocities, would result in lower mass detection.

Table 3.2. Surface, deep-focused geophysical techniques deployed at Sleipner from 1994 and the total injected amount of CO_2 at the time of each survey. Modified from IEAGHG (2015).

Year	3D seismic	2D seismic	Gravity	CSEM	Total CO_2
1994	Baseline				
1995					
1996					Injection starts
1997					
1998					
1999	✓				2.35 Mt
2000					
2001	✓				4.25 Mt
2002	✓		✓		4.97 Mt
2003					
2004	✓				6.84 Mt
2005			✓		7.74 Mt
2006	✓	✓			8.40 Mt
2007					
2008	✓			✓	10.15 Mt
2009			✓		11.05 Mt
2010	✓				12.06 Mt
2011					
2012	✓				
2013			✓		~14 Mt

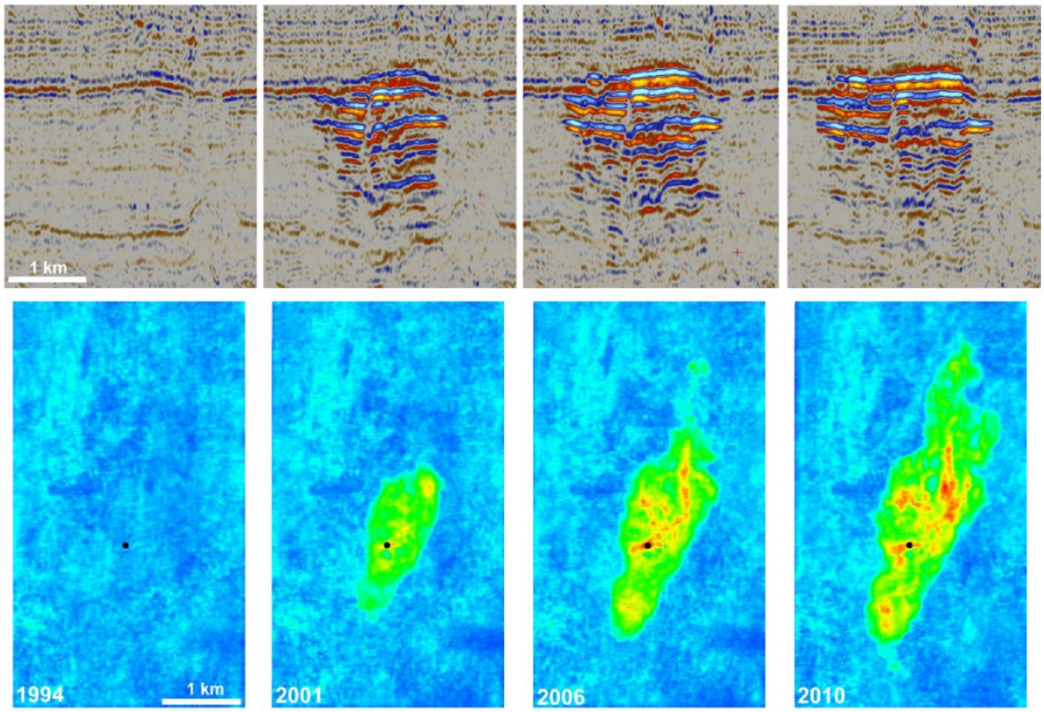

Figure 3.1. Growth and evolution of the Sleipner plume from 1994 (baseline) to 2010. Top panels show time-lapse images of the CO_2 plume (N-S cross-section). Bottom panels show the development of the plume in map view. Modified from (IEAGHG, 2015).

Conformance assurance

The key conformance parameter at Sleipner is the ability to match successfully the simulated migration of the plume with current observed plume evolution. This is based on history matching the simulated growth of the plume against layer geometry from time-lapse seismic surveys.

Earlier work, such as Arts et al., (2004) and Chadwick at al., (2005) and Chadwick at al., (2006b), has shown that reflection amplitudes are directly related to layer thicknesses. While more recently, a number of studies, such as Chadwick and Noy (2010), Singh et al., (2010), Cavanagh (2013) and Cavanagh and Nazarian, (2014), have tried to model, understand and match simulated CO_2 growth with the observed monitor data. However, matching the growth of the plume has proven difficult due to uncertainties regarding the most appropriate governing equations for flow simulation (Cavanagh, 2013, Cavanagh and Haszeldine, 2014).

Understanding of the internal reservoir behaviour of the plume is yet to be achieved. Significant uncertainties remain, in particular regarding the interaction between the CO_2 plume and the intra-reservoir mudstones, the temperature of the plume and the fine-scale distribution of dispersed CO_2 between the reflective layers (Chadwick et al., 2006b). As the structural geometry of the sealing intra-reservoir mudstones is not precisely known, the simulated thicknesses of the CO_2 accumulations are not tightly constrained, and hence do not match the observed seismic data. In order to history match the simulated with the observed, a reservoir model was built assuming purely horizontal intra-reservoir mudstones (Figure 3.2). This assumption resulted in the characteristic 'Christmas-tree' profile caused by accumulations of CO_2 beneath the thin layers. Migration of the CO_2 to the top reservoir is proposed via a single main chimney.

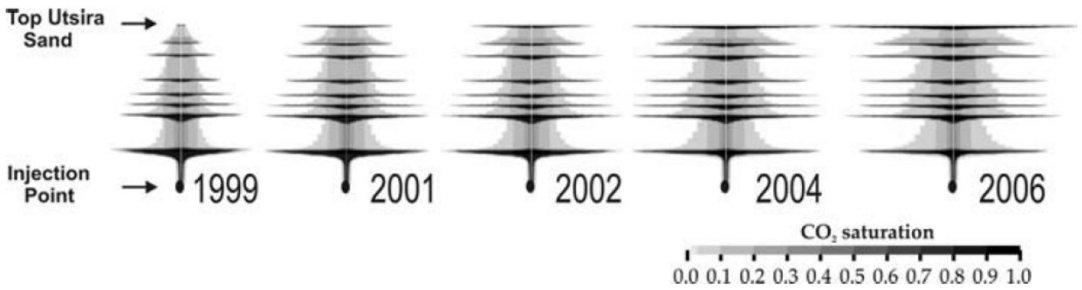

Figure 3.2. Simulated growth of the CO_2 plume from 1999 to 2006. Modified from Chadwick and Noy (2010).

History matching of the topmost layer of CO_2, trapped beneath the reservoir top-seal, has proven difficult due to the very rapid northward migration at the top reservoir between 2001 and 2006. Initially, variable flow parameters, such as lower densities and viscosities for CO_2 were used. However, recent work has shown accurate plume modelling can be achieved once pressure dissipation has been accounted for (e.g. Figure 3.3) (Cavanagh, 2013).

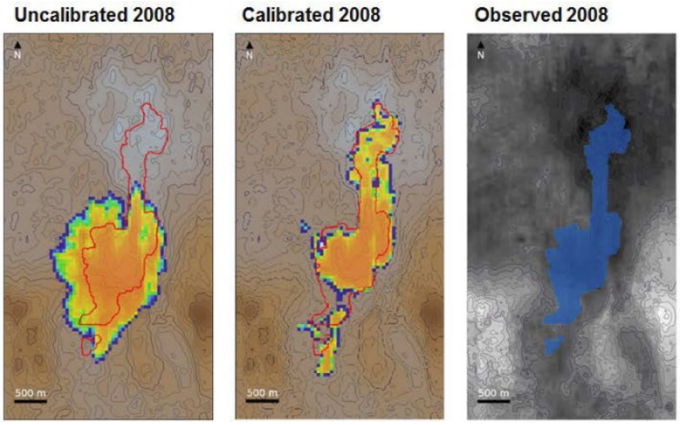

Figure 3.3. Near equilibrium match for the 2008 monitor survey to the observed CO_2 distribution below the cap rock once the simulation has been calibrated, allowing for pressure dissipation. Modified from Cavanagh (2014).

Arts et al., (2004), Chadwick et al., (2005) and Arts et al., (2009) aimed to quantify plume reflectivity and velocity push-down to verify the measured amount of injected CO_2. A 3D model of the 1999 plume was built and compared with the observed surveys of that time (Figure 3.4). A satisfactory match was obtained where 85% of the injected CO_2 was accounted for. When calculating the velocity model, one of the key assumptions was that the CO_2 was uniformly distributed throughout the reservoir.

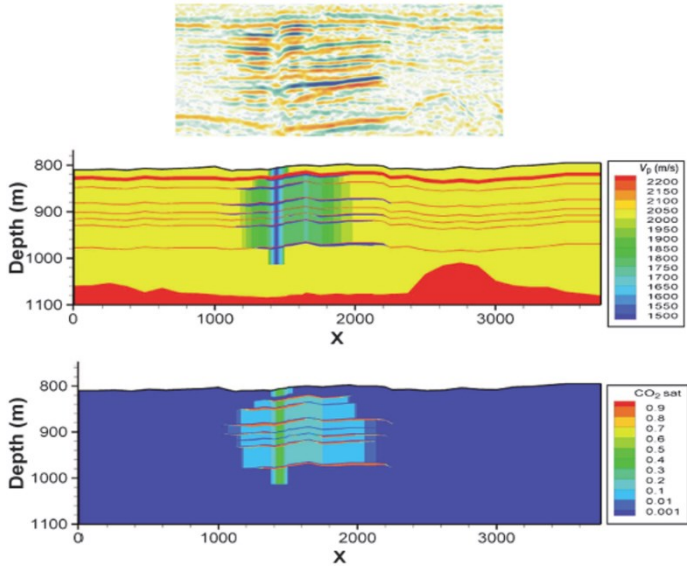

Figure 3.4. Simulated Sleipner plume in 1999 derived from acoustic modelling assuming a uniform saturation distribution. Top figure highlights the time-lapse seismic cross-section of that monitor survey, bottom is the simulated CO_2 saturation. Modified from Arts et al., (2009).

CSEM survey findings

A 2D sea bottom CSEM survey was acquired at Sleipner in 2008 with the intention of estimating the electrical resistivity of the injected CO_2. The survey profile comprised 27 seabed receivers, covering 9.5km with a total tow-line length of around 30km. Two tows were carried out, one at frequencies from 0.5 to 7 Hz, and the second at frequencies from 0.25 to 3.5 Hz (IEAGHG, 2015).

There is close to nothing published about the survey findings as the initial results were inconclusive. A single publication, by Park et al., (2013) detailed two major challenges when interpreting the Sleipner CSEM data: 1) there is no CSEM baseline survey, 2) relatively low saturations, peaking at roughly 50%, and hence, low resistivity values within the plume of roughly 10-20 Ωm were simulated to result in an anomaly change of roughly 5%, which is thought to be below a detection threshold. The detection threshold was not defined. Furthermore, one of the main challenges is the presence of 6 groups of seabed pipes crossing the survey line, which interfere significantly with the CSEM data. A lack of understanding of the overburden, namely through shallow heterogeneities, are also thought to have generated artefacts that are mixed with the plume response.

The overall negative results from the Sleipner CSEM survey have impacted negatively the deployment and potential effectiveness of the monitoring technique in future CCS projects. However, it is clear that the technique has been disadvantaged by the lack of a true baseline survey and the technique itself should not be discounted from future projects because of this. A thorough feasibility study should be performed pre-acquisition to provide information as to the applicability of the technique, in particular as this is a site-specific issue. No real feasibility study has been conducted demonstrating this.

3.1.2 Snøhvit

The Snøhvit CO_2 storage project is located offshore northern Norway in the Barents Sea. The field is a gas complex comprising three gas reservoirs: Snøhvit, Albatross and Askeladd (Hansen et al., 2013). The reservoir itself is composed of a series of fault-blocks with significant structural compartmentalisation (Figure 3.6). Gas production first commenced in August 2007. The CO_2 is separated from the produced gas and reinjected into the Tubåen Formation through a single injector at a rate of 0.8 Mt per year through three perforation intervals. A total of 23 Mt of CO_2 is planned for storage over the lifetime of the project (IEAGHG, 2015).

The Tubåen Formation is 45-75 m thick and comprises sandstones with thin shale layers and minor coals. Porosities range from 10 to 15% with permeabilities in the region of 185 – 883 mD. The reservoir is very heterogeneous with significant lateral and vertical permeability barriers. Following pressure build-up, CO_2 injection was switched into the Stø Formation in 2011. The Stø Formation is a 70-100 m thick sandstone with alternating thin shales and mudstones. The CO_2 is stored purely within the saline reservoir and does not interact with the hydrocarbon field.

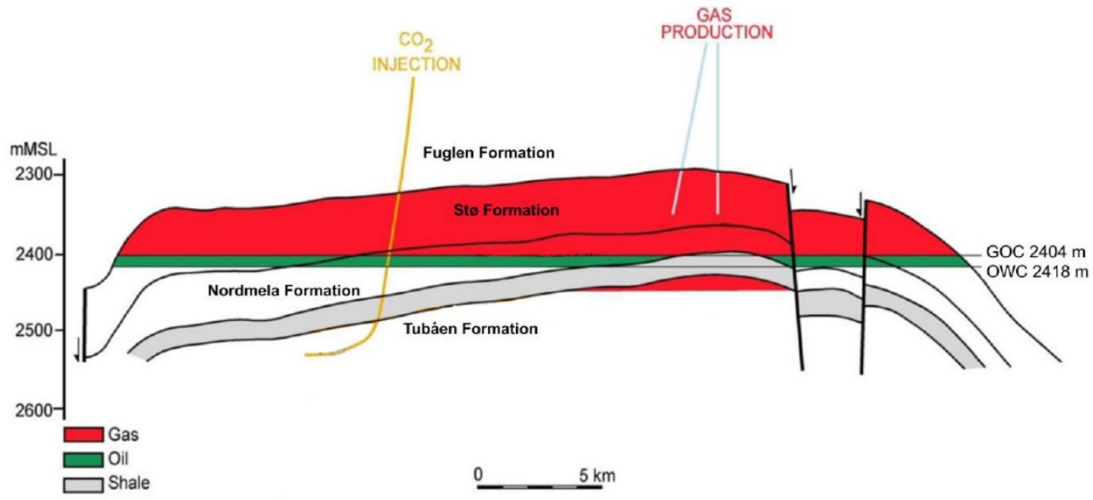

Figure 3.5. West-east simplified cross-section through the Snøhvit gas complex. Modified from IEAGHG (2015).

The main monitoring objectives at Snøhvit are:

1. Ensure injection pressures do not exceed the fracture threshold,
2. Monitor CO_2 migration and ensure no leakage to shallower depths.

The geophysical monitoring program involves the acquisition of time-lapse 3D seismic surveys as well as two seabed gravity surveys (Table 3.3).

Table 3.3. Surface, deep-focused geophysical techniques deployed at Snøhvit. Modified from IEAGHG (2015).

Year	3D seismic	Seabed gravity
2003	✓	
2004		
2005		
2006		
2007		✓
2008		
2009	✓	
2010		
2011	✓	✓
2012	✓	

Containment assurance

The 3D seismic surveys clearly image changes in the reservoir due to the injected CO_2 (Figure 3.7). Reflectivity and time-shifts are seen close to the injection point while more diffuse changes are observed away from the injection zone due to pressure effects. Current datasets show no evidence of a loss of containment out of the Tubåen Formation. To date, no current quantitative analysis of leakage detection thresholds has been carried out (IEAGHG, 2015).

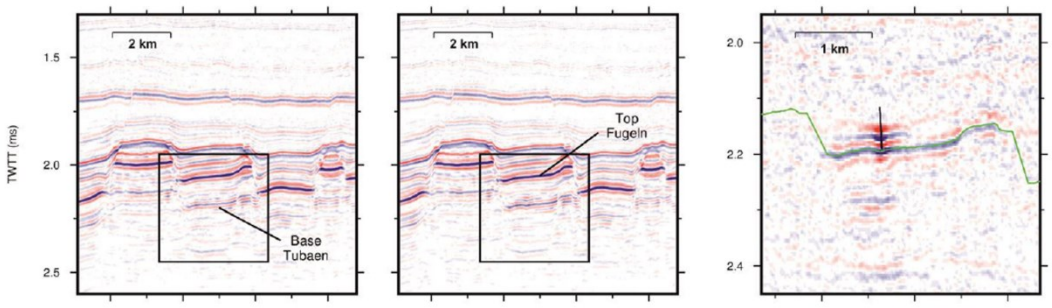

Figure 3.6. Seismic section through the injection point showing the 2003 baseline survey (left), 2009 monitor survey (middle) and the time-lapse difference (right). Modified from IEAGHG (2015).

Conformance assurance

The key conformance parameter at Snøhvit is the ability to map not only the CO_2 plume but also the pressure footprint due to injection. However, unlike Sleipner, only a few publications detail the monitoring results at Snøhvit. Current research has proved the ability to discriminate between fluid saturation and pressure changes within the reservoir (Grude et al., 2013), while more recent work has estimated the distribution and saturation of the CO_2 in the Tubåen sandstone unit (Grude et al., 2014). However, when calculating the velocity model, the authors assumed the CO_2 distribution within the plume to be uniform with maximum saturations equal to $1 - S_{wir}$.

Summary

It is clear that 4D seismic deployed throughout the lifespan of the Sleipner and Snøhvit CCS project have provided a powerful tool, capable of imaging the CO_2 plume to a high level of detail. However, understanding the internal structure of the plume, as well as history matching the migration of the plume at the top-seal has proven difficult. There are still uncertainties as to the potential to detect accurately a leak outside the reservoir (migrating front of CO_2) as well as the most relevant velocity end-member model when monitoring for conformance. A uniform saturation distribution was assumed at both fields.

Unfortunately, the CSEM survey deployed at Sleipner returned inconclusive results, namely due to a lack of a true baseline survey. Although the Sleipner CSEM survey negatively impacted the applicability of CSEM at other CCS sites, it should not be discounted altogether as it is very site-specific and requires a baseline survey pre-acquisition.

4. Monitorability workflow

I present the monitorability workflow developed specifically for this project. The three-stage model-driven workflow is based on typical reservoir simulation to geophysical forward modelling workflows used in the oil and gas industry. This workflow is a modification of those workflows with a focus on CO_2 monitoring. The workflow models variations in the time-lapse signal through the application of fluid-flow modelling, rock physics modelling and seismic and CSEM forward modelling. I describe each stage in the workflow, with a focus on the rock physics modelling and the interplay between CO_2 saturation, the geophysical response and geological heterogeneity.

The workflow described in this chapter has been published under the title *Seismic monitoring of CO_2 plume growth, evolution and migration in a heterogeneous reservoir: Role, impact and importance of patchy saturation* in Eid et al., (2015a).

4.1 Introduction

Reservoir simulation to geophysical forward modelling workflows are typically used before, during, and after CO_2 injection to determine what a given sensor would measure in a given environment. The process involves the simulation of CO_2 injection into a geological model, which is then used to generate a synthetic seismic section or a synthetic EM response. This tool is used during initial storage-site assessment stages to determine whether the injected CO_2 will generate an interpretable change.

Synthetic models generated during and after injection facilitate the interpretation of processed data and assist in the process of history matching. Current best practice of such workflows for CO_2 storage monitoring using seismic and EM techniques varies considerably due to practical experience and field deployment.

4.1.1 Seismic monitoring workflows

For seismic techniques, fluid-flow to synthetic seismic workflows have been successfully used to history match the migration of the CO_2 plume at Sleipner (Chadwick et al., 2006a, Singh et al., 2010, Boait et al., 2012). When generating synthetic seismic sections for CO_2 monitoring, current workflows focus on one rock-physics end-member: a uniform saturation distribution. This end-member assumes immiscible and homogenously distributed phases throughout the pore space. This assumption may be valid in homogeneous, virgin reservoirs. However, during CO_2 injection, the equilibrium distribution of fluid phases (brine and CO_2) may be disturbed, resulting in a non-uniform phase distribution: a patchy saturation distribution. There is confusion in the current literature as to the most appropriate rock-physics end-member model to simulate this. Table 4.1 provides a summary of published papers, in chronological order, of the assumed rock-physics end-member models used to generate the synthetic seismic response. Most of the publications assume a uniform saturation distribution or mention patchy saturation with no application. This highlights the confusion behind the range of pore-fluid saturation distributions which could be encountered and is therefore critical when assessing the potential of seismic techniques to monitor injected CO_2.

Table 4.1. Summary of current CCS publications on seismic monitorability in chronological order, with a focus on the assumed rock-physics fluid saturation end-member model.

Publication	Summary	Fluid saturation
Chadwick et al., (2004)	4D seismic imaging of the CO_2 plume at the Sleipner Field. Focus on high reflection amplitude and velocity push-down effects.	Uniform, but mention patchy.
Chadwick et al., (2005)	4D quantification of CO_2 plume growth at the Sleipner CCS site. Uniform fluid saturation assumed and accounted for 85% of injected CO_2.	Uniform
Arts et al., (2007)	Generated synthetic seismic sections of the Sleipner CCS site to match real time-lapse seismic data.	Uniform
Arts et al., (2009)	Acoustic and elastic modelling of seismic time-lapse data from the Sleipner CCS site.	Uniform
Kazemeini et al., (2010)	Modelled the CO_2 response of seismic data from the Ketzin CCS site. CO_2 was simulated in a homogeneous reservoir with a single, constant saturation value.	Uniform & patchy
Mukhopadhyay et al., (2010)	Modelled CO_2 migration in brine aquifers through time-lapse seismic monitoring.	Uniform
Cairns et al., (2012)	Assess the ability of seismic techniques to identify trapping mechanisms during CCS. Simple scenario of a plume in a homogeneous reservoir.	Uniform & patchy
Nader et al., (2012)	Effectiveness of seismic detection of CO_2 migration near the Aquistore CO_2 injection site.	Uniform
Pevzner et al., (2013)	Modelled the feasibility of time-lapse monitoring of small quantities of CO_2 at the Otway Project site. CO_2 was modelled as a structurally trapped, and highly saturated accumulation.	Uniform
White (2013b)	Quantitative CO_2 estimates from time-lapse 3D data from the Weyburn-Midale CO_2 storage project.	Uniform
Grude et al., (2014)	Estimated the distribution & saturation of the CO_2 in the Tubåen sandstone unit at the Snøhvit CO_2 storage site.	Uniform
Padhi et al., (2014)	Generated a synthetic seismic signature assuming patchy saturation for time-lapse monitoring.	Patchy
Chadwick et al., (2014)	Leakage detection and measurements in subsurface volumes from 3D seismic data at the Sleipner CCS site. Modelled CO_2 as a structurally trapped, and highly saturated accumulation.	Uniform
Si et al., (2015)	Compared the p-wave impedence inverse sections for both uniform and patchy saturation, however did not generate and compare synthetic seismic sections.	Uniform and patchy

4.1.2 CSEM monitoring workflows

No monitoring workflow has been published for the application and deployment of CSEM techniques at CCS sites. However, the feasibility of CSEM monitoring of offshore oil and gas reservoirs has been studied extensively (Lien and Mannseth, 2008, Orange et al., 2009, Black and Zhdanov, 2009, Andréis and MacGregor, 2011, Kang et al., 2012, Bhuyian et al., 2012). The authors simulate successfully the ability of CSEM techniques to detect fluid changes in the reservoir due to oil or gas production. However, in each study, the generated synthetic time-lapse responses were modelled in the frequency domain only and using either a 1D or 2D model, or a very simple 3D model. Table 4.2 summarises the modelled source frequency and the type of reservoir model for each study.

Table 4.2. Summary of modelled source frequency and type of reservoir model analysed.

Publication	Source frequency	Reservoir model
Lien and Mannseth, (2008)	0.1 Hz	2D
Orange et al., (2009)	0.1 Hz	2D
Black and Zhdanov (2009)	0.01, 0.3 Hz	2D
Ellis and Sinha (2010)	0.5, 0.125 Hz	1D
Andréis and MacGregor (2011)	0.3, 0.9, 1.5 Hz	3D
Bhuyian et al., (2011)	0.25, 0.5, 1, 2 Hz	3D
Kang et al., (2012)	0.1, 0.5 Hz	2D
Bhuyian et al., (2012)	0.25, 0.5, 1, 2 Hz	3D

Current research models the EM response in the frequency-domain. This is only one approach. Another approach is modelling the synthetic EM response in the time-domain through the application of the multi-transient electromagnetic (MTEM) method. Frequency-domain CSEM measures the amplitude and phase for certain defined frequencies, while MTEM measures the transient change of the received signal containing the full frequency spectrum. This is a clear advantage over

frequency-domain CSEM. Another advantage is the ability to image a clear arrival time, associated with only the subsurface anomaly, when analysed in time-lapse.

The advantages of analysing the EM response in the time-domain have been demonstrated by Wright et al., (2002) and Ziolkowski et al., (2007). Wright et al., (2002) demonstrate the potential for monitoring the movement of subsurface fluids by comparing the difference in the measured earth response at two production times. Ziolkowski et al., (2007) present a detailed explanation of the time-domain CSEM technique, generating synthetic earth responses for 1D examples, as well as a 3D synthetic earth response of an underground gas storage demonstration site in southwestern France. Both publications highlight the effectiveness of the time-domain CSEM method, in particular the ability to visualise the data as common-offset sections.

4.1.3 Monitorability workflow

To address the limitations of current reservoir simulation to geophysical forward modelling workflows for both seismic and EM application, I have developed a flexible workflow which can be adapted for both methods. The workflow describes a numerical modelling approach to model variations in the synthetic time-lapse response due to CO_2 migration. The workflow consists of fluid-flow modelling, rock-physics modelling and synthetic seismic or CSEM forward modelling, as illustrated in Figure 4.1. The baseline and monitor surveys are compared to assess the change in geophysical signal over time. This workflow has been applied throughout the project to assess the ability of seismic techniques to monitor CO_2 containment and conformance for a range of CO_2 storage scenarios.

For seismic monitoring, to account for the uncertainties regarding the fluid saturation distribution, I have modified typical fluid-flow to synthetic seismic workflows to model both end-member models – uniform and patchy – in order to generate the widest range of velocity distributions which could be encountered. As the range of saturations in a pore space is constrained by limits for irreducible saturation, I further modified the patchy curve, so that it starts from a given irreducible water saturation.

For CSEM monitoring, I build on the work presented by Wright et al., (2002) and Ziolkowski et al., (2010) and model the time-domain EM response to CO_2 injection and storage in a saline reservoir. The workflow assesses the CO_2 storage monitoring potential of CSEM techniques by simulating the EM response over a potential CO_2 storage site in the time-domain. I model the effect of CO_2 injection on the EM response by comparing the measured earth response of the baseline survey and a monitor survey. Furthermore, I visualise the synthetic data and common-offset sections.

This chapter explains the different stages in the monitorability workflow. First, I explain the basic requirements for fluid-flow modelling. Second, I detail the effect of fluid saturation on both seismic and EM properties. I focus on the interplay between CO_2 saturation, the geophysical signal and geological heterogeneity. Last, I describe the geophysical modelling workflow, defining the entities needed for the generation of both seismic and CSEM synthetic surveys. I also define the towed streamer survey design and acquisition for both seismic and CSEM. As the input parameters for each stage are site and simulation specific, I only describe each step in the workflow. The input parameters are explained in detail for each piece of work which applies the monitorability workflow.

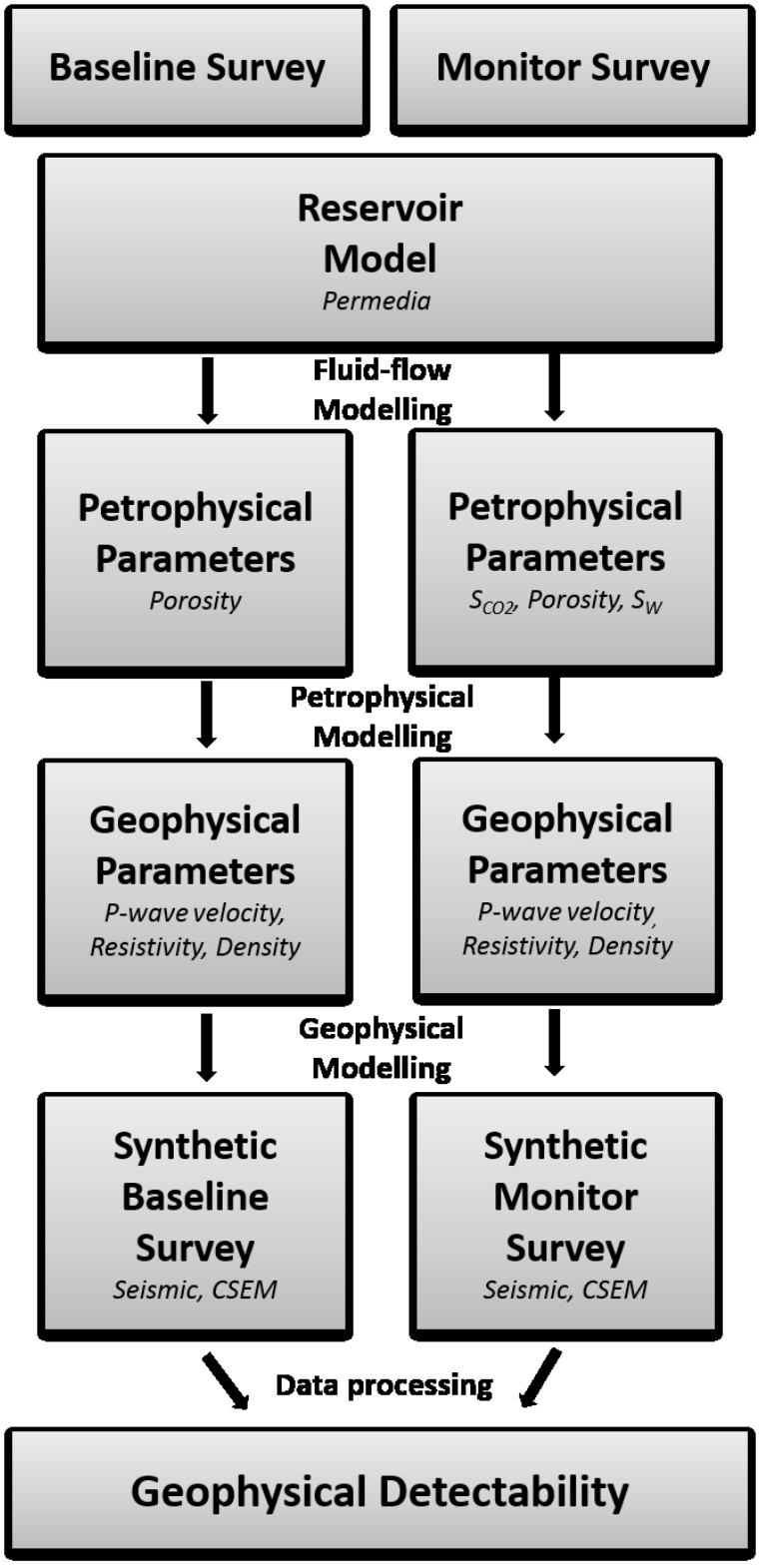

Figure 4.1. Monitorability workflow detailing the numerical modelling approach to model the time-lapse response of injected CO_2.

4.2 Fluid-flow modelling

Permedia's CO_2 black oil simulator (BOS) (Permedia, 2014) has been used throughout the project to simulate the injection and migration of CO_2 in the subsurface. Permedia's CO_2 BOS is specifically adapted to handle CO_2 plume development and brine dissolution and has been numerically validated against SPE comparative models: SPE1, SPE2, SPE7, SPE9 and SPE10 (Permedia, 2014). Permedia's CO_2 BOS uses typical governing equations for classical black oil simulators, principally material balance and Darcy flow. Material balance is the conservation of materials, where the amount of mass leaving a controlled volume is equal to the amount of mass entering the volume minus the amount of mass accumulated in the volume (Hantschel and Kauerauf, 2009). Darcy's Law is the relationship between the pressure gradient and the rate of fluid flow through a porous medium. This is illustrated as (Ringrose and Bentley, 2015):

$$q = \frac{-k}{\eta} (\nabla P + pgz) \tag{4.1}$$

where q is the flow rate (m^3/s), k is the permeability (m^2), η is the viscosity (Pa.s), ∇P is the pressure difference (Pa) and pgz is the pressure gradient due to gravity. The flow can be laminar steady state with constant pressure gradient and constant saturation or unsteady flow with varying pressure gradient and fluid saturation (Tiab and Donaldson, 2011).

4.2.1 Modelling structure

The general structure of reservoir fluid-flow models includes:

- Geological model,
- Fluid properties,
- Rock/fluid properties data,
- Well data and injection strategy.

The basic framework for geological models consists of interfaces (horizons and faults) between different rock types. The model is divided into grid cells of properties that

depend on the geology. For fluid-flow simulations, density and viscosity of each fluid are needed. In addition, the phase and solubility of the injected CO_2 (liquid, gas or supercritical) is calculated based on input temperature and pressure values. Throughout the thesis, an assumption is made that the CO_2 will constantly be in a supercritical state. This is where CO_2 flows like a gas but with a density of a liquid (Figure 4.2). This occurs at temperatures higher than 31.1°C and pressures greater than 73.9 bar, (IPCC, 2005).

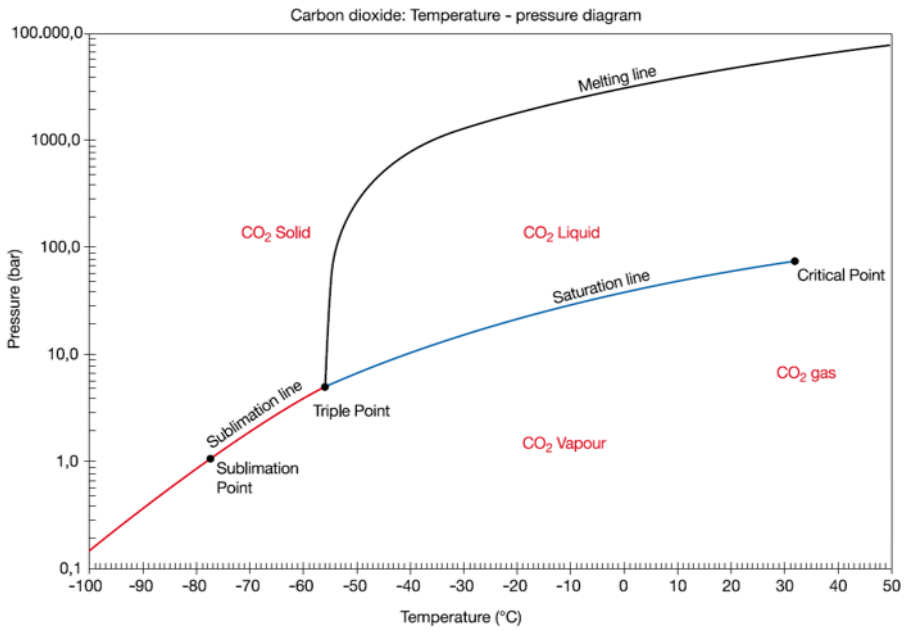

Figure 4.2. CO_2 phase diagram showing the change in state corresponding with change sin pressure and temperature. Modified from IPCC (2005).

Relative-permeability and capillary pressure curves are input into the simulator to model the interaction between the two fluid phases (CO_2 and water) as well as the capillary forces between the two fluids. Lastly, a specification of the well location, as well as the injection strategy is needed for each well.

When applying the monitorability workflow, I specify the unique geological model, input fluid properties and well and injection strategy. The results from the fluid-flow modelling determine the time-steps used in the remaining stages of the workflow.

4.3 Rock physics modelling

Once the water-CO_2 distributions in the reservoir have been determined, the corresponding changes in the petrophysical properties for each simulated grid block and each time-step are calculated. I now describe the effect of fluid saturation on both seismic and EM properties.

4.3.1 Effect of fluid saturation on seismic properties

The Gassmann fluid substitution workflow (Smith et al., 2003) is used to model the effect of fluid saturation on seismic properties. Fluid substitution is an important part of seismic rock physics analysis, producing a tool for fluid modelling and quantification of various fluid scenarios which may result in an observed anomaly. The primary objective of fluid substitution is to model the seismic properties and density of a reservoir at a given pore fluid saturation.

Seismic velocity can be estimated using known rock moduli and density. P-wave velocities in isotropic media are estimated as (Mavko et al., 2009, Reynolds, 2011),

$$\mathrm{V_p} = \sqrt{\frac{\mathrm{K_{sat}} + {}^{4}/_{3}\mu}{\rho_{\mathrm{bulk}}}} \tag{4.2}$$

where Vp is the P-wave velocity, K_{sat} and μ are the saturated bulk and shear moduli, and ρ_{bulk} is the mass density. K_{sat} and μ can be calculated using different empirical and theoretical methods relating the elastic-wave velocities to the pore, fluid and frame properties (Kazemeini et al., 2010). The density of the saturated rock can be computed using a simple mass balance equation,

$$\rho_{bulk} = (1 - \varphi)\rho_m + \varphi\rho_{fl} \tag{4.3}$$

where φ is porosity, ρ_m is the density of the matrix and ρ_{fl} is the density of the fluid. The matrix density can be estimated by arithmetic averaging of the individual minerals as,

$$\rho_{matrix} = V_{clay}\rho_{clay} + V_{qtz}\rho_{qtz} \tag{4.4}$$

where ρ and V are the density and volume fractions of the clay and quartz minerals, respectively.

Gassmann's equation (Gassmann, 1951) is one of the most commonly used theoretical approaches to estimate the effect of fluid changes on elastic properties. Gassmann's equation relates the bulk modulus of a saturated rock (K_{sat}) to its porosity (φ), fluid bulk modulus (K_{fl}), matrix bulk modulus (K_m), and dry frame bulk modulus (K_{dry}) as:

$$K_{sat} = K_{dry} + \frac{\left(1-\frac{K_{dry}}{K_m}\right)^2}{\frac{\varphi}{K_{fl}} + \frac{(1-\varphi)}{K_m} - \frac{K_{dry}}{K^2 m}}. \quad (4.5)$$

Calculation of the saturated bulk modulus (K_{sat}) is a two-part process. It involves the calculation of the dry bulk modulus of the rock frame, drained of its initial fluid, after which the bulk modulus of the rock saturated with desired fluids is calculated (Smith et al., 2003). I should note that there are many alternative forms of the Gassmann equation (4.5), but I have found this form to be the most appropriate when performing fluid substitution.

Several assumptions limit the applicability of Gassmann's equation. These have been thoroughly discussed by Berryman (1999), Wang (2001),Smith et al., (2003), Han and Batzle (2004), Adam et al., (2006) and Dvorkin et al., (2014). The model is first assumed to be homogeneous and isotropic, and that the pore space is connected. This assumption is not honoured when the rock framework is composed of multiple minerals of large contrasts in elastic stiffness. Gassmann's equation is also only valid at low frequencies (< 100 Hz) (Wang, 2001, Mavko et al., 2009) such that induced pore pressures are equilibrated over a length scale much greater than a pore dimension and much less than the wavelength of the passing seismic wave (Wang, 2001, Smith et al., 2003). This allows for pore fluid to flow and eliminate pore-pressure gradients induced by the passing seismic wave. Gassmann's equation also assumes that the pores are filled with a frictionless fluid. This implies that the viscosity of the saturating fluid is zero. This assumption also assumes full equilibrium of pore fluid

flow. The application of Gassmann's equations also assumes immiscible and homogeneously distributed phases throughout the pore space (uniform fluid saturation). This assumption may be valid in homogeneous, virgin reservoirs or trapped hydrocarbon accumulations which have come to equilibrium over long geological timescales. During drilling, production, or CO_2 injection however, the equilibrium distribution of phases may be disturbed, resulting in a non-uniform phase distribution.

K_{dry} & μ_{dry} - Dry frame bulk modulus and shear modulus

Prior to the calculation of Gassmann's equation, it is necessary to determine the dry frame bulk modulus K_{dry} and shear modulus μ_{dry}, of the porous rock. This is the low-frequency drained bulk and shear modulus of the rock and, once calculated, is held constant throughout (Smith et al., 2003).

K_{dry} may be derived from (1) laboratory measurements, such as velocity measurements from controlled humidity-dried core, (2) empirical relationships, or (3) direct calculations from log data (Wang, 2001, Smith et al., 2003). Since I have no laboratory or well log measurements, I apply an empirical relationship to calculate K_{dry} and μ_{dry} for the modelled lithologies.

The application of empirical models is based on the knowledge of how grains and pores are arranged relative to each other. This allows for the calculation of K_{dry} as a function of porosity. Initially, this is performed by calculating the Voigt (1928) and Reuss (1929) end-member bounds for K_{dry}. The Voigt ($K^{(V)}_{dry}$)and Reuss ($K^{(R)}_{dry}$) bounds on dry rock modulus are (Mavko and Mukerji, 1995):

$$K^{(V)}_{dry} = K_{min}(1-\varphi) + K_{air}\ , \tag{4.6}$$

$$K^{(R)}_{dry} = \left[\frac{(1-\varphi)}{K_{min}} + \frac{\varphi}{K_{air}}\right]^{-1}. \tag{4.7}$$

where, K_{min} is the mineral bulk modulus, φ is the porosity, and K_{air} is the bulk modulus of the pore-filling gas, which is assumed to be zero.

These bounds are the largest ranges of possible dry rock moduli (Mavko and Mukerji, 1995, Han and Batzle, 2004). At zero porosity, the rock has the properties of the mineral. At the high-porosity limit, the elastic properties are determined by the elastic contact theory. K_{dry} will always lie between the two cases. The Voigt bound explains the theoretical stiffest way to mix load-bearing grains and pore-filling material. This is a representation of contact cement. While the Reuss bound explains the theoretical softest way to mix load-bearing grains. This describes the effect of sorting.

However, as demonstrated by Han and Batzle (2004), reservoir rocks are far from the Voigt and Reuss bounds (Figure 4.3). There is a great difference between the calculated bounds and measured values from rocks. Most rocks have an 'upper limit' to their porosity. This is termed critical porosity (φ_c) (Nur et al., 1998). To account for this, the Voigt bound is modified by φ_c to provide tighter constraints for dry and fluid saturated bulk moduli. This varies amongst differing lithologies. For this reason, Avseth et al., (2005) suggest the use of different rock physics models for different geological scenarios. I now describe the two rock physics models used in this thesis to calculate K_{dry}.

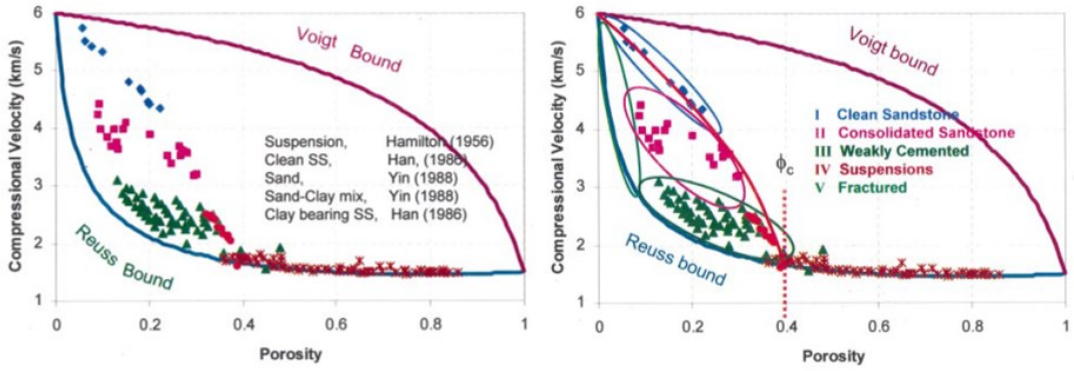

Figure 4.3. Measured compressional velocity distributions for a range of lithologies in comparison with the Voigt and Reuss bounds (left) and critical porosity (right). Figure modified from Han and Batzle (2004).

The friable sand model (Dvorkin and Nur, 1996) was used to calculate K_{dry} for all sandstone lithologies in this thesis. The friable sand model calculates the elastic properties of the grains for two sorting end members: a 'well sorted' reservoir at a

critical porosity (φ_c) of 40% for sandstones (Nur et al., 1998), and a poorly sorted sand at zero porosity. Critical porosity represents the porosity at the time of deposition, as depicted in Figure 4.4. The 'well sorted' sand member is represented as a well-sorted package of similar grains whose elastic properties are determined by the grain contacts. The poorly sorted sands are modelled as the 'well-sorted' end member modified with the addition of smaller grains deposited in the pore space. The addition of the smaller grains deteriorates sorting, decreases porosity and slightly increases the stiffness of the rock (Avseth et al., 2005).

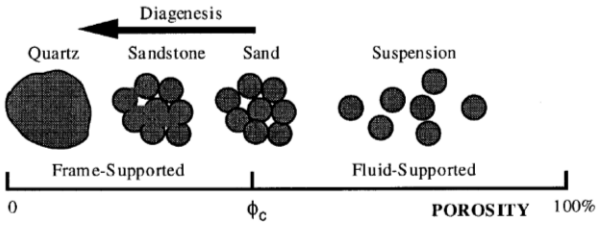

Figure 4.4. Diagenesis of sand and the assumed porosity at each stage. φ_c is the porosity at the time of deposition. Modified from Nur et al., (1998).

First the Hertz-Mindlin contact theory (Mindlin, 1949) is used to predict the change in K_{dry} at a critical porosity. The Hertz-Mindlin contact theory (Mindlin, 1949) describes the mechanical interaction between two uncemented elastic grains. Following Avseth et al., (2005), the elastic moduli of the well-sorted sand end member at critical porosity is given by:

$$K_{HM} = \left(\frac{{n_c}^2(1-\varphi_c)^2\mu^2}{18\pi^2(1-v)^2}P\right)^{\frac{1}{3}} \tag{4.8}$$

$$\mu_{HM} = \frac{5-4v}{5(2-v)}\left(\frac{3{n_c}^2(1-\varphi_c)^2\mu^2}{2\pi^2(1-v)^2}P\right)^{\frac{1}{3}} \tag{4.9}$$

where K_{HM} and μ_{HM} are the Hertz-Mindlin dry rock bulk and shear moduli at a critical porosity φ_c. P is the effective pressure, μ and v are the shear modulus and Poisson's ratio of the solid phase, and n_c is the coordination number (Avseth et al., 2005).

Poisson's ratio, expressed in terms of the bulk and shear moduli, is expressed as:

$$v = \frac{3K_m - 2\mu}{2(3K_m + \mu)} \tag{4.10}$$

Poisson's ratio is an elastic constant that is a measure of the compressibility of material perpendicular to applied stress. For sandstones, there is a wide range, of which the mean is roughly 0.2, while for carbonate rocks it is 0.3 and is above 0.3 for shales.

The coordination number, n_c is the average number of contacts that each grain has with surrounding grains (Mavko et al., 2009). n_c can be approximated by (Murphy, 1982):

$$n_c = 20 - 34\varphi + 14\varphi^2 \tag{4.11}$$

This empirical equation is based on a compilation of coordination number data from the literature. This included publications from Smith et al., (1929), Wadsworth (1960), and Bernal and Mason (1960) in which some studies counted the grain contacts of more than 5000 prepared samples (Smith et al., 1929). The calculated coordination numbers from Murphy (1982) showed a consistency of ± one standard deviation compared with the values observed by Smith et al., (1929).

Once K_{dry} is calculated at a critical porosity, the elastic moduli of the poorly sorted sand end member is calculated. As the rock at zero porosity must have the properties of the mineral, the bulk (K) and shear (μ) moduli of the mineral is used.

Therefore, once the moduli of both end-member models have been calculated, the dry bulk and shear modulus of the friable sand mixture can then be calculated as follows:

$$K_{dry} = \left(\frac{\varphi/\varphi_c}{K_{HM} + (4/3)\mu_{HM}} + \frac{1 - \varphi/\varphi_c}{K + (4/3)\mu_{HM}} \right)^{-1} - 4/3\,\mu_{HM} \tag{4.12}$$

$$\mu_{dry} = \left(\frac{\varphi/\varphi_c}{\mu_{HM} + z} + \frac{1 - \varphi/\varphi_c}{\mu + z} \right)^{-1} - z \tag{4.13}$$

where,

$$z = \frac{\mu_{HM}}{6}\left(\frac{9K_{HM}+8\mu_{HM}}{K_{HM}+2\mu_{HM}}\right) \tag{4.14}$$

φ/φ_c is the original sphere-pack phase, while $1 - \varphi/\varphi_c$ is the concentration of the pure solid phase (which is added to the sphere pack to decrease porosity) in the rock (Avseth et al., 2005). The calculated K_{dry} and μ_{dry} values for the sandstone are then input directly into Gassmann's equation.

The constant clay model (Avseth et al., 2005), an adaptation of the friable-sand model which varies as a function of clay content, is used for all shale lithologies. This describes the velocity-porosity behaviour for shales with a constant V_{clay} ratio. The same equations are used as for the friable-sand model, however, the high porosity end-members vary as a function of clay content. Equations (4.12) and (4.13) are applied to obtain K_{dry} and μ_{dry} for the shales, however φ_c is set to 60-70% (Avseth et al., 2005). The higher the clay content, the higher the critical porosity.

K_m - Matrix bulk modulus

The calculation of the matrix bulk modulus K_m is a function of the composition of the rock. In the absence of core data, lithology can be approximated from wireline logs through the simple calculation of V_{clay} and the assumption of two mineral end members, quartz and clay (Smith et al., 2003). Once determined, K_m is calculated via the application of Voigt-Reuss-Hill (VRH) averaging of the mineral constituents.

The VRH method states that the calculated effective moduli of a solid will fall between two bounds controlled by the volume fraction and elastic moduli of each grain (Mavko and Mukerji, 1998). These two bounds are simply the average of the harmonic mean (Reuss average) and the arithmetic mean (Voigt average) of the minerals. The Voigt and Reuss averages represent the upper and lower bounds of the effective elastic modulus and are interpreted as the ratio of average stress and average strain (Mavko et al., 2009). As stress and strain are generally unknown and are expected to be non-uniform, the Voigt bound is calculated assuming uniform strain,

while the Reuss bound is calculated assuming uniform stress. The VRH average is the arithmetic average of the Voigt bound and the Reuss bound and provides an estimate of the moduli which can be input directly into Gassmann's equation (Figure 4.5).

For a rock consisting purely of quartz and clay, the calculation of the VRH average is expressed as:

$$K_{Reuss} = \left[\frac{V_{clay}}{K_{clay}} + \frac{V_{qtz}}{K_{qtz}}\right]^{-1} \tag{4.15}$$

$$K_{Voigt} = V_{clay}K_{clay} + V_{qtz}K_{qtz} \tag{4.16}$$

$$K_{VRH} = \frac{1}{2}\left(K_{Reuss} + K_{Voigt}\right) \tag{4.17}$$

where V and K are the volume fraction and bulk modulus of the two components.

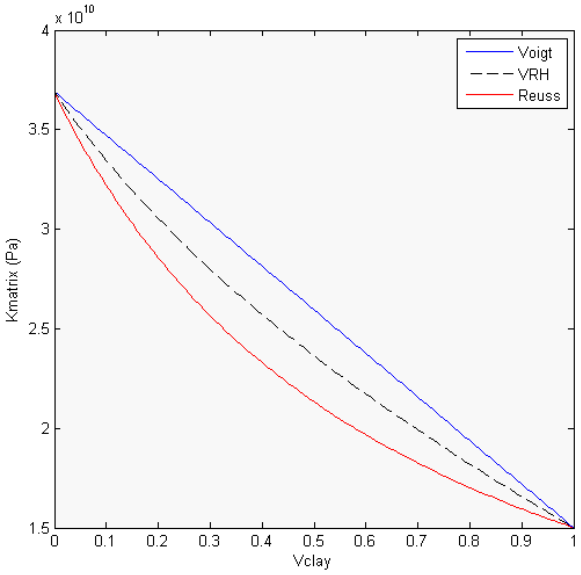

Figure 4.5. Matrix properties calculated using the VRH-average of individual mineral end-member components- a 100% quartz (K = 37 GPa) and 100% wet clay (K = 15GPa)

Laboratory measured velocity-porosity relationships for clastic sediments have been demonstrated to fall between the two bounds (Marion, 1990, Han and Batzle, 2004). However, it should be noted that the measured values fall closer to the Reuss bound. No material has been found to follow the Voigt bound. Mavko et al., (2009) attribute this to the fact that measured mixtures can never be as stiff as the calculated Voigt

bound. This limitation is generally known and accepted in the industry and that the VRH average is seen as a reasonable and sufficient approximation as the moduli are very close to begin with. Other alternative approaches are available, such as the Xu and White (1995) model, for clay-sand mixtures.

K_{fl} – Fluid bulk modulus

The mixing of two immiscible fluids in a porous rock results in velocities that are different from those resulting from saturation with a single fluid (Domenico, 1976, Gregory, 1976). This is caused by saturation changes in the fluid bulk modulus K_{fl}. However, velocities depend not only on saturation, but also on the spatial distribution of the phases in the pore space (Mavko and Mukerji, 1998). When the migrating CO_2 is spatially heterogeneous, two pore-fluid distribution end-member ranges can be encountered: homogeneous, uniform fluid saturation distribution, and heterogeneous, patchy fluid saturation distribution.

There has been substantial research into patchy and uniform saturation, namely in the field of wave attenuation and dispersion in porous media. Gassmann and Biot were the first to study wave propagation in fluid saturated mediums (Gassmann, 1951, Biot, 1956, Biot, 1962). This was followed by White (1975) who first considered saturation of two fluids (gas and water) where gas has a 'patchy' distribution amongst a fully water saturated rock. Dutta and Odé (1979a) and Dutta and Odé (1979b) then improved on the White (1975) theory to provide an agreement with analytical results. However, it wasn't until key publications such as Mavko and Mukerji (1995), Mavko and Mukerji (1998) , Dvorkin and Nur (1998) and Knight et al., (1998) that simplified the theory and presented it in a more applicable way.

I now discuss the theory behind patchy and uniform saturation as detailed by Mavko and Mukerji (1995) and the subsequent research which followed. I summarise their research with a focus on the interplay between CO_2 saturation, seismic wavelength and geological heterogeneity and comment on their sensitivity to increasing saturation.

Fluid saturation, seismic wavelength and geological heterogeneity

Varying saturations, when related to rock permeability and seismic wavelength, result in distinct velocity and reflectivity changes. The critical factor determining these ranges is the size of saturation heterogeneity, or saturation 'patch', d.

When the patch size exists on a scale which is very small compared with a seismic wavelength ($d \ll \lambda$), individual patches cannot be resolved, but can still influence velocity and impedance. Sub-resolution patches in this region can be divided into two states, known as relaxed and unrelaxed, dictated by hydraulic diffusivity and diffusion length (Mavko and Mukerji, 1998). These two relaxation states are related to the pore-fluid saturation end-members through the diffusion or critical length scale, L_c (m), which is given by

$$L_c = \sqrt{\frac{kK_{fl}}{f\eta}} \tag{4.18}$$

where f is the seismic frequency (Hz), k is the permeability (m^2) and K_{fl} and η are the bulk modulus (Pa) and viscosity (Pa-s) of the fluid respectively. The critical length scale suggests the spatial scale over which wave-induced increments of pore-pressures can reach equilibrium during a period of a seismic wave (Mavko and Mukerji, 1998).

Similar expressions for the calculation of the critical diffusion length scale have been published (Knight et al., 1998, Sengupta and Mavko, 2003, Toms et al., 2006, Mavko et al., 2009, Müller et al., 2010, Kazemeini et al., 2010, Cairns et al., 2012).

The critical length scale for a theoretical sandstone is plotted versus frequency in Figure. 4.6. The curve represents both the length scales over which fluid phases interconnect and partitions the two relaxation states in the reservoir. For a given frequency, a relaxed, uniform saturation distribution is assumed at a scale less than the calculated critical length scale, while unrelaxed, patchy saturations occur at a coarser scale, greater than the critical length scale. Both saturation scales are specific to sub-seismic scale resolution, where $L_c \ll \lambda$.

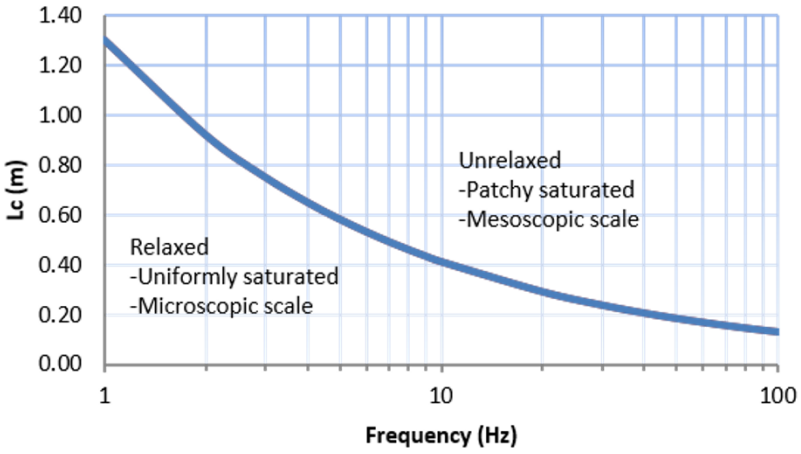

Figure 4.6. Critical length scale versus frequency for a patch saturated with CO_2 with a bulk modulus of 0.0993 GPa, viscosity of 0.58 cP and permeability of 9.87E-13 m2. These values represent CO_2 in a supercritical state, at temperature and pressure conditions of 50 °C and 15.5 MPa, respectively.

Uniform saturation

Uniform saturation refers to a scale of heterogeneity which is smaller than the critical length scale L_c and the seismic wavelength ($d < L_c \ll \lambda$). At this scale, wave-induced pressure oscillations between the different fluid phases have sufficient time to flow and relax, reaching a local isostress during a seismic period (Sengupta and Mavko, 2003). At these low frequencies, there is enough time for fluids to flow between gas- and liquid-filled areas, resulting in a less stiff porous rock which in turn results in lower wave velocities (Toms et al., 2006). The mechanisms of wave-induced pressure oscillations is illustrated in Figure 4.7. This equilibration of pore pressure allows for the assumption of a homogeneously saturated region, where the replacement of mixed fluid phases with an effective fluid bulk modulus can be applied (Domenico, 1976). This is determined through the application of the Reuss average (Reuss, 1929):

$$K_{fl} = \left(\frac{S_{CO_2}}{K_{CO_2}} + \frac{S_{brine}}{K_{brine}}\right)^{-1} \tag{4.19}$$

where S is the saturation and K is the bulk modulus of the subscript indicated fluids.

Examples of fluids distributed at this scale include irreducible water saturation (the portion of the pore volume occupied by water in a water-wet reservoir at maximum

hydrocarbon saturation) and CO_2 ganglia (isolated blobs of CO_2 occupying only one to several pores formed by detachment from the larger plume body) (Niven, 2006).

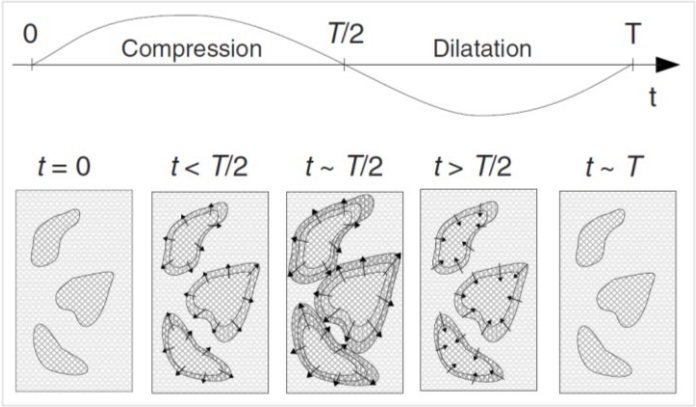

Figure 4.7. Mechanism of wave-induced fluid flow. During a seismic period, T, there will be fluid flow between the gas and liquid-filled areas (as indicated by the direction of the arrows). As pore-pressure has returned to equilibrium by the end of the seismic period, an assumption of a homogeneously saturated region can be made. Image modified from Müller et al., (2010).

Patchy saturation

Patchy saturation refers to a scale of heterogeneity which exists on a scale greater than the critical length scale but less than wavelength scale ($d > L_c \ll \lambda$). Fluid heterogeneities at this scale result in spatially varying distributions, which arise due to variations in porosity, permeability, wettability and grain types. As the patch size is larger than the critical diffusion length scale, there is not enough time for pressure equilibration during a seismic period, resulting in patches of rock which remain at different pressures. As a result, it is no longer valid to use an effective fluid bulk modulus calculated using the Reuss average. In this case, the effective rock stiffness of the rock is in an 'unrelaxed state' and is estimated using Hills (1963) constant shear modulus equation:

$$K_{fl} = \left(\frac{S_{co_2}}{K_{co_2}+(4/3)\mu_{sat}} + \frac{S_{brine}}{K_{brine}+(4/3)\mu_{sat}}\right)^{-1} - \frac{4}{3}\mu_{sat} \quad (4.20)$$

where K_{co_2} and K_{brine} are the bulk moduli of the rock saturated with CO_2 and brine, respectively. If the dry frame bulk modulus (K_{dry}) of the rock is elastically homogeneous, the shear modulus of the saturated rock is equal to the shear modulus

of the dry rock because it is not affected by pore fluids and therefore remains unchanged during fluid substitution, therefore, $\mu_{sat} = \mu_{dry}$ (Dvorkin and Nur, 1998, Kazemeini et al., 2010).

Modified-patchy saturation

Calculating the fluid bulk modulus using Hills's (1963) equation produces saturation ranges from 0 to 100%. In reality, the range of saturations in a pore space is constrained by limits for irreducible water saturation (S_{wir}) and residual saturation (R_{CO2}). This means that CO_2 saturation cannot exist at $S_{CO2} > 1\text{-}S_{wir}$, where deviation of the patchy curve starts at a given irreducible water saturation.

Following Sengupta and Mavko (2003) and Cairns et al., (2012), the effective brine (S'_{brine}) and CO_2 (S'_{CO_2}) saturations resulting from the lower limit placed due to S_{wir} is calculated as:

$$S'_{brine} = \frac{S_{brine} - S_{wir}}{1 - S_{wir}} \tag{4.21}$$

$$S'_{CO_2} = \frac{S_{CO2}}{1 - S_{wir}} \tag{4.22}$$

The modified bulk modulus of CO_2 ($K'_{sat\ CO_2}$), which is either completely brine-filled or a mix of CO_2 and residual brine, is calculated as:

$$K'_{sat\ CO_2} = \left(\frac{S_{wir}}{K_{sat\ brine}} + \frac{1 - S_{wir}}{K_{sat\ co_2}}\right)^{-1} \tag{4.23}$$

Following this, the modified Hills (1963) average during the injection of CO_2 becomes:

$$K_{fl} = \left(\frac{S'_{CO_2}}{K'_{sat\ co_2} + (4/3)\mu_{sat}} + \frac{S'_{brine}}{K_{sat\ brine} + (4/3)\mu_{sat}}\right)^{-1} - \frac{4}{3}\mu_{sat} \tag{4.24}$$

Patchy unrelaxed states result in high induced pressures and an increase in material stiffness which consequently lead to higher velocities. For this reason, patchy saturation represents the upper bound of seismic velocities as a function of saturation at seismic frequencies (Sengupta and Mavko, 2003, Cairns et al., 2012). Furthermore,

Johnson (2001) and Mavko and Mukerji (1998) have both shown that mesoscopic-scale (patchy) fluid distributions lead to a stiffer rock, and consequently higher velocities than those arising from microscopic-scale (uniform) distributions, and that these represent the upper and lower bounds of fluid bulk modulus.

Sensitivity to fluid saturation model

Figure 4.8 shows the possible range in values for P-wave velocity (V_p) predicted using the three fluid saturation distribution models: patchy, modified-patchy and uniform saturation. The results show that the change in V_p, as a function of CO_2 saturation, is heavily dependent on the saturation model used to calculate the elastic properties. These results are similar to those obtained by Sengupta and Mavko (2003), Toms et al., (2006), Lumley (2010), and Cairns et al., (2012).

The uniform saturation model predicts a rapid decrease of about 12% in V_p as CO_2 saturation increases from 0% to ~20%, while showing very little further change at higher saturations. However, patchy and modified patchy models predict a linear V_p-saturation relationship showing a linear decrease in velocity with increasing saturation. The large range of possible saturations for a given velocity demonstrates the importance of understanding and modelling the range of fluid saturation distribution models (uniform/patchy) when predicting the fluid bulk modulus prior to generating and interpreting the seismic response. Furthermore, the large range of saturations has great implications for CO_2 quantification from seismic velocities, as it highlights the level of uncertainty which could be encountered. This is evident in Figure 4.8, where an observed velocity reduction of 300 m/s could result from either 12% CO_2 assuming a uniform saturation distribution or 60% CO_2 assuming a patchy saturation distribution. Assuming purely a uniform saturation distribution could potentially underestimate the amount of stored CO_2 in the subsurface.

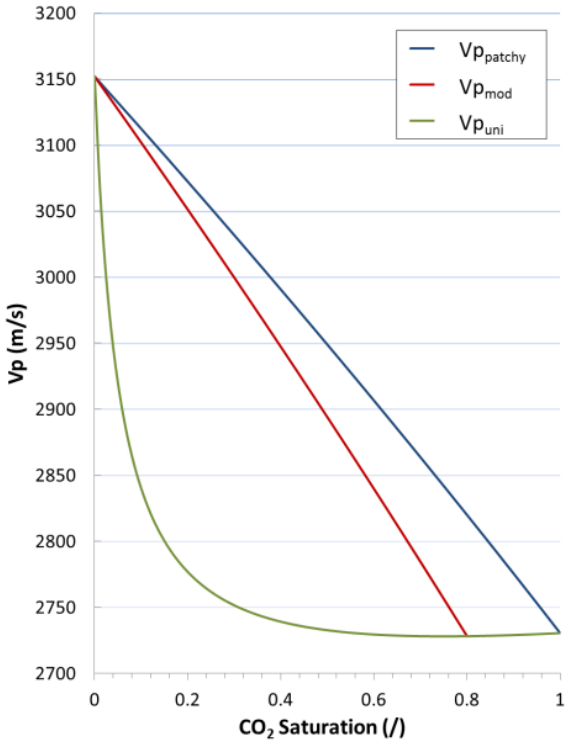

Figure 4.8. P-wave velocity (Vp) as a function of CO_2 saturation calculated assuming a Gassmann-Reuss, uniform saturation model (Vp_{uni}), Gassmann-Hill patchy model, assuming no irreducible water saturation (Vp_{patchy}), and the modified Gassmann-Hill model assuming an irreducible water saturation of 20% (Vp_{mod}).

Furthermore, the water-CO_2 distributions from the CO_2 flow modelling results represent a single 'homogeneous' saturation value for each grid cell. Each value is then used to compute velocity, where a choice of two models is available – modified patchy and uniform – depending on the critical length scale and the size of the fluid patches. As cell dimensions are typically chosen to optimize flow modelling, reservoir models are built with coarse grid-cells typically ranging from 1 – 30m. Cell dimensions at these scales are much greater than the calculated critical length scales for the range of seismic frequencies shown in Figure 4.6. This indicates that the saturation distribution in each grid cell is not clearly modelled. To account for this, I assume that each cell with a single 'homogeneous' saturation value represents the bulk saturation of the cell, whereas in fact each cell, in theory, has varying saturations of CO_2 at the meso-scale. As we are dealing with sub-seismic scale saturation distributions, I feel that this assumption is valid as saturations distributed at this scale

are not resolvable on seismic sections but still influence seismic velocity and impedance.

It should also be noted that the calculation of the end-member models assumes a single rock facies with homogeneous lithology such that K_m, K_{dry} and φ are uniform in space. Spatial variations in velocities are assumed to result only from differing pore fluid saturations (Mavko and Mukerji, 1998). This is not valid for all reservoir conditions, particularly when modelling heterogeneous reservoirs with spatially varying properties such as porosity and permeability. Heterogeneous reservoirs would result in a range of velocities distributed between the patchy and uniform saturation end-member models determined by variations in permeability, fluid viscosity, and patch size (Mavko and Mukerji, 1998, Sengupta and Mavko, 2003, Lebedev et al., 2009, Cairns et al., 2012). Furthermore, the flow of CO_2 through a volume in the subsurface results in a transition from patchy to uniform saturation with increasing time. This transition has been demonstrated in laboratory experiments by Lebedev et al., (2009), and has been suggested to occur as a result of the interplay between the characteristic size and distribution of the fluid patches and the diffusion length, controlled by properties of the rock matrix, pore fluids and signal frequency. Understanding the rate at which this transition occurs, and at what patch size and overall saturation, is still an area of research which needs to be addressed.

Whist I have not modelled the transition in this project, I have accounted for it by simulating both end member models – uniform and modified-patchy – for each time-step in order to generate the widest range of velocities which could be encountered.

Laboratory experiments and field scale observations

In laboratories, the factors controlling the formation and evolution of fluid patches during CO_2 injection can be studied through core flooding experiments, providing a link between fluid patch distribution and acoustic velocities. Recent laboratory studies, such as Cadoret et al., (1998), Lei and Xue., (2009), Lebedev et al., (2009) and Lopes et al., (2014), have provided more insight into the distribution of fluid patches and the accompanying changes in P-wave velocity and attenuation with saturation. Cadoret et al., (1998) used X-ray tomographic images to show different saturation patterns and hence, differences in measured phase velocity during drainage (CO_2 displaces water) and imbibition (water displaces CO_2). Velocities measured from drainage experiments were shown to be higher than those from imbibition experiments due to the formation of 'gas clusters' distributed nonuniformly throughout the porous rock. Lei and Xue (2009) injected CO_2 into water-saturated sandstones and monitored the relationship between saturation and P-wave velocity and attenuation using a sensor array of ultrasonic transducers. They found that velocities can be explained by wave induced fluid flow assuming patch sizes on the order of a few millimetres. Lebedev et al., (2009) performed simultaneous measurements of P-wave velocities and rock sample X-ray computer tomography imaging to allow the authors to infer the fluid distribution inside the rock samples during imbibition. Figure 4.9 shows the measured P-wave velocity as a function of saturation for the Casino Otway sandstone from the dynamic and quasi-static saturation experiments (Lebedev et al., 2009). The two saturation experiments represent two varying injection rates, one of which was 10 ml per day (dynamic) and the other was saturated up to two weeks under reduced pressure (quasi-static) to achieve a near-uniform fluid distribution.

Results from the laboratory experiment clearly show the transition from patchy to uniform saturation from 40-70%. Lebedev et al., (2009) also showed that pore-fluid patch formations are controlled by injection rate through the comparison of the two saturation injection methods, where an increased injection rate results in a quicker transition to uniform saturation.

The laboratory experiments mentioned above provide detailed information of the formation of fluid patches and the calculated changes in velocity. However, they are limited to the size of the core samples. At the field scale, the formation of fluid patches is typically linked to CO_2 injection and migration. The formation of these patches is demonstrated at the Nagaoka CCS storage site. Azuma et al., (2013) calculated CO_2 saturation through the interpretation of time-lapse neutron and sonic logs, which were then overlain on theoretical curves calculated using the uniform, patchy and modified patchy saturation models. The results (Figure 4.10) show a positive correlation between the calculated curves and the saturations calculated with the logging data, confirming the validity of the modified patchy saturation model.

The examples highlighted in this section show that the formation of patchy saturation, and the associated linear change in velocity with increasing CO_2, can be demonstrated at high frequencies of MHz at laboratory experiments and 100 kHz in logging data. However, as highlighted by Lumley (2010), whether patchy saturation has a significant effect in surface seismic data, at the 10-100 Hz frequency range, has yet to be demonstrated at the field scale.

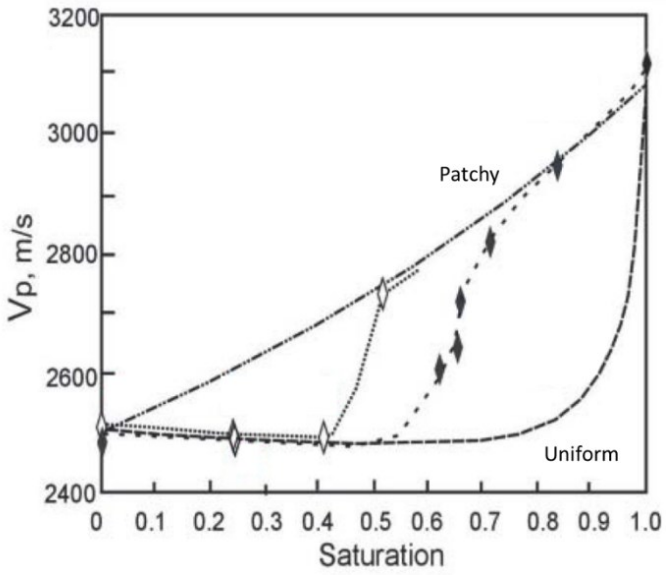

Figure 4.9. P-wave velocity as a function of saturation for the Casino Otway sandstone for the dynamic (clear diamond) and quasi-static (filled diamond) saturation experiments. Theoretical uniform and patchy bounds are shown. Modified from Lebedev et al., (2009).

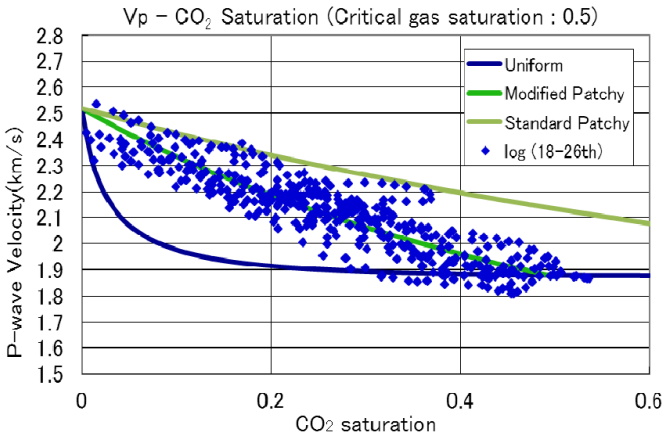

Figure 4.10. Overlay of calculated CO_2 saturation using time-lapse neutron and sonic logs on theoretical curves of uniform, patchy and modified patchy distributions. Modified from Azuma et al., (2013).

4.3.2 Effect of fluid saturation on resistivity

To assess the effect of fluid saturation on resistivity, I apply the well-known Archie equation. Archie's equation calculates the electrical resistivity of each of the simulated grid blocks as a function of water saturation, pore fluid resistivity and porosity, as given by (Gasperikova and Hoversten, 2005):

$$R_m = \frac{aR_w}{\varphi^m {S_w}^n} \tag{4.22}$$

where R_m is the total resistivity of the rock (Ω.m), φ is the porosity, R_w is the water resistivity (Ω.m), S_w is the water saturation, m is the cementation factor, n is the saturation exponent and a is the tortuosity factor.

The cementation factor, m, describes the increasing resistivity resulting from the mineral grains in the pore network. Wyllie and Rose (1950) stated that m lies in the limits of 1.3 and 3, as observed by Archie (1942). Values between 1.4 and 2 are associated with sandstones. Values closer to 2 represent more consolidated sandstones with more tortuous flow paths. Igneous and metamorphic rocks are associated with values between 1 and 1.4 while values between 2 and 2.6 are typical for carbonates.

The saturation exponent, n, is related to the wettability of the rock and models the dependency on the presence of non-conductive hydrocarbons in the pore-space (Mavko et al., 2009). For water-wet media the saturation exponent is typically around 2, but has been modelled experimentally to range from 2.5 to 9.5 in oil-wet porous media (Dunlap et al., 1991).

Lastly, the tortuosity factor, a, is used to correct for variations in compaction, pore structure and grain size (Winsauer et al., 1952). a is typically in the range of 0.5 to 1.5.

Constant values of 2 for m, 2 for n and 0.845 for a were used throughout, based on recommendations by Hacikoylu et al., (2006).

Sensitivity to fluid saturation model

Figure 4.11 shows calculated matrix resistivity values as a function of CO_2 saturation for a theoretical reservoir with 20% porosity with brine resistivity equivalent to that of seawater (0.33 Ω.m). Resistivity is plotted on a log scale to highlight the large range of resistivity values which occur due to the displacement of brine by more resistive CO_2.

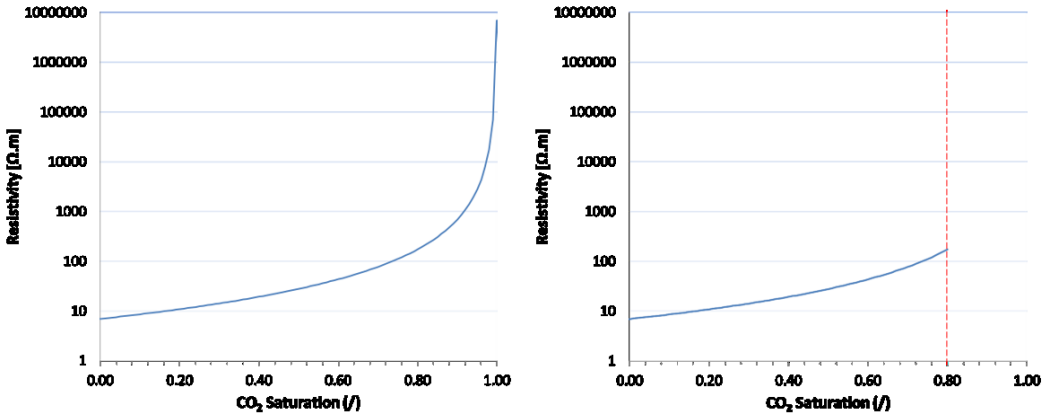

Figure 4.11. Calculated resistivity as a function of CO_2 saturation for a theoretical sandstone with porosity of 20% and brine resistivity of 0.33 Ω.m (left). Calculated resistivity assuming 20% irreducible water saturation (right).

Interestingly, an increase in resistivity of an order of magnitude is associated with CO_2 saturation at only 75%. Furthermore, assuming an irreducible water saturation of 20% would result in a maximum increase in resistivity of only 150 Ω.m with respect

to baseline (no CO_2). Changes in resistivity in that range could prove difficult to detect as larger changes in resistivity of the order of 2 to 3 magnitudes are only associated with CO_2 saturations greater than 95%. This could have important implications for the applicability of CSEM techniques when detecting CO_2 migration.

4.4 Geophysical modelling

Once the end-member velocity models and calculated resistivity models for each simulated grid blocks are calculated, synthetic seismic and EM time-lapse responses are generated by simulating the acquisition of seismic and CSEM surveys.

Nucleus+ (Taylor and Julliard, 2013) and PEMrad (Drakengren, 2008) have been used throughout the project to simulate survey acquisition and the resulting time-lapse changes for seismic and CSEM surveys, respectively. Nucleus+ is a 3D elastic finite-difference wave propagation modelling code while PEMrad is a 3D EM forward modelling code based on the method of integral equations. Appendix B verifies the use of the PEMrad modelling code. The integral equations method embeds complex 3D structures in a 1D background. Both packages compute synthetic data by constructing the response of a medium to a source. Once generated, the resultant synthetics correspond to each simulated time and provide information about the ability of seismic and CSEM to identify regions of CO_2 saturation.

4.4.1 Seismic modelling workflow

Prior to the generation of the synthetic seismic sections, three entities need to be defined:

1. 2.5D model with calculated velocity and density values;
2. Source signature;
3. Acquisition survey.

The calculated petrophysical properties are first exported from Permedia and converted to SEG-Y format in Matlab. This is done by building a Matlab structure array. The structure array needs to include the first and last data points, the time

steps, header information such as the x and y coordinates of the line and importantly, the calculated traces.

An example of the structure file used to build the SEG-Y file for the 20 year Bunter uniform velocity model is shown in Figure 4.12.

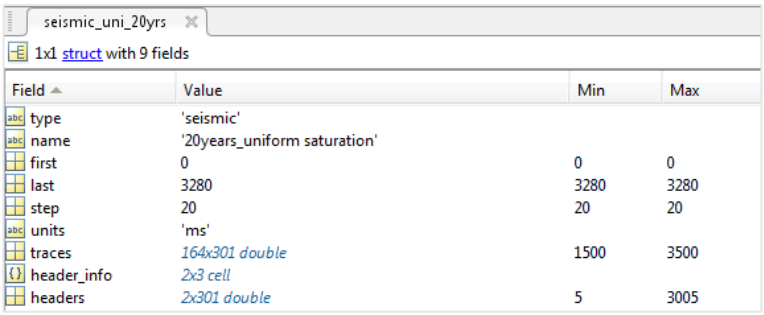
seismic_uni_20yrs

1x1 struct with 9 fields

Field	Value	Min	Max
type	'seismic'		
name	'20years_uniform saturation'		
first	0	0	0
last	3280	3280	3280
step	20	20	20
units	'ms'		
traces	164x301 double	1500	3500
header_info	2x3 cell		
headers	2x301 double	5	3005

Figure 4.12. An example of a Matlab Structure file used to build the SEG-Y file for the 20 year Bunter uniform velocity model.

Once completed, the structure file is converted to a SEG-Y file using the SeisLab toolkit (Rietsch, 2010) in Matlab. The final SEG-Y file is then imported into Nucleus+ to generate the synthetic surveys.

The source signature for all synthetic seismic surveys is a zero-phase Butterworth wavelet of 2.0 msec sample interval, with low cut and high cut frequencies of 8Hz and 90Hz and slopes of 18 and 72 dB/octave, respectively (Figure 4.13).

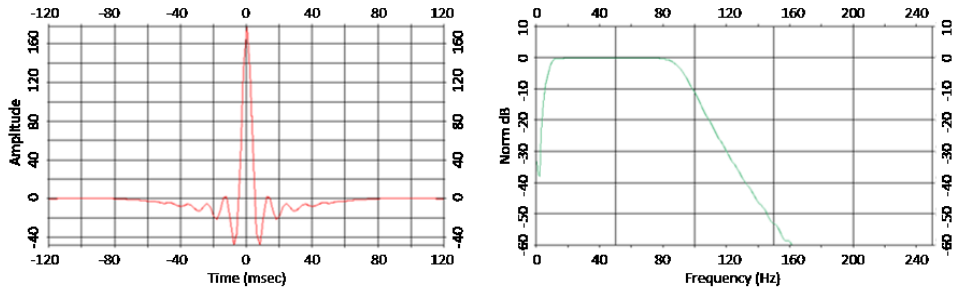

Figure 4.13. Zero-phase Butterworth wavelet at 2.0 msec sample interval. A low and high cut frequency of 8 and 90Hz and low and high cut slope of 18 and 72 db/octave were applied.

Once input into Nucleus+, the software computes the earth response at each receiver position for each source position. The ensemble of data created for one source position is called a common-source gather.

I summarise the seismic processing approach below.

- The seismic traces from the shot gathers are re-arranged into common mid-point (CMP) gathers.
- A mute is applied to remove the refracted arrivals.
- After velocity analysis, normal moveout (NMO) corrections are applied to make reflections from the same horizon line up at the same time as the zero-offset trace.
- The traces in each CMP gather are stacked to make a single normal incidence reflection seismogram.
- Resultant stacked traces are displayed side-by-side to make a seismic section in which the horizontal axis is the position of the CMP along the survey line and the vertical axis is the two-way time.
- The seismic section is then depth-migrated using the phase-shift plus interpretation (PSPI) method (Ferguson and Margrave, 2005).

All the seismic processing is done in Matlab using the CREWES toolkit (Margrave, 2003) and SeismicLab (http://seismic-lab.physics.ualberta.ca/). Once processed, the difference between the depth migrated monitor & baseline surveys are subtracted to assess whether the generated synthetics highlight differences at horizons where CO_2 concentrations have changed. An assumption is made that no noise is encountered. This is assumed due to the lack of available noise data for the modelled locations.

4.4.2 EM modelling workflow

Prior to generating the synthetic EM response, three entities need to be defined:

1. 3D reservoir model with calculated conductivity values;
2. Initialisation file;
3. Acquisition survey.

The resistivity values are first converted to conductivity (σ) as:

$$\sigma = {R_m}^{-1} \tag{4.23}$$

Once calculated, the values are exported as an ASCII file.

The initialisation file is one of the most important files used to run PEMrad as it includes the source information, the source frequencies and the 1D background. The source type for all generated synthetics is a horizontal electric dipole (HED). The background is a 1D earth model of conductivities from the seafloor to the earth's crust.

Once completed, the files are input into PEMrad where the software calculates the earth response at each receiver position for each shot position. The difference between the earth's response at the monitor survey and the baseline survey highlights the effect of the injected CO_2 in the subsurface. PEMrad is a 3D frequency-domain forward modeller. I use the code presented in Key (2012) to calculate time-domain responses from frequency-domain responses. The Matlab code from the paper is available at the SEG software library (http://software.seg.org/2012/0003/). The frequency array, the frequency response amplitudes, and the desired array of times for the time-domain response is required. I use 81 frequencies logarithmically distributed from 1×10^{-4} Hz to 1×10^{4} Hz with 10 frequencies per decade. This corresponds to 61 times from 0.001s to 100s. The results will be interpreted in the time-domain.

4.4.3 Towed streamer survey design and acquisition

Modelling the acquisition of seismic and CSEM surveys is done through the deployment of a single line towed streamer survey. For each geophysical model generated, a single line over the target is acquired- in time-lapse mode. This is seen as efficient when assessing the monitorability of geophysical techniques, as the target of the survey is known.

When designing a marine survey, the following acquisition parameters need to be decided:

- Source coordinate (S)
- Receiver coordinate (R)

- Source receiver offset (X_O)
- Number of receivers (n)
- Receiver interval (ΔX_R)
- Shot interval (ΔX_S)
- Number of shots (n_S)

An illustration showing these parameters for a seismic survey is shown in Figure 4.14.

The design of the marine geophysical surveys depends on the geometry of the simulated results from the fluid flow modelling (Stage 1). As the design of the geophysical survey is a site and simulation specific issue, each simulated model has a unique survey design. This is explained in each piece of work which applies the monitorability workflow.

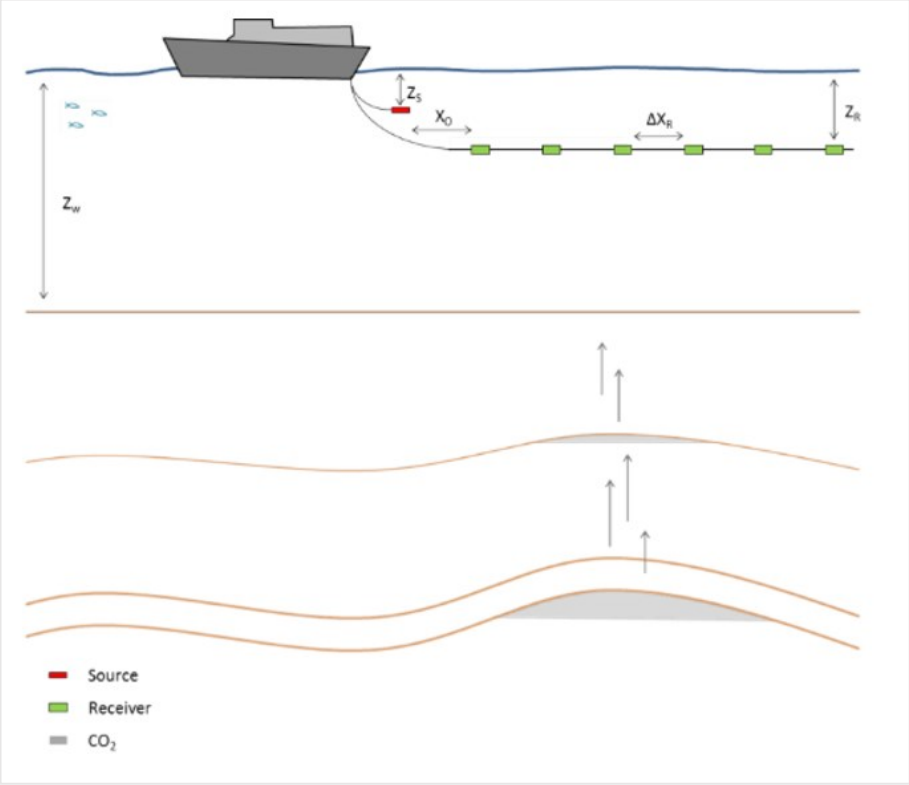

Figure 4.14. Data acquisition parameters for a typical marine survey over a theoretical CO_2 field. Z_S and Z_R represent the depth of the source and receiver respectively, while ΔX_R is the receiver interval and X_O is the source receiver offset.

Summary

I explain the different stages in the monitorability workflow developed specifically for this project. The workflow can be adapted to generate synthetic seismic sections or synthetic EM responses to model variations in the time-lapse signal. The workflow can be applied to assess the ability of seismic and EM techniques to monitor CO_2 containment and conformance.

5. Seismic monitoring of homogeneous reservoirs

I assess the ability of seismic techniques to monitor four key stages during a CCS project: Stage 1) migrating plume during injection, Stage 2) contact with primary seal, Stage 3), first instance of a breach, and Stage 4) contact with secondary seal. This is achieved by building a 3D geological model of an ideal storage complex consisting of two reservoir-seal pairs. The reservoir consists of a clean, lithologically homogeneous sandstone. A zone of weakness is included into the intraformational seal to model a loss of containment and the migration of CO_2 from the primary to the secondary reservoir. Once the CO_2 injection has been simulated, I calculate the velocities for two saturation models and generate corresponding synthetic seismic surveys for each stage. I then discuss the ability to image each stage and comment on the importance of the velocity-saturation models.

Parts of this chapter have been published in the paper *The detectability of free-phase migrating CO_2: A rock physics and seismic modelling feasibility study* in Eid et al., (2014).

5.1 Introduction

The monitorability of CO_2 storage sites is a site-specific issue which involves the monitoring and measurement of injected CO_2 in the subsurface. The operator is expected to demonstrate containment and conformance of the injected CO_2 in the intended formation, and importantly, identify any movement of CO_2 from the primary storage reservoir.

As described in Chapter 2, it is favourable that CO_2 injection occurs in a storage complex with two reservoir-seal pairs. Should a loss of containment in the primary reservoir occur, movement of CO_2 from the primary to the secondary reservoir can be expected. This is termed migration. The ability to detect CO_2 migration, that is CO_2 which is not immobilized by residual or structural trapping, termed a free-phase migrating front, is critical when demonstrating containment and conformance.

In this study I investigate the potential of surface seismic techniques to monitor four key stages during a CCS project:

1) Migrating plume during injection,
2) Contact with primary seal,
3) First instance of a breach,
4) Contact with secondary seal.

The chosen stages are important when monitoring the migration of injected CO_2 in the reservoir. The first stage demonstrates that seismic techniques are capable of imaging the initial injection period and plume migration. This is done to ensure that injection is occurring at the correct location and depth. Detection of contact with the primary seal is to ensure the filling and structural trapping of the CO_2 is as predicted. The first instance of a breach, and the contact with the secondary seal, are important monitoring stages when assessing whether the free-phase migrating front of CO_2 is capable of being imaged using current seismic techniques. This allows the possibility of an early warning should a breach in containment occur. This could allow for

remediation activities to be undertaken such that the probability of a leak outside the storage complex, to the surface, is negligible.

First, the geological model built for this study is described. A loss of containment is then simulated in a storage complex by modelling a migrating front of CO_2 moving away from the primary reservoir until reaching a zone of weakness. The CO_2 migrates vertically towards a shallower, secondary reservoir and accumulates below a secondary seal. Synthetic seismic sections of the different monitoring stages are then generated before finally discussing the ability of seismic methods to image each stage and comment on the importance of the fluid saturation distribution end-member velocity models.

5.2 Geological model

A three-dimensional hypothetical model of a sandstone reservoir separated by an intraformational seal with a zone of weakness is built for this study. The model is an adaptation of the leakage model built by Class et al., (2009) as part of a benchmark study on problems related to CO_2 storage.

The geological model represents an idealised storage complex, with two reservoir seal pairs, and a known migration pathway. The reservoirs are 400m thick and are separated by a 300m thick intraformational seal. The model covers an area of 1000m by 500m, with horizontal cell-size dimensions of 10m by 10m and vertical cell-size dimensions of 20m. The top of the model is at 1000m depth and reaches a total depth of 2150m. The model is shown in Figure 5.1.

The model consists of five surfaces representing a low angle (0.5°) dome. From top to bottom, the five surfaces represent an impermeable seal, secondary reservoir, intraformational seal, primary reservoir, and basement (Figure 5.2). The top primary reservoir surface is shown in Figure 5.3, highlighting the structure of the surface.

The reservoir consists of a clean, lithologically homogeneous sandstone. Reservoir cell properties are populated using example lithology files in Permedia based on a collection of lithological properties for common rock types. Porosity, permeability

and threshold pressure transforms with depth for both the sandstones and the shales are shown in Figure 5.4. The reservoir properties are laterally homogeneous. For this study, vertical permeability is assumed to be one tenth of the horizontal permeability.

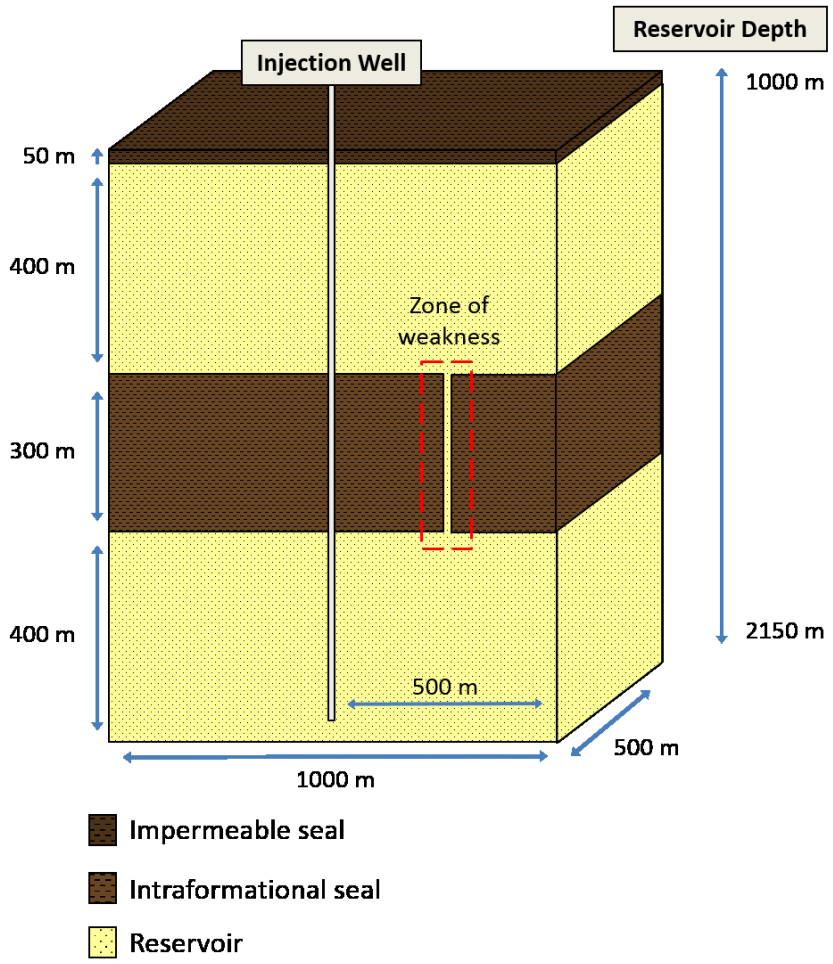

Figure 5.1. Theoretical model of a clean reservoir separated by an intraformational seal with a zone of weakness (dashed red square).

A pathway is prescribed along which CO_2 will migrate from the primary to the secondary reservoir; simulating a loss of containment. The pathway is modelled as a zone of weakness in the intraformational seal. The zone of weakness can be representative of migration through a fault or migration through, or along, a well due to improper well completion. In reality, such a pathway will most likely be unknown.

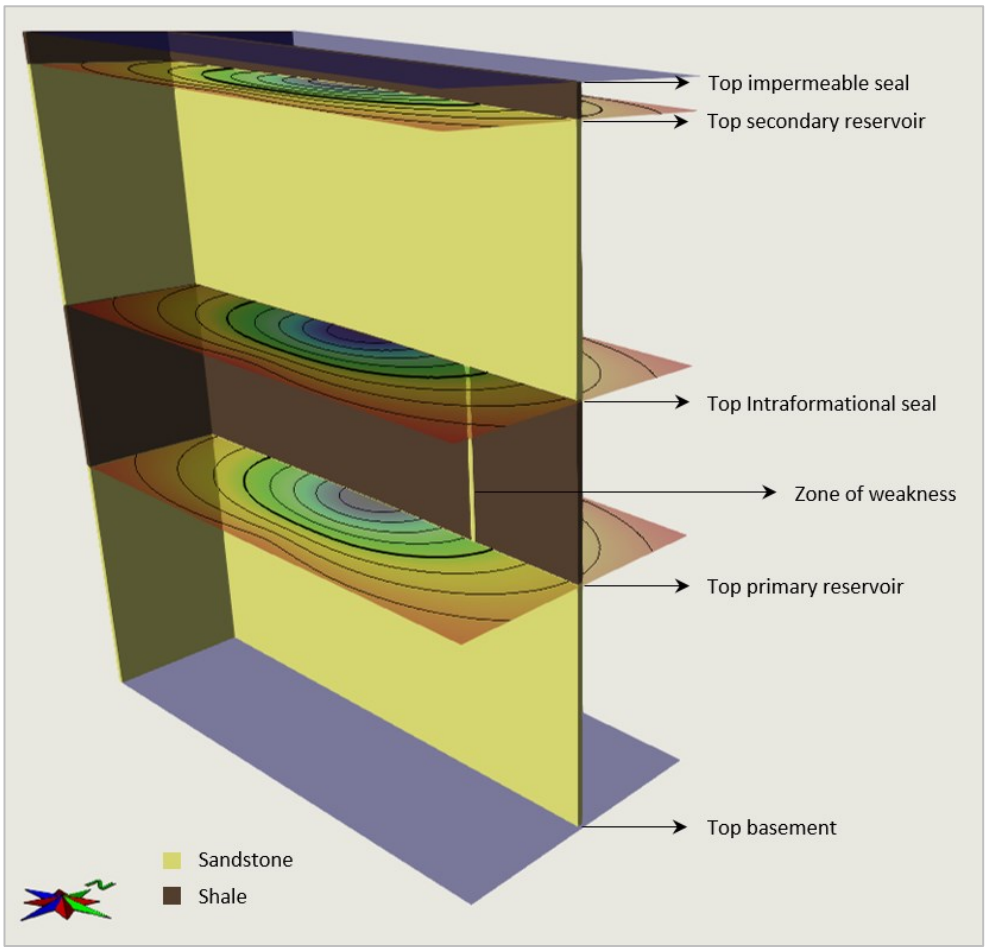

Figure 5.2. 3D view of the geological model highlighting the five surfaces and their structure. Vertical exaggeration of 1.

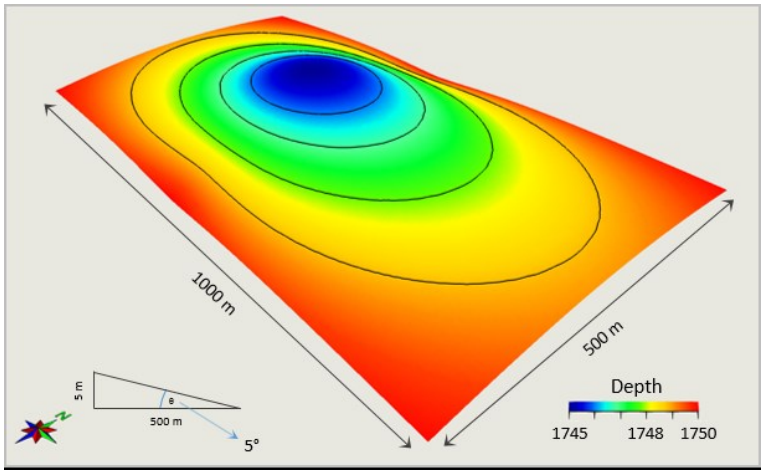

Figure 5.3. 3D view of the top primary reservoir surface contoured at 0.2m intervals highlighting the low-angle dip of the structure.

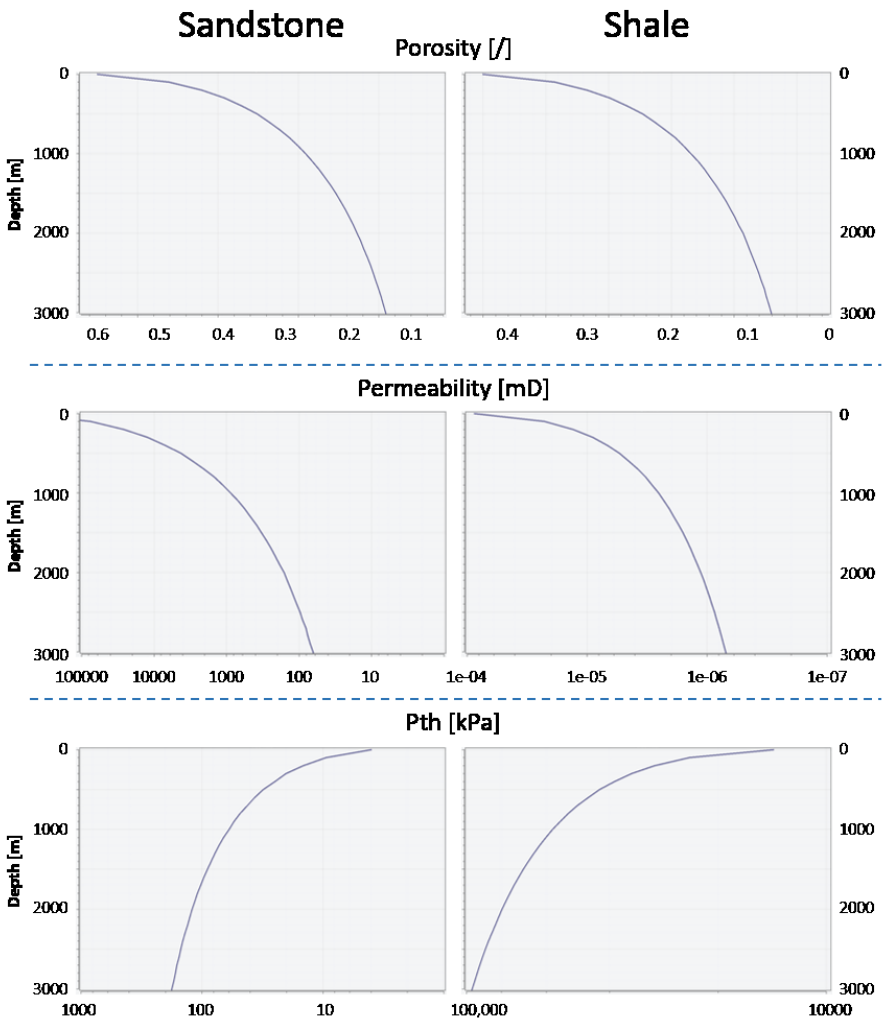

Figure 5.4. Porosity, permeability and threshold pressure transforms with depth for the sandstones and the shales in the model.

5.3 Fluid flow model

Permedia's black oil simulator (Permedia, 2014) is used to simulate a loss of containment. This is modelled as a migrating front of CO_2 which moves away from the primary reservoir, which, upon reaching a zone of weakness, continues vertically towards a shallower, secondary reservoir. CO_2 is injected at a constant rate of 0.1 MT per year for 10 years over a 50m perforation interval at 2050m. The injection well is situated at the centre of the domain, 250m away from the leakage pathway.

The relative permeability (Kr) and capillary pressure (P_c) curves used to model drainage and imbibition for CO_2 and brine were obtained from experiments

performed on the relatively clean, high porosity Cardium Sandstone by Bennion and Bachu (2006) (Figure 5.5). Imbibition is the displacement of one fluid by another. In this scenario, water imbibes back into the pore space previously occupied by CO_2, usually at the trailing edge of the plume. A fraction of the initial CO_2 becomes trapped as a result of this, rendering the CO_2 immobile (residually trapped). The imbibition curves are slightly modified to represent 20% CO_2 residual trapping (R_o), compared with the originally measured 10% (Bennion and Bachu, 2006). This is done to highlight better the differences between the end-member velocity-saturation models used in this study. Irreducible water saturation (S_{wir}) from CO_2 injection is set to 20%. The Duan and Sun (2003) equation of state is used in this study. The input BOS (black oil simulator) parameters are summarised in Table 5.1.

Table 5.1. Input BOS parameters.

Simulation parameters		
Sea bed temperature	*°C*	5
Temperature gradient	*°C/km*	30
Pressure gradient	*MPa/km*	10
Salinity	*ppm*	39000

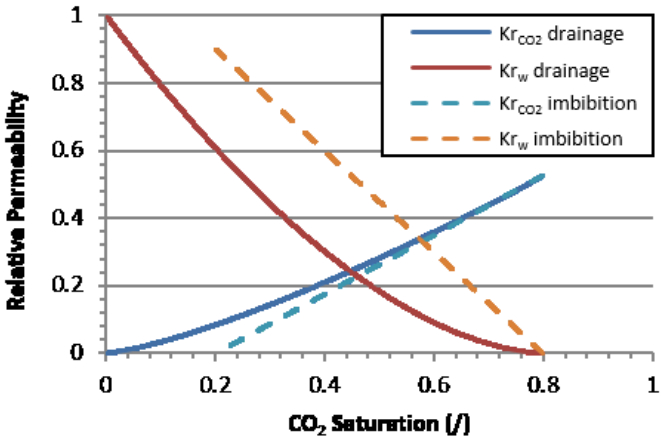

Figure 5.5. The two-phase relative permeability (Kr) curves used to model CO_2 flow in the reservoir. The solid lines refer to the reservoir undergoing drainage while the dashed lines represent imbibition. The curves represent an irriducable water saturation of 0.2 and residual CO_2 saturation of 0.2 (Bennion and Bachu, 2006).

5.3.1 CO_2 saturation distribution

Figure 5.6 shows 2D sections of the 3D simulation results of the four monitoring stages: migrating plume during injection (Stage 1), contact with primary seal (Stage 2), first instance of a breach (Stage 3) and contact with secondary seal (Stage 4). Histograms of the saturations in the grid blocks are also shown.

Fluid flow during injection is shown to be dominated by drainage, which involves the flow of CO_2 into pore spaces during injection. This flow is explained by the relative permeability curves for CO_2 and water (Figure 5.5). Increasing CO_2 saturation results in an increase in mobility, controlled by buoyancy forces. Due to the lack of heterogeneity in the reservoir, the CO_2 shows rapid vertical migration due to the large density difference between the supercritical CO_2 and brine. Once the CO_2 accumulates below the primary seal, continued injection and migration results in lateral growth in plume diameter until reaching the zone of weakness. CO_2 is modelled to breach the intraformational seal and flow into the secondary reservoir, modelled as a free-phase migrating front of CO_2 (Figure 5.6c) before making contact with the secondary seal (Figure 5.6d).

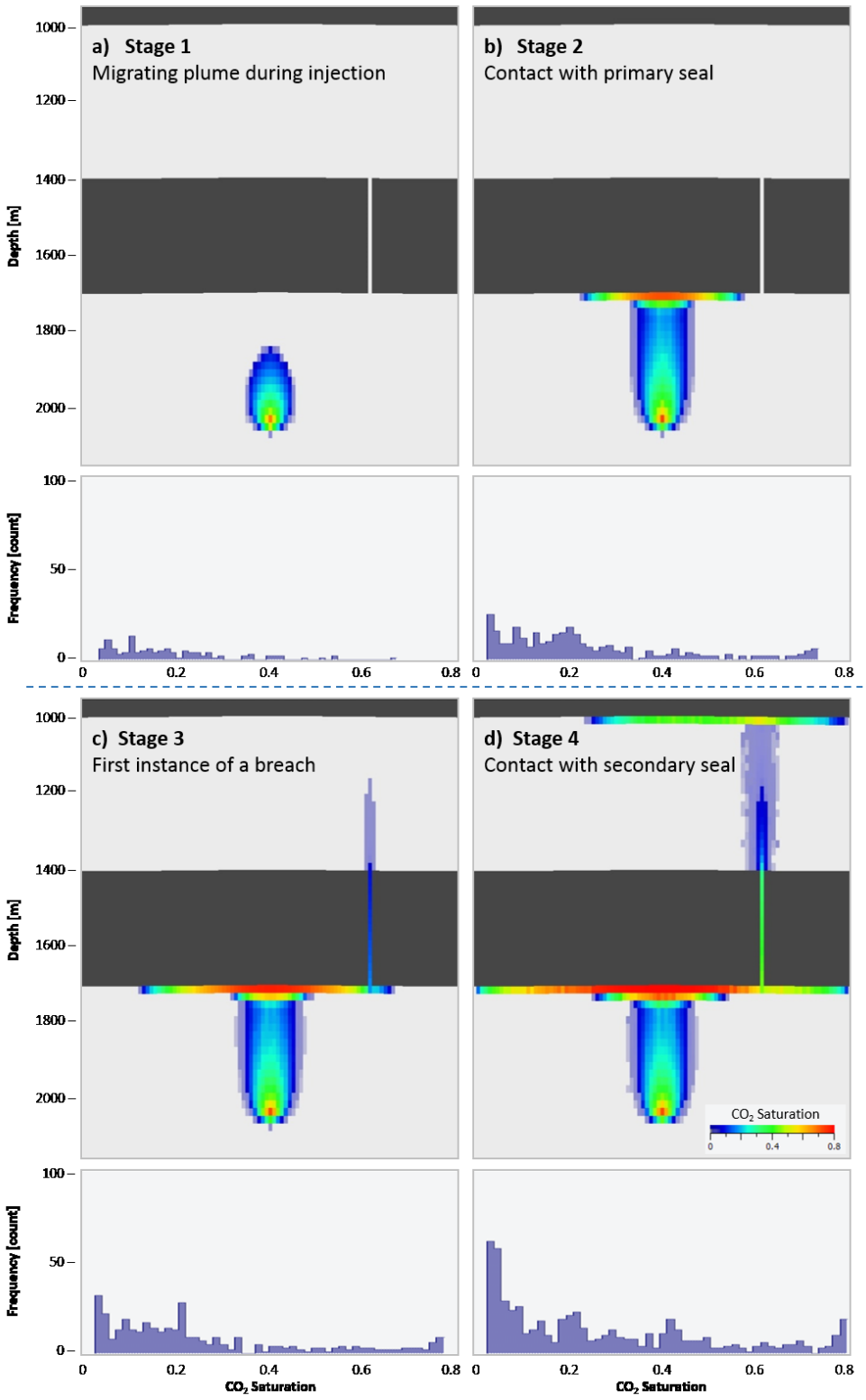

Figure. 5.6. 2D sections of the 3D simulation highlighting four key monitoring stages and the histograms showing the associated ranges in saturation in the reservoir. Vertical exaggeration of 1.

5.4 Rock physics model

To calculate the change in the elastic properties of the four modelled stages I employed the Gassmann's fluid substitution workflow. The friable-sand model (Dvorkin and Nur, 1996) is used to calculate the dry frame bulk modulus (K_{dry}) and shear modulus (μ_{dry}) for the sandstone layers. The friable-sand model is chosen due to the assumption of a pure, clean, well-consolidated sandstone reservoir. The matrix bulk modulus K_m is calculated via the application of Voigt-Reuss-Hill (VRH) method (Avseth et al., 2005). The constant-clay model (Avseth et al., 2005) is used to describe the velocity-porosity behaviour for the intraformational shale. When determining the corresponding elastic properties, both a uniform and modified-patchy saturation distribution is assumed. This is done to understand the expected ranges which could be encountered when assessing the overall ability to monitor the different stages. Input parameters for the rock physics modelling are summarised in Table 5.2. The rock-physics models have been discussed in detail in Chapter 4 section 2.

Table 5.2. Input petrophysical parameters. CO_2 and brine modulus calculated based on simulation parameters.

Petrophysical parameters			
Fluid properties			
CO_2	Density		From simulation
	Saturation		From simulation
	Bulk modulus	*GPa*	0.0993
Brine	Density		From simulation
	Saturation		From simulation
	Bulk modulus	*GPa*	2.55
Mineral properties			
Sandstone	Vclay	%	0.01
	Density	kg/m^3	2650
Shale	Vclay	%	0.99
	Density	kg/m^3	2700

5.4.1 Homogeneous reservoir velocity distribution

The homogeneous nature of the sandstone reservoir results in a distribution of velocities which range from 2050 m/s to 3480 m/s, depending on porosity and fluid saturation.

Figures 5.7 and 5.8 represent the calculated velocity models assuming a modified-patchy and uniform saturation distribution. Analysis of the change in velocity with respect to the baseline clearly highlights the differences between the two models. Clearly evident from the uniform modelling results is the large change in velocity from the outset (Figure 5.8). The CO_2 is easily distinguishable from the baseline, resulting in a decrease of velocity in the primary reservoir of 450 m/s. This decreases to 540 m/s as the CO_2 accumulates in the secondary reservoir. A decrease of only 35 m/s is modelled in the plume body when comparing the baseline model with the calculated velocities for Stage 4. Features in the plume, such as the injection interval, are difficult to distinguish. In comparison, the velocity model calculated assuming a modified-patchy distribution (Figure 5.7) clearly distinguishes different features, in particular the structurally trapped CO_2 and the injection interval. Higher saturations, corresponding to structurally trapped CO_2, also result in a maximum decrease in velocity of 434 m/s. However, features of low saturation, such as the free-phase migrating front, result in a decrease in velocity of only 50 m/s. This compares with a maximum change of -350 m/s when assuming uniform saturation over the same feature.

The relationship between velocity and CO_2 saturation highlights the key differences between the two end-member models. As explained in Chapter 4, calculated velocities show, for a modified-patchy distribution, an approximately linear relationship between velocity and increasing saturation, whereas a uniform saturation model calculates a rapid change in velocity at low saturations of CO_2. This is apparent in Figure 5.9 where the calculated velocities for both modified-patchy and uniform models are plotted as a function of porosity, coloured by CO_2 saturation. A comparison of the two end-member models further emphasises their differences, in

particular, the ability, or lack thereof, to distinguish features in the plume body itself. As highlighted by the modified-patchy results (Figure 5.9 left), the large changes in velocities are attributed to the structurally trapped CO_2 in the reservoir. However, the free-phase migrating front of CO_2 is visible only when assuming a uniform saturation distribution. Comparing the calculated velocities for each stage, it is clear that the end-members model a very similar change in Vp. This is due to the end-member models converging as the maximum saturation is reached.

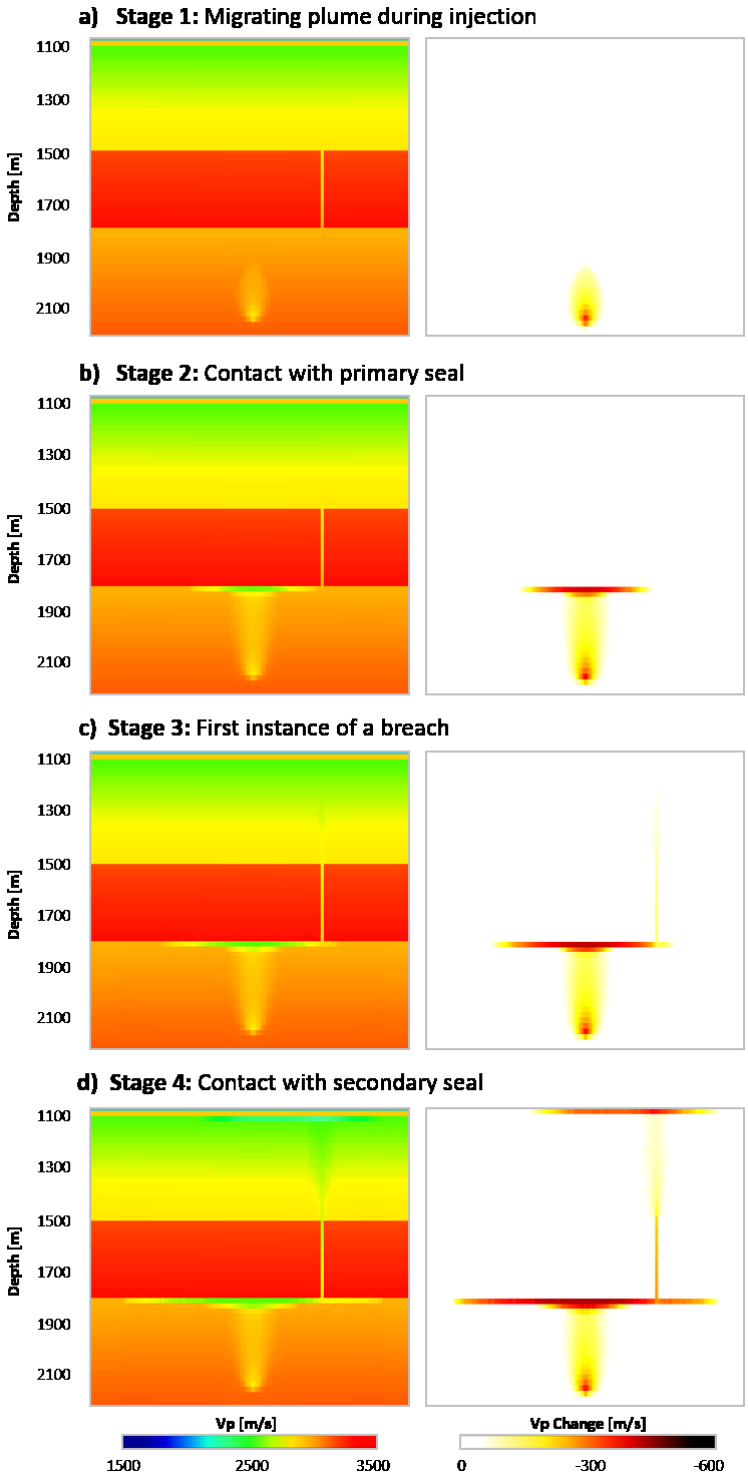

Figure 5.7. Petrophysical modelling results assuming a modified-patchy saturation distribution for the four monitoring stages highlighting the calculated velocity (left) and the change in Vp with respect to baseline. Vertical exaggeration of 1.

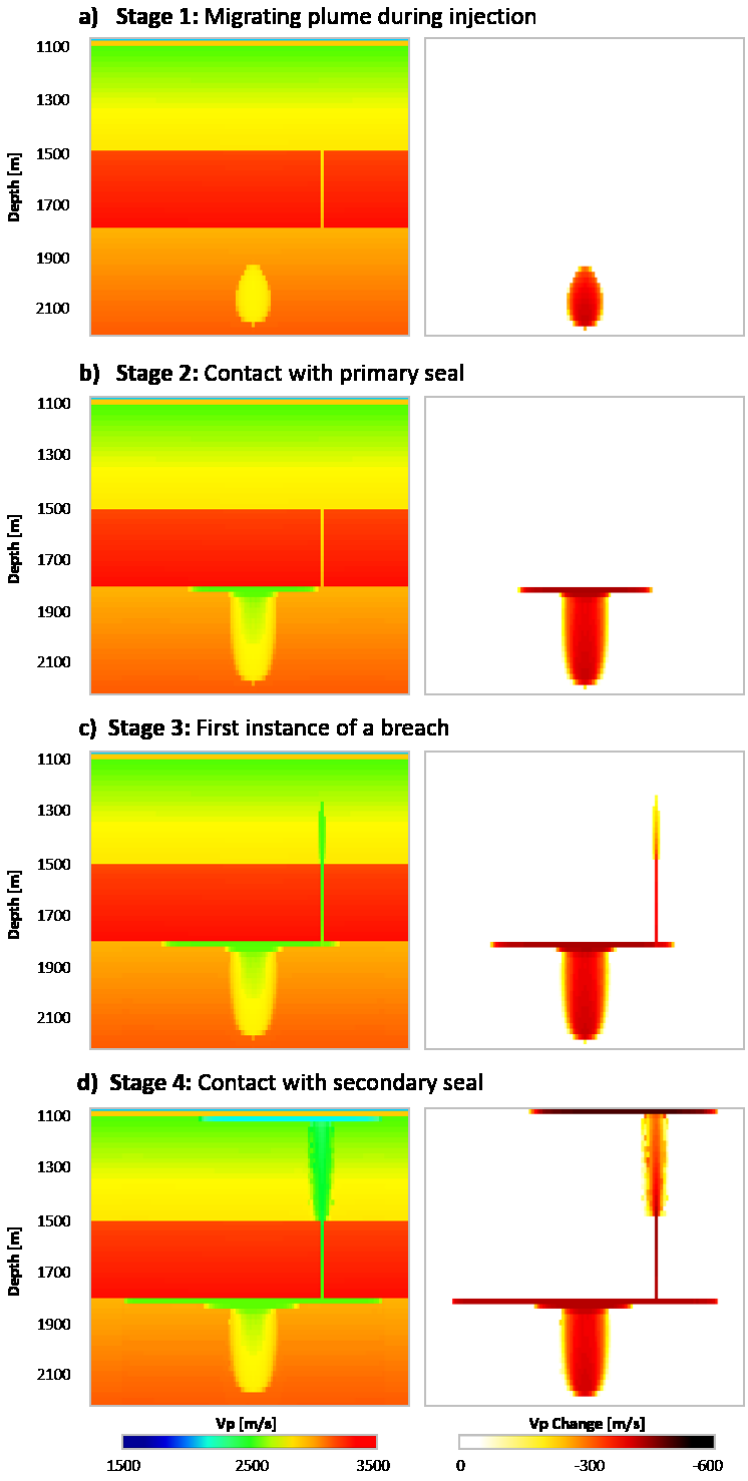

Figure 5.8. Petrophysical modelling results assuming a uniform saturation distribution for the four monitoring stages highlighting the calculated velocity (left) and the change in Vp with respect to baseline. Vertical exaggeration of 1.

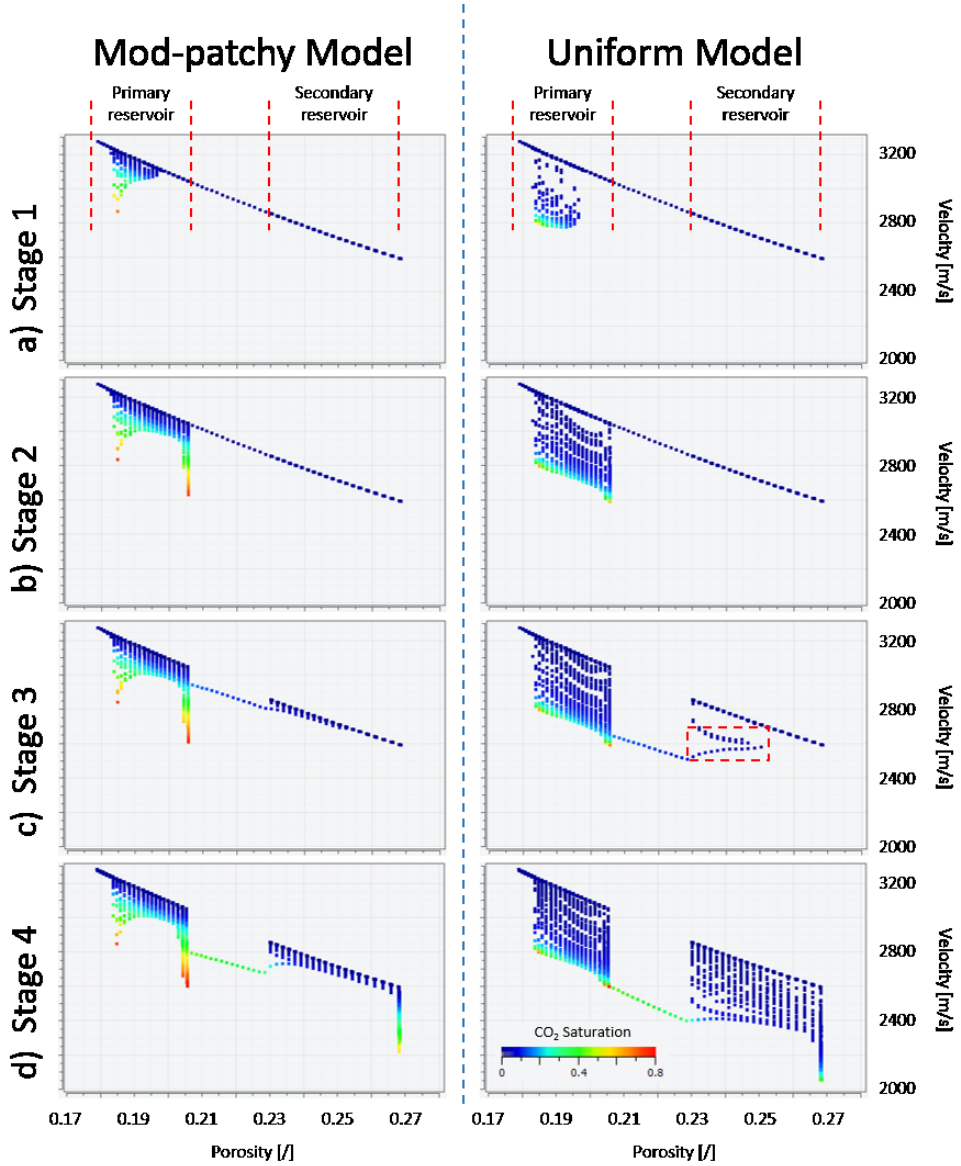

Figure. 5.9. Calculated velocity as a function of porosity, coloured by CO_2 saturation for the four monitoring stages. Velocity is calculated assuming a modified patchy (left) and uniform saturation model (right). Porosities corresponding to the primary and secondary reservoirs, are highlighted. When assuming a modified-patchy distribution, large changes in velocity correspond to structurally trapped, high saturations of CO_2. However, the change in velocity due to the migrating front of CO_2 is clearly visible when assuming a uniform saturation distribution only (red box).

5.5 Seismic forward model

To assess the potential of seismic techniques to monitor the four stages, the rock physics modelling results are incorporated into 3D elastic finite-difference wave propagation modelling. Using Nucleus+ (Taylor and Julliard, 2013), I simulate the acquisition of a single line towed streamer seismic survey (Table 5.3). To obtain full coverage across the area of interest, the velocity model is extended at both ends by 1km. Surfaces for the overburden and seafloor are also included. I assume a sea-water depth of 150m. Constant density and velocity values are assumed for each layer outside the original model (Table 5.4). Synthetic shot records are generated along the 3km east-west section corresponding directly above the zone of weakness and the resulting loss of containment. The modelling is performed for each monitoring stage, for both uniform and modified-patchy saturation cases. The source signature is a zero-phase Butterworth wavelet of 2.0 msec sample interval, with low cut and high cut frequencies of 8Hz and 90Hz and slopes of 18 and 72 dB/octave, respectively. The wavelet is shown in Chapter 4, section 4. A constant V_P/V_S ratio is used.

Table 5.3. Synthetic seismic modelling acquisition parameters.

Acquisition parameters	
Receiver spacing	12.5 m
Receiver depth	7.5 m
Source spacing	25 m
Source depth	5 m
Cable length	3000 m
Number of receivers	240
Number of shots	124
Recording length	2.5 sec

Table 5.4. Model extension parameters.

Model extension		
	Rho [kg/m^3]	Vp [m/s]
Sea	1000	1500
Overburden	2000	2000
Original model	*calculated*	*calculated*
Underburden	2500	3500

Events on the generated synthetic shot gathers arise due to changes in acoustic impedance, corresponding to changes in lithology (Figure 5.10a). The introduction of less dense and more compressible CO_2 results in an increase in reflectivity with prominent time-shifts below the plume. The modified-patchy (Figure 5.10b) and uniform (Figure 5.10c) synthetics show similar reflectivity and time-shift events.

Following the processing steps outlined in Chapter 4.4, a mute is applied to remove the refracted arrivals. Velocities from the velocity analysis are then used to apply normal moveout (NMO) corrections (Figure 5.11). The traces are then stacked to make a seismic section. The seismic section is then depth-migrated using the baseline velocity model using the phase-shift plus interpretation (PSPI) method (Ferguson and Margrave, 2005). Once migrated, a time-lapse image is then generated by subtracting the baseline survey from the monitor survey to show the effects of the CO_2 (Figure 5.12). This process is repeated for each of the four monitoring stages.

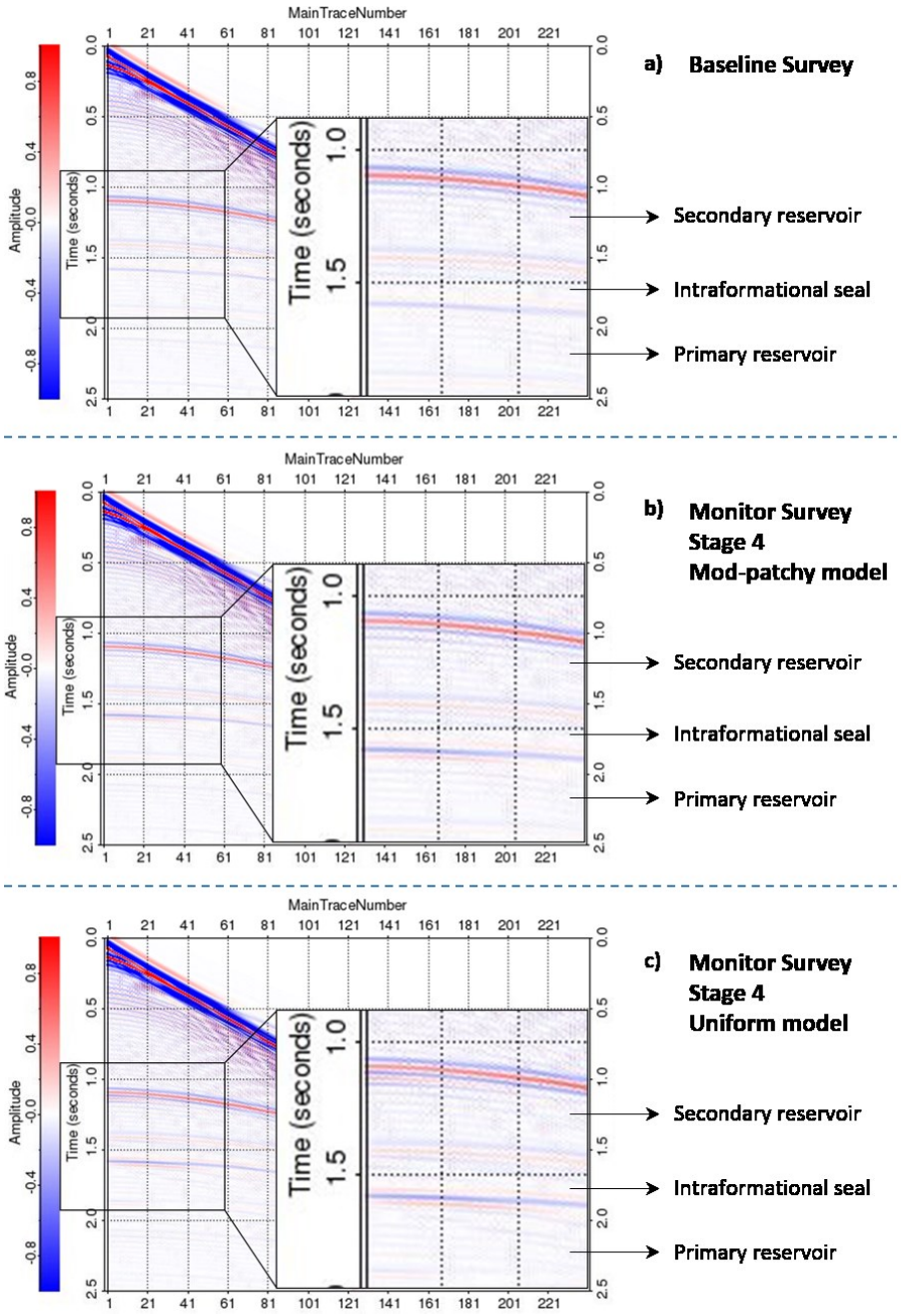

Figure 5.10. Synthetic pre-stack gather pre-injection (a) and after 20 simulated years for both modified-patchy (b) and uniform (c) saturation end-members. The storage complex has been enlarged and highlighted in the black box. Note the similar reflection amplitude responses for both end-member scenarios.

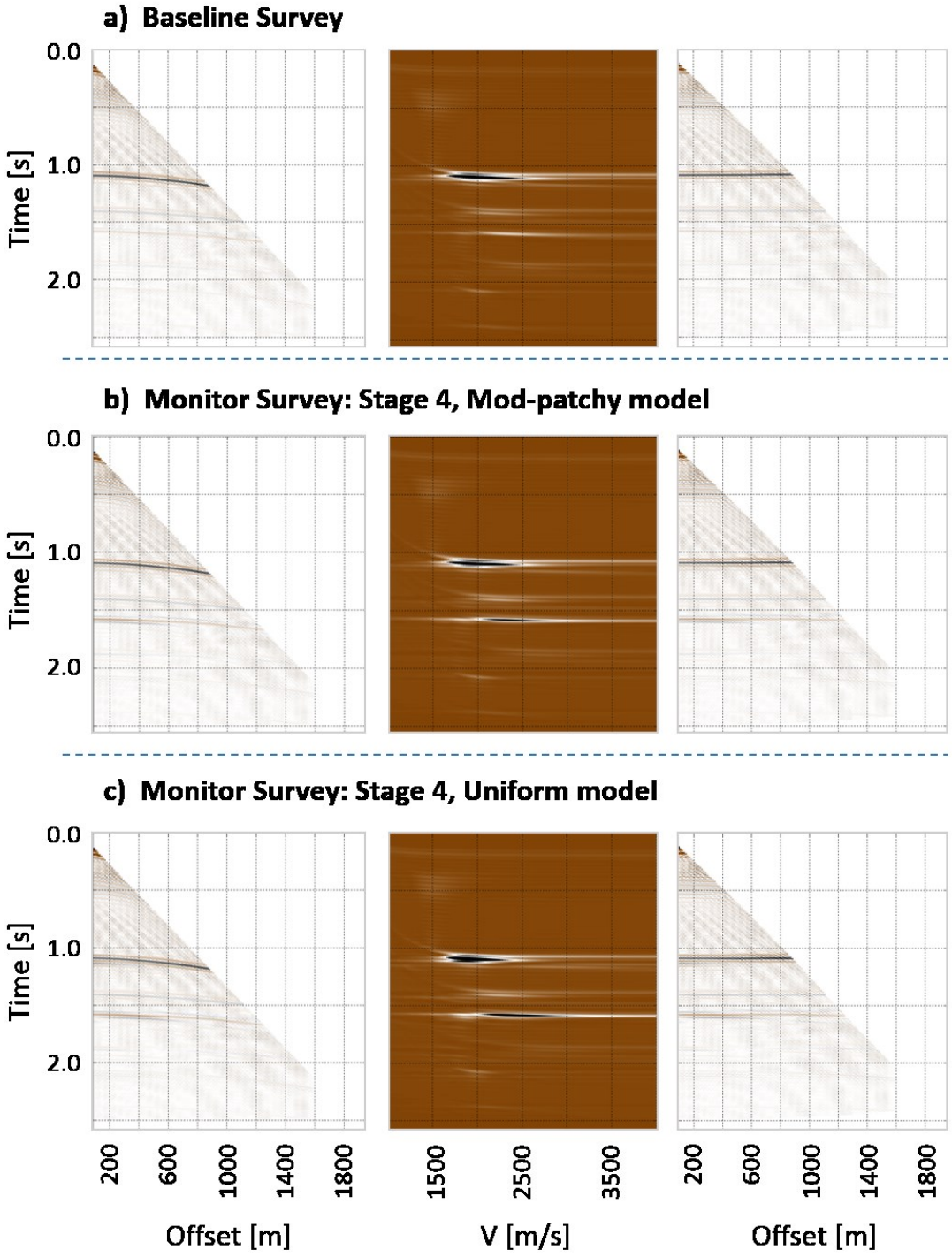

Figure 5.11. Muted CMP gather before NMO correction (left), velocity spectrum (middle) and after NMO correction (right) pre-injection (a) and after 20 simulated years for both modified-patchy (b) and uniform (c) saturation end-members.

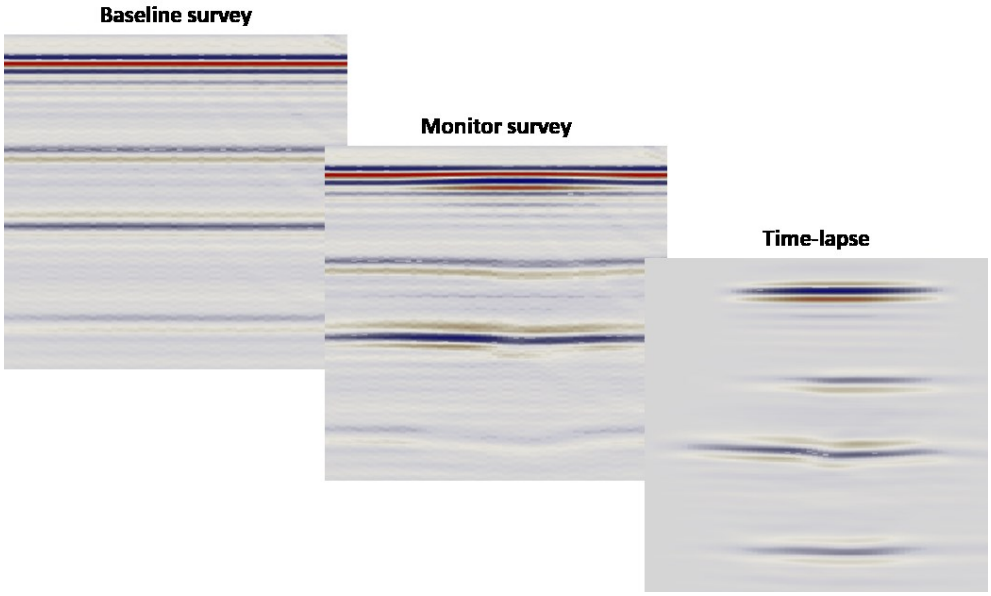

Figure 5.12. The generation of the time-lapse seismic section of the fourth monitored stage: contact with secondary seal.

5.5.1 Time-lapse seismic response

The depth-migrated baseline synthetic-seismic section, juxtaposed with the baseline P-wave velocity model, is shown in Figure. 5.13. The amplitude changes clearly represent the changing lithology in the model. The reflection at 1050m represents the topmost impermeable seal, overlying the secondary reservoir in the storage complex. The next strong reflector, at 1450m, is the top of the 300m thick intraformational seal separating the two reservoirs.

Figure 5.14 illustrates the time-lapse synthetic-seismic sections for each stage, for modified-patchy and uniform saturation models. Clearly evident are the strong reflectors and velocity push-down effects corresponding to the CO_2 in the reservoir. Minor differences are also evident between the modified-patchy and uniform synthetic seismic sections. Clearly evident however, is the lack of reflections corresponding to the plume during Stage 1, as well as the migrating front of CO_2, during Stage 3.

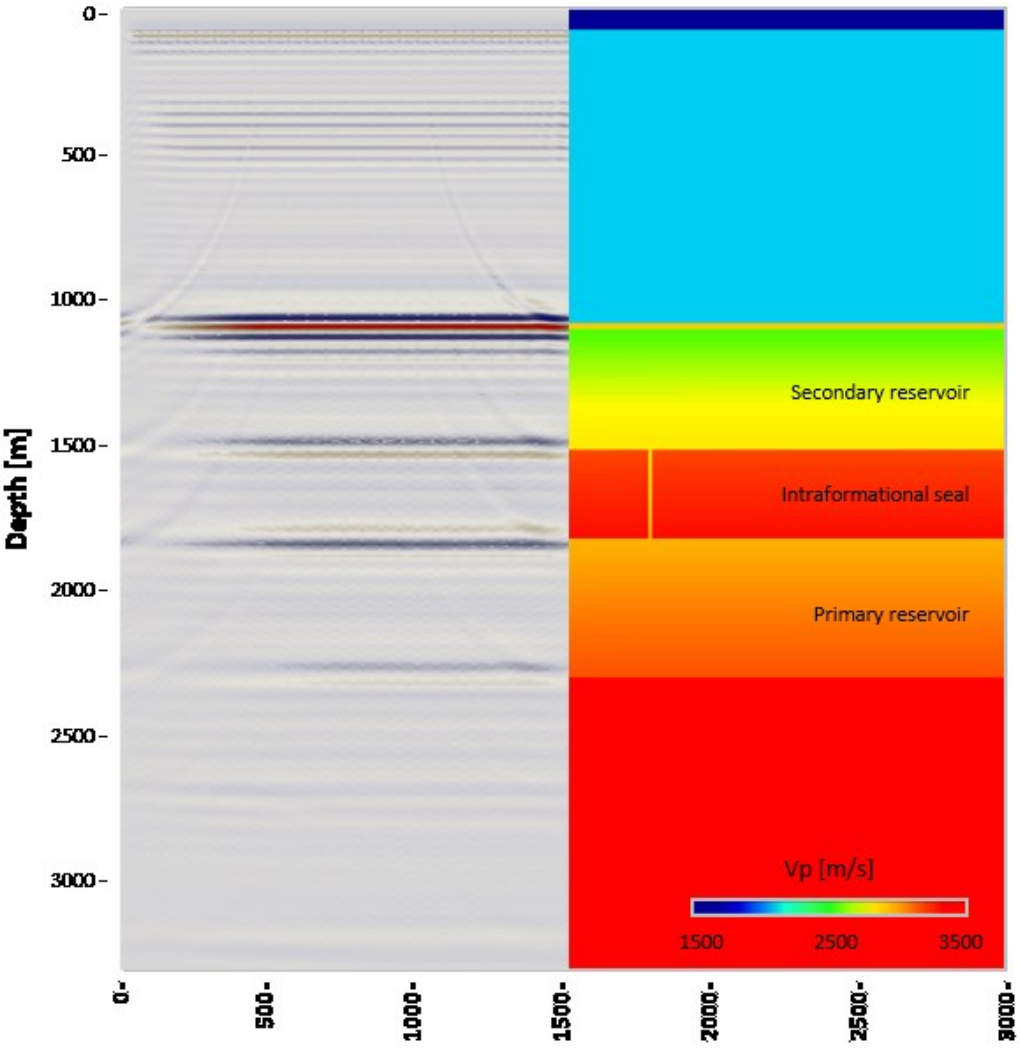

Figure. 5.13. Depth migrated seismic section (left), juxtaposed with the velocity model (right) for comparison.

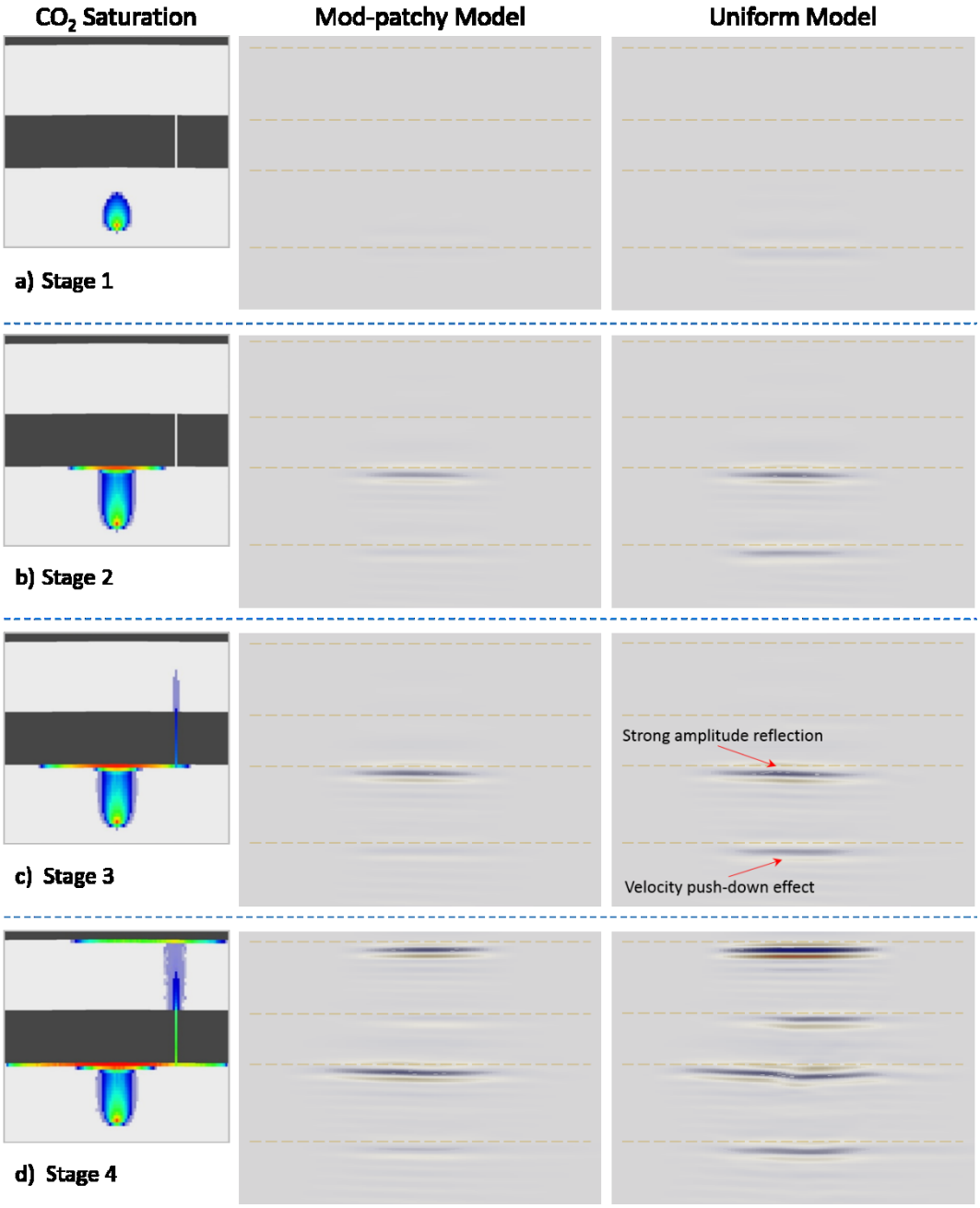

Figure. 5.14. Time-lapse synthetic seismic sections calculated using the modified-patchy and uniform velocity models for each monitored stage. The coloured lines represent the locations of the three interpreted zones in the reservoir.

5.6 Discussion

5.6.1 Monitorability of the four key stages in plume migration

The generated synthetic sections raise some concerns with respect to the ability of seismic techniques to monitor successfully the four key stages during a CCS project. In particular, the lack of reflections corresponding to free-phase migrating CO_2 is of concern.

Monitorability of the CO_2 plume during injection is simulated to show no reflection amplitudes in the primary reservoir. A very slight time-shift, of 3.5 msec, can be seen at the base of the primary reservoir, showing a slight effect of the injected CO_2 (Figure 5.14a). As expected, contact with the intraformational seal resulted in a prominent reflector at the top of the primary reservoir (Figure 5.14b). Directly below the reflector is a prominent velocity push-down effect. There are very minimal differences between the generated synthetics for Stage 2 and 3. The only obvious change is an increase in lateral size of the reflector resulting from the simulated increased growth of the CO_2 plume. No change in amplitude or velocity push-down effects are interpreted in the secondary reservoir or the intraformational seal (Figure 5.14c).

A closer look at the moment an initial loss of containment occurs is shown in Figure 5.15. The simulation shows vertical migration through the zone of weakness and into the secondary storage reservoir. The radius of the front is simulated at 30m. The migrating CO_2 is shown to consist of very low saturations, ranging from 1-10% with an average of 3% (Figure 5.15a). Saturations in this range, when modelling buoyancy-dominated CO_2 flow in the reservoir and the effects of capillary pressure and heterogeneity, have been published in papers such as Bryant et al., (2008), Silin et al., (2009) and Saadatpoor et al., (2010). Lower saturations of CO_2 play a key role as to whether the change in velocity is enough to result in a seismically interpretable response. A large difference between the two velocity saturation end-members can be seen. The modified-patchy model shows a change in velocity as great as -37 m/s, with an average of -12 m/s. The uniform modelling results show a change as high as -300 m/s, at an average of -177 m/s.

Interestingly, the generated synthetic sections show no change in amplitude in the secondary reservoir, in either the modified-patchy or uniform time-lapse sections (Figure 5.16). Furthermore, there are very little differences between the two end-member synthetic models. This suggests that the geometry of the migrating front of CO_2, and not the fluid saturation distribution model, will play a key role in detecting a loss of containment.

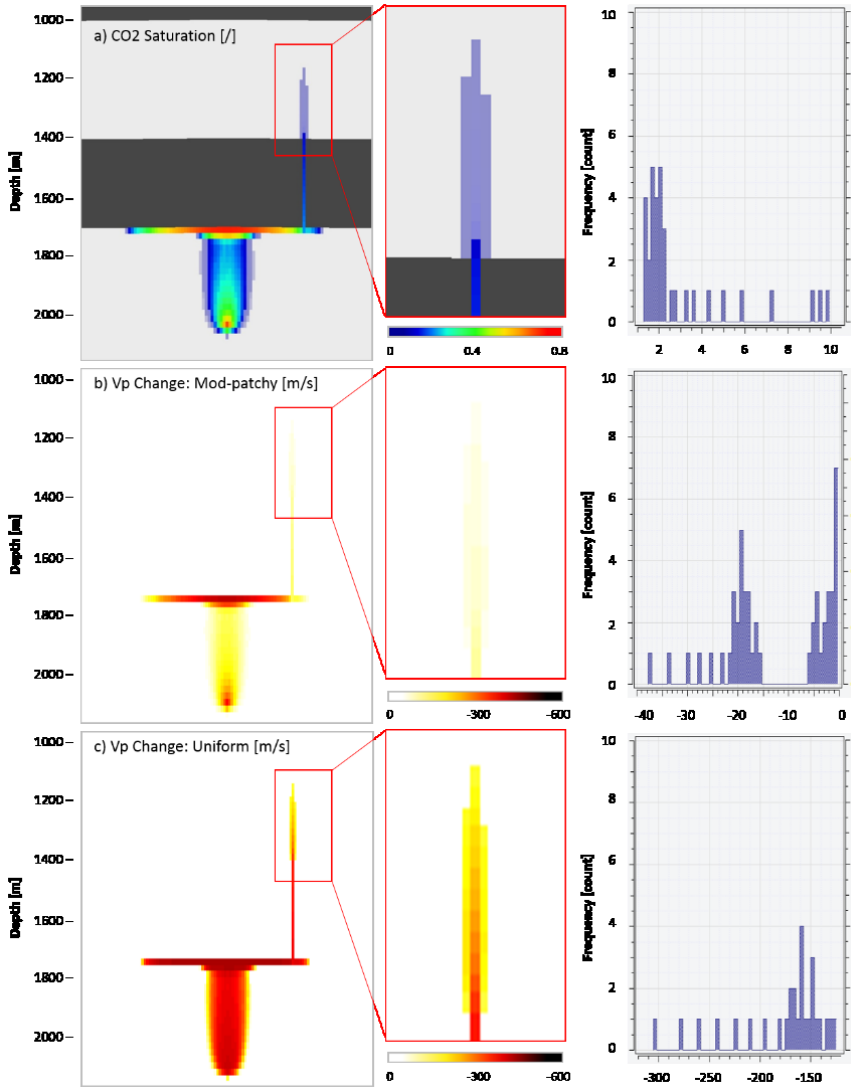

Figure 5.15. Highlighting the moment an initial loss of containment occurs, with the migrating front of CO_2 highlighted and enlarged in red (middle).b) and c) model the end-member ranges in velocity which could be expected. Histograms showing the frequency of each model is shown on the right.

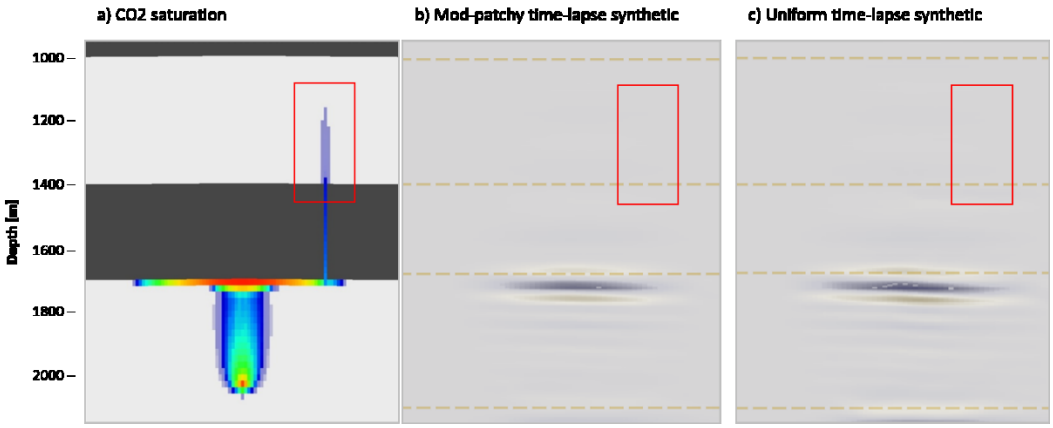

Figure 5.16. Focus on the generated synthetics for Stage 3, looking at the ability to detect an initial loss of containment. The location of the free-phase migrating front of CO_2 is highlighted in the red square.

The fourth monitoring stage, contact with the secondary seal, resulted in a large amplitude reflection corresponding to the top-most accumulation of CO_2 in the secondary reservoir (Figure 5.14d). Furthermore, prominent velocity push-down effects can be seen at the top intraformational seal and the top basement. Modelling suggests that the CO_2 plume will become visible on seismic sections once the CO_2 has accumulated below a seal in the secondary reservoir.

Interestingly, a prominent velocity push-down effect of 8 msec, for a uniform saturation distribution, is interpreted below the intraformational seal during Stage 4. This corresponds to the location of the zone of weakness. A closer look at the time-lapse sections of the difference between the Stage 4 and 3 synthetics shows this (Figure 5.17). The increased velocity push-down effect is interpreted as a high amplitude reflector directly below the modelled zone of weakness (Figure 5.17c, highlighted in the red box). This corresponds to 110 Tonnes of free-phase migrating CO_2.

Applying the same methodology, I looked at the time-lapse section of Stage 3 and Stage 2 (Figure 5.18). Although not as obvious as the time-lapse section for the later stage, a weak amplitude anomaly can be seen in the secondary reservoir due to the migrating front of CO_2 (Figure 5.18a). This very weak amplitude reflection is attributed to the migrating front of CO_2 resulting in a velocity push-down effect of

2 msec at the top intraformational seal. This velocity pushdown effect is also evident in the primary storage reservoir (Figure 5.18a, red highlighted box) and is attributed to 14.5 Tonnes of CO_2.

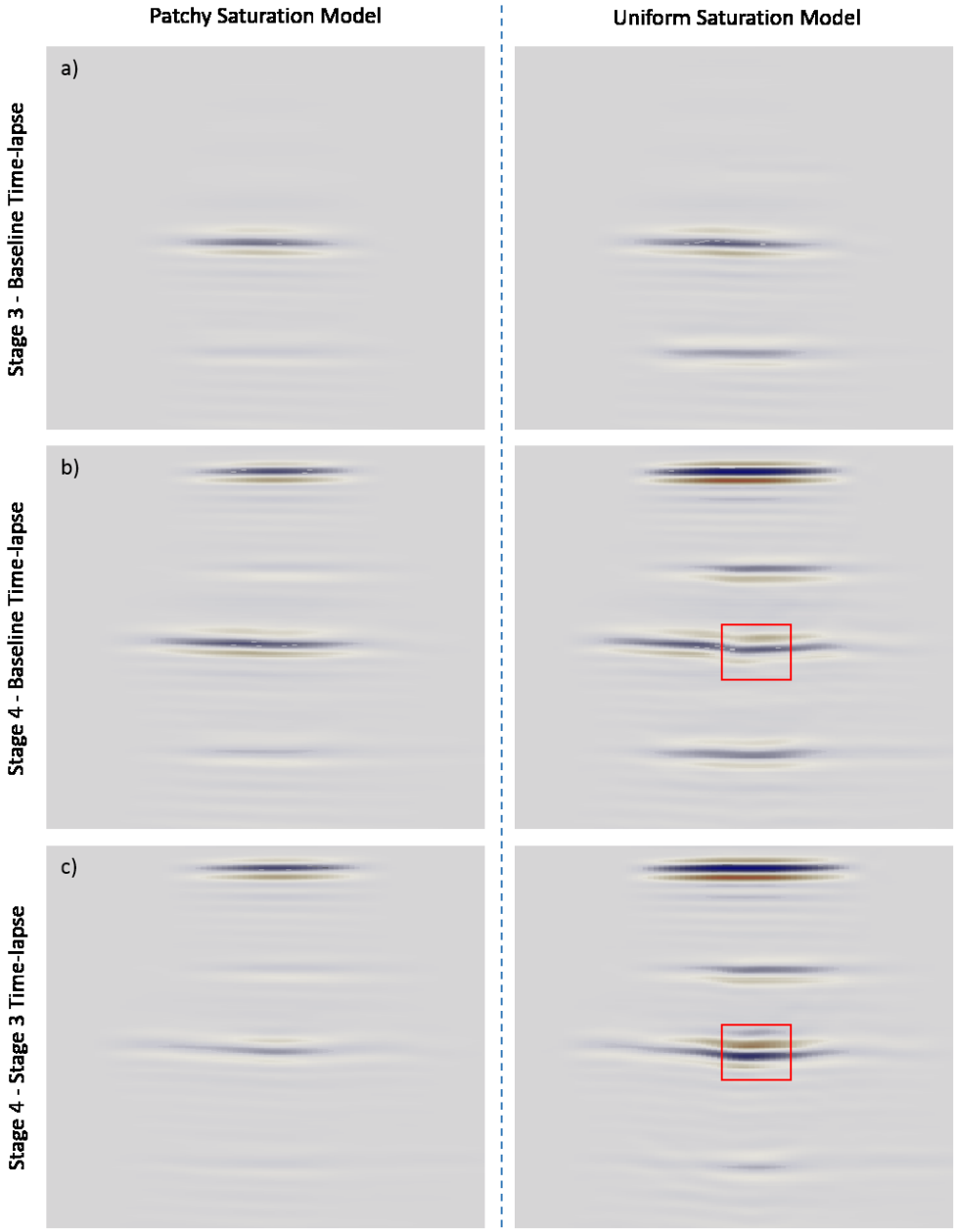

Figure 5.17. Time-lapse sections showing the difference between Stage 3 and 4 with the baseline (a and b) as well as the difference between Stage 4 and 3 (c) highlighting the change in amplitude during that time. The red square highlights the area with an increased velocity push-down effect, as well as high-amplitude reflectors, attributed to the larger volume of CO_2 migrating directly above through the zone of weakness.

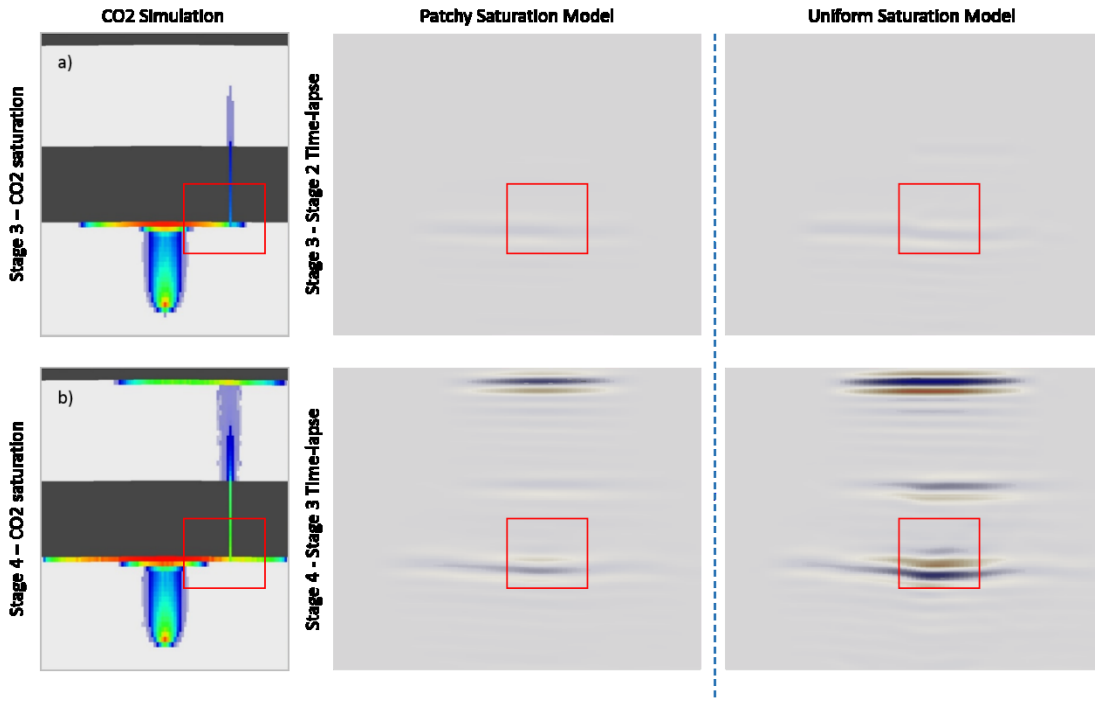

Figure 5.18. Time-lapse sections showing the difference between Stage 3 and 2 (a) and Stage 4 and 3 (b). The red square highlights the area with an increased velocity push-down effect attributed to the larger volume of CO_2 migrating directly above through the zone of weakness.

These results suggest that seismic techniques could be used to identify the location of a zone of weakness which has resulted in CO_2 migration outside the primary storage reservoir. This is done not only by interpreting reflection amplitudes, but also by identifying velocity push-down effects in the primary storage reservoir by generating time-lapse seismic sections of monitor surveys, not just the baseline survey, during the monitoring program. However, this assumes that the migrating front of CO_2 will have a uniform saturation distribution, resulting in large changes in velocity at low saturations (as highlighted in Figure 5.15).

5.7 Conclusions

The key contribution of this study is to assess the ability of seismic techniques to monitor the following key stages during a CCS project: Stage (1) migrating plume during injection, Stage (2) contact with primary seal, Stage (3), first instance of a breach and Stage (4) contact with secondary seal.

To assess the feasibility for seismic monitoring of these stages, I estimated the time-lapse signal over a theoretical, clean, homogeneous sandstone reservoir through the application of the monitorability workflow presented in Chapter 4.

Once a migrating CO_2 front was simulated, the corresponding elastic properties were determined by calculating two saturation end-member models: uniform and modified-patchy saturation. This was done to understand the expected ranges which could be encountered when assessing the ability to detect the different stages.

Initial analysis of the results suggests that the main monitoring stages which could be visible on the synthetic seismic sections are the structurally trapped accumulations of highly saturated CO_2. These accumulations resulted in large amplitude reflections, as well as large velocity push-down effects, below the reservoir. Further analysis suggests the use of time-lapse imaging of two monitor surveys to identify the location of velocity push-down effects resulting purely from a loss of containment. This could provide valuable information regarding the location of a zone of weakness which has resulted in CO_2 migration outside the primary storage reservoir. This is done not only by interpreting reflection amplitudes, but also by identifying velocity push-down effects in the storage reservoirs.

From this a conservative conclusion could be made that seismic monitoring of the four key monitoring stages is feasible; however, with great dependence on the saturation model when monitoring a loss of containment. In reality this might not be the case, as the noise-free synthetic seismic sections show velocity push-down effects for a migrating front with a radius as small as 30m. This could be too optimistic, as the model was implemented at a cross-section across the exact known migration

point. However, with this knowledge, feasibility studies conducted prior to injection could provide valuable information regarding potential migration hotspots which could assist in the design and construction of future surveys aiding the detection of a loss of containment. Furthermore, the overall monitorability of a migrating plume for the scenario chosen in this study is not a definite answer, as the saturations are controlled by the relative permeability and capillary pressure curves input into the simulation, where different curves, as well as varying injection rates, may calculate a greater range of CO_2 saturations, and therefore, a greater change in elastic behaviour. This demonstrates that the detectability of a migrating CO_2 front is a site-specific issue which depends not only on the geophysical parameters of the seismic survey, but also on the geological variations and spatial distribution of the CO_2 in the reservoir. Assessing these site-specific variations through the application of the monitorability workflow during initial storage-site assessment stages, could provide valuable information regarding the ability to detect CO_2 migration, aiding the ability to detect a loss of containment.

Summary

I assess the feasibility of seismic methods to monitor four key stages during a CCS project: Stage (1) migrating plume during injection, Stage (2) contact with primary seal, Stage (3), first instance of a breach, and Stage (4) contact with secondary seal. I demonstrate the ability of seismic techniques to detect structurally trapped CO_2 in the primary and secondary reservoirs. Initially, free-phase migrating CO_2 did not result in an interpretably response. However, I have shown that time-lapse images of two monitor surveys can be used to identify and locate velocity push-down effects in the reservoir. This provides valuable information regarding the location of the modelled zone of weakness which encouraged CO_2 migration outside the primary storage reservoir. However, this is shown to be dependent on the saturation model used, as the location of the loss of containment is only visible when assuming a uniform saturation distribution.

6. Seismic monitoring of heterogeneous reservoirs

Through the application of the monitorability workflow presented in Chapter 4, I assess the ability of seismic methods to image plume growth, evolution, and migration in a heterogeneous saline reservoir in the UK sector of the North Sea. I simulate the injection of CO_2 for 20 years and continue the simulation for a further 10 years post injection to allow for continued migration and residual trapping. To account for the uncertainties regarding the fluid saturation distribution, end-member models – uniform and patchy – are used to generate the widest range of velocity distributions which could be encountered. The end-member velocity models are then used to simulate the expected time-lapse seismic responses. I then discuss the monitorability of plume growth in a reservoir as well as the implications for the detection of a migrating front.

This chapter is a modification of the published paper *Seismic monitoring of CO_2 plume growth, evolution and migration in a heterogeneous reservoir: Role, impact and importance of patchy saturation* in Eid et al., (2015a). The theory behind the workflow has been taken out and explained in Chapter 4.

6.1 Introduction

Seismic techniques are commonly used to monitor CO_2 containment and conformance over the lifetime of a project. Through the application of time-lapse seismic surveys, pilot CO_2 sequestration sites such as Sleipner (Arts et al., 2004, Arts et al., 2008), Weyburn (Wilson and Monea, 2004) and Ketzin (Bergmann et al., 2011, Ivandic et al., 2012, Ivandic et al., 2015) have successfully monitored structurally trapped CO_2, because the displacement of brine by less dense and more compressible CO_2 results in changes in the acoustic properties of the reservoir (Pearce, 2005). However, the ability to accurately image a free-phase migrating CO_2 plume during injection remains challenging due to uncertainties regarding the pore-scale distribution of fluids in the reservoir, and in turn, the most appropriate rock-physics model to simulate this. As the seismic response depends not only on the fluid type - liquid or gas - but also on the fine-scale spatial distribution of the phases (White, 1975, Mavko and Mukerji, 1998), end-member fluid distribution models are used to calculate the possible range of expected velocities prior to generating and interpreting the seismic response.

Fluid-flow to seismic modelling workflows are typically used to determine what a given sensor would measure in a given environment. As described in Chapter 4, this tool is used during, and after, CO_2 injection to facilitate the interpretation of processed data and to assist in the process of history matching. However, often when comparing synthetic and real time-lapse seismic data for CO_2 conformance, reservoirs are assumed to be homogeneous, for example in Chadwick et al., (2006a) and Arts et al., (2007). This does not result in an accurate representation of the processes which occur in the field.

In this study I account for this by computing the time-lapse seismic responses of a heterogeneous saline reservoir in the UK sector of the North Sea. The incorporation of reservoir heterogeneity results in a range of saturations. This complexity allows for a more representative velocity distribution. To account for the uncertainties regarding the fluid saturation distribution, end-member models – uniform and patchy – are

used to generate the widest range of velocity distributions to try to understand the velocity-saturation behaviour which could be encountered. The uniform and modified-patchy velocity models are then used to simulate time-lapse seismic responses to assess the potential for seismic methods to image CO_2 plume growth and evolution in a heterogeneous reservoir, as well as the potential to detect a free-phase migrating front of CO_2.

In this chapter I simulate a migrating plume, and investigate the range of seismic responses due to the injected CO_2 by assessing variations in the time-lapse signal over a heterogeneous sandstone reservoir through the application of the monitorability workflow (Chapter 4).

6.2 Geological model

The model used in this study is an adaptation from Williams et al., (2013), representing part of the Triassic Bunter Sandstone Formation in the UK sector of the North Sea (Figure. 6.1). This formation has been identified as having the potential to store large amounts of CO_2 in the saline reservoirs (Holloway et al., 2006, Heinemann et al., 2012). The model contains 3 dip-closed structures formed by post-depositional halokinesis in the underlying halite-dominated strata of the Zechstein Group. These domes are unaffected by faulting and form ideal traps for injected CO_2. The reservoir is overlain by mudstones of the Haisborough Group, forming an effective seal.

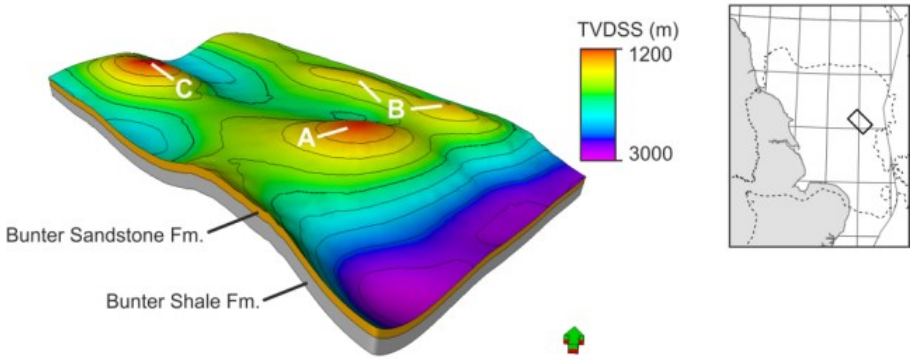

Figure 6.1. Bunter Sandstone Model with each dome labelled and a location map (modified from Williams et al., 2013).

Williams et al., (2013) partitioned the formation into five zones according to changes in depositional environment interpreted from petrophysical analysis and a regional depositional model for the Bunter Sandstone. The inferred reservoir properties in the model were based on geophysical log analysis. The porosity is strongly influenced by variations in lithology, and ranges from 10% to 30% (Figure. 6.2). Williams et al., (2013) provide a detailed description of the reservoir model.

Each interpreted zone plays an important role in the growth and evolution of the injected CO_2. The zones provide obstacles to migration, allowing for accumulations beneath each barrier and allowing for an assessment of the potential of seismic techniques to detect them.

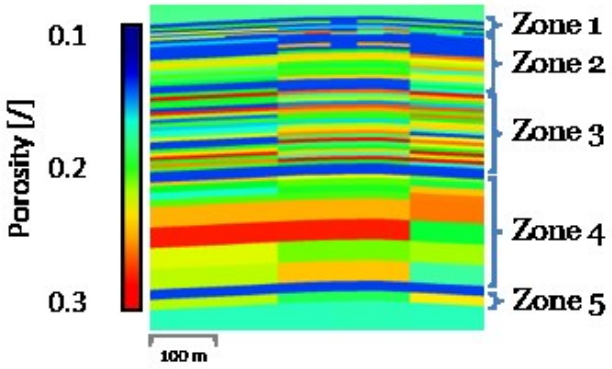

Figure 6.2. Cross section through the reservoir highlighting the degree of heterogeneity in porosity.

Often, when comparing synthetic and real time-lapse seismic data for CO_2 detection or quantification, reservoirs are assumed to be homogeneous, for example in Chadwick et al., (2006a) and Arts et al., (2007). If I did this here it would result in CO_2 saturations which are bi-modal in distribution with maximum saturation values equal to $1-S_{wir}$ (irreducible water saturation). Incorporating reservoir heterogeneity allows the range of saturations and hence velocity distributions to be assessed more accurately due to the tortuous migration caused by the intra-reservoir baffles. This has been demonstrated by Ghanbari et al., (2006) through the simulation of CO_2 storage in both a homogeneous and a heterogeneous model. The addition of shale layers in the model resulted in CO_2 accumulations below these baffles causing the CO_2 to flow laterally rather than vertically, distorting migration. This allows for a

more accurate way to assess, understand and compare the saturation scales and phase distributions which can be expected.

For this study, I have modified the reservoir model, with a focus purely on dome A, and have included surfaces for the overburden up to the sea bed (Figure. 6.3). The surfaces were interpreted by PGS from their SNS MegaSurvey 3D seismic dataset (Williams et al., 2013) and were validated from existing well data and formation tops. No faults were found in the modelled area. Dome A has been chosen for this study as it provides a significant structural closure, allowing for large volumes of CO_2 to be accommodated. The top seal is also situated at an appropriate reservoir depth (1200m) for CO_2 storage. At this depth, pressures and temperatures are above the critical point, where the CO_2 is in a 'supercritical state', with the density of a liquid and the viscosity of a gas (Cook, 2012). The original model assumed all barriers in the Bunter Sandstone Formation were impermeable, with 0% porosity and 0 mD permeability. To allow for CO_2 plume growth and migration through these barriers up to the top seal, as well as accurate velocity calculations, I have assumed 13% porosity and 15mD permeability for all barriers in each zone. All cells with 13% porosity and 15mD permeability are assumed to be shales, while any cells with greater porosity and permeability are assumed to be sandstones. A kv/kh ratio of 0.1 is used.

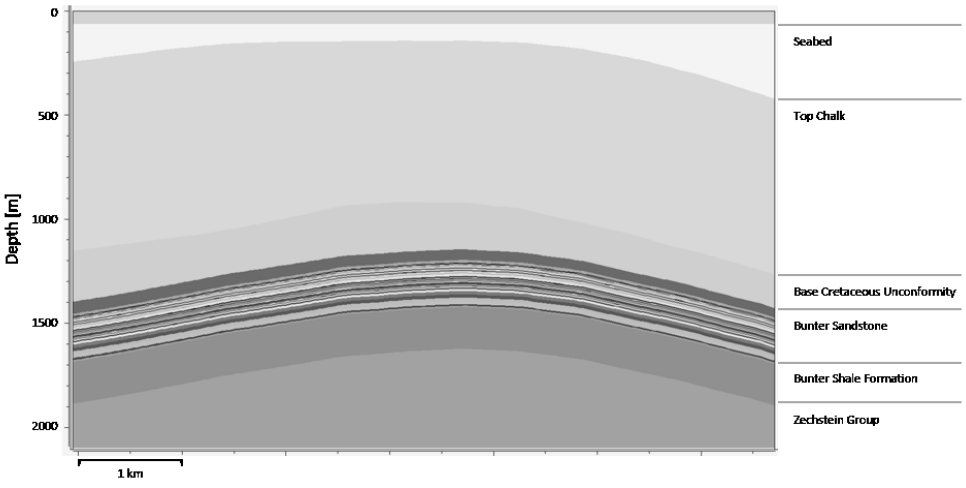

Figure 6.3. Cross-section through the entire geological model with interpreted surfaces on the right (vertical exaggeration of 2). SNS MegaSurvey data courtesy of PGS.

The modified 3D model covers an area of 6750m x 4650m with horizontal cell-size dimensions of 45m x 45m throughout. Vertical cell-size in the Bunter Sandstone Formation varies from 1m to 15m depending on variations in lithology observed on the geophysical logs.

6.3 Fluid flow model

Permedia's black oil simulator (Permedia, 2014) is used to simulate the migration and plume evolution of the injected CO_2 in the Bunter Sandstone, with a focus on accumulations below baffles in each zone. CO_2 injection is modelled through a single well at a constant rate of 0.1 Mt/year for 20 years through a 20m perforation interval into a high porosity sand in Zone 4 (Figure. 6.4). The simulation is extended for 10 years post injection to allow for continued migration and residual trapping.

As there are no measured relative permeability or capillary pressure curves for the Bunter Sandstone, measurements from Bennion and Bachu's (2006) Cardium Sandstone are used to model drainage and imbibition for brine and CO_2 (Figure. 6.5). I use the equation of state presented by Duan and Sun (2003) in this study. The input BOS (black oil simulator) parameters are summarised in Table 6.1.

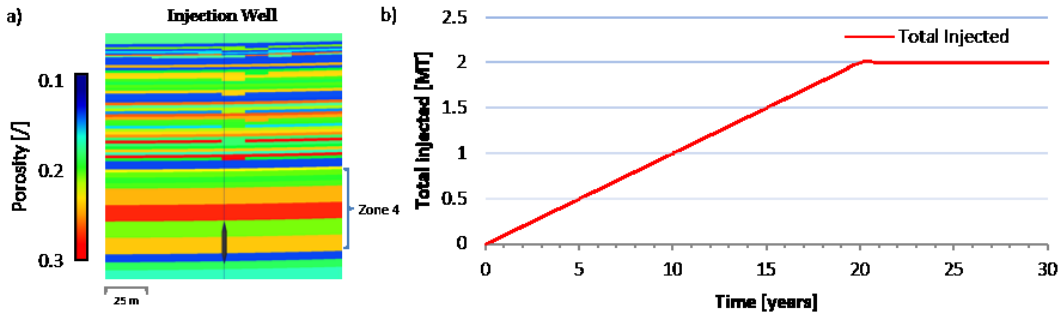

Figure 6.4. a) Cross-section through the reservoir showing the injection well and 20m perforation interval (black), b) Summary of the total injected CO_2 over simulated years.

Table 6.1. Input BOS parameters as recommended by Williams et al., (2013).

Simulation parameters		
Sea bed temperature	*°C*	4
Temperature gradient	*°C/km*	36.5
Pressure gradient	*MPa/km*	10.07
Salinity	*ppm*	130,000

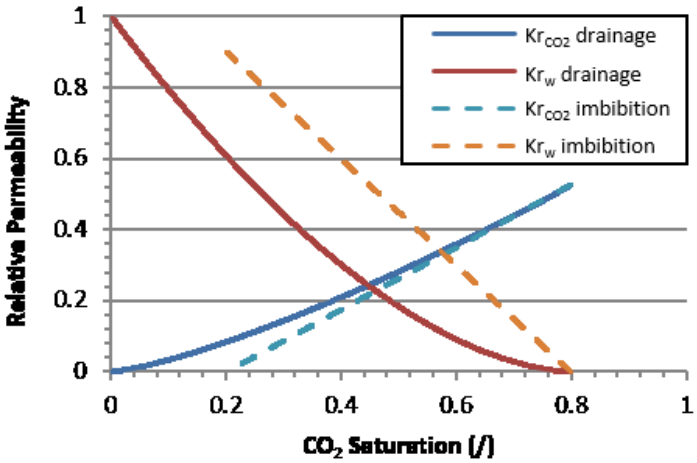

Figure 6.5 The two-phase relative permeability (Kr) curves used to model CO_2 flow in the reservoir. The solid lines refer to the reservoir undergoing drainage while the dashed lines represent imbibition. The curves represent an irriducable water saturation of 0.2 and residual CO_2 saturation of 0.2 (Bennion and Bachu, 2006).

6.3.1 CO_2 saturation distribution

Figure. 6.6(a-c) shows 2D sections of the 3D simulation results at three stages (5 years, 11 years and 20 years) of plume evolution in the reservoir. Figure 6.6(d-f) shows the histogram of saturations in the grid blocks. After 5 years and 0.5MT of injected CO_2, the plume has accumulated below two intra-formational baffles in Zone 4 with a mean and maximum saturation of 17% and 50%, respectively. After 11 years of injection, the plume has breached the baffle at the top of Zone 4 and has penetrated into Zone 3 while also growing laterally (Figure. 6.6b). Increasing CO_2 concentrations

below the baffles in Zone 4 are shown at an average of 20%, with maximum saturations of 55%. A migrating leg west of the plume is also evident due to increased lateral migration reaching an area with no sealing lithology. After 20 years of injection, CO_2 breaches the baffle at the top of Zone 3 and penetrates into Zone 2, resulting in a free-phase migrating front of dimensions 271m by 30 m. Saturations in the reservoir as a whole are shown at an average of 23%, with maximum saturations of 62%. The saturation of the CO_2 is shown to be very heterogeneous due to the heterogeneous nature of the reservoir.

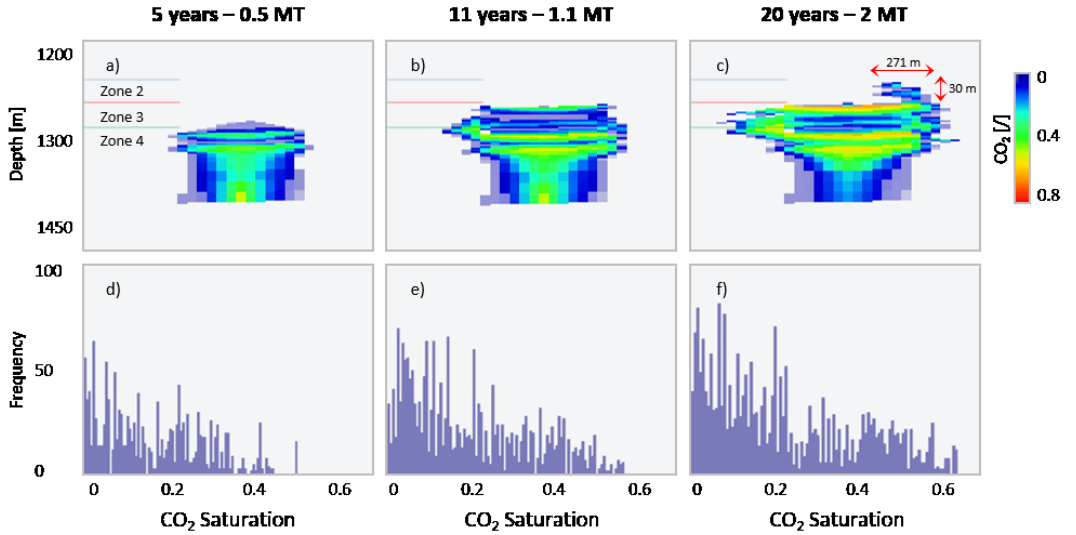

Figure 6.6. 2D sections of the 3D simulation highlighting three stages of plume evolution, and histograms showing the associated ranges in saturations in the Bunter Sandstone reservoir, after 5, 11 and 20 simulated years. Vertical exaggeration of 3.

6.4 Rock physics model

As detailed in section 3 of Chapter 4, Gassmann's fluid substitution workflow is applied to assess the effect of the fluid saturation on the seismic properties. The friable-sand model (Dvorkin and Nur, 1996) is used to calculate the dry frame bulk modulus (K_{dry}) and shear modulus (μ_{dry}) for the sandstone layers. The friable-sand model is deemed most appropriate for the Bunter Sandstone reservoir due to the level of sorting, lack of cementation and range of porosities interpreted from the well log analysis. The matrix bulk modulus K_m is calculated via the application of Voigt-Reuss-Hill (VRH) method (Avseth et al., 2005). The constant-clay model (Avseth et

al., 2005) is used to describe the velocity-porosity behaviour for shales. I calculated the range in expected velocities by calculating both uniform and modified-patchy saturation end-members. Input parameters for the rock physics modelling are summarised in Table 6.2.

Table 6.2. Input petrophysical parameters. CO_2 and brine modulus calculated based on simulation parameters (Table 6.1). Vclay values based on calculated Vclay log from Williams et al., (2013).

Petrophysical parameters			
Fluid properties			
CO_2	Density		From simulation
	Saturation		From simulation
	Bulk modulus	*GPa*	0.0993
Brine	Density		From simulation
	Saturation		From simulation
	Bulk modulus	*GPa*	2.55
Mineral properties			
Sandstone	Vclay	%	0.1
	Density	kg/m^3	2650
Shale	Vclay	%	0.9
	Density	kg/m^3	2700

6.4.1 Heterogeneous reservoir velocity distribution

The heterogeneous nature of the Bunter Sandstone reservoir results in a distribution of velocities which range from 1800 m/s to 3500 m/s, depending on lithology, porosity and fluid saturation (Figure. 6.7). These ranges match typical velocities for shales and saturated sandstones (Bourbié et al., 1987) and are dependent on porosity and fluid saturation.

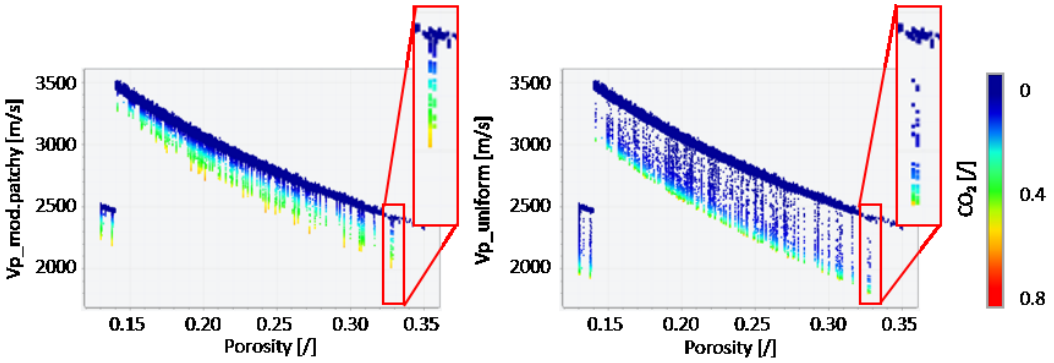

Figure 6.7. Calculated velocity as a function of porosity for the Bunter Sandstone, coloured by CO_2 saturation. Velocity is calculated assuming both a modified patchy (left) and uniform saturation model (right). Calculated velocities less than 13% porosity correspond to shale layers in the model.

The calculated velocities for the Bunter Sandstone reservoir show an approximately linear relationship between velocity and porosity, as expected. An increase in CO_2 saturation of 80% shows a maximum decrease in velocity from -350 to -550 m/s depending on the velocity model used. The saturation change demonstrates the key differences between uniform and modified-patchy saturation, where patchy saturation results in a linear change in velocity with increasing fluid content, the uniform saturation results in a sharp decrease in velocity at low saturations, with minimal to no change thereafter.

Figure. 6.8 is the calculated velocity models assuming both modified-patchy and uniform saturation for each stage of CO_2 plume evolution. Analysis of the change in velocity with the baseline clearly shows the differences between the two models. A focus on the uniform velocity modelling results (Figure. 6.8g-l) shows that the change in velocity is as great as -550 m/s from the outset, with a very minimal change in velocity of only -5 m/s in the plume body when comparing each stage. Large changes in velocity are evident throughout each stage allowing for clear distinction between the CO_2 plume and the reservoir. However, features in the plume itself, such as the immobile CO_2 accumulations below intra-formational baffles, are difficult to distinguish from the plume. The velocity model calculated assuming a modified-patchy saturation model (Figure. 6.8a-f) shows the main differences between the two models as it allows features in the plume body to be distinguished. A maximum

velocity change of only -220 m/s is evident after 5 years. With increasing accumulations below the intra-reservoir baffles, the change in velocity is shown to be as great as -270 m/s after 11 years and -450 m/s after 20 years. This change in velocity is similar to those calculated assuming a uniform saturation distribution. At these high saturations, the magnitude of the velocity change is independent of the model used as the calculated velocities converge as the maximum saturation is reached. A focus on the free-phase migrating front of CO_2 in Zone 2 after 20 years shows a change of velocity of roughly -110 m/s for the modified-patchy model and -400 m/s for the uniform model.

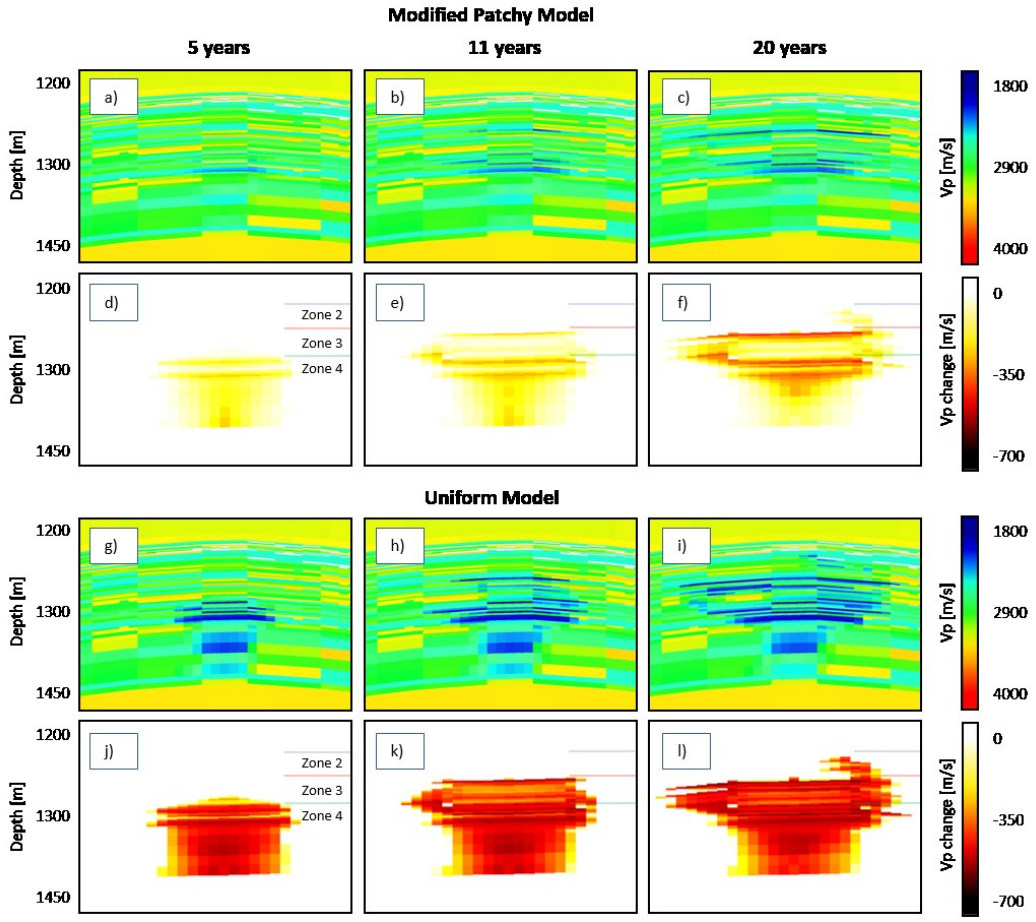

Figure 6.8. Results highlighting the petrophysical modelling results. (a-c) show the calculated V_p assuming a modified-patchy model, (d-f) highlighting the change with V_p, (g-i) calculated V_p assuming a uniform saturation model, (m-o) highlighting the change in V_p with baseline. The coloured line represent the locations of the three interpreted zones in the reservoir. Vertical exaggeration of 3.

6.5 Seismic forward model

Using Nucleus+ (Taylor and Julliard, 2013), I simulate the acquisition of a single line towed streamer seismic survey based on acquisition parameters similar to real time-lapse data (Table 6.3). The source signature is a zero-phase Butterworth wavelet of 2.0 msec sample interval, with low cut and high cut frequencies of 8Hz and 90Hz and slopes of 18 and 72 dB/octave, respectively. Synthetic shot records are generated along a 6km east-west section. The modelling is performed for each of the monitoring stages, for both uniform and modified-patchy saturation cases.

Table 6.3. Synthetic seismic modelling acquisition parameters

Acquisition parameters	
Receiver spacing	25 m
Receiver depth	7.5 m
Source spacing	25 m
Source depth	5 m
Cable length	5500 m
Number of receivers	236
Number of shots	220
Recording length	2 sec

Synthetic shot gathers differ depending on the position of the recording spread. Pre-injection, events on the gather arise due to variations in the geological interface due to changes in acoustic impedance (Figure 6.9a). Once CO_2 has been introduced into the reservoir, reflectivity is increased with more prominent time-shifts below the plume. The uniform modelling results show larger reflectivity and time-shifts (Figure 6.9c) when compared with the modified-patchy modelling results (Figure 6.9b).

A mute is applied to remove the refracted arrivals. Velocities chosen following velocity analysis are used to apply normal moveout (NMO) corrections (Figure 6.9).

The traces are then stacked making a seismic section. The seismic section is then depth-migrated using the baseline velocity model using the phase-shift plus interpretation (PSPI) method (Ferguson and Margrave, 2005). The PSPI method is chosen as it accounts for lateral variation in velocity (Han, 1998), which is clearly evident when dealing with heterogeneous reservoirs (Section 6.4.1). A time-lapse image is then generated by subtracting the baseline survey from the monitor survey to show the effect of the CO_2 (Figure 6.11).

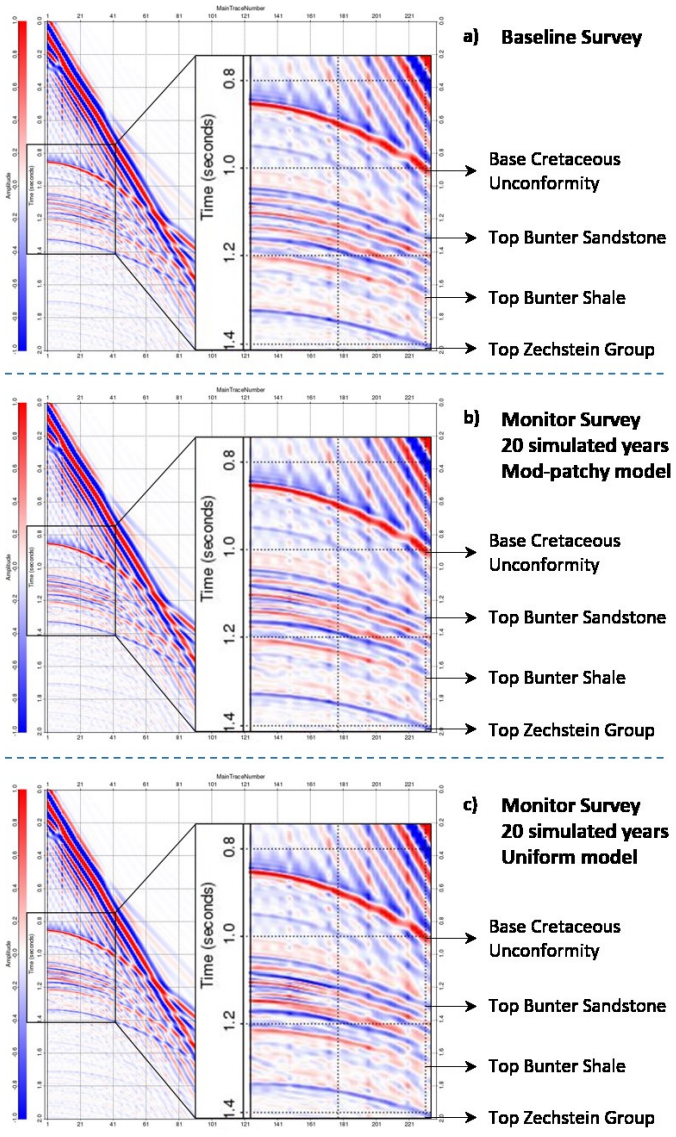

Figurere 6.9 Synthetic pre-stack gather pre-injection (a) and after 20 simulated years for both modified-patchy (b) and uniform (c) saturation end-members. The Bunter Sandstone reservoir has been enlarged and highlighted in the black box. Note the enhanced reflectivity and increased time-shifts due to the CO_2 plume.

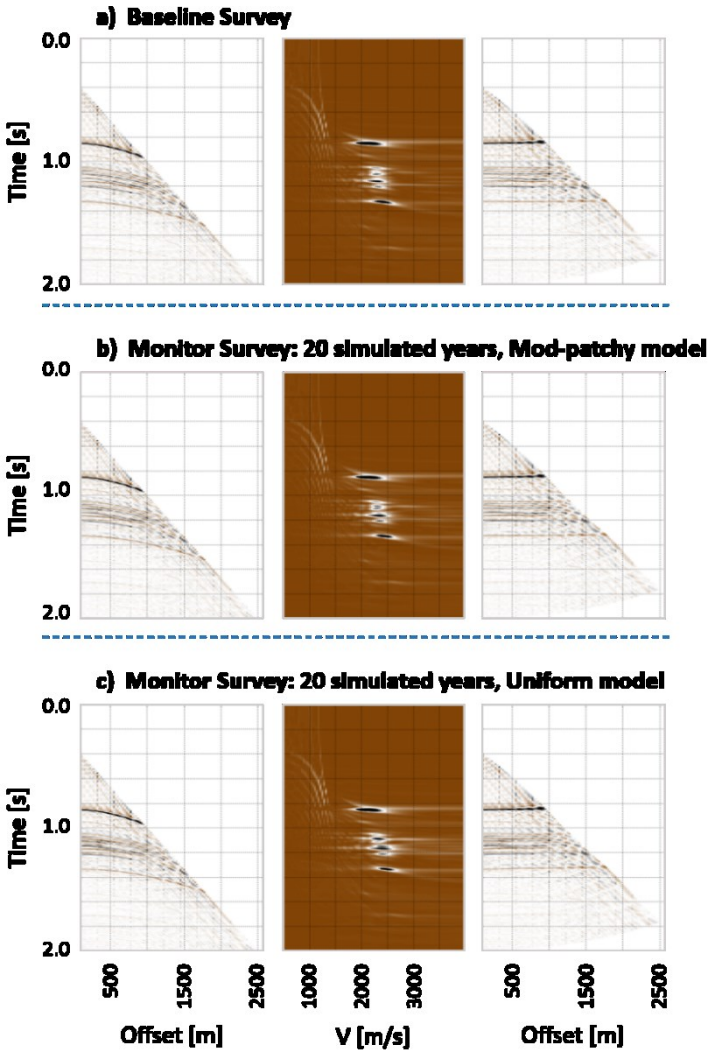

Figure 6.10 Muted CMP gather before NMO correction (left), velocity spectrum (middle) and after NMO correction (right) pre-injection (a) and after 20 simulated years for both modified-patchy (b) and uniform (c) saturation end-members.

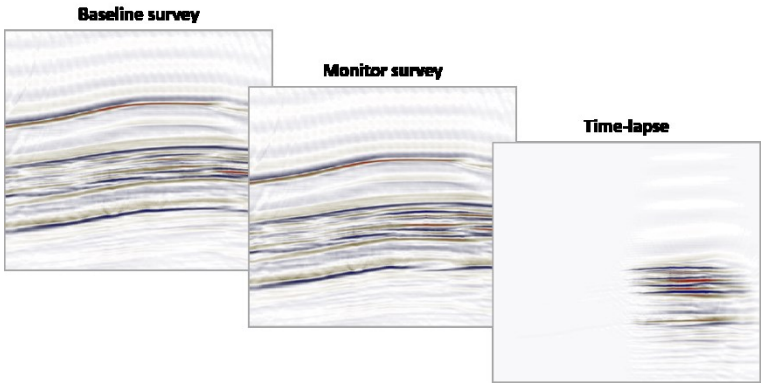

Figure 6.11. Time-lapse seismic section of the CO_2 plume after 20 simulated years. A uniform saturation distribution was assumed.

6.5.1 Time-lapse seismic response

The depth-migrated baseline seismic section, juxtaposed with the baseline P-wave velocity model, is shown in Figure. 6.12. Strong amplitude reflections are clearly evident at interfaces where the seismic velocity changes abruptly. In the Bunter reservoir, reflectivity is increased due to increased heterogeneity, producing lateral changes in velocity. High amplitude reflections in the reservoir correspond to the low porosity sands.

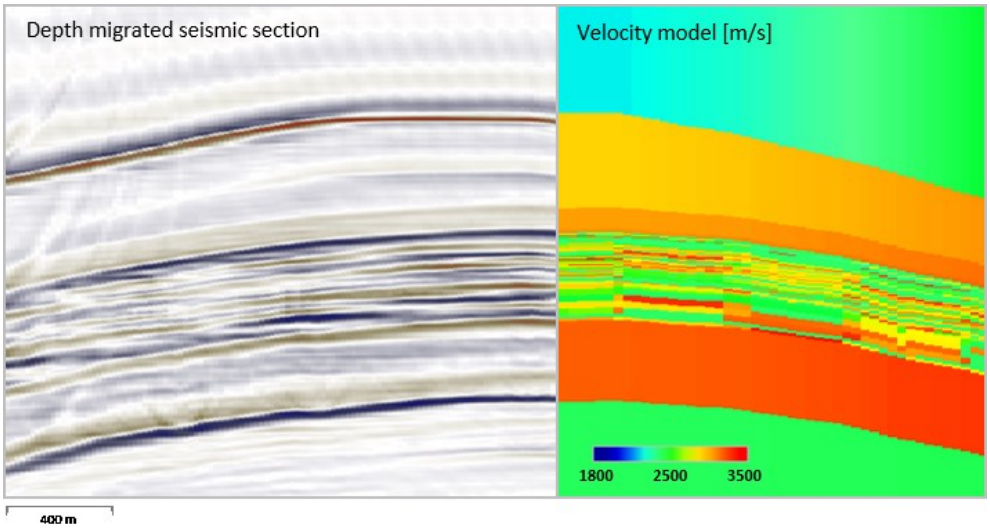

Figure 6.12. Depth migrated seismic section (left), juxtaposed with the velocity model (right) for comparison. Vertical exaggeration of 2.

The introduction of CO_2 into the reservoir results in an increase in reflectivity and a prominent time-shift. The time-lapse sections (Figure. 6.13d-i) show clear differences between the uniform and modified-patchy saturation models. The synthetic seismic results calculated using the uniform velocity model show a clear change in amplitude, as well as a prominent time-shift below the plume. The synthetics calculated using the modified-patchy model are very different, with lower amplitude reflections, often corresponding to zones of highly saturated, structurally trapped CO_2.

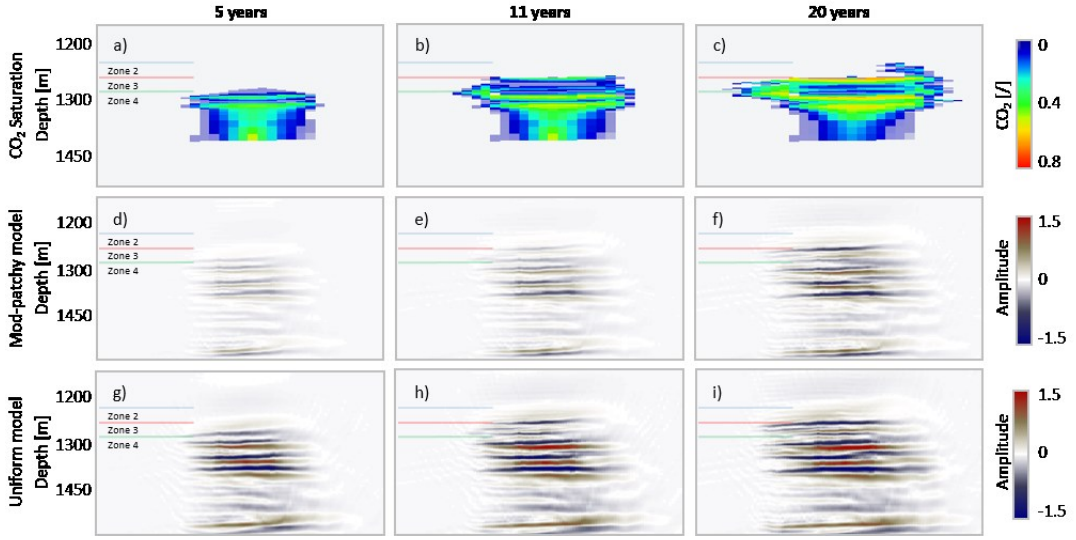

Figure 6.13. Time-lapse synthetic seismic sections calculated using the modified-patchy and uniform velocity models for each stage in plume growth. The coloured lines represent the locations of the three interpreted zones in the reservoir. Vertical exaggeration of 3.

6.6 Discussion

6.6.1 Monitorability of plume growth in a reservoir

A comparison of the three modelled stages provides confidence in the ability of seismic techniques to image plume growth and evolution in the reservoir, as the top-most reflector in each seismic section corresponds to the top-most accumulation of CO_2.

Furthermore, a detailed look at the plume after 20 years (Figure. 6.14) shows negative seismic impedance contrasts corresponding to the structurally trapped CO_2. Interpretation of the modified-patchy model shows three primary reflectors, which can be attributed to the three main CO_2 accumulations. The amplitude of the reflector is also shown to be strongest at the centre, gradually becoming weaker farther out in both directions, as shown in the enlarged box in Figure. 6.14. Although this can also be interpreted in the uniform seismic section, it proves more difficult as each reflector shows a large change in amplitude throughout. As the subtle change in amplitude is directly related to the concentration of CO_2 in each accumulation, it suggests that patchy saturation has important implications for the detection of CO_2 movement and for the quantification of volume of CO_2 injected into the reservoir. Previously, when

quantifying the total amount of injected CO_2, a uniform saturation distribution has been assumed (for example, Chadwick et al., 2005). Through 4D seismic quantification, Chadwick et al., (2005) were able to account for 85% of the total amount of injected CO_2 in the Utsira Formation. By assuming a modified-patchy saturation distribution, a more appropriate account for the injected CO_2 might be possible. However, there is an issue of non-uniqueness due to the transition from modified-patchy to uniform saturation with increasing time.

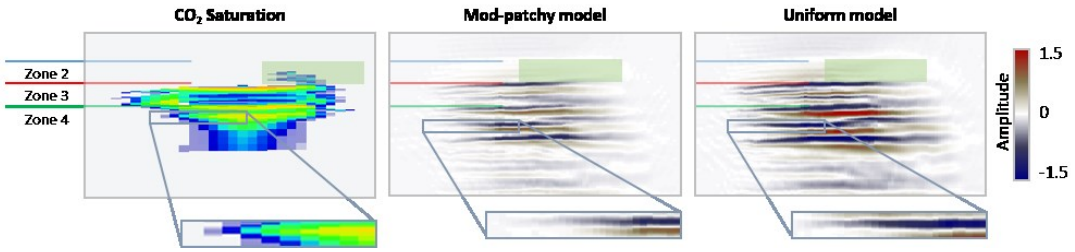

Figure 6.14. Detailed look at the simulated CO_2 plume after 20 years. The location of each reservoir zone is shown as well as the location of the free-phase migrating CO_2 front, highlighted in the olive green box. The enlarged box highlights the change in amplitude corresponding to the accumulation of CO_2 in Zone 4.

A focus on the free-phase migrating front of CO_2 in Zone 2, highlighted by the olive green box in Figure. 6.14, shows very little change in amplitude in the synthetic seismic sections for both the modified-patchy and uniform models. This shows that a migrating front of CO_2 appears to be difficult to detect. However, it should be noted that the estimated saturations in the CO_2 plume, and of the migrating front in particular, play a key role when assessing detectability, namely through the relative permeability and capillary pressure functions entered into the reservoir simulator. Therefore this is a site-specific issue, where different curves may calculate a greater range of CO_2 saturation, to which the change in velocity is particularly sensitive.

6.6.2 Implications for the detection of a migrating front

The ability to detect CO_2 migration in a reservoir is critical to the successful demonstration of containment. The detection of movement in the reservoir, in

particular if outside the primary storage reservoir or storage complex, could provide operators with an early warning system, should a loss of containment occur.

Interestingly, results from the modelling undertaken in this study, when focused on the detection of a migrating front of CO_2, show that neither the modified-patchy nor the uniform models results in an interpretable change in amplitude. This demonstrates that the detection of a free-phase migrating front of CO_2 is predominantly dependent on its spatial geometry. Once the size of the front crosses a particular detectability threshold, the pore-fluid saturation distribution models - patchy or uniform – will play an important role.

To test the importance of spatial geometry on the detection of a migrating front of CO_2, I applied the same workflow to a further stage in the simulation, after 30 years, and compared the modelled results with the results after 20 years. When focused on the migrating front alone (Figure. 6.15) the models show that the front has increased in size - from 271m to 584m (Figure. 6.15a-b) - as well as in saturation - from an average of 10% to 20% CO_2 (Figure. 6.15c-d). This results in a maximum calculated change in velocity from -135 to -297 m/s assuming a modified-patchy distribution and -466 to -527 m/s assuming a uniform distribution (Figure. 6.15e-h).

A comparison of the generated synthetic seismic sections shows a clear interpretable amplitude change in Zone 2 for a uniform distribution after 30 simulated years (Figure. 6.16f). The modified-patchy results also show a change in amplitude at this time, although this is less obvious (Figure. 6.16e). This provides confidence in the ability of seismic techniques to detect a migrating front only when a particular threshold in the lateral size of the plume has been reached. I should emphasize the point that these synthetics represent noise-free time-lapse responses. It is always possible of course that the presence of noise could result in the migrating front becoming undetectable.

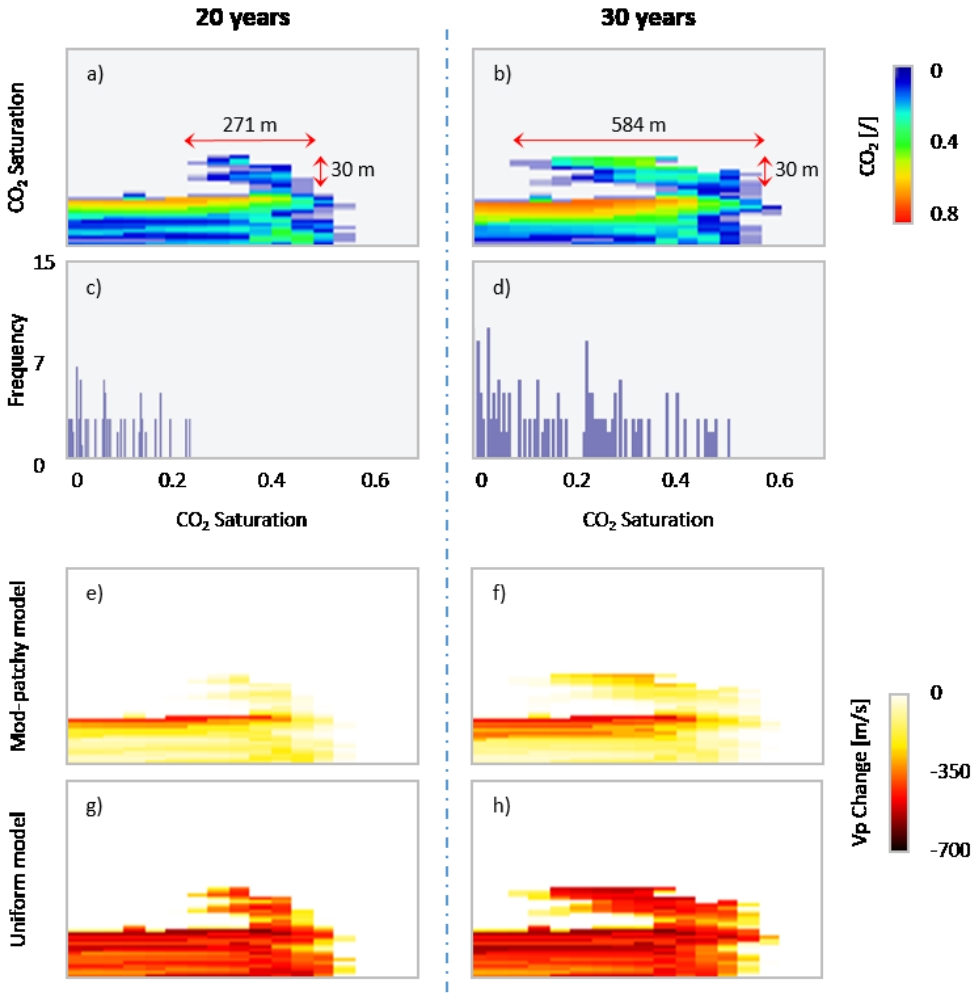

Figure 6.15. Comparison of the simulated results after 20 and 30 simulated years. (a-d) highlight the change in lateral distribution and CO_2 saturation of the migrating front while (e-h) highlight the change in velocity assuming both a modified-patchy and uniform saturation distribution. Vertical exaggeration of 3.

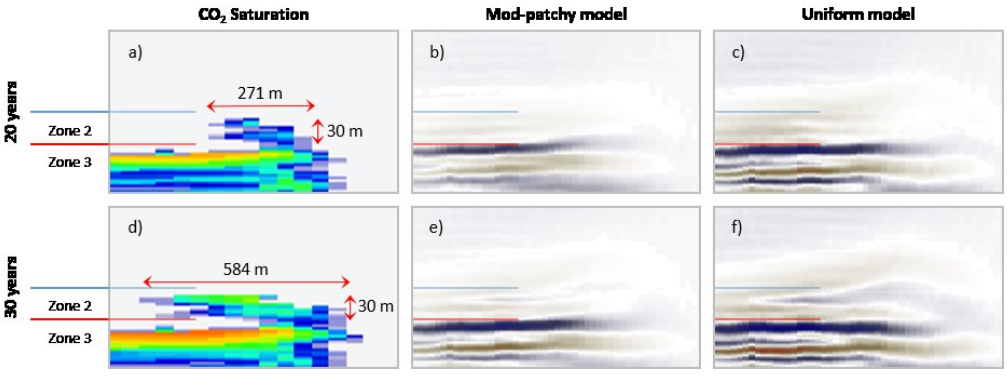

Figure. 6.16 Comparison of the seismic time-lapse modelling of the migrating front after 20 (a-c) and 30 (d-f) simulated years assuming both a modified-patchy (b and e) and uniform distribution (c and f). Vertical exaggeration of 3.

6.7 Conclusions

The key contribution of this study is to account for, and understand, the saturation scales and the phase distributions which could be encountered in a heterogeneous reservoir, therefore affecting the velocity changes resulting from the injected CO_2. Through the application of a three-stage model-driven workflow, I have modelled two end-member fluid distribution models, uniform and modified-patchy, to generate the widest range of velocity distributions for each chosen time-step. This has been done to account for the transition from patchy to uniform saturation distribution with increasing CO_2 to assess the potential of seismic monitoring techniques to image the plume growth, evolution, and migration of injected CO_2 in the subsurface.

The presence of reservoir heterogeneity added another layer of complexity to both the CO_2 flow and rock physics modelling as it resulted in a range of CO_2 saturations and distribution of velocities. Traditionally, simulated CO_2 flow modelling using a homogeneous model would result in saturations which are either structurally trapped (immobile) or mobile. This would result in CO_2 concentrations which are 'uniform' in accumulation, with maximum saturation values of $1-S_{wir}$. Rock physics modelling applied to such a scenario would result in velocities which are very similar for modified-patchy and uniform cases, as the two curves converge at high saturations. As demonstrated in Chapter 5, velocities calculated assuming either a modified-patchy or uniform distribution would not matter as they would return similar values. The addition of reservoir heterogeneity corrected for this as it resulted in a range of saturations in the reservoir due to the tortuous migration from the intra-reservoir baffles, allowing for a more accurate way to assess, understand and compare the saturation scales and the phase distributions which could be expected.

Through the application of a heterogeneous model, the generated synthetic seismic sections show clear differences between the modified-patchy and uniform saturation models. In both cases the CO_2 growth in each zone can be detected, where the top-most reflector corresponds to the top-most accumulation in the simulation. Furthermore, each accumulation of CO_2 below the intra-formational baffles in each

zone can be interpreted regardless of the assumed fluid saturation model. This provides confidence in the ability of seismic methods to detect plume growth and evolution in a saline reservoir.

A comparison of the modified-patchy and uniform synthetic seismic sections shows a clear difference in amplitude and time-shift. Although the uniform model shows high changes in amplitude and large velocity push-down effects below the plume, it proves difficult to distinguish the different CO_2 accumulations in each zone. The modified-patchy model results in a more subtle change in amplitude. As the subtle change in amplitude is directly related to the concentration of CO_2 in each accumulation, it suggests that this difference has important implications for CO_2 detectability and for quantifying the volume of CO_2 injected into the reservoir.

A free-phase migrating front of CO_2 was shown to be more difficult to detect as the ability to image this is dependent not only on the fluid saturation distribution, but also on the spatial geometry of the front. It required an increase in lateral size for the front to become detectable. This provides confidence in the ability of seismic techniques to detect a migrating front only when a particular threshold in plume-geometry has been reached. This however was imaged through noise-free synthetic time-lapse responses. It is possible that the presence of noise could result in the migrating front becoming undetectable.

Summary

I have assessed the ability of seismic methods to image CO_2 plume growth, evolution, and migration in a heterogeneous saline reservoir in the UK sector of the North Sea. Through the application of the monitorability workflow, I generated seismic sections which showed clear differences between the two saturation end-member models. A comparison of the velocity models highlights the importance that patchy saturation has for both CO_2 detectability and quantification. The generated synthetics also provide confidence in the ability to detect CO_2 plume growth and evolution in the reservoir. However, the detection of a migrating front of CO_2 was difficult to detect and was shown to be related to its spatial geometry.

7. Seismic monitoring of depleted gas fields

I assess the ability of seismic methods to detect CO_2 injected into depleted hydrocarbon fields. The Bunter Sandstone model is modified to depict a depleted gas reservoir. Two injection scenarios are modelled: 1) CO_2 injection into a depleted gas cap, and 2) CO_2 injection into a depleted gas field. The same four fluid-flow simulation results presented in Chapter 6 are used, however, an extra 20% residual gas saturation is added. The monitorability workflow (Chapter 4) is applied to generate synthetic seismic time-lapse responses assuming a uniform saturation model and a patchy saturation model. The results which highlight the effect of patchy saturation on the seismic detectability of depleted hydrocarbon fields.

7.1 Introduction

The main challenge faced when monitoring CO_2 injected in depleted hydrocarbon fields is that up to four fluids may be present in the reservoir. This is compared with two fluids co-existing when CO_2 is injected in saline reservoirs. This has important implications for CO_2 seismic monitoring, as the acoustic properties of the reservoir are affected by the saturation of the fluid type as well as the fine-scale spatial distribution of the phases (White, 1975, Mavko and Mukerji, 1998).

It is generally assumed that CO_2 injected in depleted hydrocarbon reservoirs will be difficult to image. This is due to an amount of residually trapped oil or gas lowering the overall compressibility of the reservoir. This is based on the assumption that all fluid phases in the reservoir – oil, gas and CO_2 – are uniformly saturated. However, as explained in Chapter 4, the injection of CO_2 in a reservoir can result in a non-uniform, partially saturated, phase distribution: patchy saturation.

The presence of patchy saturation can greatly affect the elastic properties of the reservoir. This is modelled in Figure 7.1. The calculated change in velocity (V_p), as a function of CO_2 saturation, is calculated for a theoretical sandstone reservoir. Two scenarios are modelled: 1) increasing CO_2 saturation in a saline reservoir, with a baseline gas saturation of 0%, and 2) increasing CO_2 saturation in a depleted gas reservoir, with a baseline residual gas saturation of 20% (orange shade). The change in velocity is calculated assuming uniform saturation (green curve) and patchy saturation (red curve). CO_2 injected in a virgin saline reservoir results in a decrease in V_p of 425 m/s; a change of 13.5%. However, the presence of 20% residually trapped gas would lower the initial velocity in the reservoir to 3050 m/s. Increasing CO_2 saturation to 80% would result in a decrease in V_p of 55 m/s assuming a uniform saturation distribution. This represents a change of only 2% compared with the baseline level with no CO_2 but 20% residual gas. However, assuming a patchy saturation would result in a decrease in V_p of 325 m/s. This represents a change of 10.5% compared with the baseline level.

The larger change in velocity due to patchy saturation demonstrates the potential of seismic techniques to detect CO_2 injected in depleted hydrocarbon reservoirs. Furthermore, the ability to seismically image and detect CO_2 injected in depleted hydrocarbon fields could demonstrate the presence of patchy saturation. As explained in Chapter 4, patchy saturation has been demonstrated only at MHz frequencies in laboratory experiments (Lebedev et al., 2009) and at 100 kHz in logging data (Azuma et al., 2013).

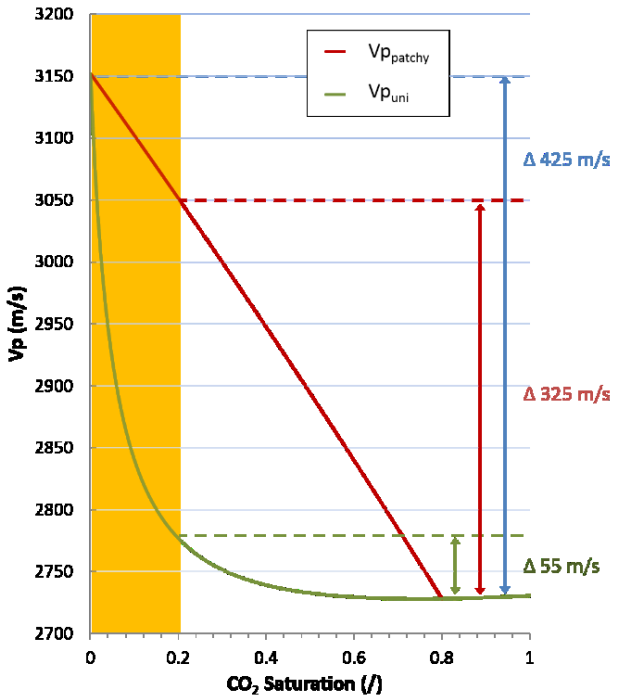

Figure 7.1. P-wave velocity as a function of CO_2 saturation calculated assuming a uniform saturation model (Vp_{uni}) and a patchy saturation model (Vp_{patchy}). Two scenarios are shown: 1) increasing CO_2 saturation in a saline reservoir, with a baseline gas saturation of 0%, and 2) a depleted gas reservoir; with a baseline residual gas saturation of 20% (orange shade). The arrows depict the change in velocity for each scenario: 1) blue arrow, saline reservoir, 2) red arrow, depleted gas field assuming patchy saturation, and 3) green arrow, depleted gas field assuming a uniform saturation.

Two CCS projects have deployed surface seismic methods to monitor CO_2 injected in depleted hydrocarbon fields: the CO_2CRC Otway Project (Jenkins et al., 2012) and the IEA Weyburn CO_2 Monitoring and Storage Project (White et al., 2004).

The CO_2CRC Otway Project performed a small scale study, injecting 66000 tonnes of CO_2 in a depleted gas field (Jenkins et al., 2012). The aim of the monitoring plan was

to detect CO_2 injected in the reservoir. The injection well was perforated at a residual gas zone, estimated at 20% (Urosevic et al., 2010). Modelling undertaken before seismic acquisition predicted a very subtle change in elastic properties with increasing CO_2 saturation due to the presence of the residual gas in the reservoir. This prediction was made assuming: 1) a homogeneous reservoir, and 2) a uniform saturation distribution of all fluids (Urosevic et al., 2010). Two 3D seismic surveys were acquired. First, a baseline survey in 2008 and second, a monitor survey in 2009 after 35000 tonnes of CO_2 was injected in the Waarre C sand. Figure 7.2 shows the in-line and crossline sections for the baseline and monitor surveys. Clearly evident is the anomalous effect attributed to the injected CO_2.

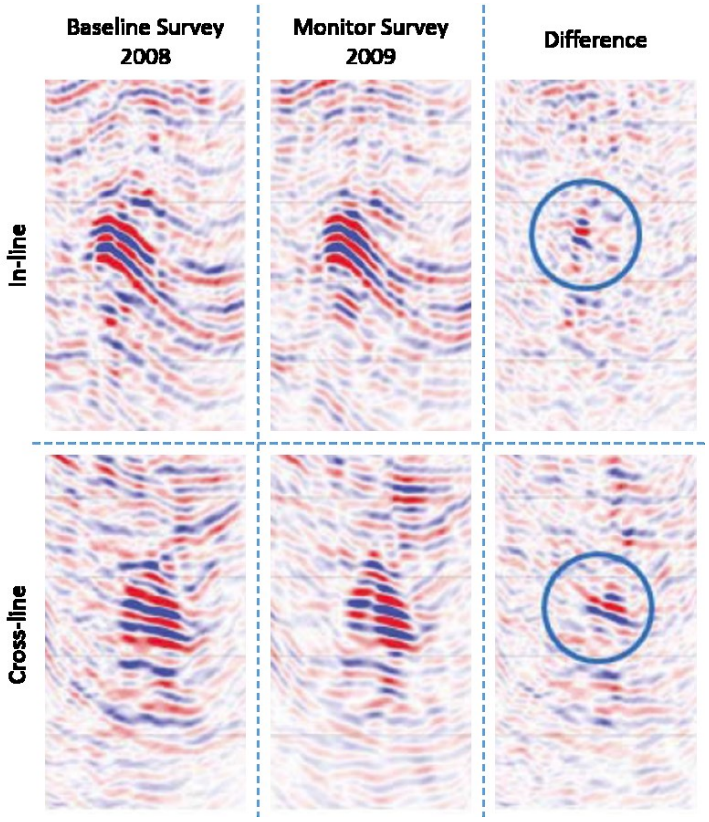

Figure 7.2. Cross-equalised baseline and monitor cubes at the Otway site. The top image is the in-line, the bottom is the cross-line. The difference between the baseline and monitor is calculated. The anomalous effect at the Waarre C sand is circled. Image is modified from Urosevic et al., (2010).

The observed amplitude changes were greater than predicted in the synthetic seismic sections (Urosevic et al., 2010). This could be explained due to the presence of patchy saturation in the reservoir; a uniform saturation distribution was assumed when

generating the synthetic seismic sections. Urosevic et al., (2010) do state that greater heterogeneity and/or patchy saturation could increase the magnitude of the time-lapse seismic response. Although the effect of patchy saturation was not addressed further, the authors concluded by stating that 3D time-lapse seismic can monitor CO_2 injected in depleted gas fields.

The IEA Weyburn CO_2 Monitoring and Storage Project is an active CCS site. Initiated in 2000, the project investigates the technical and economic feasibility of CO_2 storage in a depleted oil reservoir. The project aims to monitor and verify the progress of the injected CO_2. Approximately 3.5 million tonnes of CO_2 is injected each year (White, 2009). Interestingly, feasibility studies modelling CO_2 injected in the depleted oil reservoir focus only on one scenario: CO_2 displacing brine (two-phases) (White, 2009, Wandler et al., 2012). The displacement of oil by CO_2 is not modelled.

Following the baseline survey in 1999, and the start of injection in 2000, four full-scale monitor surveys were acquired in 2001, 2002, 2004 and 2007. White (2009) and White (2013a) present time-lapse amplitude difference maps for the entire reservoir, demonstrating the ability to outline the CO_2 plumes seismically. Figure 7.3 shows the time-lapse amplitude difference maps for the Midale Marley horizon in the reservoir. The CO_2 is imaged clearly as negative amplitude differences in each monitor survey.

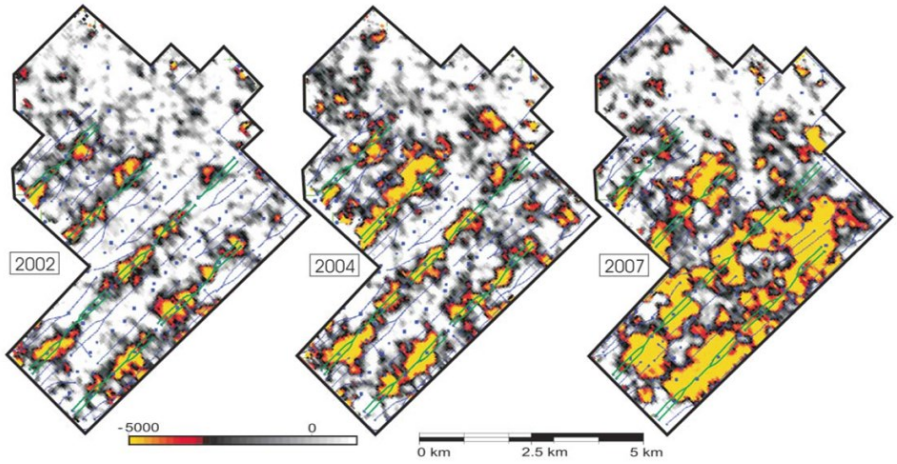

Figure 7.3. Time-lapse amplitude difference maps for the Midale Marley horizon. The CO_2 is clearly imaged as negative amplitude differences in each monitor survey. The blue lines represent oil production wells. The green lines represent CO_2 injection wells. Modified from White (2009).

Njiekak et al., (2013) performed a rock-physics study to understand the effects of changing CO_2 phase on seismic waves at the Weyburn site. When simulating the effect of the CO_2 plume, the authors assumed uniform saturation in the reservoir. The authors acknowledge the presence of patchy saturation in the reservoir; however, they state that patchy saturation in the reservoir cannot be quantitatively determined and so was not modelled. The authors suggest the need for an end-member study in order to constrain more complex and more probable cases of patchy saturation.

The Otway and Weyburn projects demonstrate the potential of seismic methods to image CO_2 injected in a depleted gas field, and an oil field, respectively. The results from the Otway and Weyburn sites potentially demonstrate patchy saturation in the field. The injected CO_2 was imaged at each site with the presence of residual oil or gas saturation. Should the CO_2 be uniformly saturated, the resulting amplitude change would have been very small, and most likely undetectable, when compared with the baseline model. When history matching the CO_2 plume with observed seismic data, the simulated amplitude changes were less than those observed in the field. I suggest this is because the synthetic seismic sections were modelled assuming only uniform saturation. Patchy saturation could account for the underestimation. This is highlighted in Urosevic et al., (2010) and Njiekak et al., (2013), as both authors suggest the possibility of patchy saturation playing an important role in the seismic detectability of depleted hydrocarbon fields.

In this chapter, I present a benchmark study modelling the potential of seismic methods to detect CO_2 injected in a depleted gas field due to the presence of patchy saturation. As a reservoir model of a depleted hydrocarbon field was not available, the Bunter Sandstone model is modified to include 20% residual gas saturation; the same residual saturation in the Otway project (Urosevic et al., 2010). Two CO_2 injection scenarios are modelled: 1) CO_2 injection in a depleted gas cap; and 2) CO_2 injection in a depleted gas field. The synthetic seismic sections assuming patchy and uniform saturation are generated and compared by applying the monitorability workflow (Chapter 4).

7.2 Geological models

The geological model chosen for this study is the Bunter Sandstone model, as it provides a direct comparison to the synthetic seismic responses presented in Chapter 6. No reservoir model of a depleted hydrocarbon field was available.

As the Bunter Sandstone model is a saline reservoir in the North Sea, the fluid properties of the reservoir are modified to depict a depleted gas field. This is done by adding 20% residual gas saturation to the baseline model. Two CO_2 injection scenarios are simulated: 1) CO_2 injection below, then migration into a depleted gas cap, and 2) CO_2 injection directly into a depleted gas field (Figure 7.4).

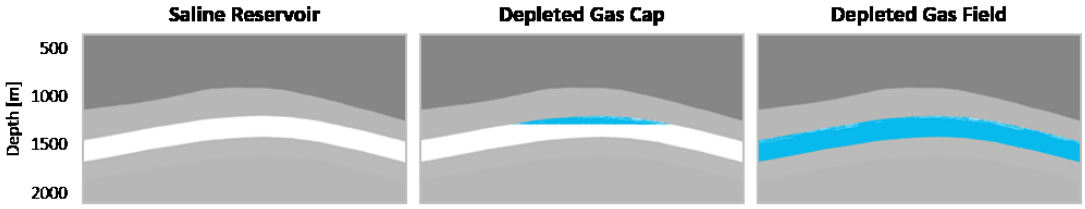

Figure 7.4. 2D sections of the three CO_2 injection scenarios: 1) saline reservoir, 2) depleted gas cap and 3) depleted gas field. The blue colour represents 20% residual CO_2 saturation. Vertical exaggeration of 2.

7.3 Fluid flow models

The same four fluid-flow simulation results as presented in Chapter 6 are used; CO_2 plume after 5 years, 11 years, 20 years and 30 years. This is done to allow for an accurate comparison between the saline reservoir model scenarios and the depleted gas reservoir scenarios. To incorporate residual saturation in the simulation results, 20% residual gas was added to the pore-saturation in the gas cap and depleted gas field. A consequence of this is that the maximum CO_2 saturation in the model is now 100%, therefore assuming no irreducible water saturation. This is compared with a maximum CO_2 saturation of 80% in the saline reservoir study, due to an irreducible water saturation of 20%.

Figure 7.5 shows 2D sections of the 3D simulation results of the three injection scenarios. The light blue colour is the 20% residually trapped CO_2. The only difference between the saline reservoir and depleted gas field simulation results is the extra 20% saturation added to the CO_2 plume. The depleted gas cap scenario shows the CO_2 plume accumulating below the gas cap after 5 years. After 11 years, the CO_2 plume crosses the residual gas-water contact and continues migrating vertically to the top seal. Of interest is whether seismic methods can detect the CO_2 plume crossing the residual gas-water contact. This could be a monitoring milestone.

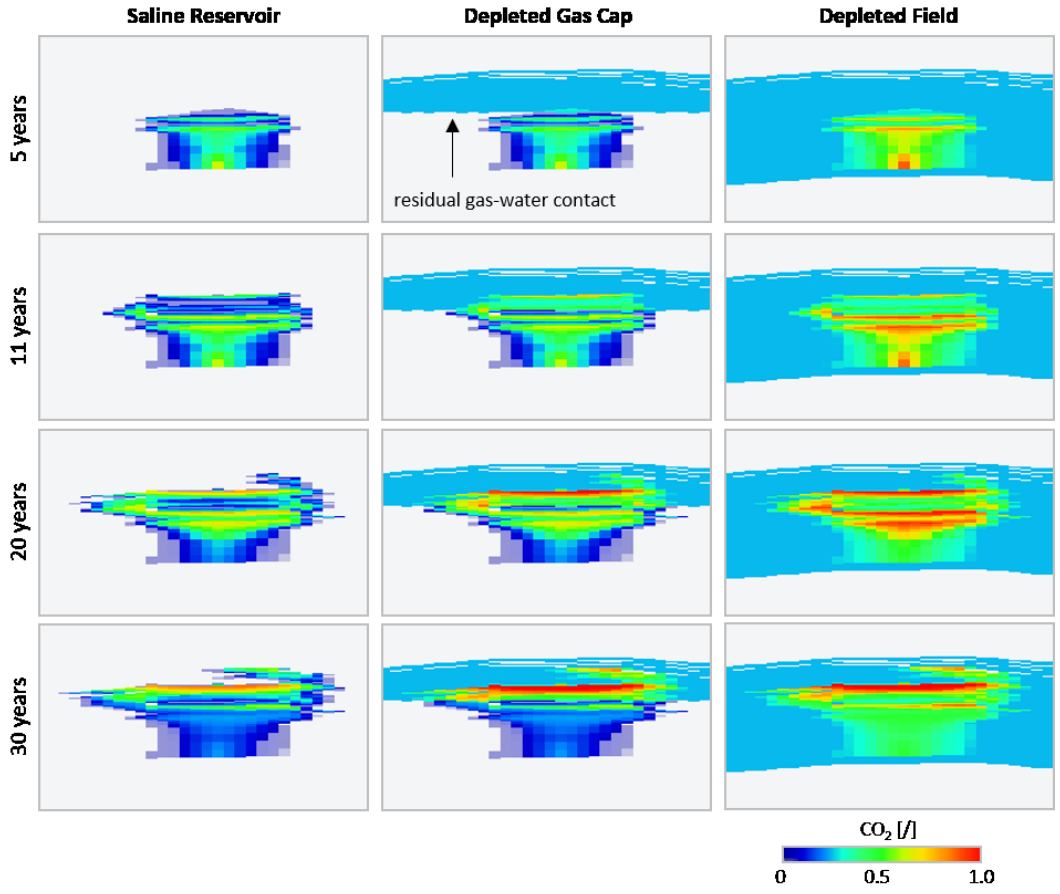

Figure 7.5. 2D snapshots of the modified 3D fluid-flow simulation results of the three injection scenarios: saline reservoir, depleted gas cap and depleted gas field. The 20% residual gas saturation is shown in light blue. Vertical exaggeration of 3.

7.4 Rock physics models

For each scenario, the change in velocity is calculated assuming patchy and uniform saturation distributions. For the uniform saturation model, all the fluids in the reservoir – water, CO_2 and residual gas – are assumed to be uniformly saturated. The presence of residually trapped gas complicates the rock physics modelling for the patchy saturation end-member. Three assumptions are made when calculating the change in velocity due to patchy saturation:

1) The residually trapped gas is uniformly saturated in the reservoir. Therefore, the reservoir is in pore-pressure equilibrium pre CO_2-injection. Hence, the change in velocity for all regions with residual saturation is calculated using the uniform saturation rock-physics model.
2) The injection of CO_2 will disrupt the reservoir equilibrium, resulting in patchy saturation. Therefore, the change in velocity associated with the CO_2 plume is calculated using only the patchy saturation rock-physics model.
3) The petrophysical properties of the residual gas is assumed to be identical to the injected CO_2.

Figure 7.6 shows 2D baseline velocity sections of the 3D CO_2 injection scenarios. Clearly evident is the decrease in velocity due to the presence of residually trapped gas. The ranges in calculated velocities for each scenario are summarised in Table 7.1. The residual gas decreases the baseline velocity in the reservoir by an average of 478 m/s for the depleted gas cap scenario, and 379 m/s for the depleted gas field scenario.

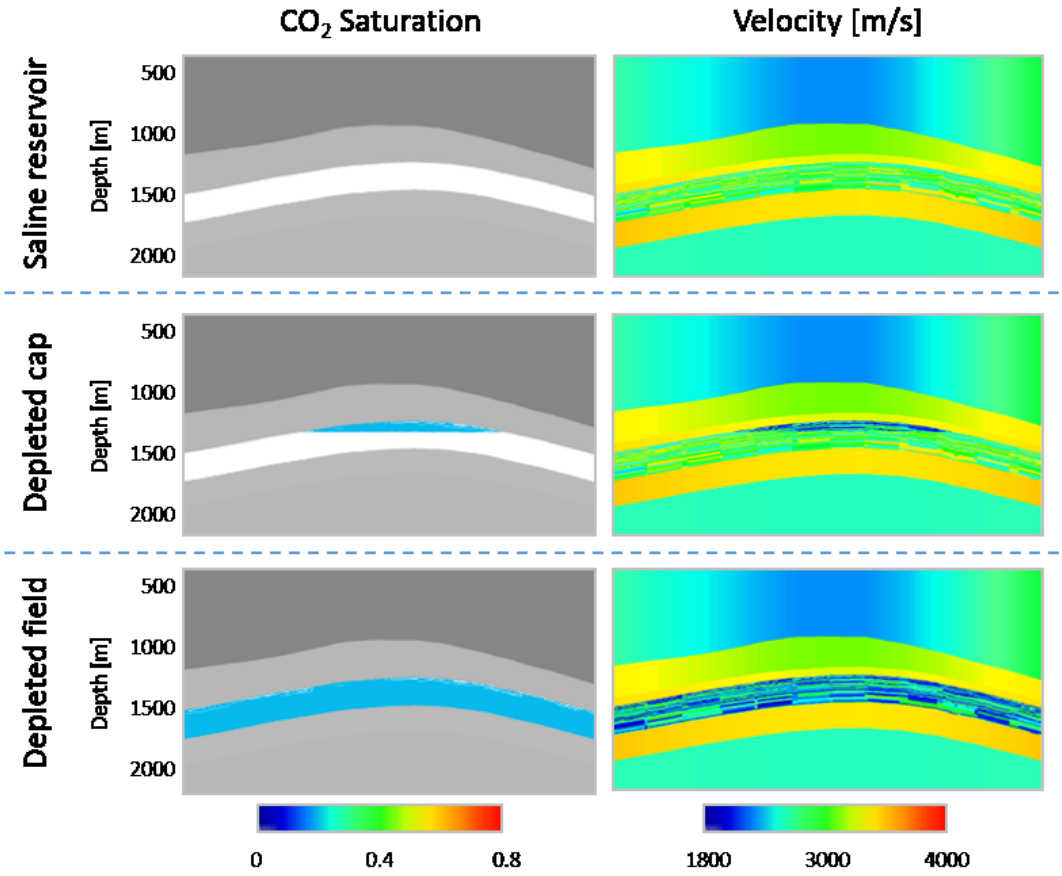

Figure 7.6. 2D sections of the 3D models showing the calculated baseline velocity models of the three scenarios. Vertical exaggeration of 2.

Table 7.1. Calculated reservoir velocities for the Bunter Sandstone reservoir for the three injection scenarios. Velocities for the depleted cap scenario are calculated above the residual gas-water contact and below the residual gas-water contact.

Velocity	Saline reservoir	Depleted cap		Depleted field
m/s		Above	Below	
Min	2314	1778	2318	1586
Max	3512	3085	3513	3550
Range	1198	1307	1195	1964
Mean	2820	2342	2823	2441

Figures 7.7 to 7.10 show 2D snapshots of the 3D rock-physics models of the four simulated times. The modelled CO_2 saturation and the change in velocity are shown for each simulated time assuming both patchy and uniform saturation. The results are interpreted for each scenario separately.

Saline reservoir:

- **Patchy model**: a gradual change in velocity is modelled due to the linear relationship between velocity and increasing CO_2 saturation.
- **Uniform model**: a large change in velocity is observed at the outset. Features in the plume are difficult to distinguish.
- The saline reservoir rock-physics models are the same as those presented in Chapter 7.

Depleted gas cap:

- **Patchy model**: A decrease in velocity of 300 m/s is modelled when the CO_2 is below the residual gas-water contact. As the CO_2 crosses the residual gas-water contact, an increase in velocity of 350 m/s is modelled.
- **Uniform model**: A large decrease in velocity of 560m/s is modelled from the outset when the CO_2 is below the residual gas-water contact. A decrease in velocity of only 110 m/s is observed once the CO_2 crosses the residual gas-water contact.

Depleted gas field:

- **Patchy model**: An increase in velocity is modelled from the outset, reaching a maximum of 350 m/s. The largest increase in velocity is associated with lowest saturation of CO_2. Large CO_2 accumulations, associated with structurally trapped CO_2, result in an increase in velocity of 100 m/s only.
- **Uniform model**: From the outset, a maximum decrease in velocity of 110 m/s is modelled. This change in velocity is constant for each simulated time.

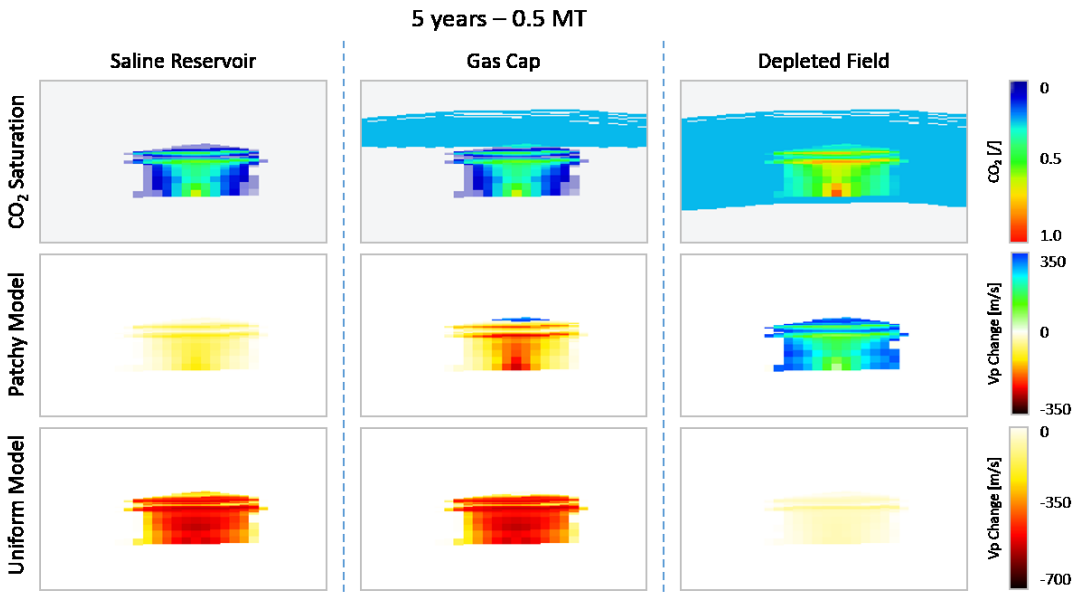

Figure 7.7. 2D snapshots of the 3D rock-physics modelling results for the CO_2 plume after 5 years. The change in velocity calculated assuming both a uniform saturation and patchy saturation are shown for each injection scenario. A total amount of 0.5 Mt of CO_2 has been injected at this stage. The light blue colour in the reservoir represents 20% residual gas saturation. Vertical exaggeration of 3.

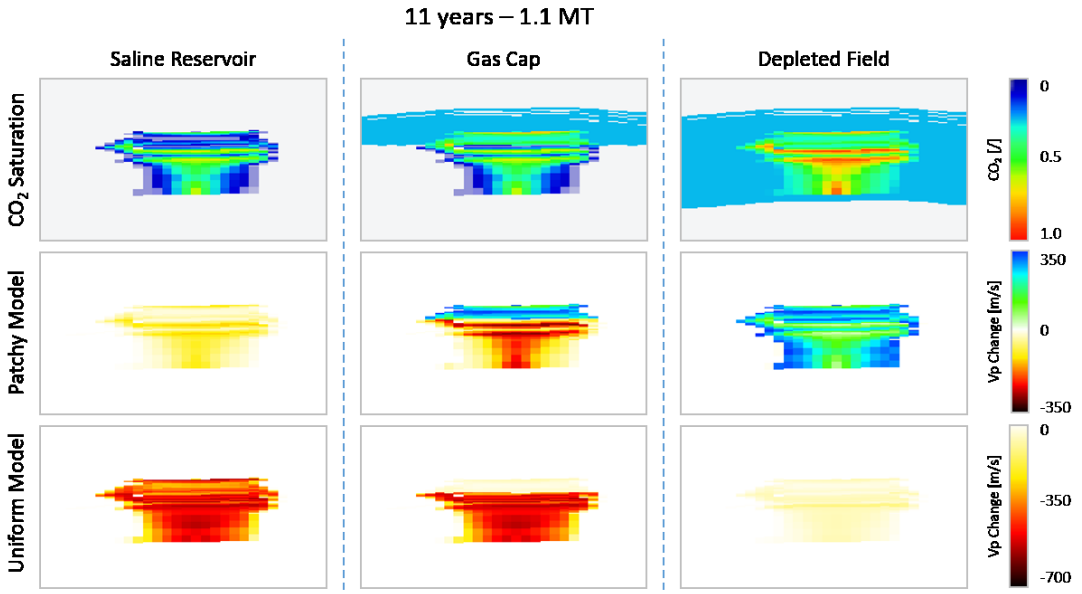

Figure 7.8. 2D snapshots of the 3D rock-physics modelling results for the CO_2 plume after 11 years. The change in velocity calculated assuming both a uniform saturation and patchy saturation are shown for each injection scenario. A total amount of 1.1 Mt of CO_2 has been injected at this stage. The light blue colour in the reservoir represents 20% residual gas saturation. Vertical exaggeration of 3.

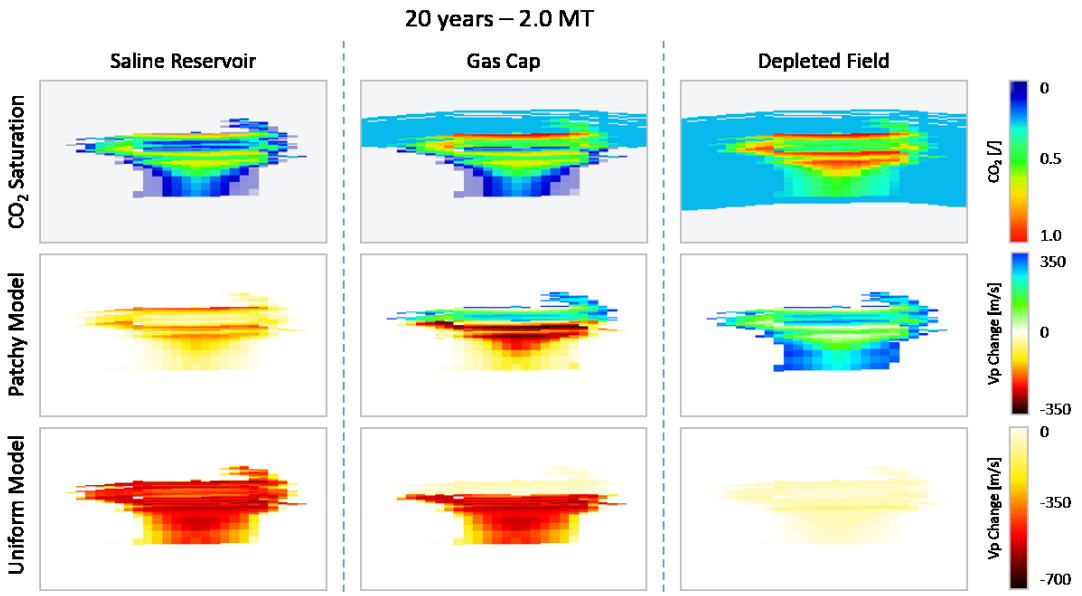

Figure 7.9. 2D snapshots of the 3D rock-physics modelling results for the CO_2 plume after 20 years. The change in velocity calculated assuming both a uniform saturation and patchy saturation are shown for each injection scenario. A total amount of 2 Mt of CO_2 has been injected at this stage. The light blue colour in the reservoir represents 20% residual gas saturation. Vertical exaggeration of 3.

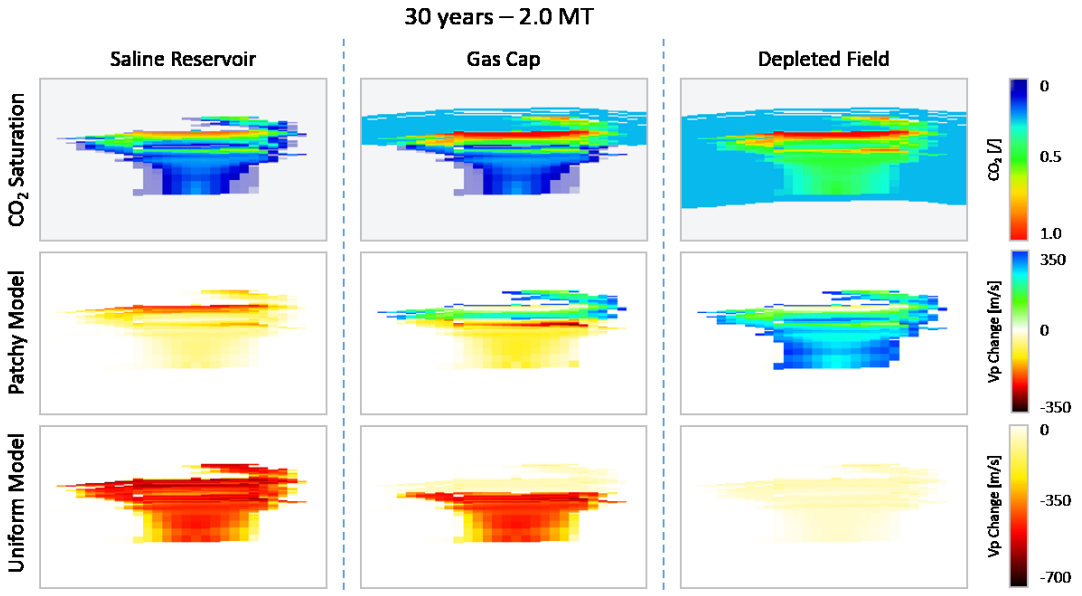

Figure 7.10. 2D snapshots of the 3D rock-physics modelling results for the CO_2 plume after 30 years. The change in velocity calculated assuming both a uniform saturation and patchy saturation are shown for each injection scenario. A total amount of 2 Mt of CO_2 has been injected at this stage. The light blue colour in the reservoir represents 20% residual gas saturation. Vertical exaggeration of 3.

7.5 Seismic forward models

Using Nucleus+ (Taylor and Julliard, 2013), I simulate the acquisition of a single line towed streamer seismic survey based on the same acquisition parameters as presented in Chapter 6 (Table 7.2). The source signature is a zero-phase Butterworth wavelet of 2.0 msec sample interval, with low cut and high cut frequencies of 8Hz and 90Hz and slopes of 18 and 72 dB/octave, respectively. Synthetic shot records are generated along a 6km east-west section. The modelling is performed for each injection scenario, simulated time, and for both uniform and patchy saturation models.

To allow for a direct comparison with the synthetic seismic sections generated in Chapter 6, I apply the same processing steps. First, a mute is applied to remove the refracted arrivals. Second, velocities chosen following velocity analysis are used to apply normal moveout (NMO) corrections. The traces are then stacked making a seismic section. The seismic section is then depth-migrated using the baseline velocity model using the phase-shift plus interpretation (PSPI) method (Ferguson and Margrave, 2005). Last, a time-lapse image is generated by subtracting the baseline survey from the monitor survey to highlight the effect of the CO_2

Table 7.2. Synthetic seismic modelling acquisition parameters

Acquisition parameters	
Receiver spacing	25 m
Receiver depth	7.5 m
Source spacing	25 m
Source depth	5 m
Cable length	5500 m
Number of receivers	236
Number of shots	220
Recording length	2 sec

7.5.1 Time-lapse seismic response

The depth-migrated seismic section, juxtaposed with the baseline velocity model, for each of the three injection scenarios, is shown in Figure 7.11. Clearly evident are the strong amplitude reflections at interfaces where the seismic velocity changes abruptly. A comparison of the saline reservoir and depleted field scenario shows stronger amplitude reflectors due to the velocity difference in the reservoir. Large amplitude reflections, corresponding to the depleted gas cap, can be interpreted.

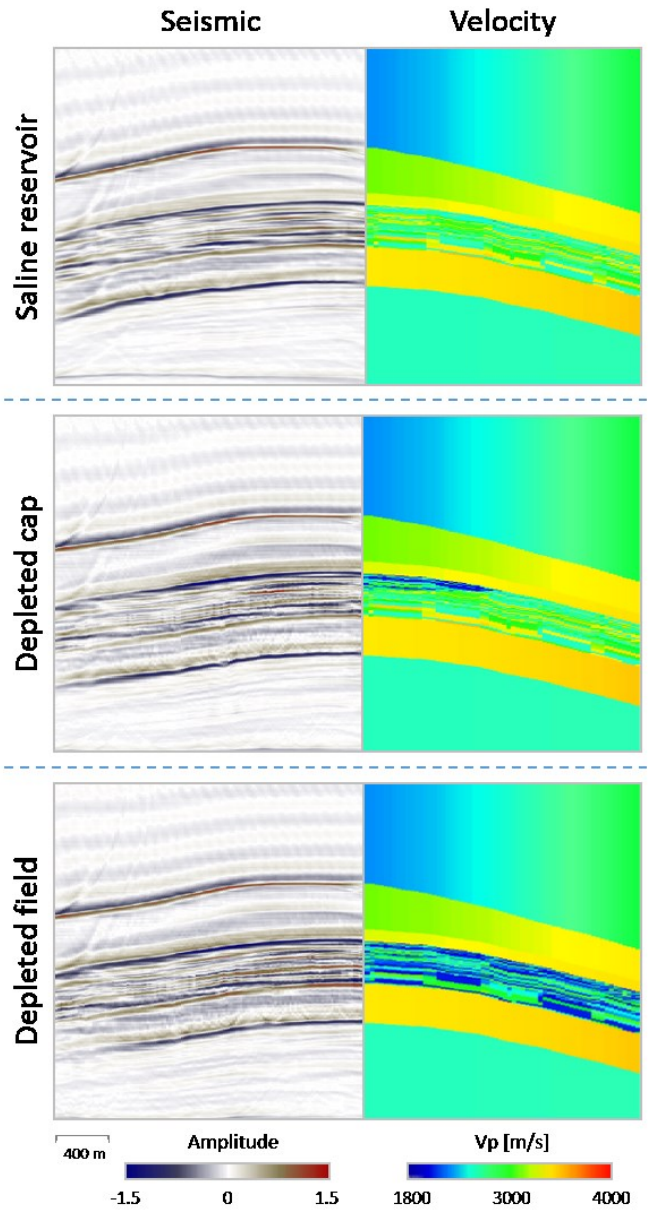

Figure 7.11. Depth-migrated seismic sections (left) juxtaposed with the associated baseline velocity models (right) of the three injection scenarios. Vertical exaggeration of 2.

Figures 7.12 to 7.15 show the time-lapse synthetic seismic sections of the four simulated times. The simulated CO_2 saturation, change in velocity, and synthetic seismic sections, are shown for each simulated time, assuming both patchy and uniform saturation. The synthetic seismic sections suggest the following:

Saline reservoir:

- **Patchy model**: Lower amplitude reflections often corresponding to highly saturated, structurally trapped CO_2.
- **Uniform model**: A clear change in amplitude is interpreted from the outset, along with a prominent velocity push-down effect.
- The saline reservoir synthetic seismic sections are the same as those presented in Chapter 7.

Depleted gas cap:

- **Patchy model:** A clear amplitude anomaly can be interpreted when the CO_2 plume is below the residual gas-water contact. A large amplitude reflector is interpreted once the CO_2 plume crosses the residual gas-water contact.
- **Uniform model:** A clear change in amplitude is interpreted from the outset. However, the amplitude anomaly shows no change with time as the top-most reflector corresponds to the accumulation directly below the residual gas-water contact.

Depleted gas field:

- **Patchy model:** A large amplitude anomaly, as well as a larger velocity push-down effect, is interpreted from the outset.
- **Uniform model:** Very subtle changes in amplitude are interpreted from the outset, with no change thereafter.

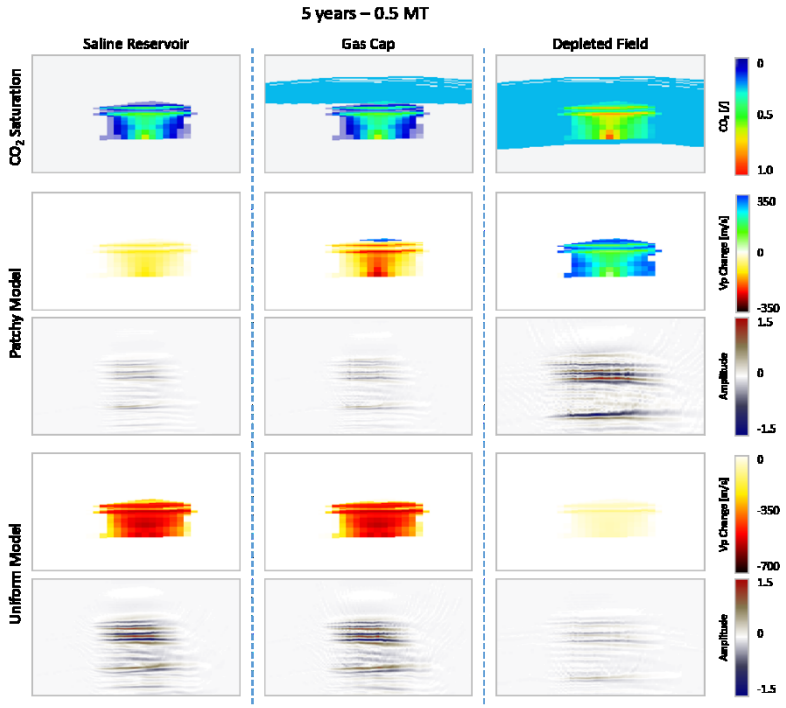

Figure 7.12. Modelling results for the CO_2 plume after 5 years showing the CO_2 saturation, change in velocity and synthetic seismic results for each injection scenario. The results are shown assuming either a patchy or uniform saturation. Vertical exaggeration of 3.

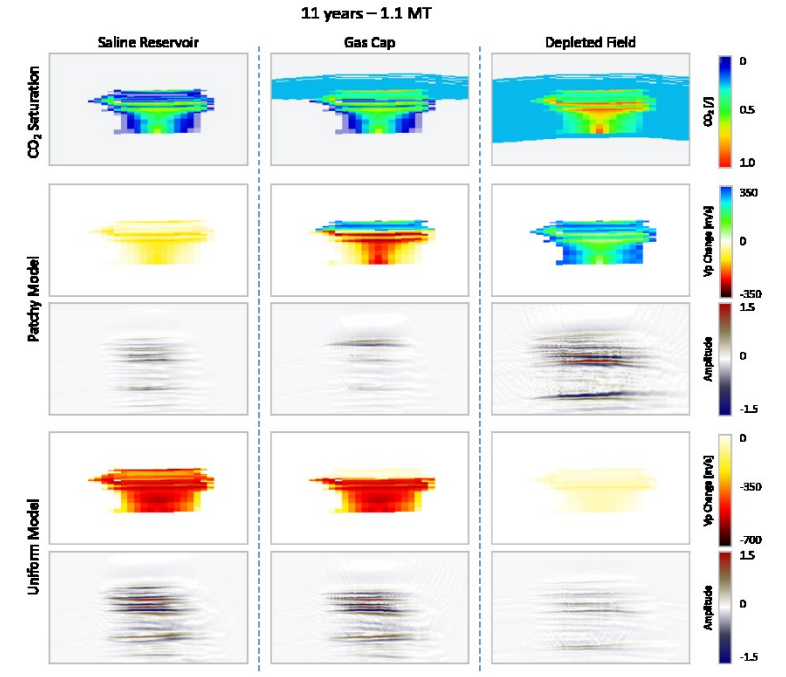

Figure 7.13. Modelling results for the CO_2 plume after 11 years showing the CO_2 saturation, change in velocity and synthetic seismic results for each injection scenario. The results are shown assuming either a patchy or uniform saturation. Vertical exaggeration of 3.

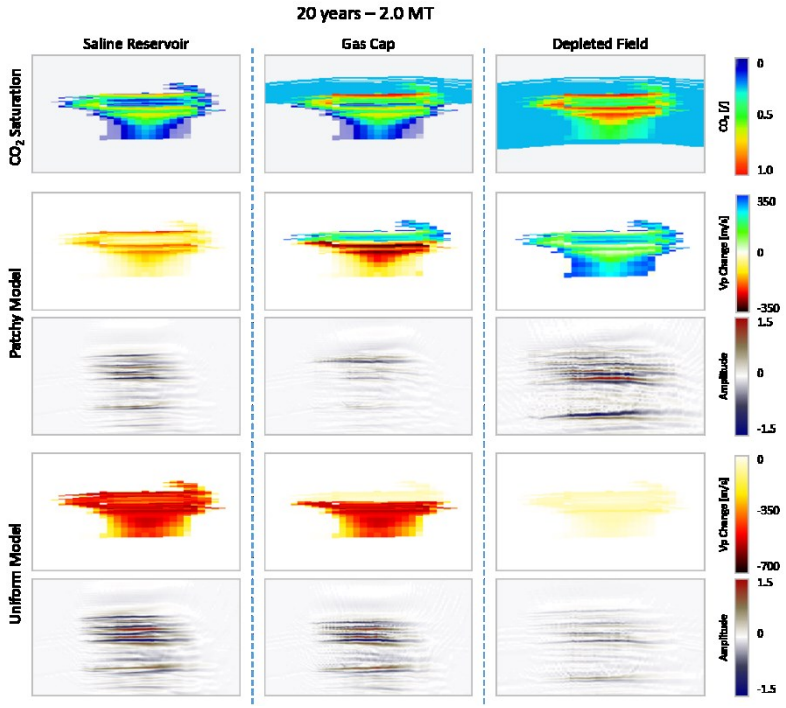

Figure 7.14. Modelling results for the CO_2 plume after 20 years showing the CO_2 saturation, change in velocity and synthetic seismic results for each injection scenario. The results are shown assuming either a patchy or uniform saturation. Vertical exaggeration of 3.

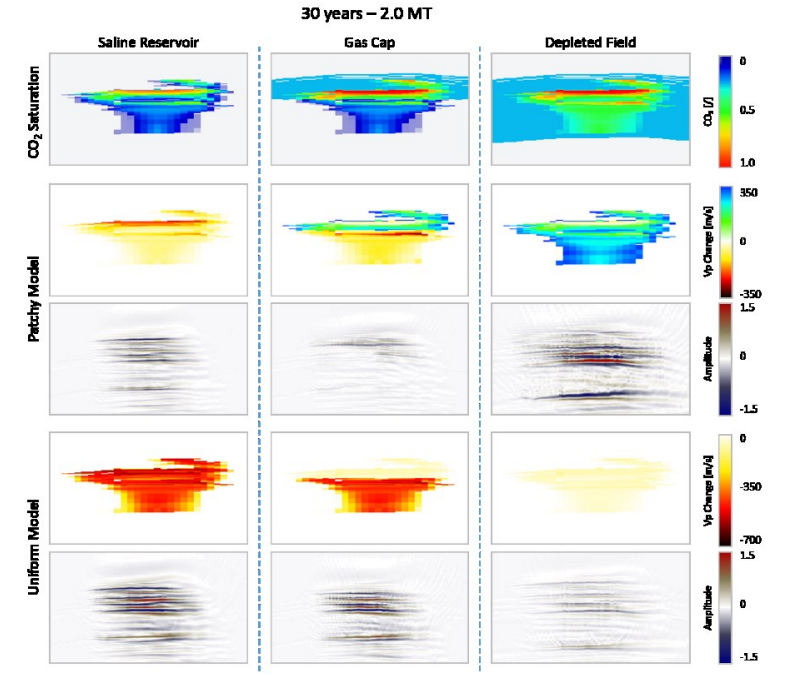

Figure 7.15. Modelling results for the CO_2 plume after 30 years showing the CO_2 saturation, change in velocity and synthetic seismic results for each injection scenario. The results are shown assuming either a patchy or uniform saturation. Vertical exaggeration of 3.

7.6 Discussion

The synthetic seismic sections generated as part of this study demonstrate the potential of seismic methods to image CO_2 injected into depleted hydrocarbon fields, such as a depleted gas field or a depleted gas cap.

The assumption of a uniform saturation distribution within the reservoir highlighted two main points:

1) The injection of CO_2 into a depleted gas field will result in very subtle changes in amplitude. This is due to the residual saturation lowering the compressibility in the reservoir.
2) If the CO_2 is injected below a gas cap, the plume will be seismically detectable until it crosses the residual gas-water contact. A very subtle change in amplitude is interpreted once the plume crosses the residual gas-water contact

These results are as expected, and in most cases, have been demonstrated in the literature, for example Urosevic et al., (2010). However, the synthetic seismic sections generated assuming a patchy saturation distribution yield interesting results.

The injection of CO_2 below a gas cap resulted in an amplitude anomaly when the plume was below the residual gas-water contact. Once the plume crossed the residual gas-water contact, a large amplitude reflector is evident, masking the effect of deeper reflectors (Figure 7.16). This is due to the large velocity contrast at the residual gas-water interface. This acts as a high velocity layer, which causes a significant portion of seismic energy to get scattered. Targets beneath high velocity layers are difficult to image seismically (Purnell, 1992, Evans et al., 1996, Leslie and Evans, 1999). Interestingly, the velocity contrast decreases with time. This is obvious when comparing the large amplitude reflector at 11 years with the large amplitude reflector at 30 years.

The concept of increasing velocity in the reservoir due CO_2 injection is interesting as it is expected that the introduction of CO_2 will lower the compressibility of the reservoir. This is typical for CO_2 injected into saline reservoirs or when assuming a

uniform saturation distribution. However, the presence of patchy saturation has shown to increase reservoir velocity when the injected CO_2 interacts with the residual gas saturation.

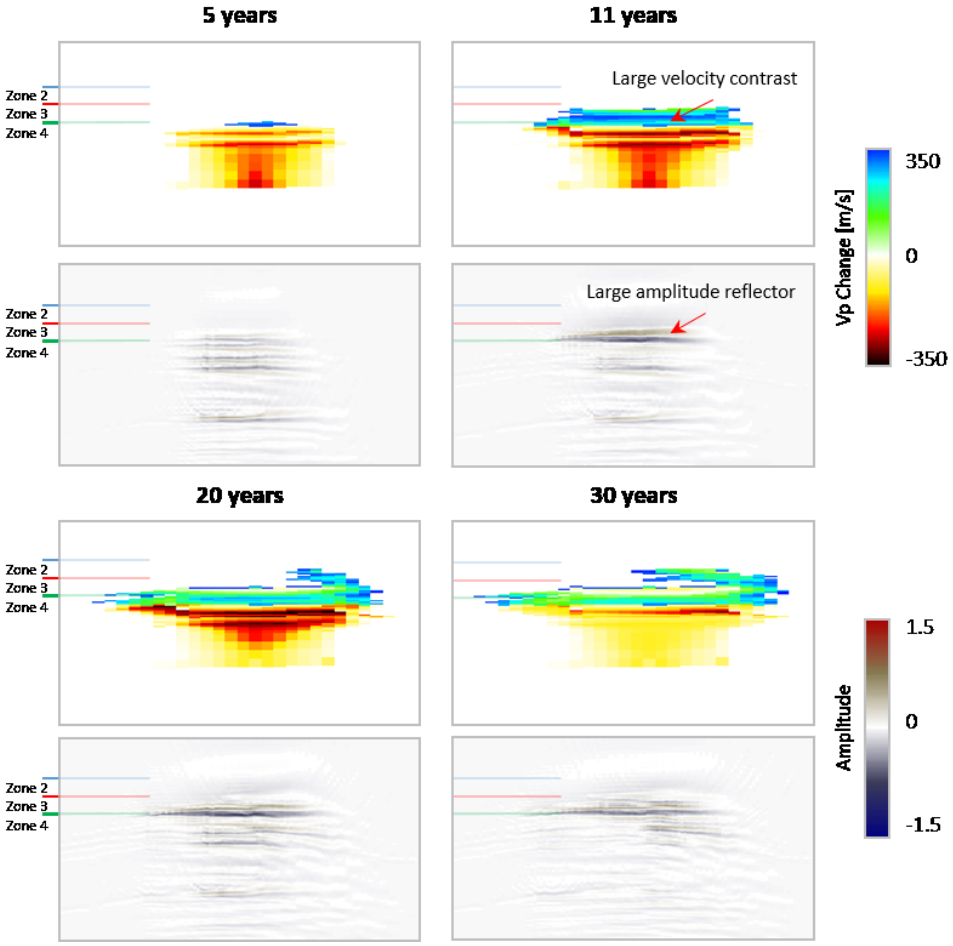

Figure 7.16. Rock-physics and synthetic-seismic modelling of the depleted gas cap scenario. The large velocity contrast, and the resultant large amplitude reflector is highlighted.

Furthermore, the largest change in velocity corresponds to the lowest saturation in the plume. This can be explained by modelling the relationship between velocity and CO_2 saturation (Figure 7.17). The baseline velocity in the reservoir – assuming 20% residual gas saturation – is modelled at 2780 m/s (Step (1) in Figure 7.17). At this stage, the residual saturation in the reservoir is in pore-pressure equilibrium, and hence, uniformly saturated. The injection of CO_2 in the reservoir disrupts the reservoir equilibrium, resulting in a patchy saturation distribution of fluids within the CO_2 plume. This increases the stiffness of the reservoir which in turn results in higher

wave velocities (Step (2) in Figure 7.17). The addition of CO_2 in the reservoir will result in an increase in velocity of 270 m/s. The velocity of the reservoir will then decrease with increasing CO_2 saturation. This explains why the amplitude of the reflectors decreases with time.

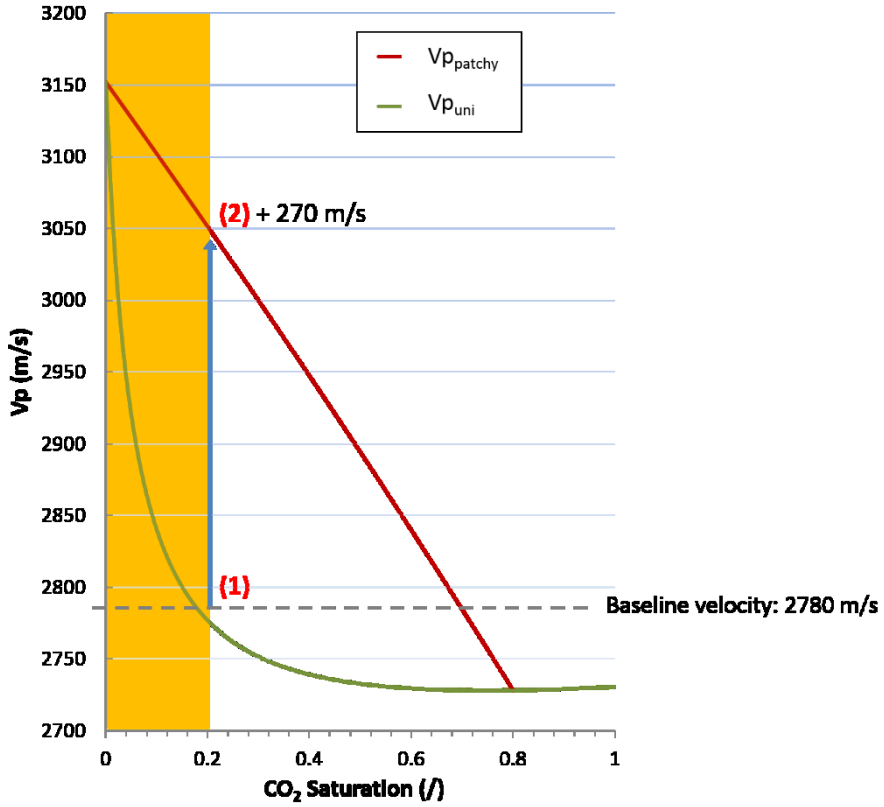

Figure 7.17. P-wave velocity as a function of CO_2 saturation calculated assuming a uniform saturation model (V_{puni}) and a patchy saturation model ($V_{ppatchy}$). Step (1) is the baseline velocity pre-injection. Step (2) represents the increasing velocity due to injected CO_2 when assuming a patchy saturation distribution.

The large increase in velocity explains the large amplitude anomaly, as well as the large velocity push-down effect, interpreted from the outset in the synthetic seismic sections of the depleted gas field scenario (Figure 7.18). The anomaly shows large amplitude reflectors at the base of the reservoir. This is associated with residually trapped CO_2 at the tail of the plume. Of interest however, is the decrease in amplitude over time in the body of the plume. This is evident in the seismic amplitude reflections, as well as the change in velocity, which corresponds to the CO_2 accumulation in the top of zone 3.

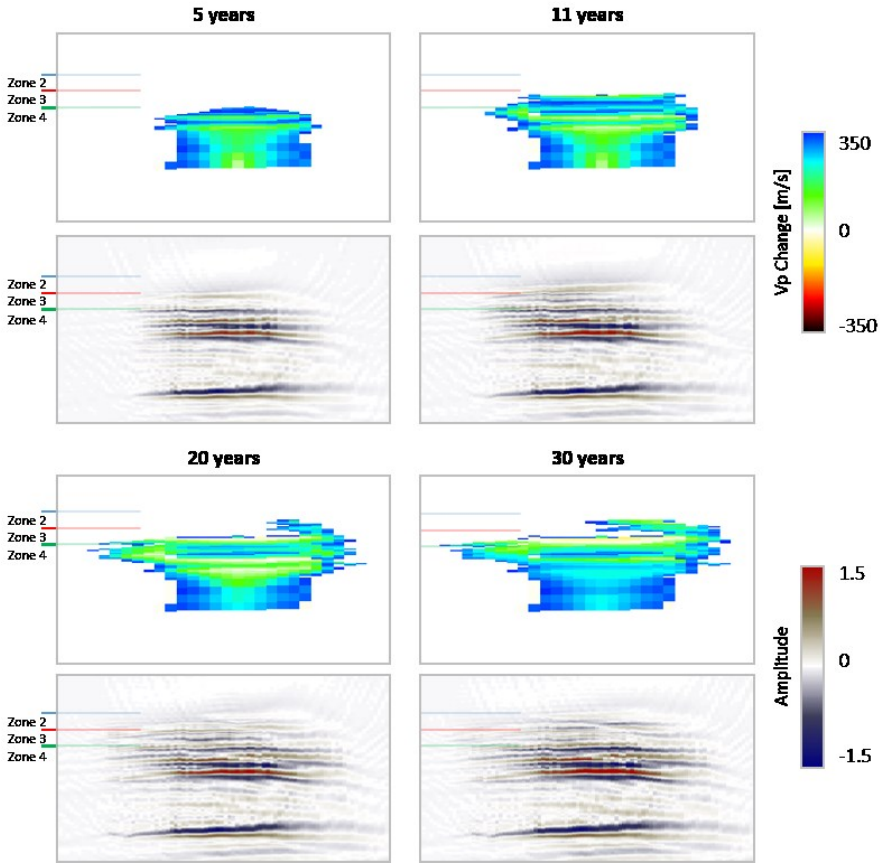

Figure 7.18. Rock-physics and synthetic-seismic modelling of the depleted gas field scenario.

Figure 7.19 highlights the CO_2 accumulation at the top of zone 3, showing the change in velocity with time. A maximum CO_2 saturation of 60% is modelled at the top of zone 3 after 11 years. This corresponds to an increase in velocity of 250 m/s. After 20 years, CO_2 saturation increases to 80%, which results in an increase in velocity of 20 m/s when compared with the baseline velocity model. After 30 years, with a maximum saturation of 90%, a decrease in velocity of 57 m/s is modelled compared with the baseline model. The change in velocity with time also results in a change in amplitude polarity on the synthetic seismic sections; from positive to negative.

The change in velocity with time models the transition of calculated velocities from a patchy to uniform saturation distribution. At maximum CO_2 saturation the change in velocity calculated is the same whether assuming patchy or uniform saturation. This transition can be seen in Figure 7.20, which shows the synthetic seismic section after 30 years calculated assuming a patchy and uniform saturation distribution. The

accumulation in zone 3 is highlighted. The top half of the amplitude anomaly is very similar to the amplitude anomaly calculated assuming a uniform saturation model. The top half of the anomaly corresponds to the main CO_2 accumulations which are structurally trapped. The large amplitude reflectors at the bottom of the anomaly are interpreted as the tail of the CO_2 plume which consists of residually trapped CO_2.

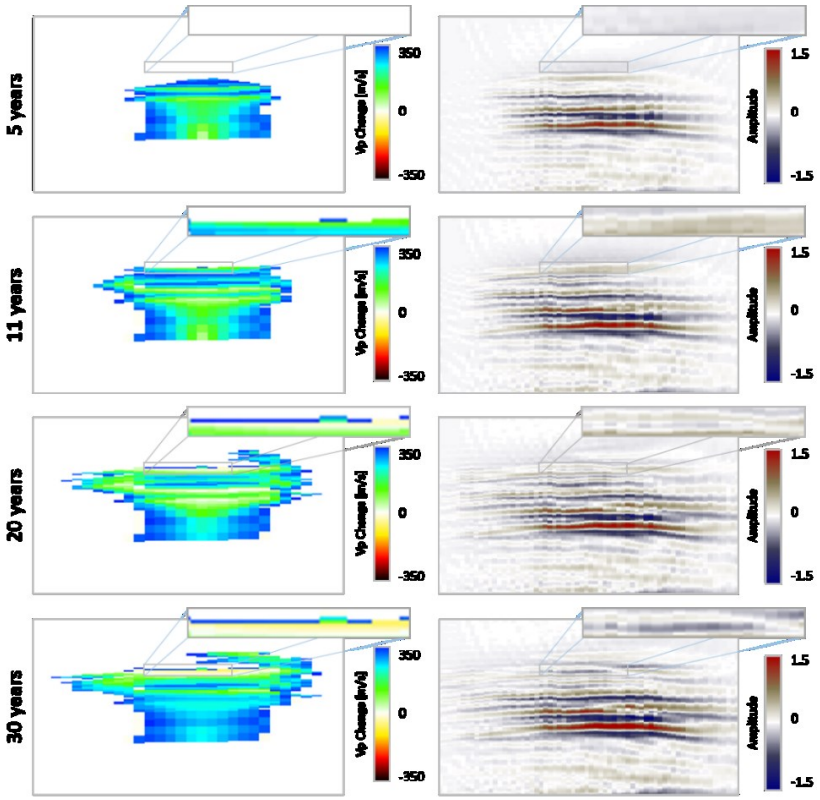

Figure 7.19. Focus on the CO_2 accumulation at the top of zone 3. The change in velocity, and associated synthetic seismic section, is shown for each simulated time. A change in velocity, as well as a change in amplitude, is interpreted.

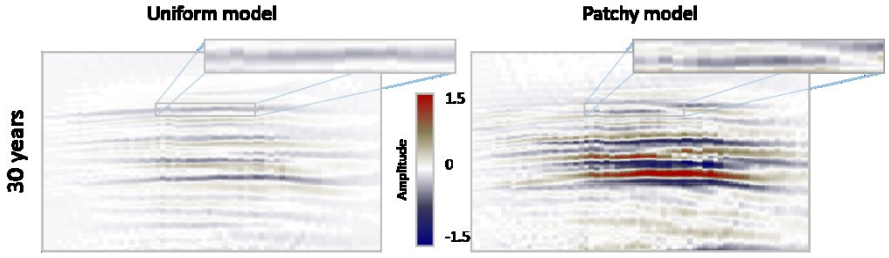

Figure 7.20. A comparison of the synthetic seismic sections calculated assuming uniform and patchy saturation for the 30 year simulation. The top of accumulation at the top of zone 3 is highlighted. A similarity of the reflectors is noted.

The transition in calculated velocities from patchy to uniform can be explained by modelling the relationship between velocity and CO_2 saturation (Figure 7.21). The baseline velocity of the reservoir – assuming 20% residual gas saturation – is modelled at 2780 m/s (Step 1 in Figure 7.21). An initial increase in CO_2 saturation would increase velocity by 270 m/s to 3050 m/s (Step 2). Increasing CO_2 saturation to 60% would result in an increase of 70 m/s when compared with the baseline velocity model (Step 3). When maximum CO_2 saturation is reached – at 80% for this scenario - a decrease in velocity of 55 m/s is calculated. Step 2 to Step 4 demonstrates the transition in calculated velocities from patchy to uniform saturation. At maximum saturation (for example, when the CO_2 is structurally trapped) there is no difference between the patchy and uniform synthetic seismic sections. This has important implications for the detection of CO_2 movement and for the quantification of volume of CO_2 injected into depleted hydrocarbon reservoirs.

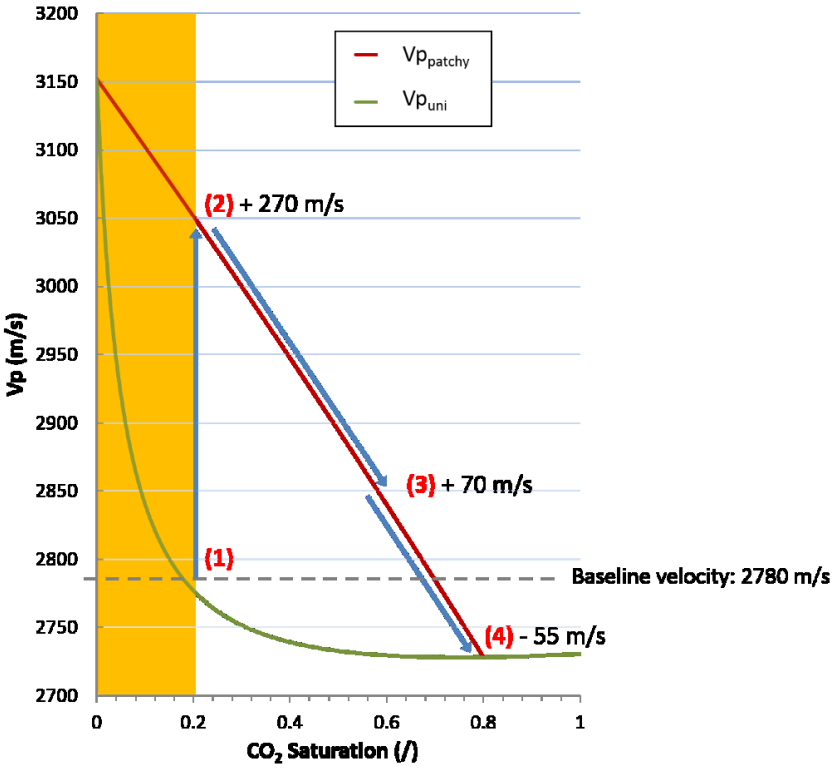

Figure 7.21. P-wave velocity as a function of CO_2 saturation calculated assuming a uniform saturation model (Vp_{puni}) and a patchy saturation model (Vp_{patchy}). Step (1) is the baseline velocity pre-injection, Step (2) represents the increasing velocity due to initial CO_2 injection, Step (3) is the increase in CO_2 saturation to 60% and Step (4) represents the change in velocity at maximum CO_2 saturation.

7.7 Conclusions

The modelling performed in this study demonstrates the potential of seismic techniques to detect CO_2 injected into depleted hydrocarbon fields.

In the literature, the presence of residual saturation in the reservoir – gas or oil - is assumed to negatively impact seismic monitorability of injected CO_2. This is due to residual gas or oil saturation lowering the overall compressibility of the reservoir. Subsequent CO_2 injection will result only in a subtle change in velocity. However, this argument is based on the assumption that the fluids in the reservoir are all in pore-pressure equilibrium, and hence, uniformly saturated. However, CO_2 injection disrupts reservoir equilibrium, resulting in a patchy saturation distribution of fluids. This increases the stiffness of the reservoir which in turn results in higher velocities.

The effect of patchy saturation on the seismic response highlighted the following:

- The injection of CO_2 results in a large increase in velocity; as opposed to a decrease in velocity which is often expected,
- The CO_2 plume can be imaged from the outset, as low CO_2 saturations result in the largest change in velocity when compared with the baseline,
- A large amplitude reflector can be expected when the CO_2 plume crosses a residual gas-water contact,
- The accumulation of CO_2 with time results in a transition from patchy to uniform saturation.

The key outcome of this study is that initial CO_2 saturation – such as a migrating front of CO_2 – will be detectable. This is due to the large increase in velocity at low saturations resulting in a large amplitude response. However, as CO_2 accumulates underneath a seal, a transition from patchy to uniform saturation can be expected. This transition will decrease the amplitude response of the CO_2 plume with time, gradually making it harder to detect when compared with the baseline. This has important implications for quantifying the amount of CO_2 stored in the reservoir, as

with time, CO_2 plume will become 'invisible' as it accumulates and is structurally trapped.

Although this work demonstrates the potential of seismic methods to image CO_2 injected into a depleted gas field, it is important to mention that one of the key assumptions in this study is that the residually trapped gas is uniformly saturated across the entire reservoir. It could be argued that the production of gas could result in a heterogeneous distribution of residual fluids in the reservoir. This is site-specific and could suggest that the residual gas has a patchy saturation distribution; not uniform. In each case, assuming patchy saturation of the depleted gas would still result in a change in velocity with increasing saturation due to the linear relationship between velocity and CO_2 saturation. Therefore, a change in amplitude, as well as the transition from patchy to uniform, would still be expected.

The effect of patchy saturation on seismic data can be confirmed by analysing data acquired over a depleted gas field. To date, a detailed study on the effect of patchy saturation has not been done. However, the presence of patchy saturation has potentially been demonstrated at both the CO_2CRC Otway Project (Jenkins et al., 2012) and the IEA Weyburn CO_2 Monitoring and Storage Project (White et al., 2004).

Summary

The ability of seismic methods to image CO_2 injected into depleted gas fields has been demonstrated by modifying the Bunter Sandstone model to include 20% residual gas saturation. Two CO_2 injection scenarios were modelled: 1) injection into a depleted gas field and 2) injection into a depleted gas cap. Through the application of the monitorability workflow, the generated synthetic seismic sections highlight the effect of patchy saturation on the seismic amplitude response. The results demonstrate the ability to image seismically the CO_2 plume from the outset as well as the transition from patchy to uniform saturation with time. This transition has important implications for the quantification of the characteristics of the CO_2 plume, as it will become seismically invisible with increasing CO_2 saturation and with time.

8. Controlled source electromagnetic feasibility study

I assess the ability of controlled source electromagnetic (CSEM) methods to detect CO_2 injected in the subsurface. The synthetic response is modelled in the time-domain through the application of the multi-transient electromagnetic (MTEM) method. The aims of this chapter are to: 1) simulate the earth impulse response to injected CO_2; 2) model the change in response to lateral and vertical CO_2 migration; and 3) assess the ability of CSEM to detect plume growth and migration in the Bunter Sandstone reservoir discussed in Chapter 6. Once completed, I provide guidelines for the interpretation of time-lapse responses due to CO_2 migration using the MTEM method and comment on the potential of CSEM to detect CO_2 injected in the Bunter Sandstone reservoir.

8.1 Introduction

The use of electromagnetic (EM) methods for the purpose of CO_2 monitoring has been proposed by several teams including Ramirez et al., (2003), Christensen et al., (2006), Um & Alumbaugh (2007), Kiessling et al., (2010) and Bourgeois & Girard (2010). The strength of EM is the ability to detect changes in electrical conductivity due to the displacement of brine by more resistive CO_2 (Reynolds, 2011). As brine is highly conductive, expressions such as Archie's equation (Archie, 1942) can be used to describe accurately the electrical resistivity of sedimentary rocks as a function of water saturation, pore fluid resistivity and porosity (Gasperikova and Hoversten, 2005). The expected change in resistivity measured by EM techniques, when comparing a baseline survey with a monitor survey, may be an order of magnitude or more.

Field deployment of CSEM methods for CO_2 storage monitoring is still relatively untested. As explained in Chapter 3, the method has been deployed at the Sleipner CCS site only, yielding inconclusive results. Although, I have found no evidence to suggest that the inconclusive results are related to the method itself, but instead could be related to the lack of a true baseline survey.

I have found no reports in the literature of attempts to model the effects of CO_2 migration and leakage on time-lapse CSEM. The detectability potential of CSEM for CO_2 storage has been demonstrated by JafarGandomi and Curtis (2011) and Kang et al., (2012). JafarGandomi and Curtis (2011) modelled changes in the electrical field due to a presence of a 1D block of CO_2, while Kang et al., (2012) modelled a 2D plume and the effects of increasing saturation in time-lapse. Both studies model the effectiveness of CSEM for monitoring structurally trapped CO_2, however do not define a minimum amount of detectable CO_2.

The potential application of CSEM for CCS monitoring has also been presented at two SEG meetings: Ellis and Sinha (2010) and Bhuyian et al., (2011). Both highlight the effectiveness of the technique to model a CO_2 block of constant saturation. Bhuyian et al., (2012) performed 3D CSEM time-lapse sensitivity analysis of subsurface CO_2

storage using 3D finite difference modelling in the frequency domain. The survey acquisition parameters included 25 receivers deployed in a 1km by 1km grid geometry at the seafloor. The source was a horizontal electric dipole (HED), positioned around each receiver in a 20 by 20km grid (100m source spacing) 30m above the seafloor. The authors demonstrated the effect of CO_2 expansion on the time-lapse CSEM response in the frequency-domain for frequencies ranging from 0.1 to 1.25 Hz. The variation in lateral extent was shown to be more sensitive to the time-lapse response compared with vertical changes.

When modelling the potential of CSEM for deployment at CCS sites, the generated synthetic time-lapse responses are modelled in the frequency domain and using either a 1D or 2D model, or a very simple 3D model. This is only one approach. Another approach is modelling the synthetic EM response in the time-domain through the application of the multi-transient electromagnetic (MTEM) method. Wright et al., (2002) and Ziolkowski et al., (2007) show the advantages of collecting CSEM data with the MTEM method. The principle advantage of the MTEM method is that it allows the complete Earth impulse response to be recovered from the data. It can be argued that the MTEM method is more applicable to CO_2 storage monitoring as the transient signal contains the full frequency spectrum. This could allow for the ability to image subsurface CO_2 anomalies more accurately. The theory behind the MTEM method has been detailed in Wright et al., (2002) and Ziolkowski et al., (2007).

In this chapter, I perform a feasibility study to assess the ability of CSEM to detect CO_2 injected in the subsurface by modelling the synthetic impulse response. This study aims to:

1) Demonstrate the change in the earth impulse response to CO_2 injected in the subsurface;
2) Model the change in response to lateral and vertical CO_2 migration;
3) Assess the ability of CSEM to detect plume growth and migration in a reservoir;

First, I summarise the MTEM method and model the earth impulse response to a simple CO_2 layer in 1D and 3D. Second, I model the response to a 3D CO_2 plume, gradually increasing the width and depth of the CO_2, noting the modelled change in amplitude and arrival time for each scenario. This is an analogue to lateral and vertical migration of trapped CO_2. Finally, I apply the monitorability workflow presented in Chapter 4 to the heterogeneous Bunter Sandstone model of Chapter 6. I assess the ability of CSEM to image and detect CO_2 plume growth, evolution, and migration by simulating the injection of 2 MT of CO_2 over 20 years

8.2 The MTEM method

The multi-transient electromagnetic (MTEM) is a CSEM method. The method involves the injection of a time-varying current between two source electrodes (Ziolkowski, 2007). The method utilizes a horizontal electric dipole (HED) source and an in-line receiver cable consisting of electric dipoles. The HED source excites current flow in the subsurface (Constable and Srnka, 2007). The electric currents can range from a few hundred amperes up to 1000 A. Figure 8.1 shows a layout of a towed-streamer MTEM offshore survey.

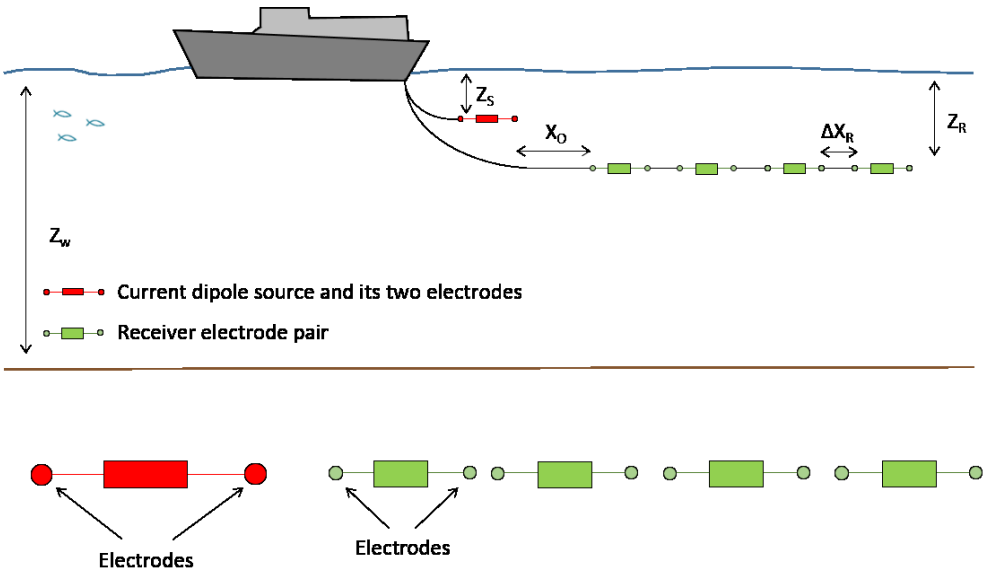

Figure 8.1. Data acquisition parameters for a towed source and receiver system. Z_S and Z_R represent the depth of the source and receiver respectively, while ΔX_R is the receiver interval and X_O is the source-receiver offset. Z_w is the water depth.

The injected current is a finite source signal, for instance a single period of a pseudo-random binary sequence (PRBS). The source current is measured and recorded, and is the input to the earth. The time-varying voltage response between each pair of receiver electrodes is also measured simultaneously.

The measured voltage response at the receiver is given by (Ziolkowski et al., 2007)

$$v_l(t) = Sr(t) * \ g(t) + N(t), \tag{8.1}$$

where v_l is the measured voltage, $Sr(t)$ is the system response, the asterisk * denotes convolution, $g(t)$ is the earth impulse response and $N(t)$ is the uncorrelated noise.

The MTEM method describes an indirect method of recovering the earth impulse response $g(t)$ by deconvolution of the measured output as $v_l(t)$ and $Sr(t)$ are known. Deconvolution compresses the energy from the PRBS into a single time sample and compresses the received signal into the impulse response. This results in an increase in the signal-to-noise ratio and allows for further time-domain processing. Figure 8.2 is a land data example from Ziolkowski (2007) demonstrating (a) the measured current input from a PRBS source time function, (b) the measured voltage output at one receiver, and (c) the earth impulse response as a result of deconvolution. One response with two components can be expected. The first arrival is a large impulse; this is the air wave. This is usually separated from the earth impulse response. Ziolkowski et al. (2011) describe this separation as a result of causality. This is the process in which the air wave travels to the receiver faster than the earth response and arrives first. The earth response travels more slowly and arrives second. Any resistivity changes in the subsurface result in a change in the earth impulse response.

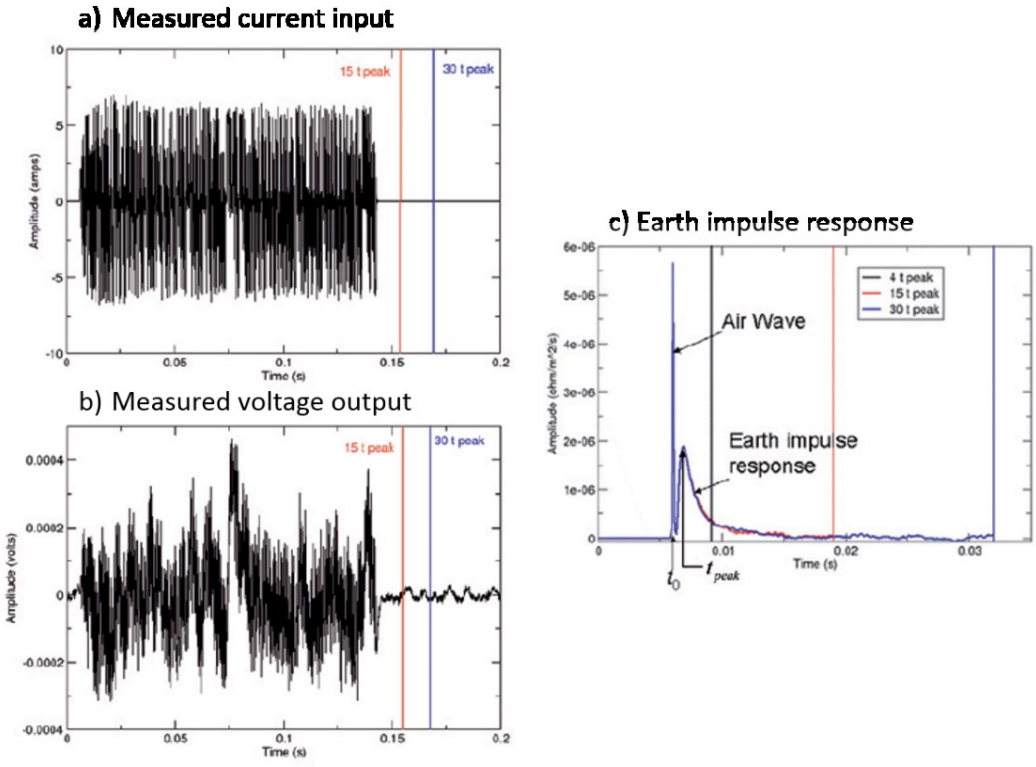

Figure 8.2. Land data example from Ziolkowski (2007) demonstrating (a) the measured current input from a PRBS source time function, (b) the receiver response for the input signal shown in (a) and (c) the earth impulse response as a result of deconvolution. One response with two components is expected. The first is the air wave, the second is the earth impulse response.
Modified from Ziolkowski (2007).

The MTEM method obtains the full impulse response of the earth. This is because MTEM measures the broad-bandwidth response which can be set to any desired frequency range. Of importance is the input source time function: the PRBS source. A PRBS is a sequence with $N = 2^n - 1$ samples, where n is the order of the sequence. It switches between plus and minus of the source strength at pseudo-random multiples of some basic time interval Δt (Ziolkowski et al., 2011). The PRBS has an amplitude spectrum that is flat within the frequency interval

$$\frac{1}{N\Delta t} \leq f \leq \frac{1}{2\Delta t}. \tag{8.2}$$

Conventional CSEM uses a continuous signal that is generally characterised by a square wave with a fundamental frequency in a range of 0.1 Hz to 10 Hz, depending

on the size and depth of the target, and its odd harmonics of the fundamental frequency.

Ziolkowski et al., (2011) compare the transient PRBS used in MTEM to the transient square-wave source signature used in conventional CSEM. Figure 8.3 is an example of a source current signature and corresponding amplitude spectrum for a transient PRBS and a transient square-wave from Ziolkowski et al., (2011). The PRBS spectrum is almost level, while the square-wave source has a spectrum which peaks at the fundamental frequency of 0.1 Hz and its odd harmonics. Since the amplitude spectrum of conventional CSEM data is incomplete, it is impossible to construct the impulse response from the data.

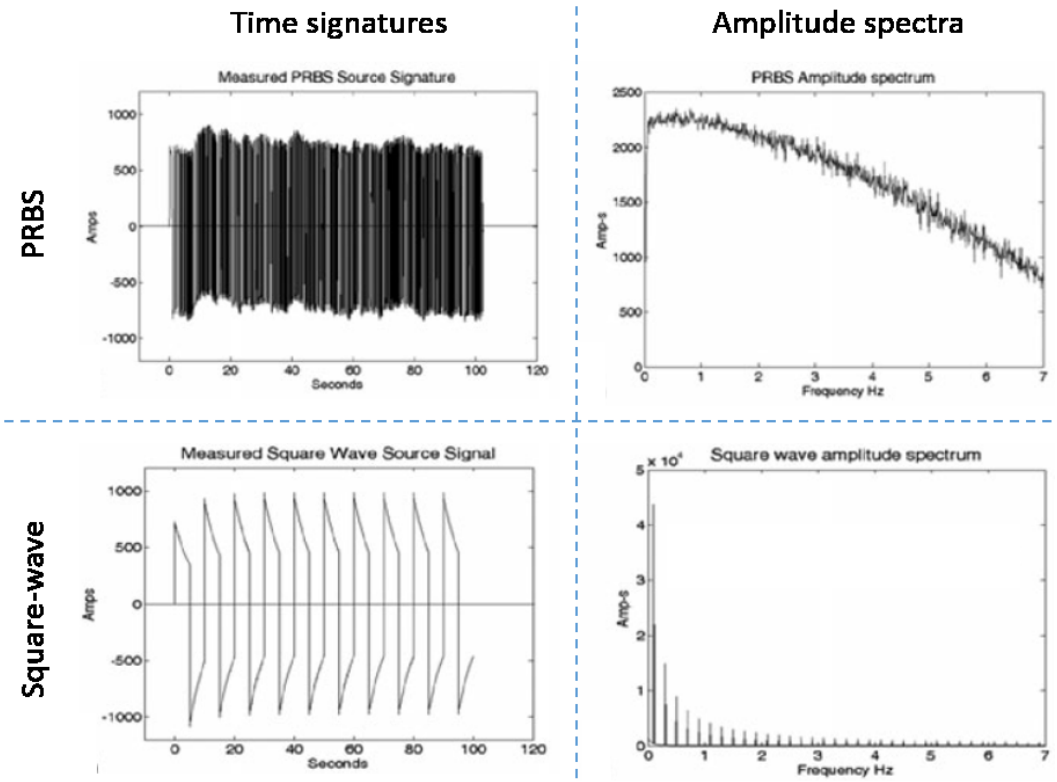

Figure 8.3. A comparison of the source current signature and corresponding amplitude spectrum for a transient PRBS and a transient square-wave data. Modified from Ziolkowski et al., (2011). The square wave represents the traditional signal used in conventional CSEM.

I now model the broad-bandwidth impulse response to CO_2 storage and migration in the subsurface. I model the application of the MTEM method in shallow water with a single line towed source and receiver system.

8.2.1 1D CO_2 model response

I model the synthetic earth impulse response to the presence of a 1D CO_2 layer placed in a 1 Ω.m half-space. The CO_2 is 100m thick with a resistivity of 100 Ω.m. A 100m sea-water depth is assumed with a resistivity of 0.3 Ω.m.

Four scenarios are modelled (Figure 8.4):

1) No CO_2 layer;
2) CO_2 layer at 700m depth;
3) CO_2 layer at 1000m depth;
4) Two CO_2 layers, at 700m and 1000m depth.

The scenarios are an analogue for CO_2 storage and migration in a reservoir. Acquisition parameters are detailed in Table 8.1.

Table 8.1. Synthetic MTEM modelling acquisition parameters

Acquisition parameters			
Source	x	3000	m
	Strength	1	A.m
	Depth	10	m
	Frequencies	0.0001 to 10000	Hz
	Times	0.001 to 100	Sec
Receiver	Min-offset	1000	m
	Max-offset	5000	m
	Spacing	1000	m
	Depth	50	m

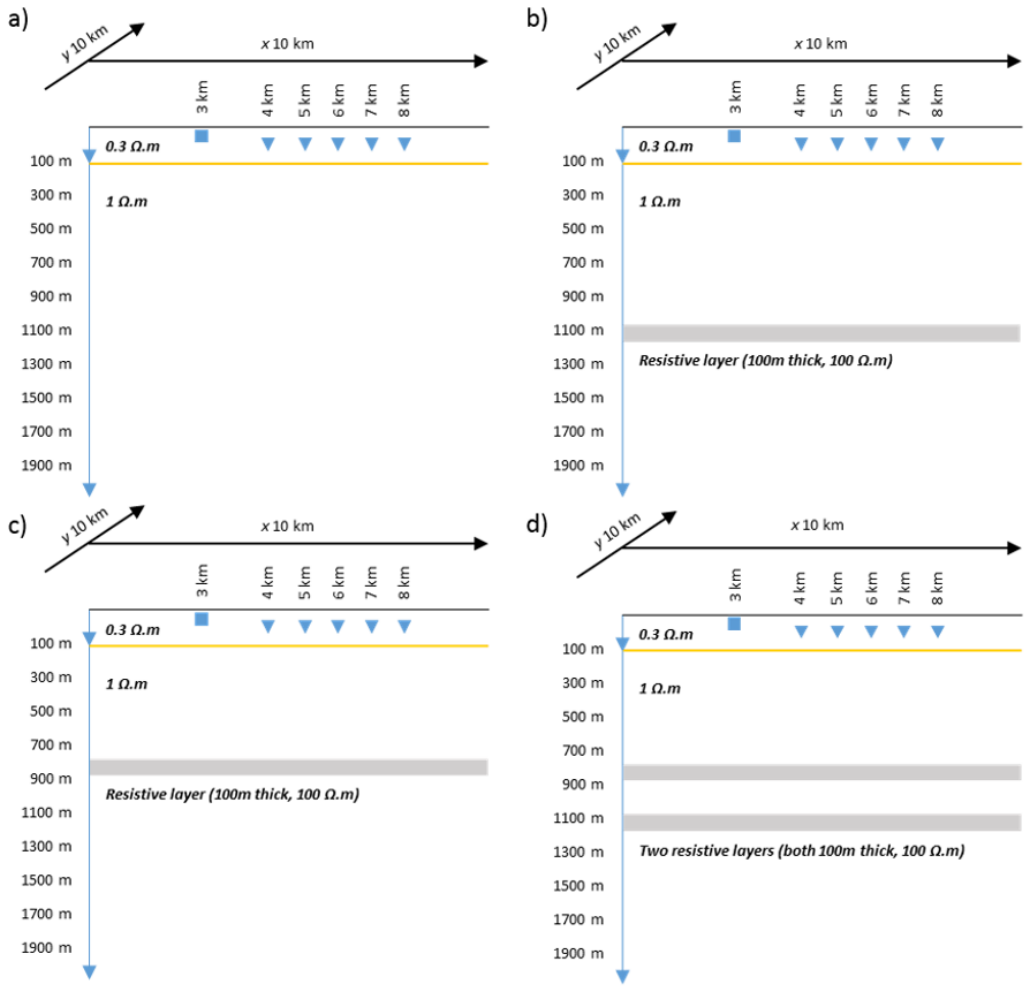

Figure 8.4. Four scenarios modelling the response of a 1 Ω.m half-space model with a) no CO_2 layer, b) CO_2 layer at 700m depth, c) CO_2 layer at 1000m depth and d) two CO_2 layers at 700m and 1000m depth. The CO_2 layers are all 100m thick with a constant resistivity of 100 Ω.m.

Figure 8.5 shows the simulated responses for each modelled scenario, computed for offsets 2000m to 5000m. The black curve is the baseline model with no CO_2 resistor, the blue curve is the CO_2 layer at 700m depth, the red curve is the CO_2 layer at 1000m depth and the green curve is the two layer model with CO_2 at 700m and 1000m depth. Figure 8.6 shows the time-lapse responses (baseline subtracted from the monitor) for each modelled scenario.

Analysis of the results suggests the following:

- The addition of a resistive CO_2 layer results in an increase in amplitude compared with the baseline results.
- A shallower CO_2 layer results in an earlier arrival time, as well as an increase in amplitude, compared with a deeper layer of CO_2.
- There is very little difference between the 700m scenario and the two layer scenario at shorter offsets, however a clear difference is modelled at larger offsets.
- The time-lapse amplitude arrival times for both the 700m scenario and the two layer model are the same. The only difference is the increase in amplitude.

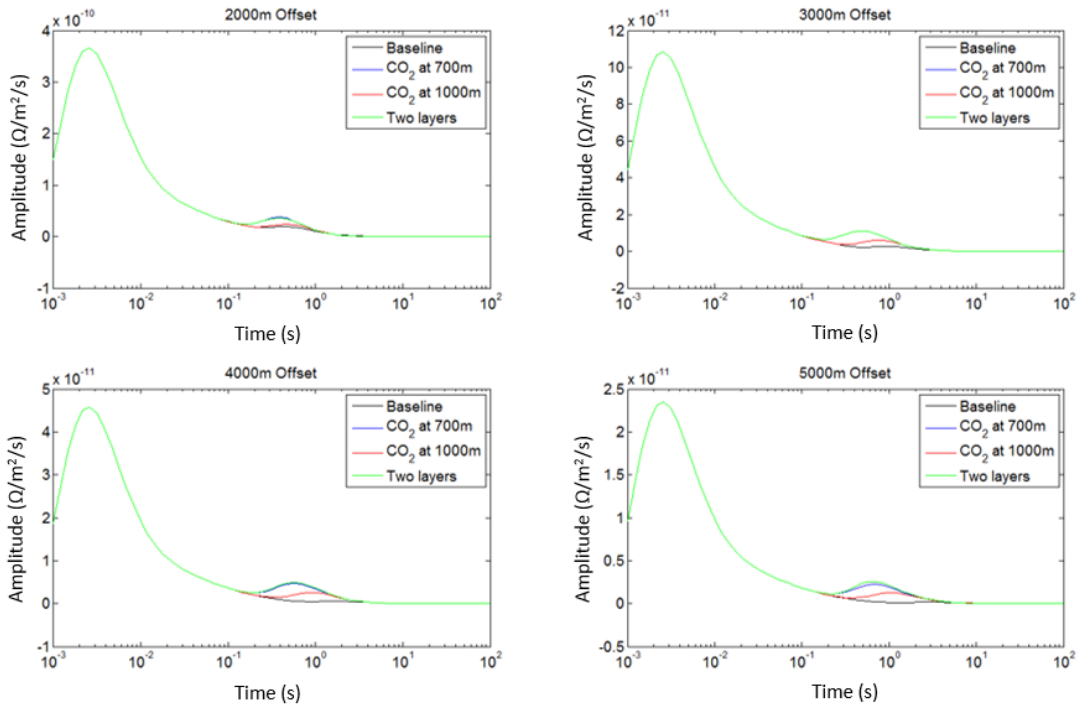

Figure 8.5. Earth impulse responses of the four modelled scenarios: no CO_2 layer (black); CO_2 layer at 700m depth (blue); CO_2 layer at 1000m depth (red); and two CO_2 layers at 700 & 1000m depth (green).

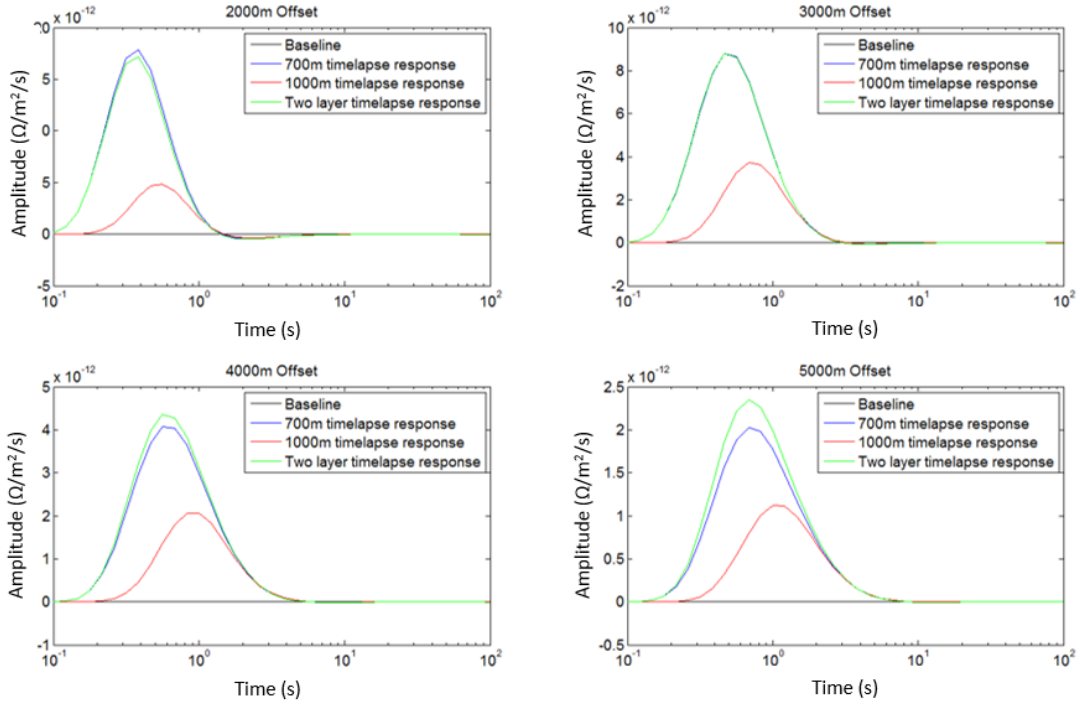

Figure 8.6. Time-lapse responses with the baseline of the four modelled scenarios: CO_2 layer at 700m depth (blue); CO_2 layer at 1000m depth (red); and two CO_2 layers at 700 & 1000m depth (green).

These results represent the earth impulse response to a 1D model. I now model the response to a 3D model based on acquisition parameters similar to real towed-streamer data acquisition.

8.2.3 3D CO_2 model response

The same four scenarios are modelled, however, the CO_2 layer now has dimensions of 1000m in x by 1000m in y by 100m in z. The CO_2 has a resistivity of 100 Ω.m. The 3D CO_2 body is placed in the 1D background consisting of a 1 Ω.m half-space below 100m of sea water of 0.3 Ω.m resistivity.

The same four scenarios are modelled (Figure 8.7):

1) No CO_2 layer;
2) CO_2 layer at 700m depth;
3) CO_2 layer at 1000m depth;
4) Two CO_2 layers, at 700m and 1000m depth.

The 2D survey acquisition parameters are similar to real towed-streamer data acquired in the field (Table 8.2).

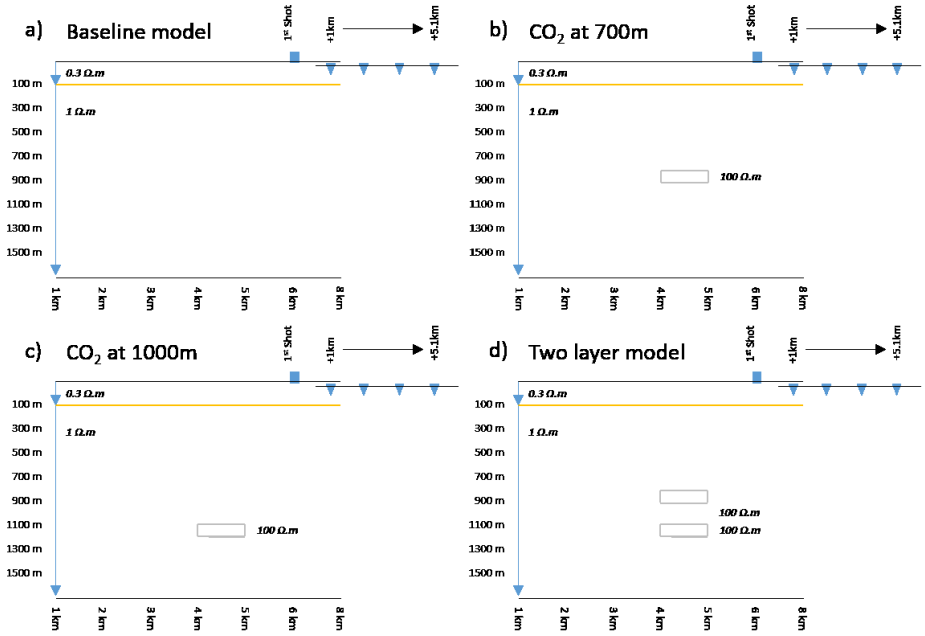

Figure 8.7. Four modelled scenarios assessing the response to a 3D CO_2 body. a) is the baseline model with no CO_2, b) CO_2 at 700m, c) CO_2 at 1000m and d) two CO_2 bodies at 700m and 1000m depth. The CO_2 body has dimensions of 1000m in x by 1000m in y and 100m in z.

Table 8.2. 2D acquisition parameters for the simple 3D model response study. Coordinates are in the x-dimensions. The 2D survey was acquired across the middle of the CO_2 body at y-dimensions 500m.

Acquisition parameters			
Source	First shot	6000	m
	Last shot	0	m
	Spacing	200	m
	Number of shots	31	-
	Depth	10	m
	Strength	2.16 x 10^6	A.m
	Frequencies	0.0001 to 10000	Hz
	Times	0.001 to 100	Sec
Receiver	Min-offset	500	m
	Max-offset	5100	m
	Spacing	200	m
	Number of receivers	24	-
	Depth	50	m

Figure 8.8 shows the simulated earth impulse responses (left) and time-lapse responses (right) for each modelled scenario, for shot coordinate 2200m and offset 2300m. The black curve is the baseline model with no CO_2, the blue curve includes a CO_2 body at 700m depth, the red curve is the CO_2 body at 1000m depth and the green curve is the two layer model with CO_2 at 700m and 1000m.

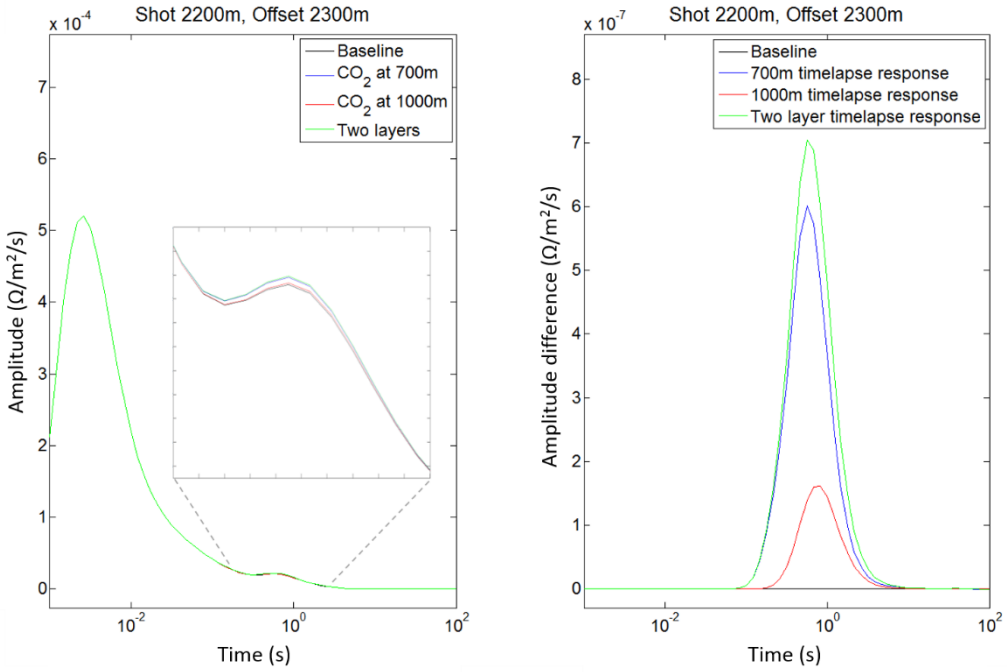

Figure 8.8. Earth impulse responses (left) and time-lapse response with the baseline (right) of the four modelled scenarios: no CO_2 layer (black); CO_2 body at 700m depth (blue); CO_2 body at 1000m depth (red); and two CO_2 bodies at 700 & 1000m depth (green). The grey box is a close-up image of the change in amplitude.

These results represent the simulated response at a single shot and a single offset. I now model the time-lapse impulse responses as a series of common-offset sections for the CO_2 model at 1000m depth (Figure 8.9) and the two-layered model (Figure 8.10). The source-receiver midpoint is the horizontal coordinate and time is the vertical coordinate. Visualising data as common-offset sections is a standard display in seismic processing (Ziolkowski et al., 2007). The amplitudes are normalised and corrected for the decay of the impulse response with offset $1/r_{off}^5$ (Ziolkowski and Wright, 2007). r_{off} is the source-receiver offset in meters.

The common-offset sections show a clear anomaly across the area in which the CO_2 body is modelled. The anomaly is seen where expected and at the correct x-coordinate. The CO_2 body at 1000m depth is imaged clearly at offsets greater than 1900m (Figure 8.9). The two-layer model, with CO_2 modelled at depths of 700m and 1000m, is imaged clearly at offsets greater than 1500m (Figure 8.10). This is expected as changes in resistivity have sensitivity at offsets around twice the target depth (Wright et al., 2002, Ziolkowski et al., 2007). Should the CO_2 migrate or leak to shallower depths, the anomaly will be detected at shorter offsets. This is demonstrated in Figure 8.11 by comparing the simulated amplitude versus offset at a single location for both the single layer CO_2 at 1000m and the two layer CO_2 at 700m and 1000m. It is clear that the migrating CO_2 will result in an earlier arrival of the response, as well an increase in amplitude, at shorter offsets.

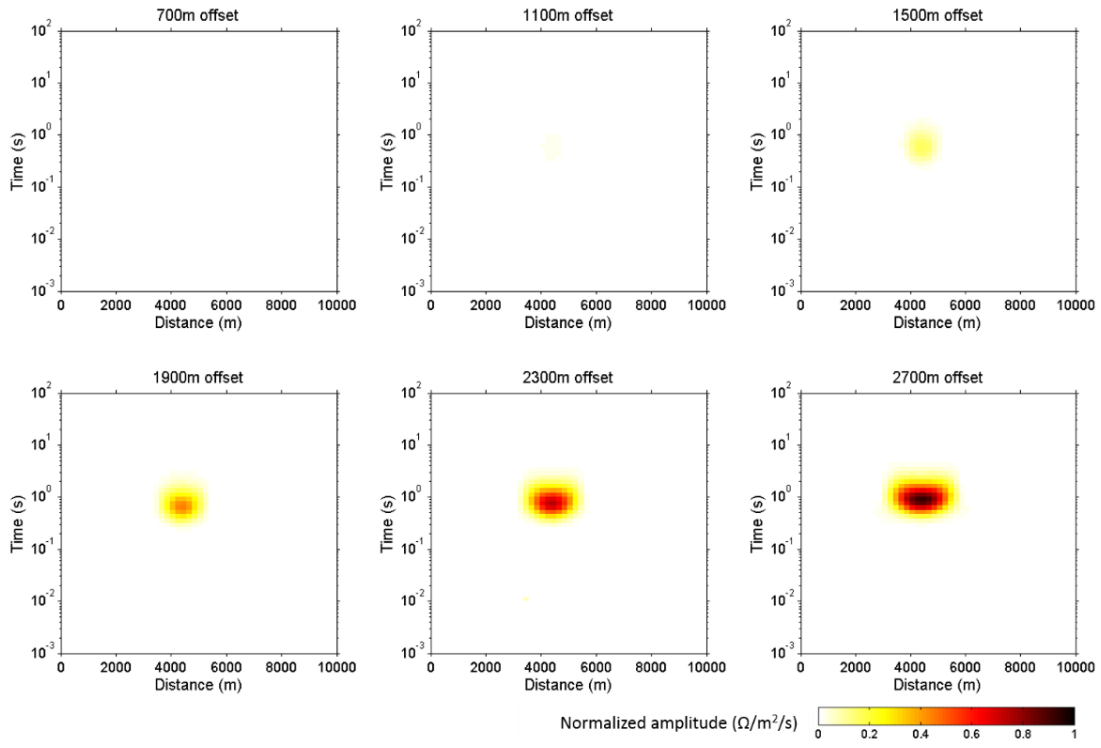

Figure 8.9. Time-lapse common-offset sections of the earth's impulse response for the CO_2 model at 1000m depth. The horizontal coordinate is the midpoint while the vertical coordinate is time. The presence of the CO_2 anomaly is clearly imaged in the time-lapse sections.

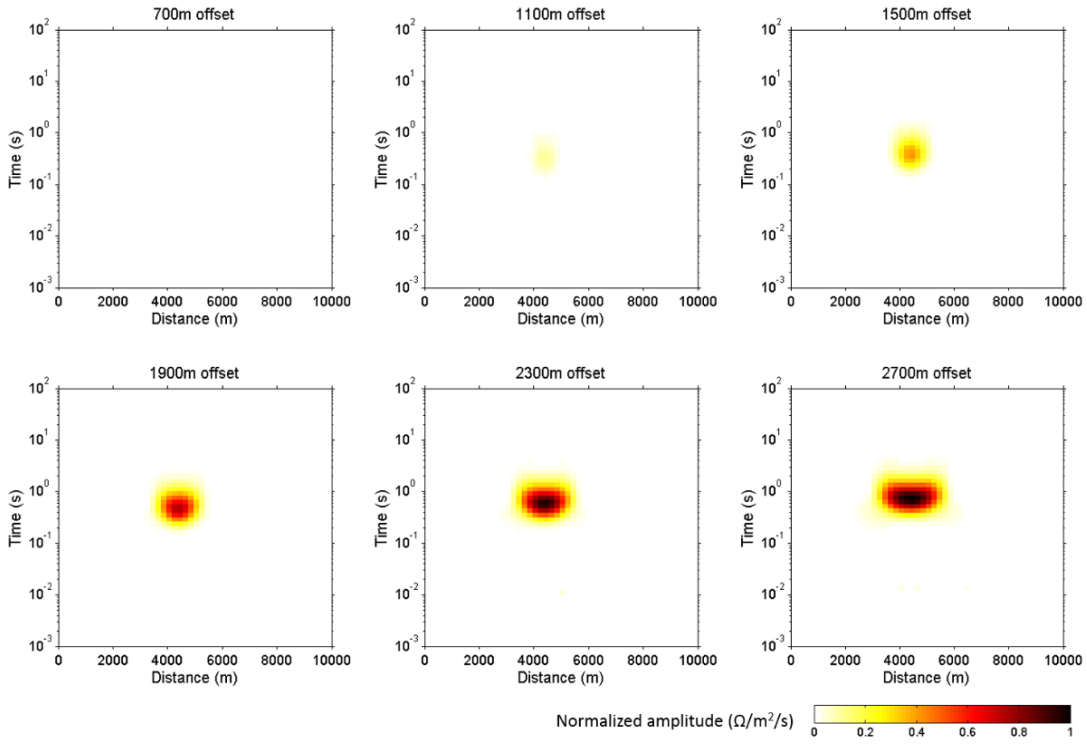

Figure 8.10. Time-lapse common-offset sections of the earth's impulse response for the two layer CO_2 model, at depth of 700m and 1000m. The horizontal coordinate is the midpoint while the vertical coordinate is time. The presence of the CO_2 anomaly is clearly imaged in the time-lapse sections.

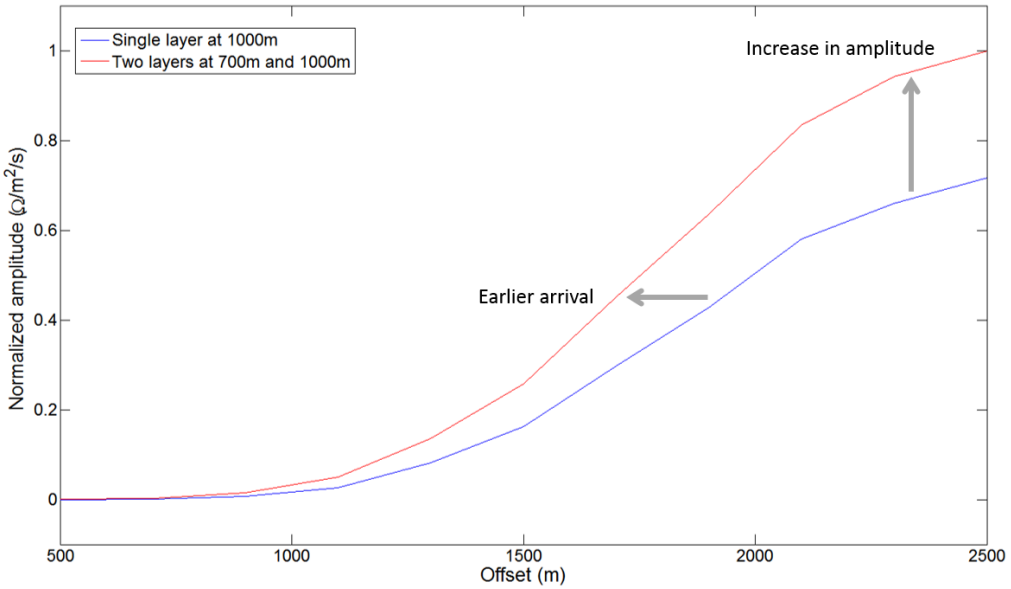

Figure 8.11. A comparison of the normalized amplitude versus offset for the single layer CO_2 at 1000m (blue) and the two layer CO_2 at 700m and 1000m (red). The amplitude is measured at midpoint 4350m and time 0.46s. Clearly evident is the earlier arrival time, as well as the increase in amplitude, of the response at shorter offsets due to a shallower CO_2 layer.

The results demonstrate the potential of CSEM to detect CO_2 injected in the subsurface. First, it is clear that a 3D CO_2 body will result in a change in the earth impulse response when compared with a baseline model with no CO_2. Second, should CO_2 migrate to a shallower level, an earlier arrival time, as well as an increase in amplitude, is expected. Third, when displayed as time-lapse common-offset sections, the CO_2 anomaly is modelled clearly and in the right coordinates. Should the CO_2 migrate to shallower levels, the anomaly will be detectable at shorter offsets. This suggests that CSEM, through the MTEM method, can 1) detect stored CO_2 and 2) detect a loss of containment.

8.3 CO_2 migration study

As the impulse response to CO_2 in the subsurface has been simulated, I model the expected change in amplitude as a result of lateral and vertical migration. For both studies, the 3D CO_2 body is 100m thick with a constant resistivity of 100 Ω.m. The 3D model is placed in a 1D background of 1 Ω.m half-space below 100m of sea water of 0.3 Ω.m resistivity. Acquisition parameters for both scenarios are the same as for the simple 3D model response study (Table 8.2).

First, I model the expected change in amplitude due to lateral CO_2 migration by modelling four different CO_2 extents, all at a depth of 1000m (Figure 8.12):

- 500m in *x* by 500m in *y*;
- 1000m in *x* by 1000m in *y*;
- 1500m in *x* by 1500m in *y*;
- 2000m in *x* by 2000m in *y*.

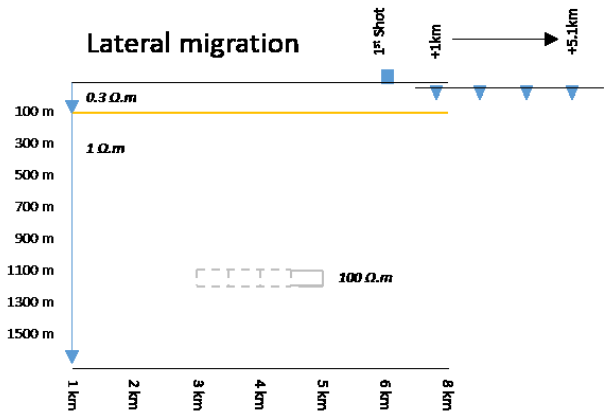

Figure 8.12. Scenarios for the lateral migration study. Four different extents are modelled: 500m in x by 500m in y, 1000m in x by 1000m in y, 1500m in x by 1500m in y, and 2000m in x by 2000m in y. For each study the CO_2 body is 100m thick with a resistivity of 100 Ω.m. The 3D model is placed in a 1D back consisting of a 1 Ω.m half-space

Second, I model the expected change in amplitude due to vertical CO_2 migration by modelling four different CO_2 depths. The plume has dimensions 1000 in *x* by 1000m in *y* (Figure 8.13):

- 500m;
- 750m;
- 1000m;
- 1250m.

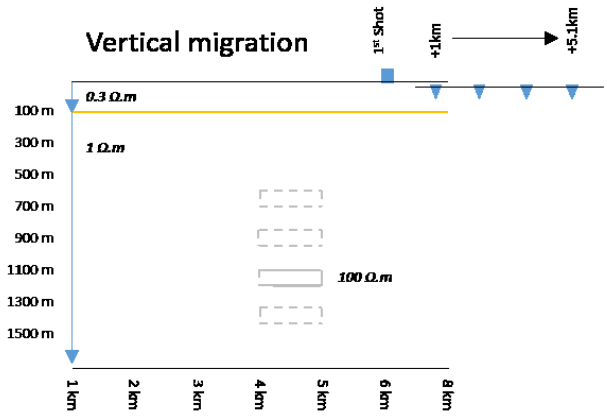

Figure 8.13. Scenarios for the vertical migration study. Four different CO_2 depths are modelled: 500m, 750m, 1000m and 1250m. For each study the CO_2 has dimensions 1000m in x by 1000m in y with a resistivity of 100 Ω.m. The 3D model is placed in a 1D back consisting of a 1 Ω.m half-space

8.3.1 Lateral CO_2 migration

Figure 8.14. shows the simulated earth impulse responses (left) and time-lapse amplitude changes (right) for shot coordinate 1200m and offset 5100m. The black curve is the baseline model with no CO_2, the blue curve is the 500m by 500m wide CO_2 body, the red curve is 1000m by 1000m, the green curve is 1500m by 1500m and the teal curve is the 2000m by 2000m wide CO_2 body. Clearly evident is the increase in amplitude resulting from an increase in width. The time-lapse amplitude arrival times for each scenario are the same.

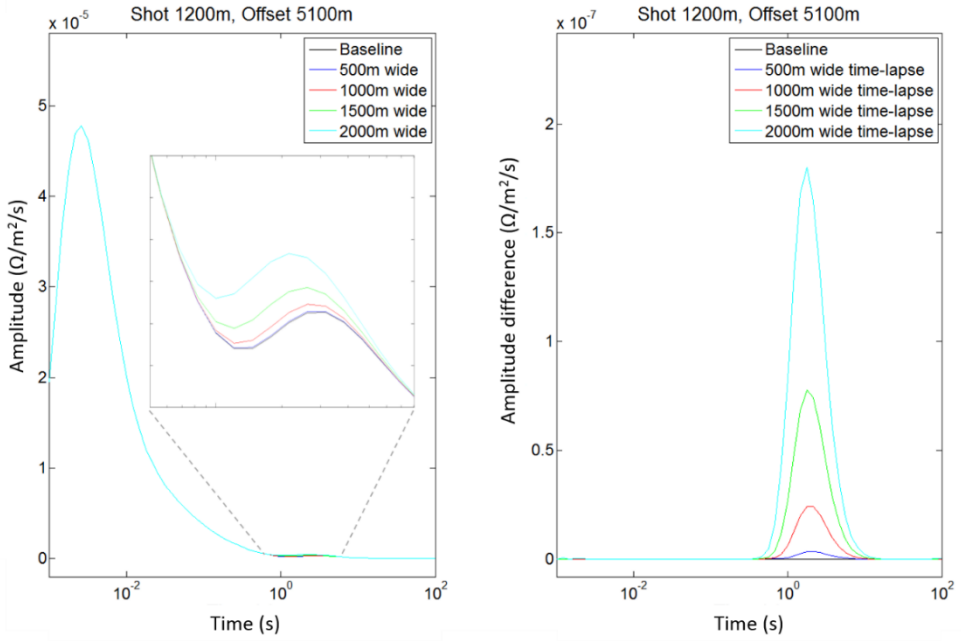

Figure 8.14. Earth impulse responses (left) and time-lapse responses with the baseline (right) of the four modelled scenarios: no CO_2 layer (black); 500m wide CO_2 body (blue); 1000m wide CO_2 body (red); 1500m wide CO_2 body (green); 2000m wide CO_2 body (teal). The grey box is a close-up image of the change in amplitude.

8.3.2 Vertical CO_2 migration

Figure 8.15. shows the simulated responses (left) and time-lapse amplitude changes (right) for shot coordinate 2200m and offset 2300m. The black curve is the baseline model with no CO_2, the blue curve is the CO_2 at 500m depth, red curve at 750m depth, green curve at 1000m depth and teal curve at 1250m depth. Clearly evident is the

large increase in amplitude associated with vertical migration. Furthermore, earlier time-lapse arrival times are noted for CO_2 at shallower depths.

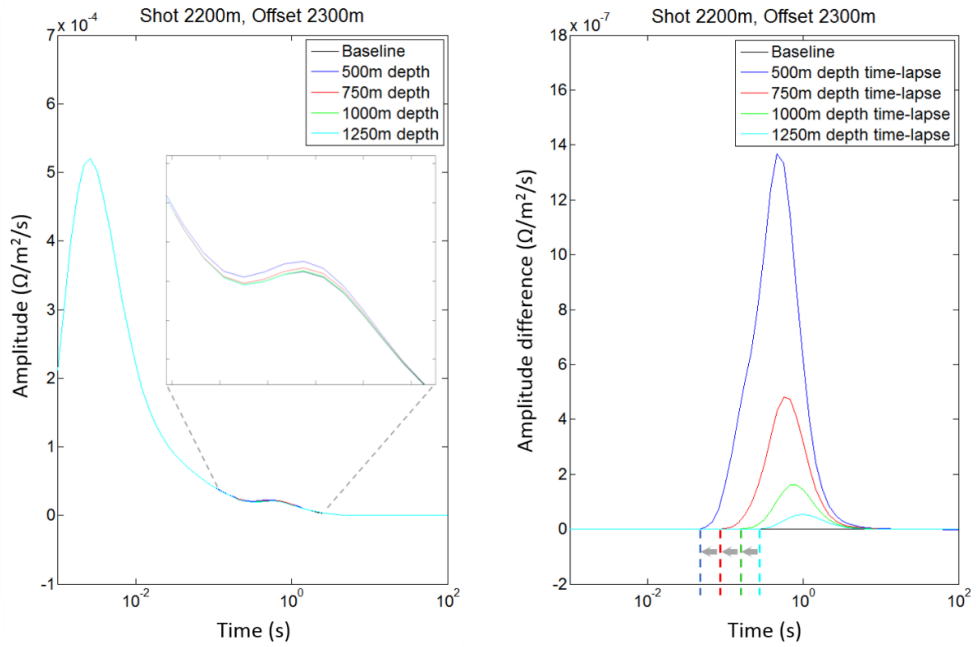

Figure 8.15. Earth impulse responses (left) and time-lapse response (right) of the four modelled scenarios: no CO_2 layer (black); CO_2 at 500m depth (blue); CO_2 at 750m depth (red); CO_2 at 1000m depth (green); CO_2 at 1250m depth (teal). The grey box is a close-up image of the change in amplitude. The grey arrows depict the change in amplitude arrival times associated with each depth.

The results from the lateral and vertical CO_2 migration study demonstrate the potential of CSEM to detect movement of CO_2 in the subsurface. The results highlight two key points when interpreting the time-lapse response. First, if a change in amplitude with no change in arrival time is detected, this would indicate lateral migration of CO_2. An example of this would be CO_2 migrating below the top seal of the storage reservoir. Second, should a change in both amplitude and arrival time be detected, this would indicate a possible loss of containment in the reservoir as the CO_2 plume has migrated to shallower depths.

The models currently assessed in this chapter represent simple 1D and 3D models of a single CO_2 body with constant resistivity. This does not represent the complexity that is often encountered in the field. For this reason, I assess the ability of CSEM to

detect CO_2 plume growth and migration on the heterogeneous Bunter Sandstone model presented in Chapter 6. I model the impulse response.

8.4 Bunter Sandstone model

In this section, I assess the ability of CSEM to detect plume growth and evolution in the Bunter Sandstone reservoir. The reservoir model is the same model presented in Chapter 6 in the Seismic monitoring study. I apply the monitorability workflow detailed in Chapter 4.

8.4.1 Reservoir and fluid-flow model modification

The Bunter Sandstone reservoir model has been described in detail in Chapter 6, section 2. The same fluid-flow simulation results are used. However, the dimensions of the fluid-flow are modified to decrease computational time, as the input model for the MTEM modelling is a 3D model.

I now detail the steps taken to simplify the fluid-flow modelling results while ensuring a high level of detail in plume geometry and heterogeneity. This process was repeated for the 5 year, 11 year and 20 year fluid-flow simulation results. The following steps were applied to the 20 year Bunter simulation result.

3D model size reduction

The first step was to reduce the 3D model dimensions of the original fluid-flow model in Chapter 6. The model had the following dimensions (Figure 8.16):

- x: 439945 to 446709m, total of 6.7 km
- y: 5986800 to 5991440, total of 4.6 km
- z: 0 to 2080, total of 2.08 km

I constrained the 3D model dimensions based on the location of the simulated plume. The new 3D model has the following dimensions:

- x: 442500 to 444500, total of 2 km
- y: 5988500 to 5990000, total of 1.5 km
- z: 1200 to 1500, total of 300 m

The new model limitations for the 20 year Bunter simulation are shown as blue lines in Figure 8.16. The red box shows the extent and final dimensions of the new 3D model.

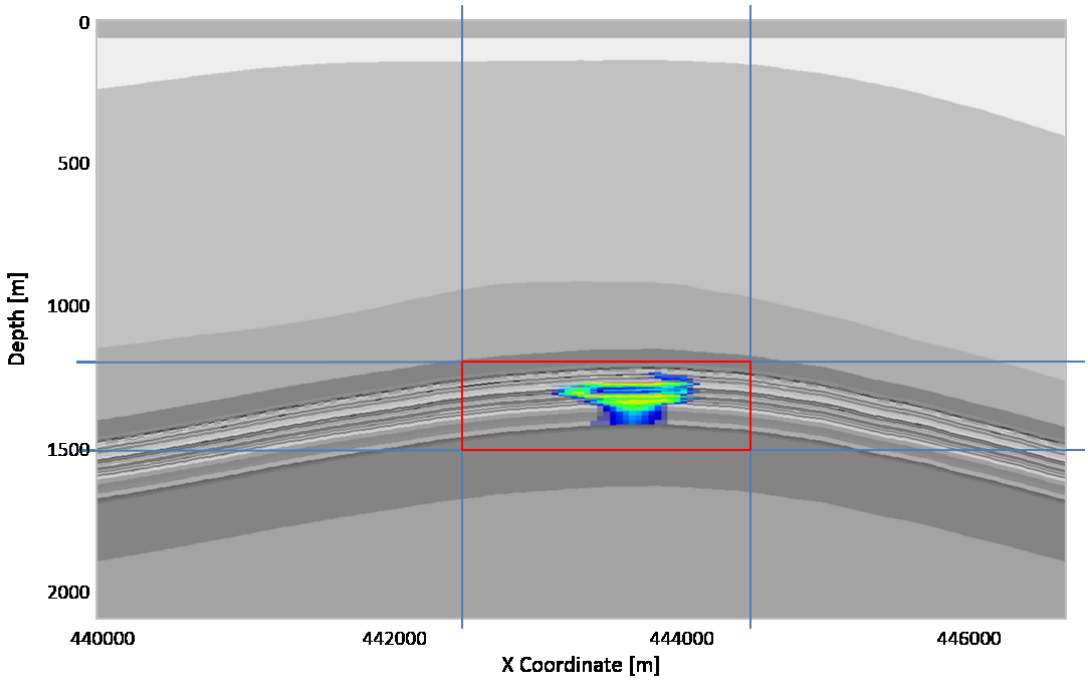

Figure 8.16. The new 3D Bunter Sandstone model is shown in red. X-coordinate has been reduced to 442500 – 444500m and the depth of the 3D model has been reduced to 1200 – 1500m.The blue lines represent the new coordinates. The simulated plume is shown for the 20 year simulation and shows the location of the plume with respect to the new 3D model dimensions. Vertical exaggeration of 3.

Upscaling of the reservoir model

As computational time increases with the number of cells in the model, upscaling of the 3D reservoir properties is required. Upscaling is the substitution of a region of fine grid cells with an equivalent region made up of coarser grid cells. Upscaling is performed for each of the cells in the coarse grid, where the reservoir properties are typically averaged.

The main priority is to ensure the new upscaled model consists of cell size dimensions as large as possible, without over-simplifying the simulated plume geometry and heterogeneity. In particular, the accumulations of CO_2 in each zone have to be present. An example of this is Figure 8.17 for the original 20 year Bunter simulation. CO_2

accumulations are modelled at the top of zone 4 and zone 3, as well as a free-phase migrating front in zone 2.

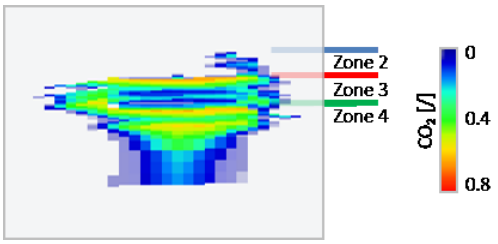

Figure 8.17. Original 20 year Bunter fluid-flow simulation result showing the distribution of CO_2 in the different zones in the reservoir. The main priority is to ensure the new upscaled model shows CO_2 accumulations in each zone.

The reduced 3D model has a total cell count of 1,067,872 cells with cell-size dimensions of 45m in the x and y coordinates, and 1 to 15m in the z coordinate. In order to decrease computational time, I test eight different models, each with different cell-size dimensions and total cell counts. These are detailed in Table 8.3.

Table 8.3. The eight different cell-size dimensions tested.

Cell-size dimensions (m)			**Total cells (count)**
x	y	z	
40	40	2	285000
80	80	2	71250
100	100	2	45000
150	150	2	19500
100	100	4	22500
100	100	6	15000
150	**150**	**4**	**9750**
150	150	6	6500

A 2D slice of the 3D simulated plume of the eight different upscaled models is shown in Figure 8.18. The upscaling process is clearly evident as the cell sizes are increased and the CO_2 saturations smoothed. The model of 150m by 150m by 4m cell dimensions, of total cell count 9750, was chosen as the three different zones are distinguishable. Two main accumulations are still modelled at the top of zone 3 and

4, while a migrating front in zone 2 of correct dimensions is still evident. The 150 by 150 by 6m model was discounted as the migrating front was smoothed to half the original size.

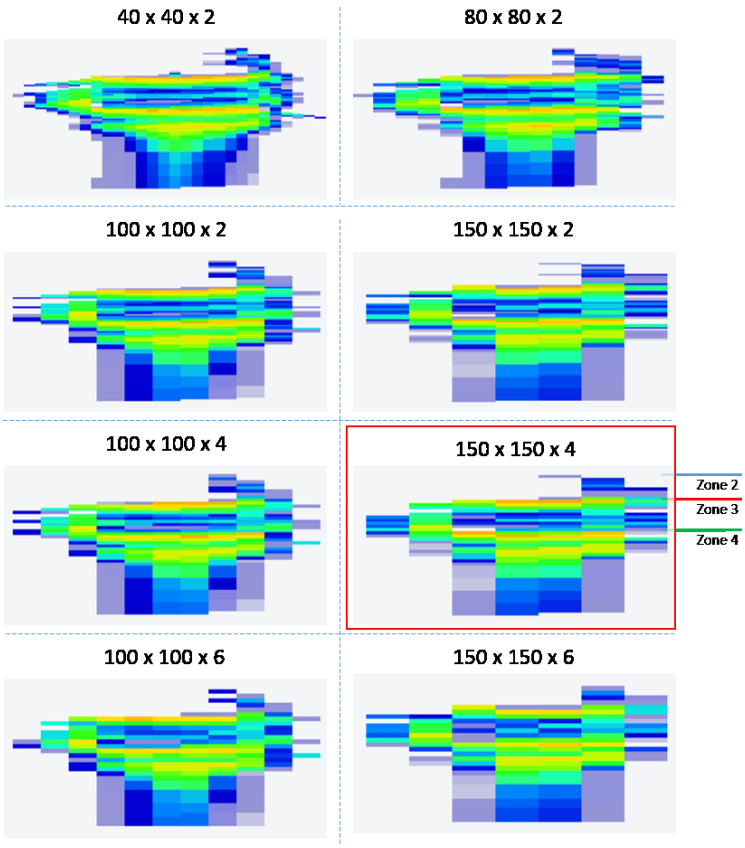

Figure 8.18. Comparison of the eight different upscaled models tested. The modelled plume is the 20 year Bunter simulation. The model of 150 by 150 by 4m cell dimensions, of total cell count 9750, was chosen as the three different zones are distinguishable clearly.

Figure 8.19 is a comparison of the original model of 45 by 45 by 1 to 15m cell size (left) and the new upscaled model of 150 by 150 by 4 m cell size.

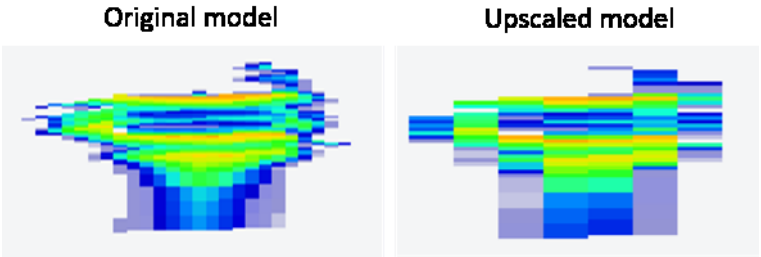

Figure 8.19. Comparison of the original model of 45 x 45 x 1-15m cell size (left) and the new upscaled model of 150 x 150 x 45 m cell size (right).

Background model simplification

Initial computational time for the upscaled model took 1.8 hours for a single shot. 32 cores were used. In order to reduce the computational time further, I average the calculated resistivity values of each formation in the 3D reservoir model using Archie's equation. The average resistivity value is then used for all the cells which do not contain any simulated CO_2. The heterogeneous resistivity values calculated for the CO_2 plume are not modified.

The average resistivity values for the three formations are:

- Base Cretaceous unconformity, 8 Ω.m
- Bunter Sandstone Formation, 2 Ω.m
- Bunter Shale Formation, 9 Ω.m

Figure 8.20 is a comparison of the upscaled model and the simplified model.

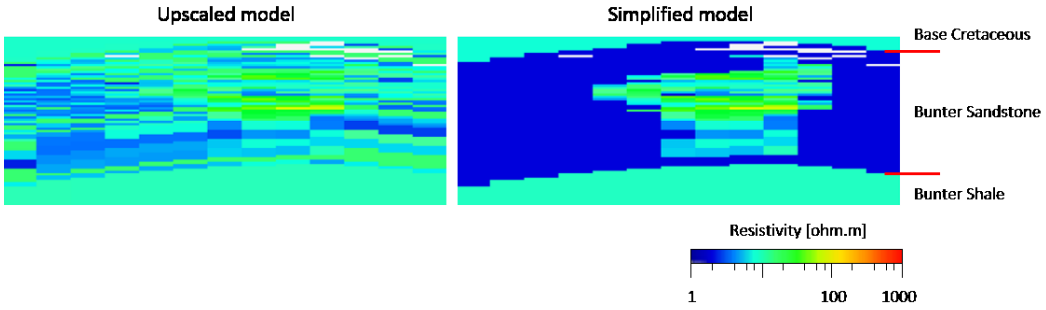

Figure 8.20. A comparison of the upscaled model and the simplified model. The simplified model contains average resistivity values for each cell with no CO_2. This ensures the heterogeneous resistivity values in the CO_2 plume are kept the same.

Figure 8.21 is a comparison of the calculated earth impulse response for the upscaled and simplified model. The black and blue curves represent the baseline model. The green and red curves represent the CO_2 model. A comparison of the percentage change between the baseline model and the CO_2 model for both the upscaled models (Figure 8.21 left) and simplified models (Figure 8.21 right) is detailed in Table 8.4. The computational time for the simplified model for a single shot took 54 min, reducing

computational time by 51%. The difference in the change in recorded amplitude was 11.5% when comparing the upscaled model with the simplified model.

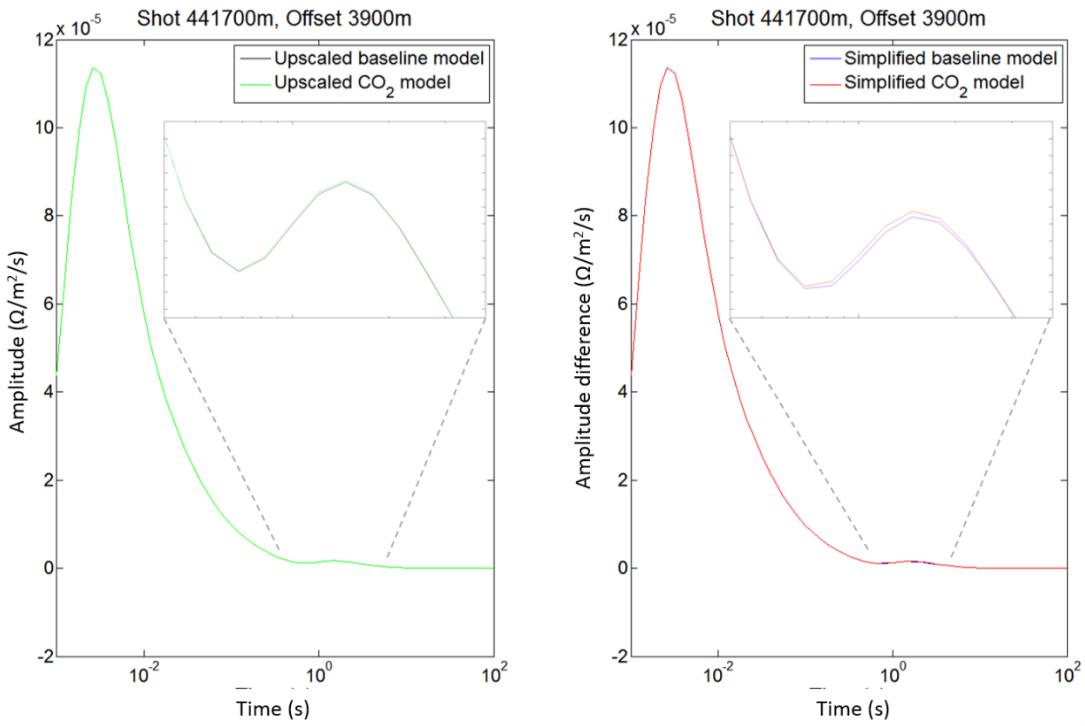

Figure 8.21. Comparison of the calculated earth impulse response for the upscaled and simplified models. The black and blue curves represent the baseline model with no CO_2. The green and red curves represent the CO_2 model after 20 simulated years.

Table 8.4. A comparison of the computational time and modelled amplitude of the upscaled and simplified model. Simplifying the model decreased computational time by 51% and resulted in a change in amplitude of 11.5% at 1.5 seconds.

Models	**Comp-time**	**Amplitude at 1.5 s**	
	min	*Baseline*	*Zone2*
Upscaled	111	1.74E-06	1.75E-06
Simplified	54	1.54E-06	1.57E-06
% change	51%	11.5%	11.5%

8.4.2 Fluid-flow and rock physics model

Following the simplification of the Bunter Sandstone fluid-flow simulation results, I apply the monitorability workflow to assess the ability of CSEM to monitor the three stages in plume growth and evolution, as detailed in Chapter 6. 2D snapshots of the 3D plume for the three stages are shown in Figure 8.22, along with a histogram detailing the change in resistivity between the monitor survey and the baseline survey. Resistivity values are calculated for each cell using Archie's equation, as detailed in Chapter 4.

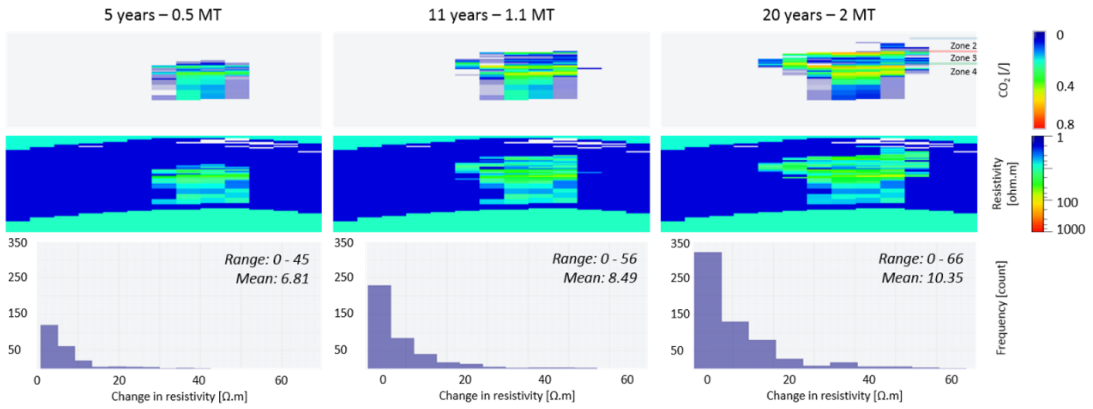

Figure 8.22. 2D snapshots of the 3D simulated plume for the three simulated stages. Top row is showing the CO_2 saturation distribution in the Bunter reservoir. The middle row is showing the calculated resistivity values using Archie's equation. The bottom show are histograms detailing the change in calculated resistivity with respect to the baseline for each model.

Interestingly, the mean change in resistivity is calculated at only 6.8 Ω.m after 5 years, reaching a maximum of 45 Ω.m. The mean change in resistivity is only 4 Ω.m greater than the background resistivity for the Bunter Sandstone formation. After 11 years this increases to a mean of 8 Ω.m with a maximum of 56 Ω.m. After 20 years, the mean resistivity is 10 Ω.m, with a maximum change in resistivity of 66 Ω.m.

The 3D resistivity models are then input into PEMrad to model the impulse response.

8.4.3 MTEM method

I simulate the earth's impulse response for each model using PEMrad (Drakengren, 2008). For each scenario, the 3D resistivity model is placed in a 1D background of 1 Ω.m half-space (Figure 8.23). 66m of sea-water with a resistivity of 0.3 Ω.m is assumed for each scenario. The 2D survey acquisition parameters are detailed in Table 8.5.

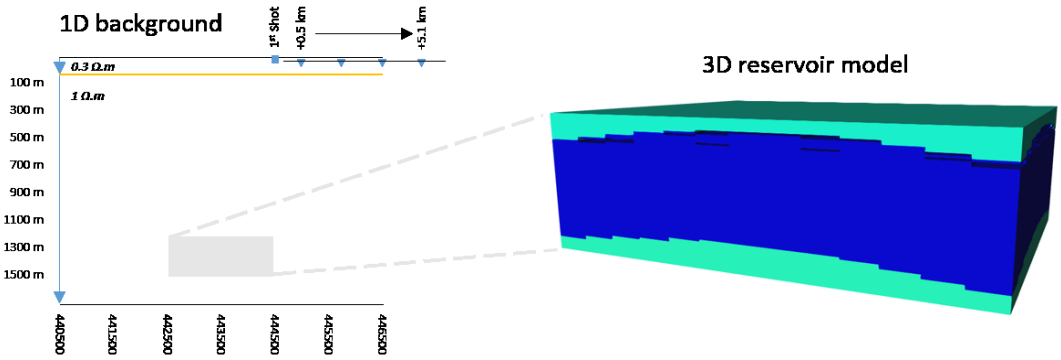

Figure 8.23. 1D background used in this study (left). The 3D reservoir is placed in the 1D background.

Table 8.5. 2D acquisition parameters for the Bunter Sandstone MTEM study. Coordinates are in the x dimension. The 2D survey was acquired across the middle of the plume at y-coordinate 5989250.

Acquisition parameters			
Source	First shot	444500	m
	Last shot	437300	m
	Spacing	200	m
	Number of shots	37	-
	Depth	10	m
	Strength	2.16 million	A.m
	Frequencies	0.0001 to 10000	Hz
	Times	0.001 to 100	Sec
Receiver	Min-offset	500	m
	Max-offset	5100	m
	Spacing	200	m
	Number of receivers	24	-
	Depth	40	m

Figure 8.24. shows the calculated earth impulse responses (left) and time-lapse amplitude changes (right) for shot coordinate 441700m and offset 3900m. The black curve is the baseline model with no CO_2, the red curve is the 5 year simulation, green curve is the 11 year simulation and the blue curve is the 20 year simulation. Clearly evident is the increase in amplitude between each simulation. A comparison of the time-lapse amplitude arrival times of the three simulations shows no change (Figure 8.24. right).

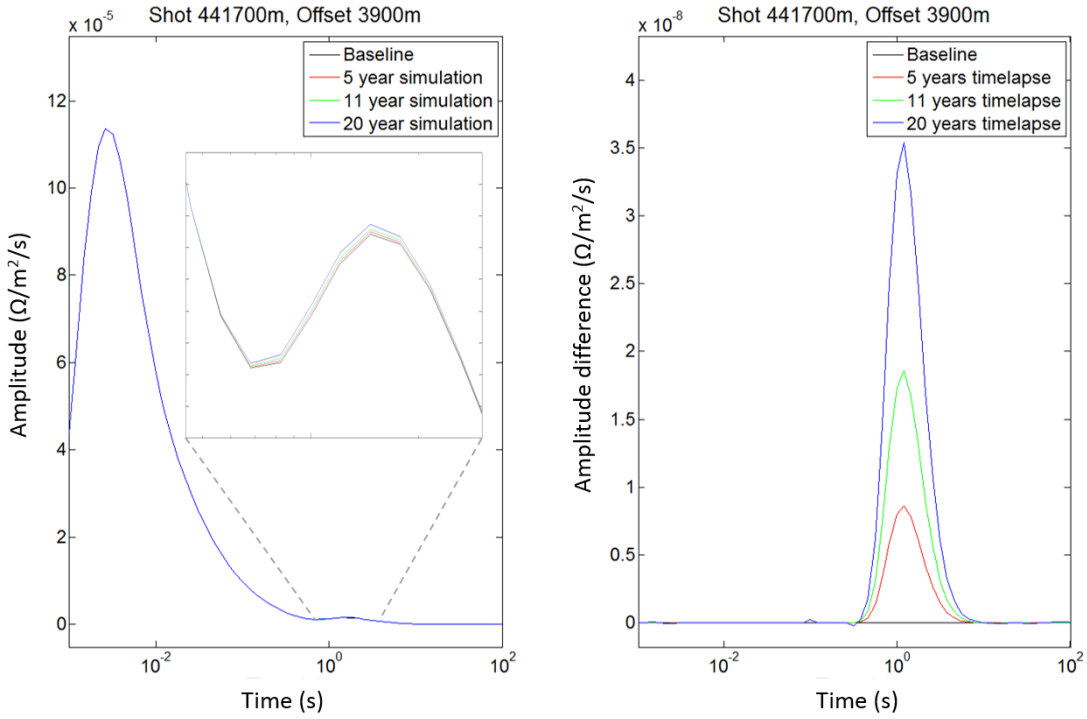

Figure 8.24. Earth impulse responses (left) and time-lapse response with the baseline (right) of the modelled simulations: no CO_2 layer (black); 5 year simulation (red); 11 year simulation (green); 20 year simulation (blue). The grey box is a close-up image of the change in amplitude. Note the increase in amplitude with each simulation.

8.5 Discussion

8.5.1 Monitorability of plume growth in the Bunter reservoir

Lessons learnt from the CO_2 migration study show that vertical CO_2 migration should result in earlier arrival times of the simulated impulse response. However, all that is modelled between the different surveys is an increase in amplitude (Figure 8.24). Clearly evident from Figure 8.22 is the vertical and lateral migration of the CO_2 plume with time.

This suggests that CSEM can be used to monitor lateral migration of CO_2 in the Bunter Sandstone reservoir. However, vertical migration is shown to be difficult to monitor as the movement of CO_2 from zone 4 to zone 2 was not detected. The migrating distance between each of the zones is 35m.

The modelled time-lapse impulse response data is displayed as a series of common-offset sections for the 5 year (Figure 8.25), 11 year (Figure 8.26) and 20 year simulation results (Figure 8.27). I display four offsets: 900m, 1500m, 2100m and 2700m. The source-receiver midpoint is the horizontal coordinate and time is the vertical coordinate. The presence of the CO_2 plume is imaged clearly at the modelled coordinates for each simulated time. However, a comparison of the earth impulse responses of the three models shows very small to no differences.

There are two main reasons for this. First, all three models have very similar time-lapse amplitude arrival times, therefore each plume will be imaged at the same measured time when displayed as common-offset sections. This is demonstrated in Figure 8.28 by comparing the simulated amplitude versus offset of each simulation. There are very small differences between the three responses. Second, the time-lapse amplitude changes of the three models are very small. A closer look at the maximum amplitude time-lapse change with respect to baseline shows a change in amplitude of only 0.52% after 5 years, 1.10% after 11 years and 2.01% after 20 years (Table 8.6).

Although I have modelled and imaged the CO_2 plume clearly, it is important to mention that it is highly unlikely that a change in amplitude of 2.01% after 20 years

will result in a detectable change in the field using towed-streamer CSEM. The deployment of stationary receivers at the sea-bottom, along with a stationary source, could increase detectability. Ziolkowski et al., (2010) showed that a 4% change between two datasets can be achieved using stationary sea-bottom receivers. To increase the signal-to-noise ratio, the operator can collect data for a long period of time, allowing the impulse response from a whole sequence of MTEM recordings to be summed. The signal enhances relative to the noise as the signal is the same every time, but the noise is different.

Table 8.6. Peak earth impulse response for each model and the percentage change with respect to baseline.

Models	Amplitude at 1.5 s	% change
Baseline	1.542E-06	-
5 year	1.550E-06	0.52%
11 year	1.559E-06	1.10%
20 year	1.573E-06	2.01%

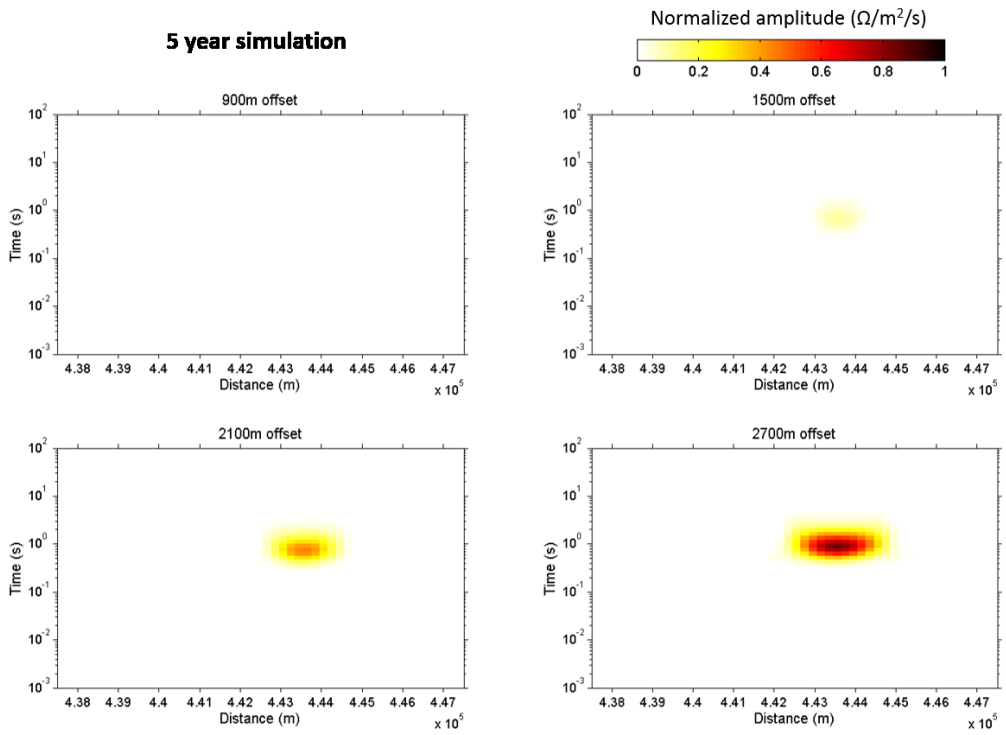

Figure 8.25. Time-lapse common-offset sections of the earth's impulse response for the 5 year simulation. The horizontal coordinate is the midpoint while the vertical coordinate is time.

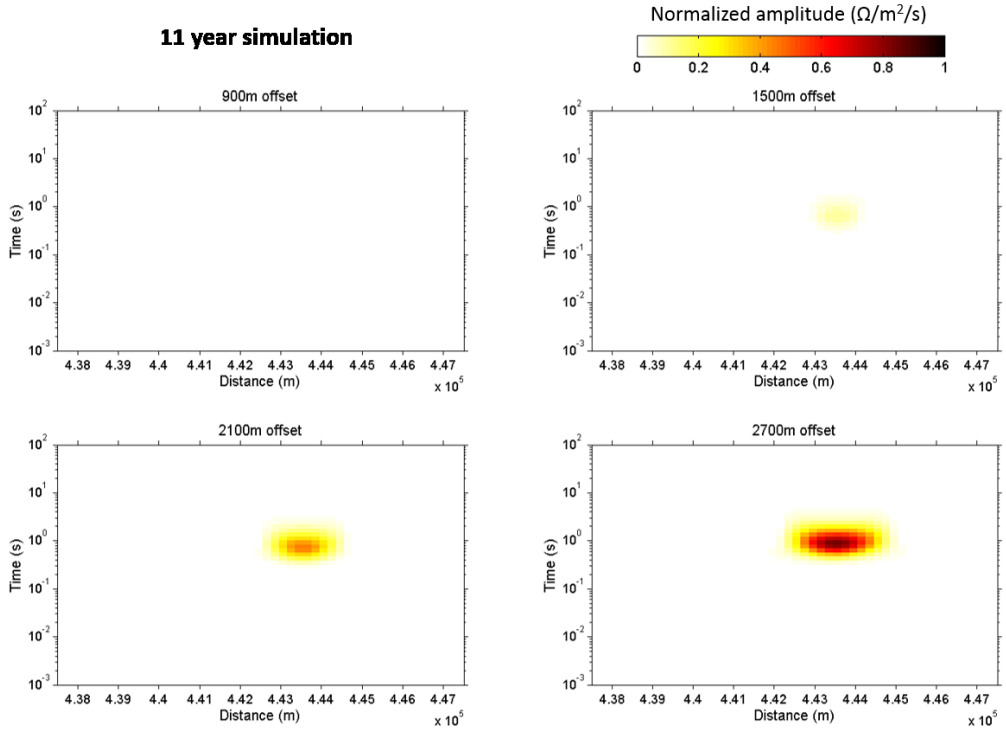

Figure 8.26. Time-lapse common-offset sections of the earth's impulse response for the 11 year simulation. The horizontal coordinate is the midpoint while the vertical coordinate is time.

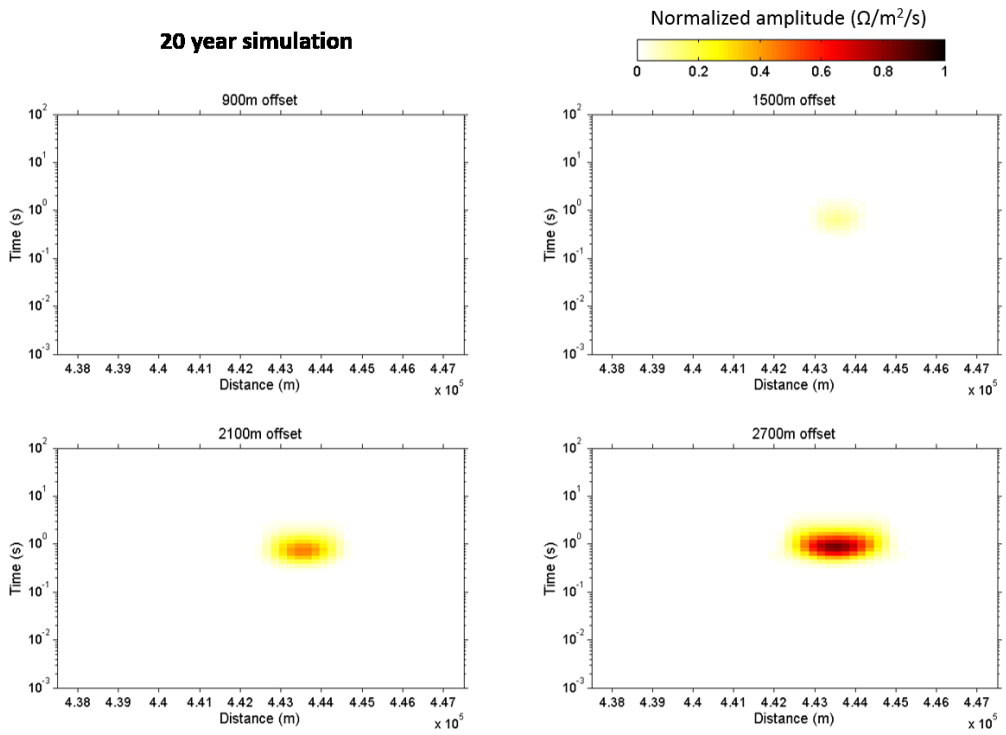

Figure 8.27. Time-lapse common-offset sections of the earth's impulse response for the 20 year simulation. The horizontal coordinate is the midpoint while the vertical coordinate is time.

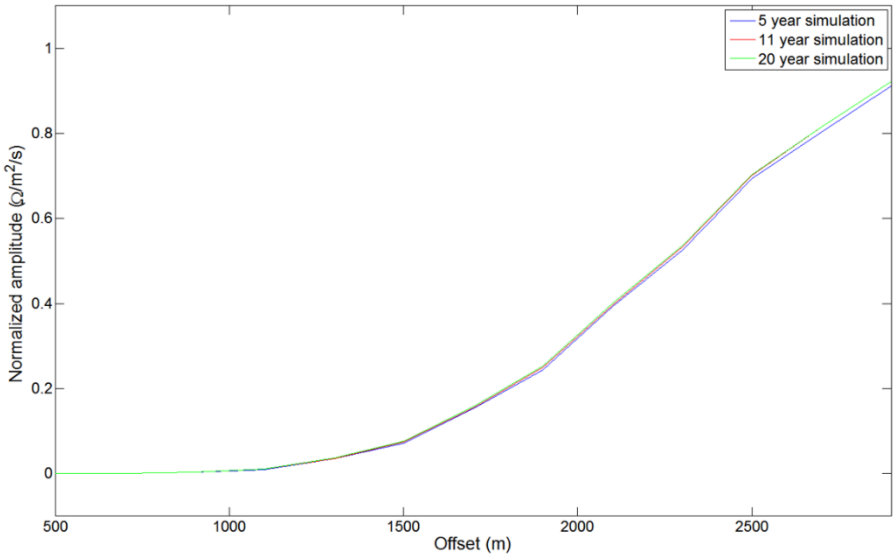

Figure 8.28. A comparison of the normalized amplitude versus offset for the 5 year simulation (blue), 11 year simulation (red) and 20 year simulation (green). The amplitude is measured at midpoint 443500m and time 0.82s. There are very little to no differences between the three responses.

8.5.2 Sensitivity of the resistivity model

The small changes in amplitude can be explained due to the resistivity models used to generate the synthetic response. After 20 years, the simulated CO_2 plume had a mean change in resistivity of 10.35 Ω.m, with a maximum of 66 Ω.m. The modelled baseline resistivity of the Bunter Sandstone was 2 Ω.m. The mean change in resistivity is only 8.35 Ω.m greater than the baseline resistivity. This can be explained by looking at the relationship between resistivity and CO_2 saturation.

Using Archie's equation, I calculate resistivity values as a function of CO_2 saturation for a theoretical reservoir with 20% porosity with brine resistivity of 0.33 Ω.m (Figure 8.29). Figure 8.29(a) represents the maximum change in resistivity assuming 100% CO_2 saturation. However, simulated CO_2 saturations are constrained by relative-permeability and capillary pressure curves. As explained in Chapter 5, the Cardium Sandstone relative-permeability and capillary pressure curves were used for the Bunter Sandstone simulations. The curves assume 20% irreducible water saturation, which meant S_{max} = 80%. The Bunter simulation after 20 years had a maximum saturation of 62% which resulted in a maximum change in resistivity of 66 Ω.m. The calculated resistivity curves in Figure 8.29(a) are modified to account for the maximum saturation at 62% after 20 years (Figure 8.29(b)) and maximum CO_2 saturation due to irreducible water saturation at 80% Figure 8.29(c)).

An advantage of EM techniques is that the change in resistivity, when comparing a baseline survey with a monitor survey, may be an order of magnitude or more. However, as Figure 8.25 demonstrates, this might not be the case for CCS monitoring. An increase in resistivity of an order of magnitude is associated with CO_2 saturation at only 75%. Due to irreducible water saturation, the maximum change in resistivity in a reservoir will be 150 Ω.m. Changes in resistivity of the order of 2 to 3 magnitudes are associated only with CO_2 saturations greater than 95%, which is not possible.

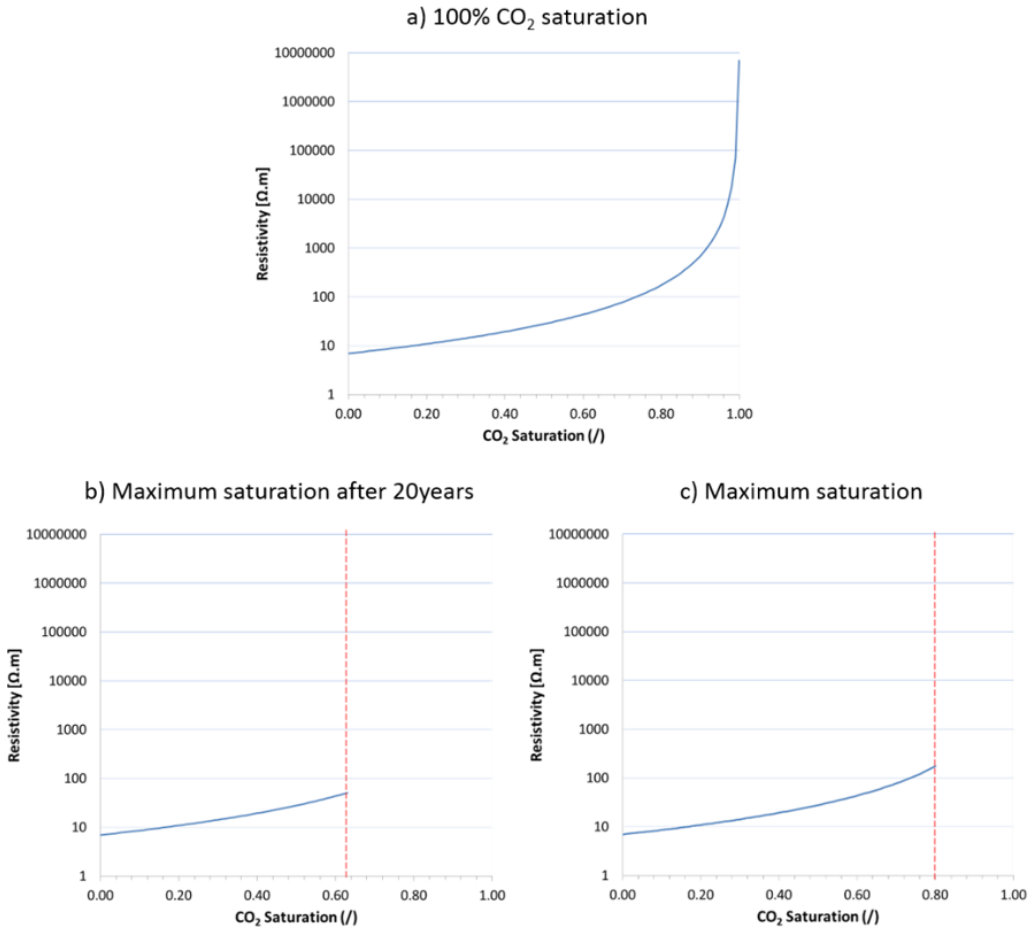

Figure 8.29. Resistivity as a function of CO_2 saturation for a theoretical sandstone with porosity of 20% and brine resistivity of 0.33 Ω.m. Calculated assuming 100% saturation (a), maximum saturation of 62% after 20 years (b) and maximum saturation of 80% due to irreducible water saturation (c).

8.6 Conclusions

The results from the modelling undertaken in this chapter demonstrate the potential of CSEM to detect CO_2 injected in the subsurface. Five guidelines are suggested when interpreting the time-lapse response due to CO_2 migration using the MTEM method:

1) A baseline survey is critical when imaging and detecting a CO_2 plume;
2) The injection of CO_2 into the subsurface will result in an increase in the amplitude of the earth impulse response;
3) A change in amplitude with no change in arrival time will indicate lateral migration;
4) An increase in amplitude along with an earlier arrival time will indicate vertical migration, and a potential loss of containment;
5) Vertical migration of CO_2 will be imaged at shorter offsets.

The modelling results on the Bunter Sandstone model demonstrate the potential of CSEM to monitor plume growth and evolution in the reservoir. The synthetic responses resulted in a change in amplitude when compared with the baseline survey with no CO_2. No change in arrival time was interpreted, even though the modelled plume showed vertical and lateral migration with time. This suggests that CSEM deployed at the Bunter Sandstone reservoir could monitor lateral CO_2 migration in the order of 150m, however vertical migration of small distances, such as 30m, will be undetectable.

However, the simulated time-lapse responses resulted in a change in amplitude of only 2% after 20 years. In the field, a change in amplitude of such a degree will most likely be undetectable. This is related to the simulated CO_2 plume saturations and the calculated resistivity values. For this reason, the deployment of towed-streamer CSEM at the Bunter reservoir might not be suitable for CCS monitoring. Instead, the deployment of stationary sea-bottom source and receivers is recommended when monitoring subsurface CO_2 migration.

Summary

I demonstrate the potential of CSEM to detect CO_2 injected in the subsurface by modelling the synthetic response in the time-domain through the application of the MTEM method. First, I calculated the earth impulse response to injected CO_2. Second, I related the change in time-lapse amplitude to CO_2 at different depths and lateral extents; an analogue to lateral and vertical migration. Third, I applied the monitorability workflow to generate synthetic earth impulse responses to three stages in CO_2 plume growth and evolution in the Bunter Sandstone model. The synthetic responses demonstrated the ability to detect lateral CO_2 migration. However, as the change in amplitude was only 2% after 20 years, it is highly unlikely that the CO_2 plume will be detectable in the field using towed-streamer CSEM.

9. Discussion and conclusions

9.1 Findings

This thesis assesses the CO_2 monitorability of seismic and CSEM. This is achieved through the development of a monitorability workflow which describes a numerical modelling approach to model variations in synthetic time-lapse responses due to CO_2 migration. The workflow is flexible and can be adapted for both seismic and CSEM to model variations in the time-lapse signal through the application of fluid-flow modelling, rock physics modelling and geophysical forward modelling. The focus of the workflow is the understanding of the interplay between CO_2 distribution, the geophysical response and geological heterogeneity.

The monitorability workflow can be used to perform detailed feasibility studies during initial storage-site assessment stages. Application of the workflow can determine whether the injected CO_2 will generate an interpretable geophysical response. This is important, as unsuccessful acquisitions can have negative impacts on the reputation of a monitoring method. A prime example of this is the CSEM survey acquired over the Sleipner CCS site. Due to a lack of a true baseline, the inconclusive results negatively impacted the applicability of CSEM at other CCS sites. A proper feasibility study can minimise failures. Furthermore, the application of the workflow during and after CO_2 injection can facilitate the interpretation of processed data and assist in history matching. The application of the workflow has been demonstrated throughout the thesis.

First, I assessed the ability of surface seismic methods to monitor CO_2 plume growth and evolution in three storage scenarios: a homogeneous saline reservoir, a heterogeneous saline reservoir, and a depleted gas field. A key contribution of the seismic monitoring study is to account for, and understand, the saturation scales and phase distributions which could be encountered. To account for the uncertainties regarding the fluid saturation distribution in the reservoir, I modelled the two end-member rock-physics models – uniform and patchy saturation – in order to generate the widest range of velocity distributions which could be encountered. I demonstrated the ability of seismic methods to image CO_2 plume growth and

evolution in the Bunter Sandstone saline reservoir and highlighted clear differences between the rock-physics models. The Bunter Sandstone reservoir is a potential CO_2 storage reservoir in the UK sector of the North Sea. The Bunter Sandstone model was then modified to depict a depleted gas field by adding 20% residual gas saturation. I assessed the importance and implication of patchy saturation and presented results which suggest that seismic methods may be able to detect CO_2 injected into depleted hydrocarbon fields. Figure 9.1 summarises the seismic monitorability workflow.

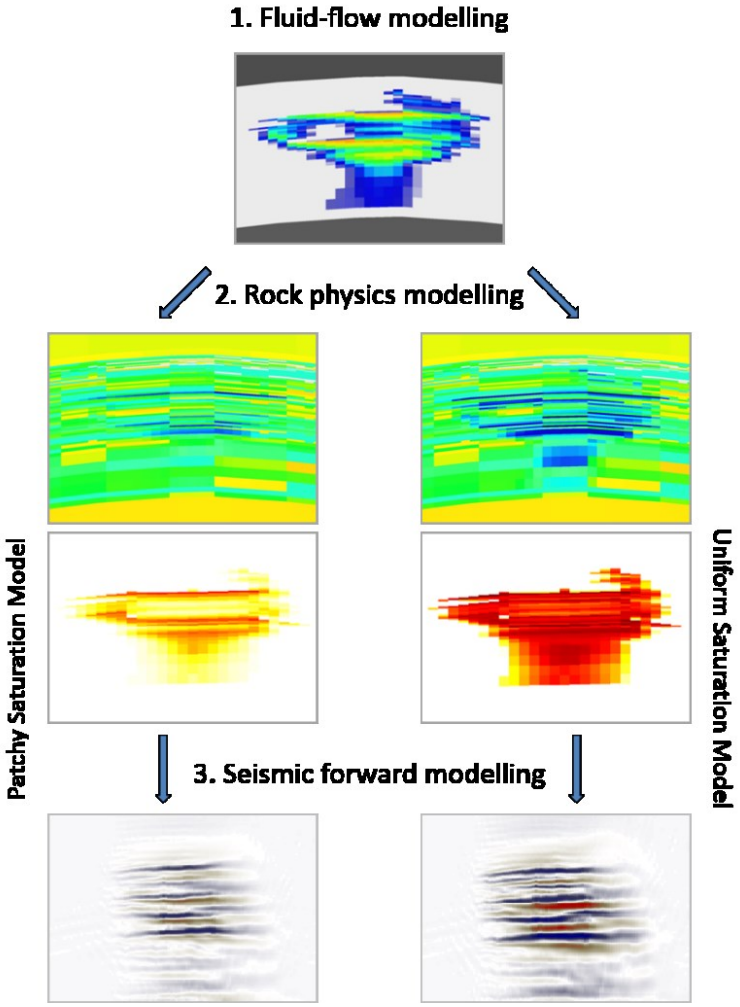

Figure 9.1. Summary of the seismic monitorability workflow for the Bunter Sandstone heterogeneous study.

Second, I conducted a feasibility study, simulating the time-lapse broad-bandwidth CSEM time-domain response of CO_2 migration following the multi-transient electromagnetic (MTEM) method. I modelled the impulse response to a simple

homogeneous 3D CO_2 body, relating the change in time-lapse amplitude to CO_2 accumulated at different depths and lateral extents; an analogue to lateral and vertical migration. The ability of CSEM to detect CO_2 plume growth and evolution within the heterogeneous Bunter Sandstone reservoir model was then assessed. I demonstrated the potential of broad bandwidth CSEM to monitor stored and migrating CO_2 and presented the synthetic results as time-lapse common-offset impulse response sections. Figure 9.2 summarises the CSEM monitorability workflow.

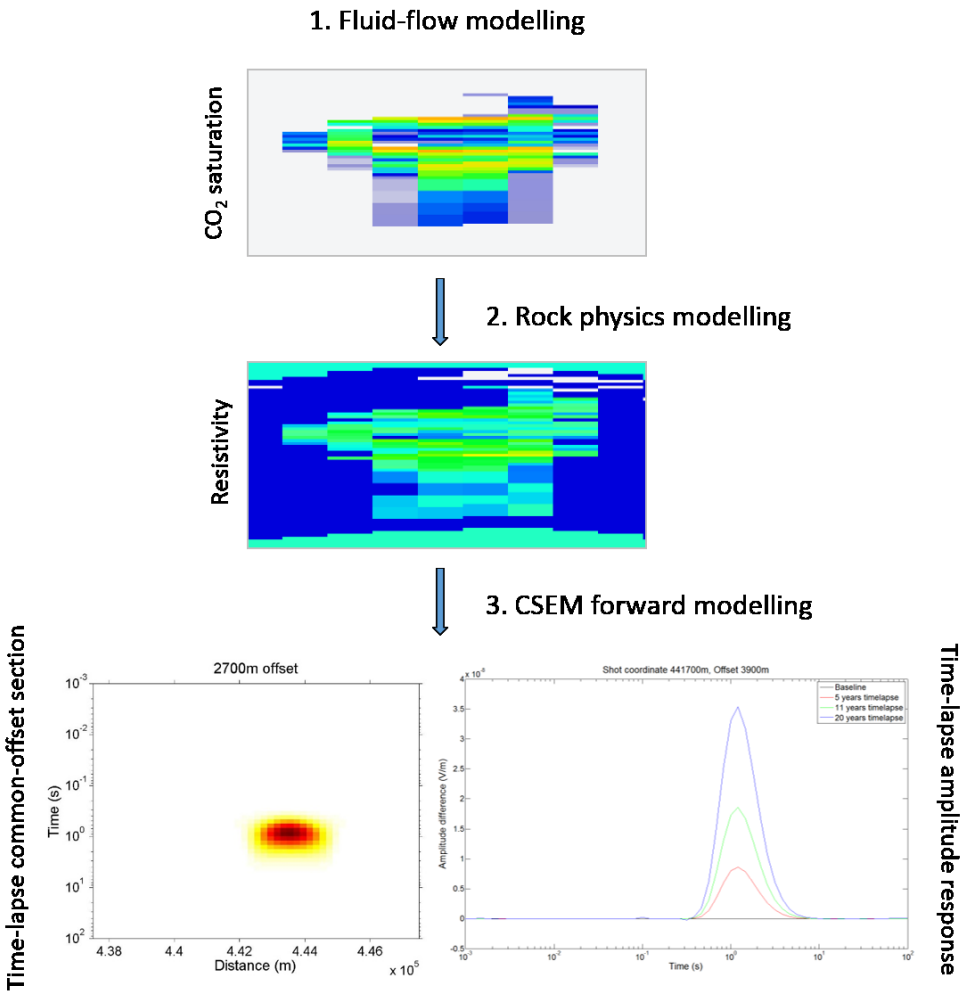

Figure 9.2. Summary of the CSEM monitorability workflow for the Bunter Sandstone study.

9.2 Implications

9.2.1 Containment assurance: Monitorability of CO_2 migration.

A key contribution of this thesis is the assessment of seismic and CSEM to detect a loss of containment, in particular a migrating front of CO_2. The ability to detect a migrating front of CO_2 is critical to the successful demonstration of containment. A migrating front of CO_2 consists of lower pore-saturations which are not immobilized by residual or structural trapping. The detection of movement in the reservoir, in particular if outside the primary storage reservoir or storage complex, could allow the possibility of an early warning should a breach in containment occur.

Seismic monitoring of a migrating front remains challenging due to uncertainties regarding the pore-scale distribution of fluids in the reservoir, and in turn, the most appropriate rock-physics model to simulate this: uniform or patchy saturation. Modelling both rock-physics models generated the widest range of velocity distributions which could be encountered.

First, I modelled a migrating front in a homogeneous reservoir (Chapter 5). A pathway was prescribed along which the CO_2 migrated from the primary to the secondary storage reservoir, simulating a loss of containment. Analysis of the synthetic seismic sections showed no change in amplitude in the secondary reservoir in either the patchy or uniform time-lapse sections (Figure 9.3). Second, I modelled a migrating front in a heterogeneous reservoir (Chapter 6). CO_2 was injected into the Bunter Sandstone reservoir and was allowed to migrate vertically through each zone. The simulated migrating front was interpreted in zone 2 after 20 simulated years. Analysis of the synthetic seismic sections showed no change in amplitude corresponding to the migrating front of CO_2. This suggested that the detection of a free-phase migrating front of CO_2 is dependent predominantly on its spatial geometry. An increase in the lateral size of the CO_2 plume resulted in a detectable response on the synthetic seismic sections (Figure 9.4). This suggests that seismic methods can detect a migrating front of CO_2 when a particular threshold in plume-geometry has been reached. For the Bunter Sandstone reservoir, an increase in lateral

migration of 300m resulted in a clear change in amplitude assuming a uniform saturation model. The patchy model also resulted in a change in amplitude, although not as obvious. This suggests that once the size of the migrating front of CO_2 crosses a particular threshold in plume geometry, the pore-fluid saturation distribution – patchy or uniform – will play an important role. It is important to mention that the generated synthetics represent noise-free time-lapse responses. It is always possible that the presence of noise could result in the migrating front becoming undetectable.

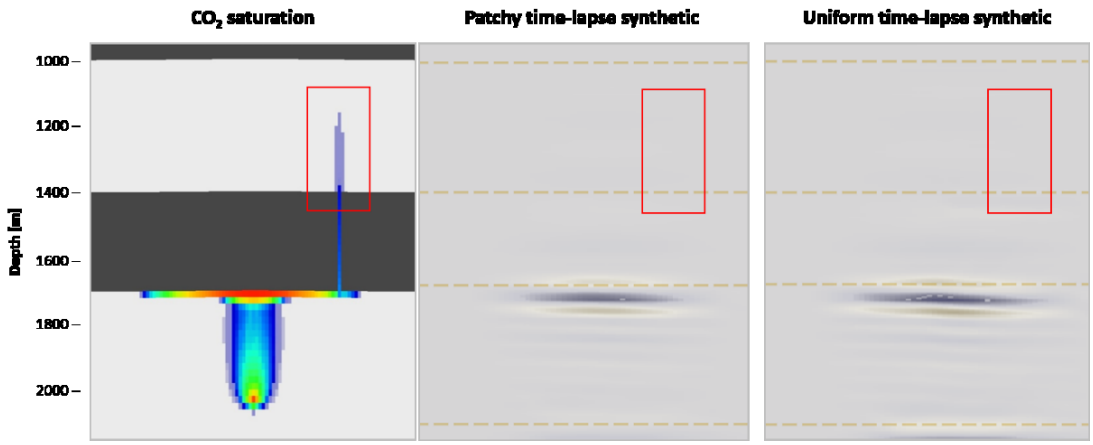

Figure 9.3. Migrating front of CO_2 modelled in a homogenous reservoir (Chapter 5). The location of the migrating front is highlighted in the red square. No change in amplitude is interpreted corresponding to the CO_2 plume in either patchy or uniform models.

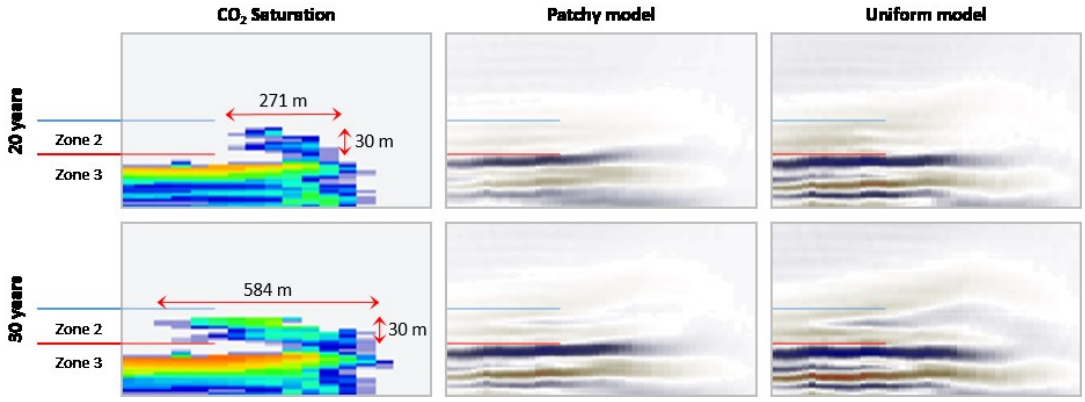

Figure 9.4. Migrating front of CO_2 in zone 2, modelled in a heterogeneous reservoir (Chapter 6). An increase in lateral size of the plume was required for it to be detectable.

Interestingly, the ability of seismic methods to detect a migrating front of CO_2 in a depleted hydrocarbon field yielded contrasting results. When assuming a patchy saturation distribution, low saturations of CO_2 –associated with CO_2 migration or a loss of containment – were modelled to result in the largest change in velocity, while high saturations of CO_2 – associated with structural trapping – were modelled to result in a decrease in amplitude with time. This suggests that, should a loss of containment occur, a migrating front of CO_2 will be detected easily from the outset.

The ability of CSEM to detect CO_2 migration was demonstrated for the first time following the MTEM method. In order to understand the expected response, I modelled the CO_2 time-lapse response in the time-domain, gradually increasing the width and depth of the CO_2 plume. Vertical CO_2 migration was modelled to result in a change in amplitude and arrival time. Lateral CO_2 migration was modelled to result in a change in amplitude only. Having understood the expected time-lapse responses, I assessed the ability of CSEM to detect a migrating front of CO_2 in the Bunter Sandstone model. Analysis of the synthetic time-lapse response showed a change amplitude only, with no change in arrival time. This suggested that the deployment of CSEM at the Bunter Sandstone reservoir will detect lateral CO_2 migration in the order of 150m, however vertical migration of small distances, such as 30m, will be undetectable. However, the simulated time-lapse responses resulted in a change in amplitude of only 2% after 20 years when compared with the baseline survey. This was attributed to the simulated CO_2 plume and the calculated resistivity values. For this reason, a recommendation was made that the deployment of towed-streamer CSEM at the Bunter reservoir might not be suitable for CCS monitoring.

It is important to note that the detection of a migrating front of CO_2 is a site-specific issue which depends not only on the geophysical parameters of the seismic or CSEM survey, but also on the geological variations and spatial distribution of the CO_2 in the reservoir. For example, the fluid saturations are controlled by the relative permeability and capillary pressure curves input into the simulation. Different curves may calculate a greater range of CO_2 saturations, and therefore, a greater change in

velocity or resistivity. Assessing these site-specific variations through the application of the monitorability workflow (Chapter 4) during initial storage-site assessment stages, could provide valuable information regarding the ability to detect CO_2 migration.

9.2.2 Conformance assurance: Inversion and quantification of CO_2

There are different types of inversions to solve distinct types of problems (Barclay et al., 2007). For seismic inversion and quantification of CO_2, the model-based approached, through iterative forward modelling, is appropriate. Model-based seismic inversion can be considered as the inverse of seismic forward modelling.

Model-based seismic inversion involves forward modelling of seismic signatures of an earth model with an assumed spatial distribution of velocity and density (Dvorkin et al., 2014). This process starts with an elastic model which is gradually modified to minimize the difference between the synthetic seismic response and the real data. This is a trial and error process; nothing is done to the actual data in an inversion scheme. When quantifying the amount of CO_2 in the reservoir, inversion aims to understand the range of models of CO_2 saturations that are consistent with the data. In order to allow for an accurate estimation of the saturation, it is necessary to know the quantitative relationship between fluid saturation and seismic characteristics. This is to reduce quantification uncertainty.

The elastic model is calculated using Gassmann's equation; typically assuming uniform saturation. However, the generation of an elastic model of the subsurface is an issue of non-uniqueness. As I have demonstrated, a large range of saturations can be associated with a single velocity. Patchy and uniform saturation represent the upper and lower bounds of seismic velocity.

This is demonstrated in Figure 9.5. A velocity of 2850 m/s can be associated with CO_2 saturations ranging from 9% to 58%. This has significant implications for CO_2 quantification from seismic velocities, as it highlights the level of uncertainty which can be encountered. Assuming a uniform saturation could underestimate the amount

of stored CO_2 in the reservoir. This could explain why Chadwick et al., (2005) underestimated the total amount of injected CO_2 in the Utsira Formation: the elastic model was calculated assuming a uniform saturation distribution. By assuming a patchy saturation distribution, a more appropriate account for the injected CO_2 might be possible.

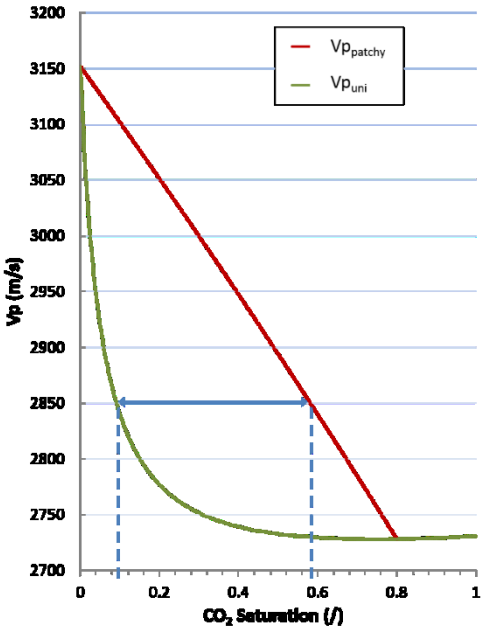

Figure 9.5. P-wave velocity as a function of CO_2 saturation calculated assuming a uniform saturation model (Vp_{uni}) and a patchy saturation model (Vp_{patchy}). The blue arrow represents the large range in CO_2 saturations which are associated with a velocity of 2850 m/s.

A recommendation would be to perform seismic inversion and CO_2 quantification assuming both patchy and uniform saturation. As both end-members are assumed, a maximum and minimum CO_2 estimate can be calculated.

CO_2 injection into depleted hydrocarbon reservoirs raises further questions regarding 4D seismic quantification. As demonstrated in Chapter 7, initial CO_2 injection will result in a large increase in velocity, enabling the CO_2 to be imaged clearly from the outset. However, with time and increasing saturation, a transition from the patchy to uniform bounds can be expected. This transition will decrease the time-lapse amplitude response with time, gradually making the CO_2 plume harder to detect when compared with the baseline. This has important implications for quantifying

the amount of CO_2 stored in the reservoir, as with time, the CO_2 plume will become 'invisible' as it accumulates and is structurally trapped. This suggests that CO_2 injected into depleted gas fields will be difficult to quantify seismically once structurally trapped.

9.2.3 Transition from patchy to uniform state

I have demonstrated the linear transition in velocities from patchy to uniform bounds with increasing time. This represents a transition in reservoir fluid pore-pressure equilibrium; from an unrelaxed to a relaxed state. The relaxation states are dictated by hydraulic diffusivity and diffusion length and are related to the pore-fluid saturation end-members through the diffusion or critical length scale (L_c). L_c suggests the spatial scale over which wave-induced increments of pore-pressures can reach equilibrium during a period of a seismic wave (Mavko and Mukerji, 1998). The critical factor determining these ranges is the size of saturation heterogeneity, or saturation 'patch', d. This is discussed in detail in Chapter 4, section 3.

Figure 9.6 describes the transition from a patchy, unrelaxed state to a uniform, relaxed state by relating the change in saturation heterogeneity (left) to the change in velocity with increasing saturation (right). At a frequency of 10 Hz, the critical length scale is 0.4 m. This suggests that the reservoir is in a relaxed state (uniform saturation) when $d < 0.4$ and an unrelaxed state (patchy saturation) $d > 0.4$. The transition from an unrelaxed to a relaxed state occurs at $d \approx 0.4$.

During injection, the initial CO_2 front will consist of spatially varying saturation distributions which arise due to variations in porosity, permeability, wettability and grain types. Therefore, as the front is migrating, the size of saturation heterogeneity will be much greater than L_c (Figure 9.6, Step 1). As $d >> L_c$, the reservoir is in an unrelaxed state. There is not enough time for pressure equilibration during a seismic period, resulting in patches of rock which remain at different pressures. This increases the stiffness of the reservoir; returning higher velocities closer to the patchy bound.

As the CO_2 migrates and begins to accumulate below a seal, pore-saturations will increase. An increase in pore-saturation will decrease d. Assuming an area consisting of 50% water saturation and 50% CO_2 saturation, d will be slightly greater than L_c (Figure 9.6, Step 2). $d < L_c$ once the CO_2 is completely trapped below a seal at maximum saturation (Figure 9.6, Step 3). At this scale, wave-induced pressure oscillations between the different fluid phases have sufficient time to flow and relax, reaching a local isostress during a seismic period. This results in a less stiff porous rock which in turn results in lower wave velocities closer to the uniform bound.

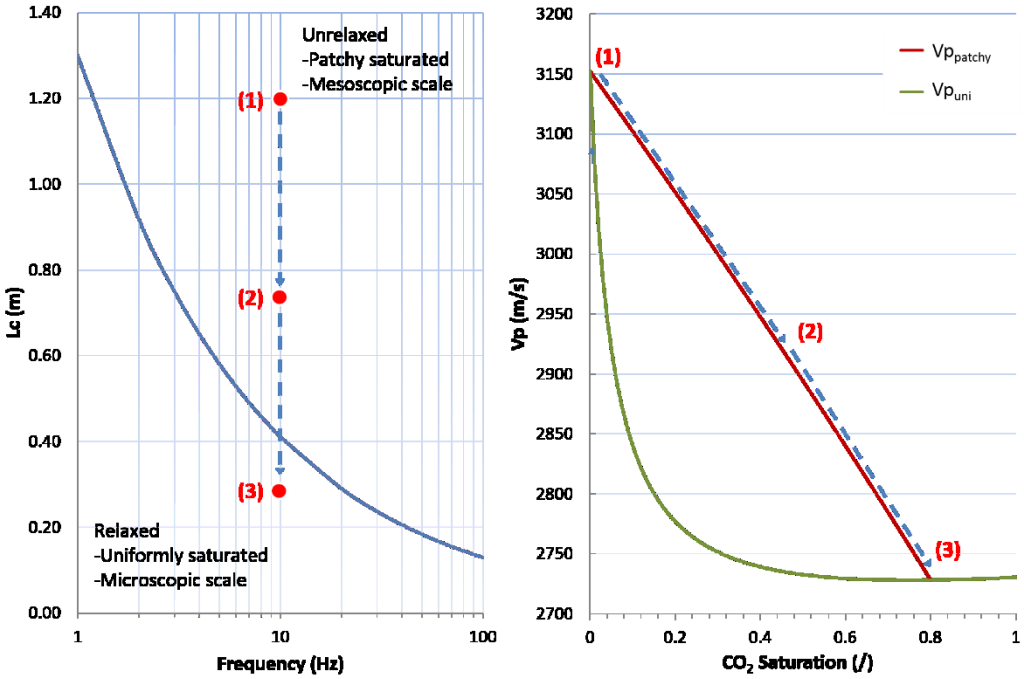

Figure 9.6. A comparison of the size of saturation heterogeneity compared with a critical length scale for a theoretical sandstone at 10 Hz (left) and relationship between the change in velocity with increasing saturation (right). The red dot represents the size of saturation heterogeneity, d. The transition from an unrelaxed (patchy) to a relaxed (uniform) state with increasing time and saturation is demonstrated.

This demonstrates the transition from an unrelaxed (patchy) to a relaxed (uniform) state with increasing time and saturation. However, this transition models drainage (CO_2 displacing water) only. CO_2 imbibition (water displacing CO_2) results in different saturation patterns and measured velocities. Knight and Nolen-Hoeksema

(1990) and Cadoret et al., (1995) measured higher velocities during drainage experiments compared with velocities measured during imbibition experiments.

Figure 9.7 describes the transition from a patchy, unrelaxed state to a uniform, relaxed state by relating the CO_2 relative-permeability (*Kr*) curve (left) to the change in velocity with increasing saturation (right). During drainage, the CO_2 will migrate and accumulate below a seal until reaching maximum saturation (S_{max}) (Figure 9.7 Step 1 to Step 3). Drainage will follow the patchy bound. As water begins to displace the CO_2 (imbibition), *Kr* is reduced until a portion of CO_2 is residually trapped in the pore-space (R_{CO2}) (Figure 9.7, Step 4 and Step 5). Imbibition will follow the uniform bound.

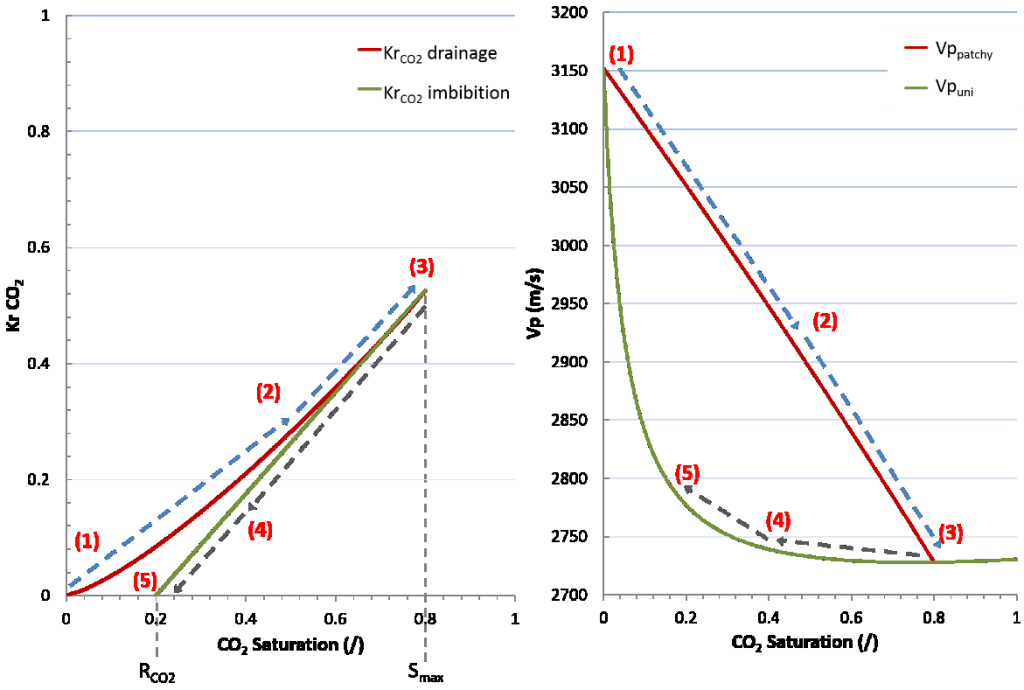

Figure 9.7. A comparison of a CO_2 relative-permeability curve (left) and the change in velocity with increasing saturation (right). The transition from an unrelaxed (patchy) to a relaxed (uniform) state during drainage and imbibition is demonstrated.

Figures 9.6 and 9.7 demonstrate the relaxation states associated with different stages in CO_2 plume growth and migration in a reservoir. The results suggest the following:

- During initial CO_2 migration, the reservoir will be in an unrelaxed state. Reservoir velocities will follow the patchy bound.
- As CO_2 migrates and accumulates below a seal, a transition from an unrelaxed (patchy) to relaxed (uniform) state will occur.
- During imbibition – such as at the tail of the CO_2 plume post injection - reservoir velocities will follow the uniform bound.

The transition has been modelled as a constant linear change along the patchy bound. However, it has been demonstrated by Lebedev et al., (2009) that a gradual transition from the patchy to the uniform bound can be expected at a given saturation. Figure 9.8 demonstrates this transition for a hypothetical scenario. Initial CO_2 migration will follow the patchy bound (Figure 9.8 Step 1) until a saturation is reached where a transition to the uniform bound will occur (Figure 9.8 Steps 2 and 3). Once the transition point is crossed, reservoir velocities will follow the uniform bound. Understanding the rate at which this transition occurs, as well as the patch size and saturation, is still an area of research which needs to be addressed.

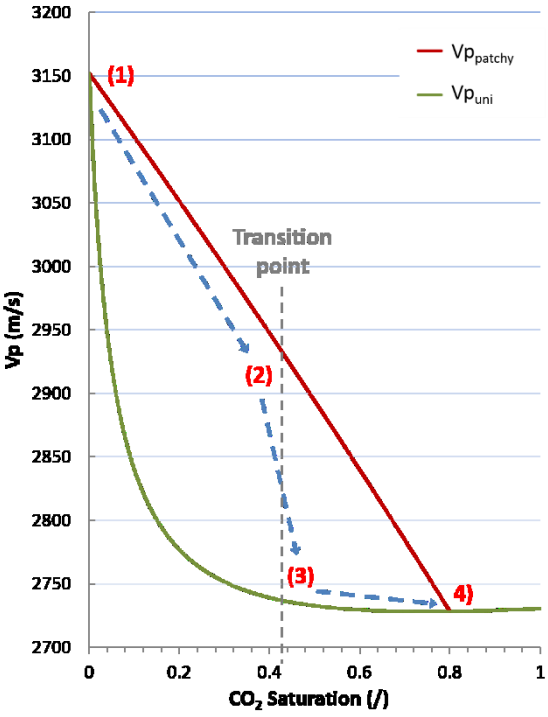

Figure 9.8. The transition from the patchy to the uniform bounds once a saturation transition point is crossed.

9.2.4 Geophysical monitoring of a depleted gas reservoir

I have demonstrated the potential of seismic methods to detect CO_2 injected into a depleted gas field (Chapter 7). However, I considered scenarios with an open reservoir. This is a reservoir which is bound by, and in communication with, an active aquifer, enabling drainage (CO_2 displacing water) and imbibition (water displacing CO_2). A reservoir with an active aquifer is termed a 'water drive reservoir' (Dake, 1983). CO_2 injection into a depleted gas reservoir with an active aquifer allows for fluid saturation changes and pressure dissipation. This is ideal for seismic and CSEM techniques, as both are sensitive to fluid saturation changes with time.

However, some reservoirs do not have an active aquifer. An example of a closed depleted gas reservoir is the P18-04 reservoir as part of the Rotterdam CCS Demonstration Project.

The Rotterdam CCS Project

The Rotterdam CCS Demonstration Project (ROAD) is a joint project by E.ON Benelex and Electrabel Nederland/GDF SUEZ Group. The ROAD project is a potential CCS site aspiring to inject CO_2 into a depleted gas reservoir.

The storage site is situated 20km off the coast of the Netherlands. The main area of interest is the P18 gas fields. The P18 gas fields consist of sandstone reservoirs of the Triassic Bunter Sandstone Subgroup. The reservoirs are discomformably overlain by siltstones, clay stones, evaporates and dolostones (Arts et al., 2012). The P18 gas fields are located in a heavily faulted area and consist primarily of sealing fault bounded compartments.

Assessing the seismic and CSEM monitorability of the P18 block was originally planned for this project. A history matched reservoir model was provided by E.ON. The model contains pre-production and post-production values for porosity, permeability, pressure and water and gas saturation. The target reservoir for injection is the P18-04 sandstone fault-block (Figure 9.9). The P18-04 sandstone block is a depleted gas field at a depth of 3220m. The reservoir is at an abandonment pressure

of 20 Bar. Initial pre-production pressure was at 340 Bar (Figure 9.10). The aim of the CO_2 injection program is to increase reservoir pressure to pre-production values.

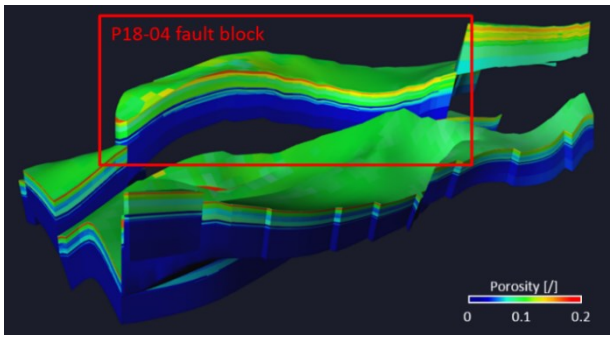

Figure 9.9. The P18 model showing reservoir porosity. The P18-04 fault block is highlighted.

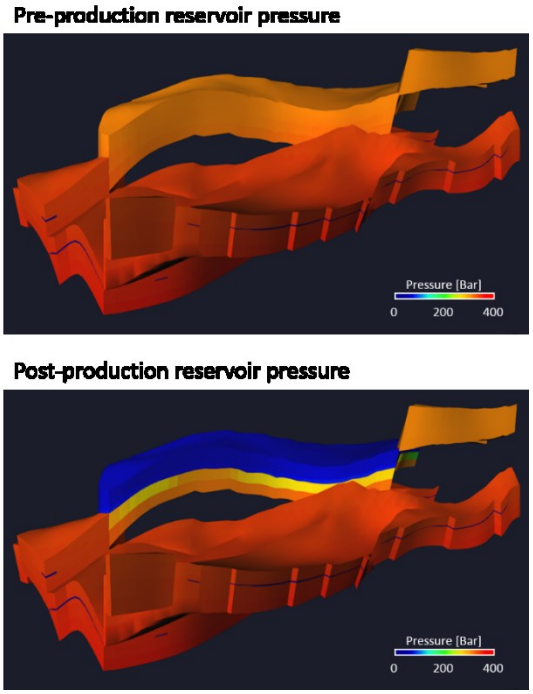

Figure 9.10. Pre-production and post-production reservoir pressure change in the P18-04 sandstone reservoir

The decrease in pressure is due to a lack of an active water drive or aquifer. This is because the reservoir is part of a closed system, bound by a sealing fault. Furthermore, very low permeable formations below the main reservoir severely limit upward flow of water. In this scenario, the reservoir behaves as a closed container.

A consequence of a closed reservoir with no aquifer support is that water is unable to flow back into the pore-space during gas production. This results in no changes in pre-production and post-production gas and water saturation (Figure 9.11). As gas is produced, the pressure decreases and the remaining gas expands to fill the available volume. The pore-fluid saturation does not change.

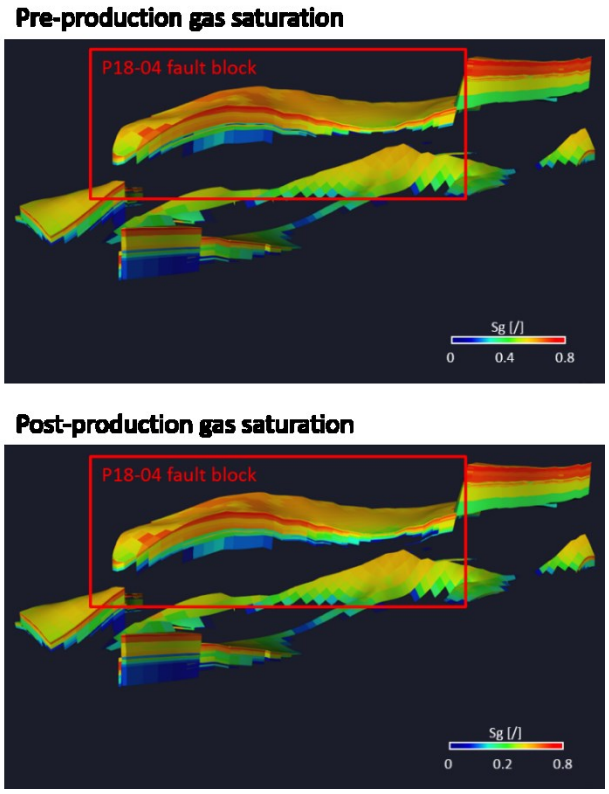

Figure 9.11. Pre-production and post-production gas saturation values. The P18-04 fault block is highlighted.

This presents a unique scenario. Should the P18-04 fault block be used for CCS, the injection of CO_2 would increase reservoir pressure to pre-production levels only. There will be no change in pore-fluid saturation, but the mass of gas will change due to the increase in pressure. As there will be no changes in fluid saturation, seismic and CSEM techniques will be unable to detect CO_2 migration in the reservoir. For this reason, I was unable to further investigate the seismic and CSEM monitorability of the P18-04 fault block. As there will be no change in saturation in the reservoir, the time-lapse surveys will show no change. Other methods, such as downhole pressure sensors, will be more effective at monitoring the migration of the CO_2 plume.

9.3 Proposals for further research

9.3.1 Demonstration of patchy saturation in the field

The presence of patchy saturation is yet to be demonstrated in the field at seismic frequencies. As detailed in Chapter 4 section 3, patchy saturation has been demonstrated at high frequencies of MHz at laboratory experiments and 100 kHz in logging data. However, as highlighted by Lumley (2010), whether patchy saturation has a significant effect in surface seismic data, at the 10-100 Hz frequency range, has yet to be demonstrated at the field scale.

The presence of patchy saturation at the field scale can be demonstrated by analysing seismic data from a site injecting CO_2 into a depleted hydrocarbon field. Through the application of the monitorability workflow (Chapter 4), synthetic seismic sections assuming both patchy and uniform saturation can be generated. The synthetic sections can be compared with the observed seismic responses. The ability to image seismically and detect CO_2 injected in depleted hydrocarbon reservoirs could potentially demonstrate the presence of patchy saturation in the field. The effect of patchy saturation can be confirmed should the CO_2 plume be imaged clearly regardless of the presence of residual oil or gas saturation. Uniform saturation can be confirmed if the resulting amplitude change is very small, and most likely undetectable, when compared to the baseline model.

Furthermore, analysis of real seismic data could confirm the ability of seismic methods to detect CO_2 injected into depleted hydrocarbon fields. Applying the monitorability workflow to a real depleted hydrocarbon reservoir could justify some of the assumptions made in Chapter 7; namely that the depleted gas in the reservoir is uniformly saturated, resulting in an increase in velocity with CO_2 injection.

9.3.2 New rock-physics model describing the transition from an unrelaxed (patchy) to relaxed (uniform) state.

The patchy and uniform bounds represent two end-member bounds of seismic velocity. However, a transition from an unrelaxed (patchy) to relaxed (uniform) state is expected. Further work is recommended to develop a rock-physics model which models the relaxation states associated with different stages in CO_2 plume growth and migration in a reservoir. In particular:

1) The transition from patchy to uniform bounds with increasing CO_2 saturation and trapping;
2) The change in velocity associated with CO_2 imbibition.

Ideally, the rock-physics model can be linked to the relative-permeability curves input into the reservoir simulation. When simulating drainage, the patchy model is applied to calculate reservoir velocity. During imbibition, the uniform model can applied. This model represents the constant linear transition along the patchy bound. The drainage rock-physics model can be developed further to account for the gradual transition which occurs at a given saturation (for example, Figure 9.11). Reservoir velocity will first follow the patchy bound, until reaching a given saturation, where the change in velocity will then follow the uniform bound.

Appendices

A. Gassmann variables and their effect on seismic velocity

A.1 Introduction

This appendix investigates the role of the dry bulk moduli (K_{dry}), matrix bulk moduli (K_m), CO_2 density (ρ) and porosity (φ) on changing velocity.

A.2 K_{dry}

A range of K_{dry} values were modelled to understand the effect of the dry bulk modulus on seismic velocity. K_{dry} values chosen for this study varied from 1GPa to 11 GPa. These values were chosen based on a recommendation by Kazemeini et al., (2010). The authors demonstrated that K_{dry} can vary from 3 GPa to 10 GPa.

Figure A.1 shows different Vp curves for each K_{dry} value. Vp was calculated assuming uniform saturation (left) and patchy saturation (right). The calculated change in velocity for each curve is shown in Figure A.2.

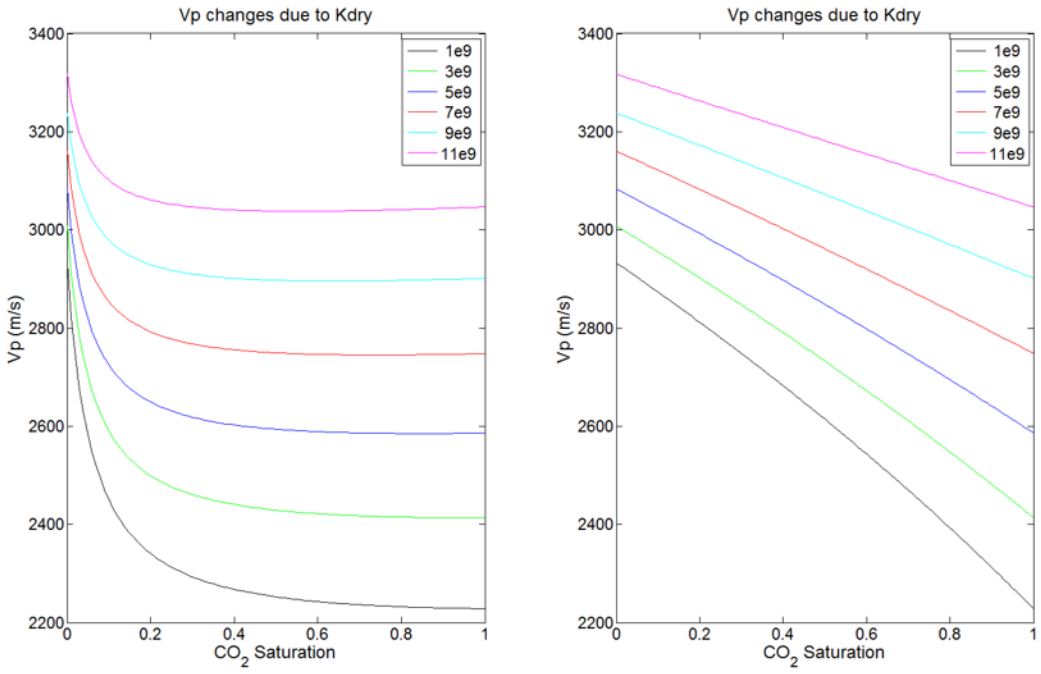

Figure A.1. Variations in K_{dry} with increasing CO_2 saturation calculated assuming uniform saturation (left) and patchy saturation (right).

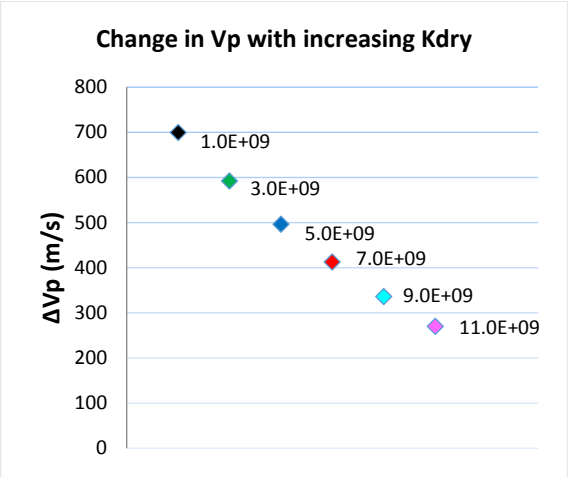

Figure A.2. Largest change in velocity compared with the baseline for each K_{dry} model.

A.3 K_m

K_m is related to the volume of clay in the reservoir. To understand the effect of increasing clay content on K_m, Vp was calculated assuming a range of clay values from 0% to 25% (Figure A.3).

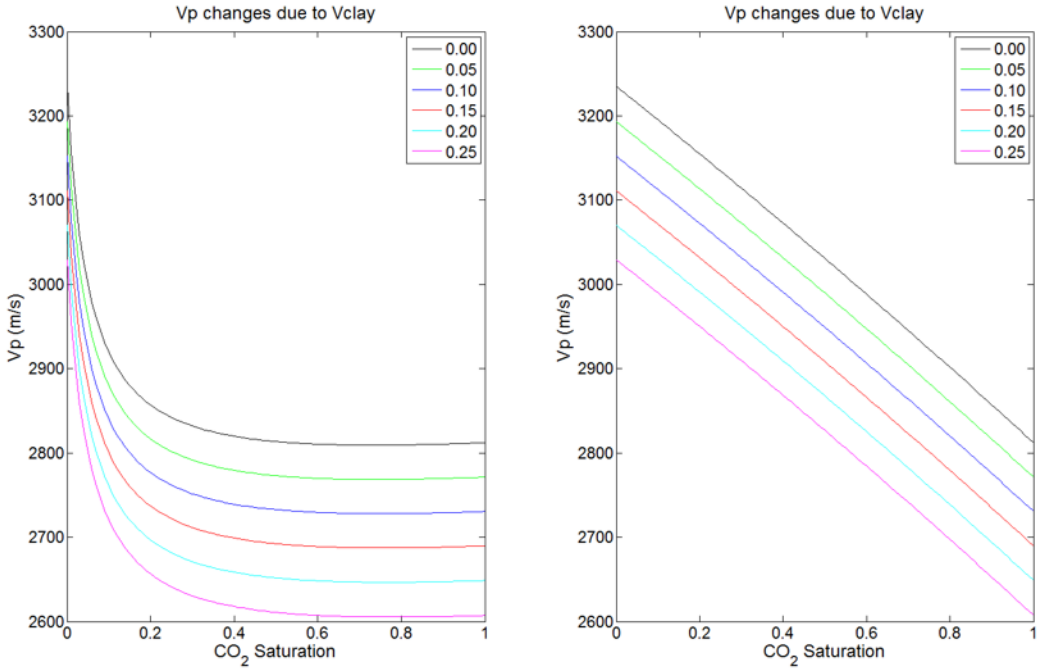

Figure A.3. The effect of different values of clay on Vp calculated assuming uniform saturation (left) and patchy saturation (right).

A.4 CO_2 density

Vp was calculated assuming four density values: 300kg/m^3, 500kg/m^3, 700kg/m^3 and 900kg/m^3 (Figure A.4). These values represent the expected change in density associated with vertical CO_2 migration. The CO_2 is in a gaseous state at 300kg/m^3 and 500kg/m^3 and in a supercritical state at 700kg/m^3 and 900kg/m^3.

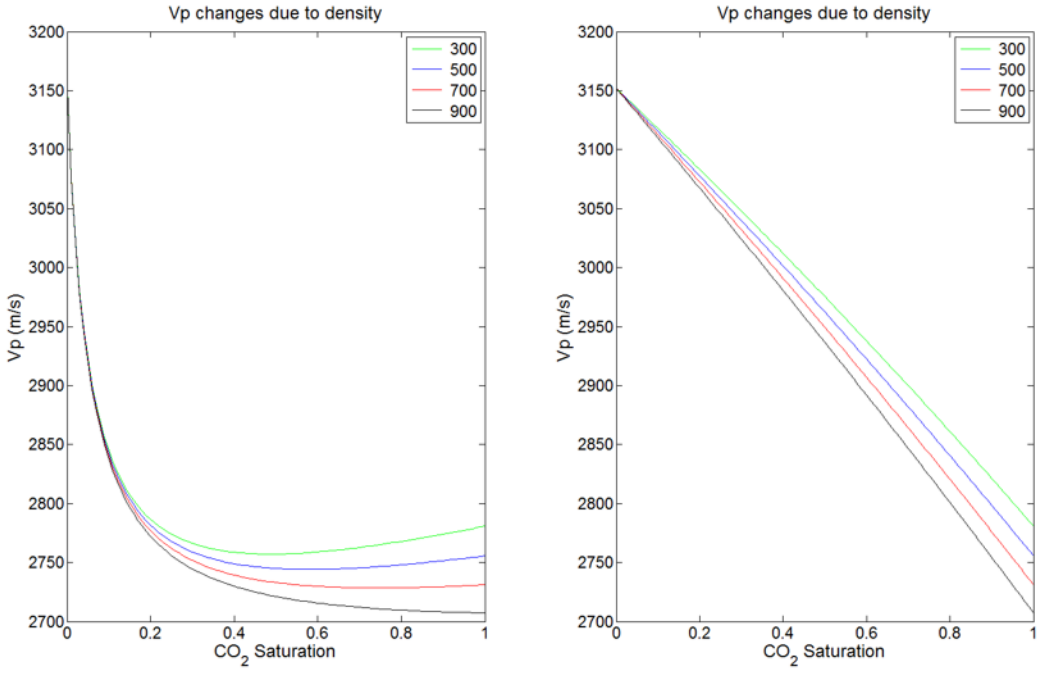

Figure A.4. Changing CO_2 density on Vp calculated assuming uniform saturation (left) and patchy saturation (right).

A.5 Porosity

Porosity is known to play a key role in the compressibility of a reservoir. I investigate this by calculating Vp assuming a range of porosity values from 15% to 40%, at 5% increments (Figure A.5). The maximum change in velocity compared with the baseline is shown in Figure A.6.

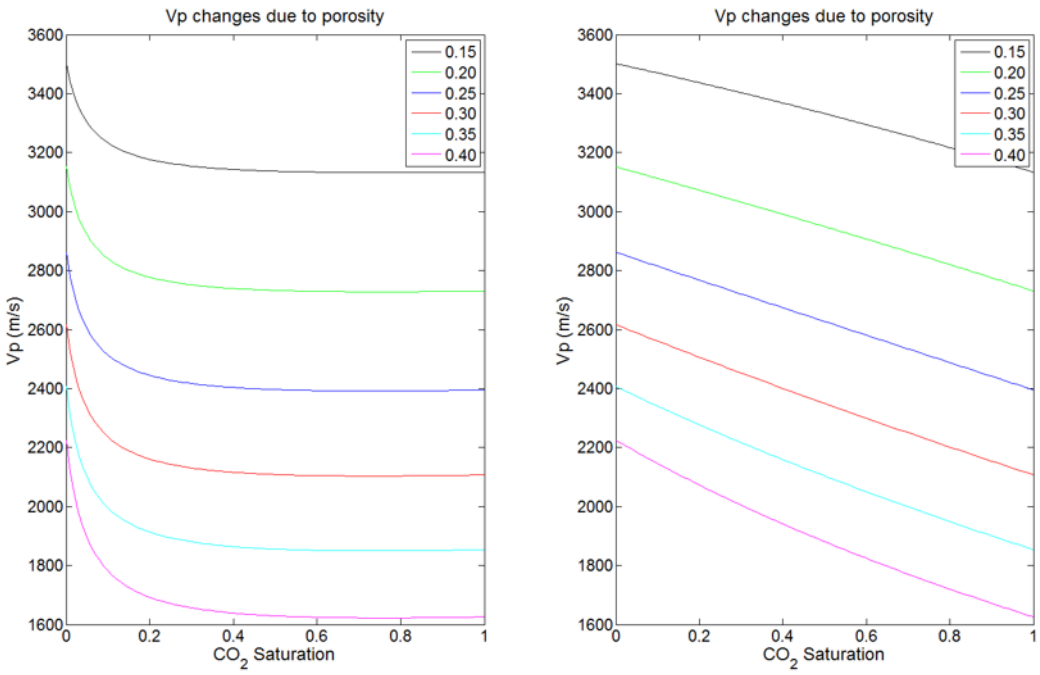

Figure A.5. The effect of changing porosity on Vp assuming uniform saturation (left) and patchy saturation (right).

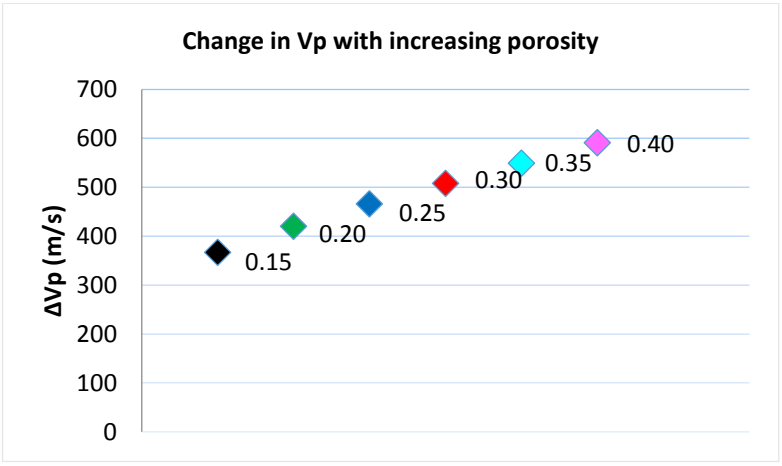

Figure A.6. Largest change in velocity compared with the baseline for each porosity model.

A.6 Summary

The results suggest the following:

- K_{dry} is inversely proportional to the change in velocity. Lower K_{dry} values will result in larger changes in velocity at maximum saturation when compared with the baseline
- Increasing clay content will decrease reservoir velocity.
- Decreasing CO_2 density will result in a slight increase in velocity above 40%.
- Porosity is inversely proportional to velocity.
- High porosity reservoirs will result in the largest change in velocity at maximum saturation when compared with the baseline.

B. Validation of PEMrad code

B.1 Introduction

This appendix aims to verify the PEMrad modelling code with the 1D MTEM forward modelling code, EX1D. EX1D is a proprietary software of PGS based upon code from Edwards (1997).

First, I verify the modelling results in 1D. Then I verify the 3D results with the 1D results but modify the cell-dimensions of the model. This is done to ensure that PEMrad can handle very fine cell-dimensions. Last, I look at the relationship between the total number of cells and computational time per frequency.

B.2 1D PEMrad - EX1D verification

I simulate the CSEM response to a simple 1D earth model using both PEMrad and EX1D. The 1D earth model consists of a 1 Ω.m half-space with 100m sea-water of 0.3 Ω.m resistivity (Figure B.1). I model the response with no CO_2 (left) and with a 100m thick CO_2 layer (right) of 100 Ω.m resistivity. Acquisition parameters are detailed in Table B.1.

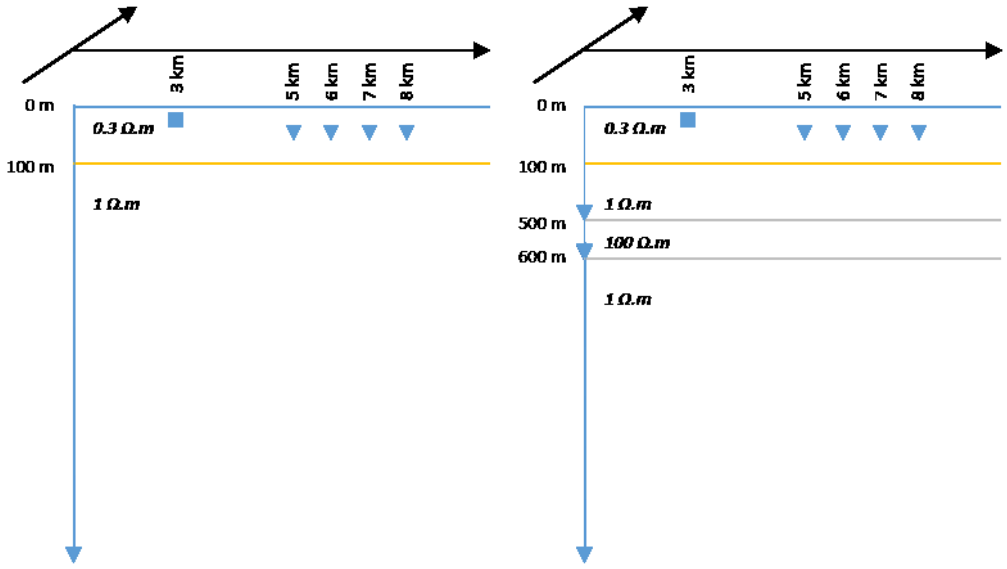

Figure B.1. 1D earth model consisting of a 1 Ω.m half-space with 100m sea-water of 0.3 Ω.m resistivity. Two scenarios are modelled: 1) no CO_2 (left), 2) CO_2 at 500m depth (right). The CO_2 layer is 100m thick with a constant resistivity of 100 Ω.m.

Table B.1. 1D model verification acquisition parameters

Acquisition parameters			
Source	Strength	1	A.m
	Depth	10	m
	Frequencies	0.0001 to 10000	Hz
	Times	0.001 to 100	Sec
Receiver	Min-offset	2000	m
	Max-offset	5000	m
	Spacing	1000	m
	Depth	50	m

The frequency-domain amplitude responses for each offset are shown in Figure B.2. The agreement of the points (EX1D) with the circles (PEMrad) validates PEMrad.

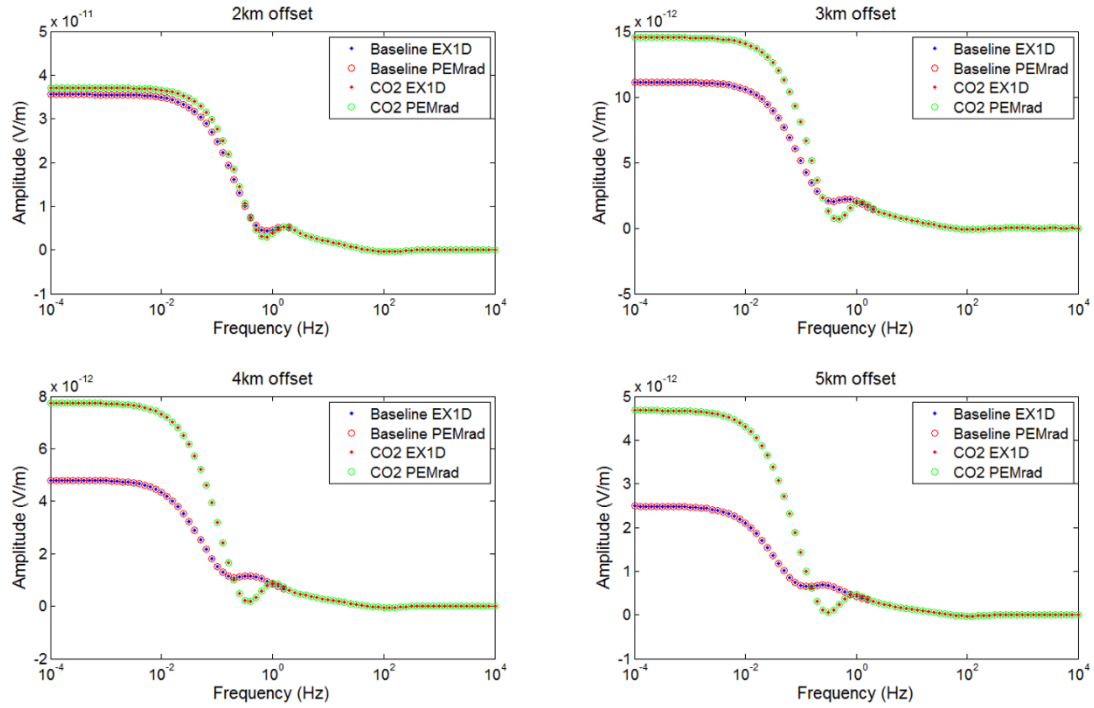

Figure B.2. Frequency-domain amplitude responses for each offset. The dots represent the EX1D modelling results while the circles present the PEMrad modelling results. The agreement of the dots and the circles validates the PEMrad results.

B.3 3D PEMrad verification

I simulate the CSEM response to a 3D earth model and compare the results to the 1D PEMrad response. The 1D earth model is a 1 Ω.m half-space with 100m sea-water of 0.3 Ω.m resistivity (Figure B.3). I model two scenarios: 1) no CO_2 (left), 2) a 3D CO_2 body of dimensions 10 km by 10 km. The CO_2 layer is 100m thick with a resistivity of 100 Ω.m resistivity. Acquisition parameters are detailed in Table B.2.

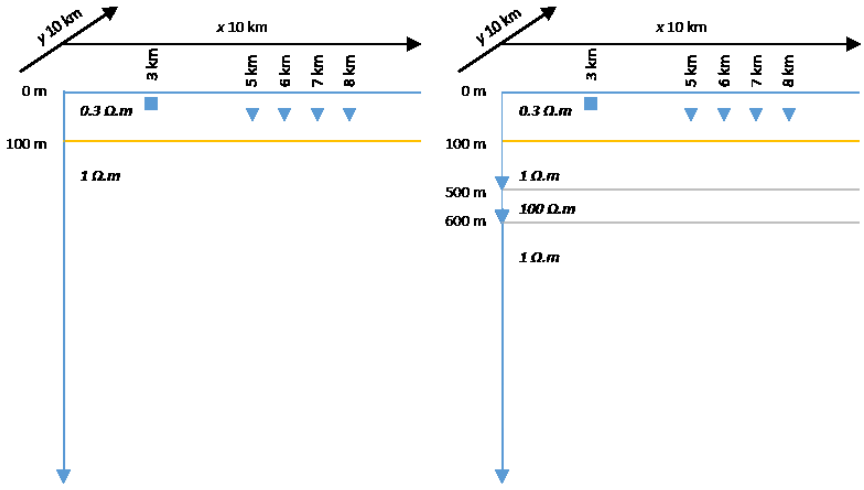

Figure B.3. 1D earth model consisting of a 1 Ω.m half-space with 100m sea-water of 0.3 Ω.m resistivity. Two scenarios are modelled: 1) no CO_2 (left), 2) 3D CO_2 body at 500m depth (right). The CO_2 body has dimensions 10 km by 10 km by 100m.

Table B.2. 3D model verification acquisition parameters

Acquisition parameters			
Source	x	3000	m
	Strength	1	A.m
	Depth	10	m
	Frequencies	0.0001 to 10000	Hz
	Times	0.001 to 100	Sec
Receiver	Min-offset	2000	m
	Max-offset	5000	m
	Spacing	1000	m
	Depth	50	m

The EM response to different cell-size dimensions of the CO_2 body are modelled (Table B.3). This is done to ensure that PEMrad can handle very fine cell-dimensions.

Table B.3. Cell-size dimensions chosen for this study.

Cell-size dimensions (m)		
x	***y***	***z***
500	500	100
500	500	20
250	250	100
250	250	20
125	125	100
125	125	20
62.5	62.5	100

The frequency-domain amplitude responses for each offset are shown in Figure B.4. The approximate agreement of the points (1D response) with the dashed lines (3D response) validates the PEMrad 3D modelling code. There is no change between the different cell-size dimensions modelled.

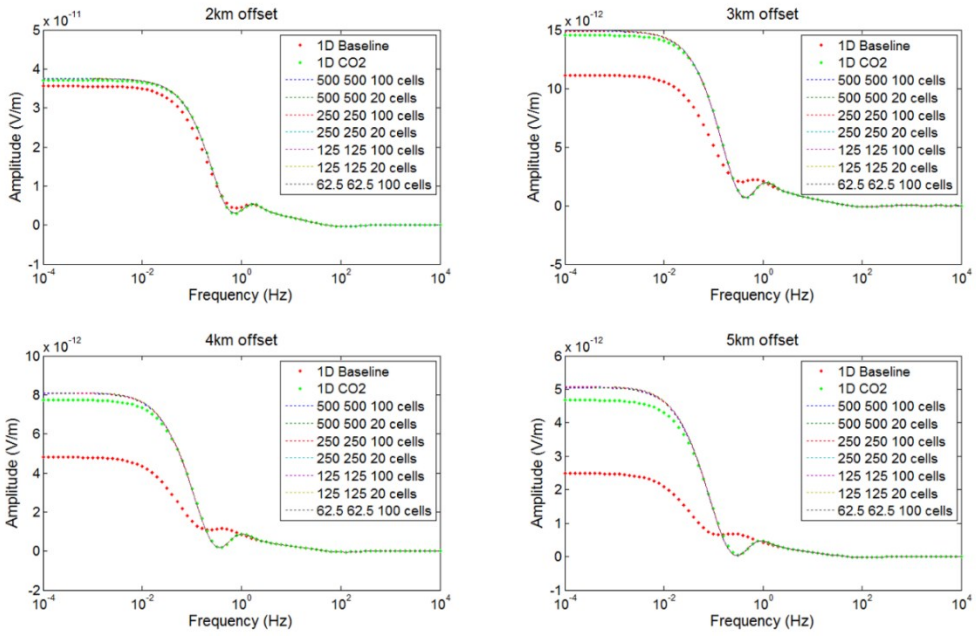

Figure B.4. Frequency-domain amplitude responses for each offset. The points represent the 1D modelling results while the dashed lines 3D modelling results. The 3D responses approximate the 1D response.

B.4 Total cell-count and computational time

I look at the relationship between the total cell-count of a model and computational time. To test this, I simulated the acquisition of a single shot with 5 receivers. Seven different cell-size dimensions were tested. The simulations were run using 16 cores.

Figure B.5 shows the relationship between total cell count and computational time (minutes) per frequency. Table B.4 details each of the models tested. The results show that an increase in the total number of cells will greatly increase computational time per frequency for a single shot.

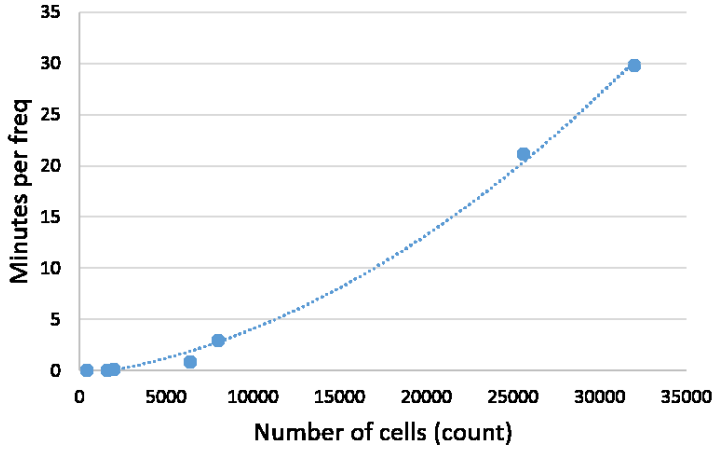

Figure B.5. The relationship between total cell count and computational time (minutes) per frequency.

B.5 Summary

I have validated the use of PEMrad by comparing the simulated amplitude response to those generated using EX1D. The 1D simulation results showed an exact agreement between the PEMrad and EX1D simulation results, while the 3D response showed an approximate agreement with the 1D results.

Table B.4. The cell-size dimensions, number of cells and total cell count for each model. Each simulation was run using 16 cores.

Cell size dimensions (m)			Number of cells			Total number of cells	Comp time	Number of freqs	Min per freq
x	*y*	*z*	*x*	*y*	*z*	*count*	*min*		
500	500	100	20	20	1	400	0.5	81	0.006
250	250	100	40	40	1	1600	3.25	81	0.04
125	125	100	80	80	1	6400	66.5	81	0.821
62.5	62.5	100	160	160	1	25600	1080	51	21.176
500	500	20	20	20	5	2000	11.5	81	0.142
250	250	20	40	40	5	8000	240	81	2.963
125	125	20	60	60	5	32000	1520	51	29.804

C. Reproducibility

C.1 Reproducibility

This entire thesis is reproducible. Provided with this thesis is a CD-ROM containing the following:

- PhD thesis
- PEMrad files
- Permedia java scripts: calculation of Vp and resistivity
- Matlab scripts: seismic processing and migration
- Data: reservoir model used in Chapter 5.

The content of the CD-ROM is outlined in Figure C.1. The directory **PhD Thesis/** contains an electronic copy of the thesis (word and PDF). The input files required to run PEMrad are in **PEMrad files/**. The script used to process and migrate the seismic data are in **Matlab scripts/**. The directory **Data/** contains the non-proprietary reservoir model used in Chapter 5.

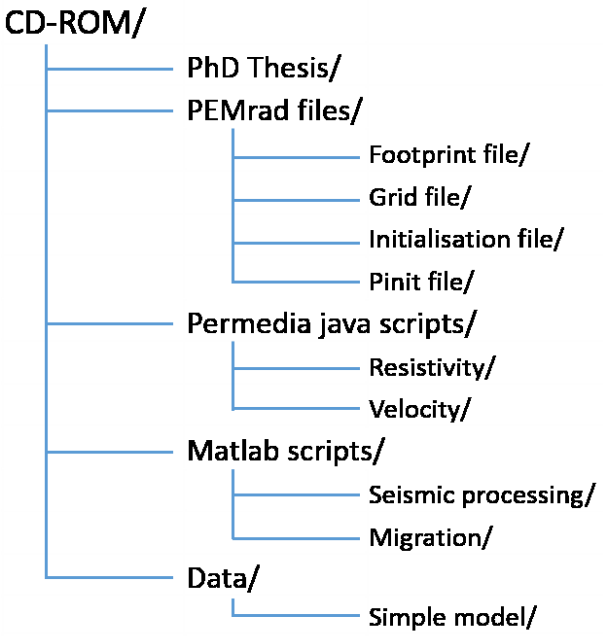

Figure C.1. Content of the CD-ROM. The CD-ROM contains everything needed to reproduce the entire thesis, apart from the proprietary data.

C.2 PEMrad files

PEMrad requires four input files to run:

- Initialisation;
- Footprint;
- Grid;
- Pinit.

The initialisation, grid and footprint files are unique for each simulation. The pinit file was provided by PGS and was used for each simulation. As a manual was not available, a lot of time and effort was needed to understand the different aspects of the files. I have included the input files for the Bunter Sandstone study (Chapter 8, section 4) on the CD-ROM.

Initialisation file

The initialisation file includes the source information, source frequencies and the 1D background model. Table C.1 details the lines required to run the initialisation file.

Table C.1. The lines required to run the initialisation file.

Initialisation file			
Source	HED (horizontal electrode dipole)		
Moment_of_source	<number>		
Output_file	<path name>		
Foot_print_file	<footprint path name>		
Cal_method	0 means '1D modelling only', 1 means 'full 3D'		
Inhomogeneity_type	1 means 'rectangular block', 4 means 'read data from grid file'		
Compu_grid_file	<3D grid file name> (This is only needed if inhomogeneity type is 4)		
Extension	Coordinate extension of the grid: Xmin, Xmax, Ymin, Ymax, Zmin, Zmax		
Frequency	<numbers>		
Layering	(1D model)		
	<depth 1>	<conductivity above 1>	<permittivity above 1>
	<depth 1>	<conductivity below 1>	<permittivity below 1>
	<depth 2>	<conductivity above 2>	<permittivity above 1>
	<depth 2>	<conductivity below 2>	<permittivity below 1>
	… continued		

Footprint file

The footprint file details the coordinates of each shot and receiver. Table C.2 details the lines required to run the footprint file.

Table C.2. The lines required to run the footprint file.

Footprint file									
# shots	# rec	0	0	0	0	0	0	0	… continued
shot 1	$x_{source\ 1}$	$y_{source\ 1}$	$z_{source\ 1}$	$dir_{source\ 1}$	$x_{rec\ 1.1}$	$y_{rec\ 1.1}$	$z_{re\ c1.1}$	$dir_{rec\ 1.1}$	…
shot 2	$x_{source\ 2}$	$y_{source\ 2}$	$z_{source\ 2}$	$dir_{source\ 2}$	$x_{rec\ 1.2}$	$y_{rec\ 1.2}$	$z_{rec\ 1.2}$	$dir_{rec\ 1.2}$	…
shot n	$x_{source\ n}$	$y_{source\ n}$	$z_{source\ n}$	$dir_{source\ 3}$	$x_{rec\ 1.n}$	$y_{rec\ 1.n}$	$z_{rec\ 1.n}$	$dir_{rec\ 1.n}$	…

Grid file

The grid file details the size and coordinates of each cell in the model. Table C.2 details the lines required to run the grid file.

Table C.3. The lines required to run the grid file.

Grid file				
x (cell size)	y (cell size)	z (cell size)	0	0
n (total cell number)	0	0	0	0
x 1	y 1	z 1	conductivity 1	permittivity 1
x 2	y 2	z 2	conductivity 2	permittivity 2
x n	y n	z n	conductivity n	permittivity n
… continued				

Pinit file

The pinit file includes a list of commands and extensions to control the execution of the PEMrad code. This file was provided by PGS. I have included the Pinit file on the CD-ROM.

C.3 Permedia java scripts

The petrophysical modelling was done using Permedia. This involved writing scripts in Java. The rock-physics models are detailed in Chapter 4, section 3.

Resistivity

The directory **Resistivity/** includes the java script written to calculate the change in resistivity. The following input parameters are required:

- a (tortuosity factor),
- m (cementation factor),
- n (saturation exponent),
- Rw (water resistivity),
- Sw (water saturation),
- Porosity.

Running the script will output:

- Rm (resistivity),
- Cond (conductivity).

Velocity

The directory **Velocity/** includes the java script written to calculate velocity assuming uniform, patchy and modified-patchy saturation. The following input parameters are required:

- Vqtz (volume of quartz),
- Porosity,
- Matrix density,
- Gas density,
- Brine density,
- Free gas (CO_2 saturation),
- Swir (irreducible water saturation),
- Pressure.

Running the script will output:

- Vp_uni (velocity assuming uniform saturation),
- Vp_patch (velocity assuming patchy saturation),
- Vp_mod (velocity assuming modified-patchy saturation),
- Vs,
- Rho_bulk (bulk density).

C.4 Matlab scripts

The seismic processing and migration was done using Matlab. This involved writing scripts. The processing steps were outlined in Chapter 4, section 4.

Seismic processing

The script used to process the synthetic data from Nucleus+ is located in the directory **Seismic processing/**. The script calls three programs: parabolic_movement, nmo and velan. These programs are accessed using the SeismicLab toolkit (http://seismic-lab.physics.ualberta.ca/).

Migration

The script used to migrate the processed data is located in the directory **Migration/**. The script calls the program pspi_stack. This program is accessed using the CREWES toolkit (Margrave, 2003).

C.5 Data

The directory **Data/** contains the non-proprietary reservoir model used in Chapter 5. The Bunter Sandstone reservoir model used in Chapters 6 to 8, and the ROAD model described in Chapter 9, are not included as they are proprietary. The Bunter Sandstone model was provided by BGS and PGS. The ROAD model was provided by E.ON.

References

ADAM, L., BATZLE, M. & BREVIK, I. 2006. Gassmann's fluid substitution and shear modulus variability in carbonates at laboratory seismic and ultrasonic frequencies. *Geophysics,* 71**,** F173-F183.

ANDRÉIS, D. & MACGREGOR, L. 2011. Using CSEM to monitor production from a complex 3D gas reservoir—A synthetic case study. *The Leading Edge,* 30**,** 1070-1079.

ARCHIE, G. E. 1942. The electrical resistivity log as an aid in determining some reservoir characteristics. *Trans. AIMe,* 146**,** 54-62.

ARTS, R., CHADWICK, A., EIKEN, O., THIBEAU, S. & NOONER, S. 2008. Ten years' experience of monitoring CO2 injection in the Utsira Sand at Sleipner, offshore Norway. *First break,* 26.

ARTS, R., CHADWICK, R., EIKEN, O., TRANI, M. & DORTLAND, S. 2007. Synthetic versus real time-lapse seismic data at the Sleipner CO2 injection site. *2007 SEG Annual Meeting*.

ARTS, R., EIKEN, O., CHADWICK, A., ZWEIGEL, P., VAN DER MEER, L. & ZINSZNER, B. 2004. Monitoring of CO2 injected at Sleipner using time-lapse seismic data. *Energy,* 29**,** 1383-1392.

ARTS, R., TRANI, M., CHADWICK, R., EIKEN, O., DORTLAND, S. & VAN DER MEER, L. 2009. Acoustic and elastic modeling of seismic time-lapse data from the Sleipner CO2 storage operation. *The American Association of Petroleum Geologists*.

ARTS, R. J., VANDEWEIJER, V. P., HOFSTEE, C., PLUYMAEKERS, M. P. D., LOEVE, D., KOPP, A. & PLUG, W. J. 2012. The feasibility of CO2 storage in the depleted P18-4 gas field offshore the Netherlands (the ROAD project). *International Journal of Greenhouse Gas Control,* 11, Supplement**,** S10-S20.

AVSETH, P., MUKERJI, T. & MAVKO, G. 2005. Quantitative seismic interpretation. *Quantitative Seismic Interpretation, by Per Avseth and Tapan Mukerji and Gary Mavko, pp. 376. ISBN 0521816017. Cambridge, UK: Cambridge University Press, March 2005.,* 1.

AZUMA, H., KONISHI, C. & XUE, Z. 2013. Introduction and Application of the Modified Patchy Saturation for Evaluating CO2 Saturation by Seismic Velocity. *Energy Procedia,* 37**,** 4024-4032.

BAINES, S. J. & WORDEN, R. H. 2004. Geological storage of carbon dioxide. *Geological Society, London, Special Publications,* 233**,** 1-6.

BARCLAY, F., BRUUN, A., RASMUSSEN, K. B., ALFARO, J. C., COOKE, A., COOKE, D., SALTER, D., GODFREY, R., LOWDEN, D. & MCHUGO, S. 2007. Seismic Inversion: Reading Between the Lines. *Oilfield Review*.

BENNION, D. & BACHU, S. Year. Dependence on temperature, pressure, and salinity of the IFT and relative permeability displacement characteristics of CO2 injected in deep saline aquifers. *In:* SPE Annual Technical Conference and Exhibition, 2006.

BENSON, S. M. 2005. Carbon Dioxide Capture and Storage in Underground Geologic Formations. *Proceedings Workshop*.

BERGMANN, P., YANG, C., LÜTH, S., JUHLIN, C. & COSMA, C. 2011. Time-lapse processing of 2D seismic profiles with testing of static correction methods at the CO2 injection site Ketzin (Germany). *Journal of Applied Geophysics,* 75**,** 124-139.

BERNAL, J. & MASON, J. 1960. Co-ordination of randomly packed spheres. *Nature,* 188.

BERRYMAN, J. G. 1999. Origin of Gassmann's equations. *Geophysics,* 64**,** 1627-1629.

BHUYIAN, A. H., GHADERI, A. & LANDRØ, M. 2011. CSEM Sensitivity Study of CO2 Layers With Uniform Versus Patchy Saturation Distributions. Society of Exploration Geophysicists.

BHUYIAN, A. H., LANDRØ, M. & JOHANSEN, S. E. 2012. 3D CSEM modeling and time-lapse sensitivity analysis for subsurface CO 2 storage. *Geophysics,* 77**,** E343-E355.

BIOT, M. A. 1956. Theory of propagation of elastic waves in a fluid saturated porous solid. I - Low frequency range. *The Journal of the Acoustical Society of America,* 28**,** 168-178.

BIOT, M. A. 1962. Mechanics of deformation and acoustic propagation in porous media. *Journal of applied physics,* 33**,** 1482-1498.

BLACK, N. & ZHDANOV, M. S. 2009. Monitoring of Hydrocarbon Reservoirs Using Marine CSEM Method. Society of Exploration Geophysicists.

BOAIT, F. C., WHITE, N. J., BICKLE, M. J., CHADWICK, R. A., NEUFELD, J. A. & HUPPERT, H. E. 2012. Spatial and temporal evolution of injected CO2 at the Sleipner Field, North Sea. *Journal of Geophysical Research: Solid Earth,* 117.

BOURBIÉ, T., COUSSY, O. & ZINSZNER, B. 1987. Acoustics of porous media: Editions Technip. *Paris, France*.

BOURGEOIS, B. & GIRARD, J. F. 2010. First modelling results of the EM response of a CO2 storage in the Paris Basin. *Oil & Gas Science and Technology–Revue de l'Institut Français du Pétrole,* 65**,** 597-614.

BRYANT, S. L., LAKSHMINARASIMHAN, S. & POPE, G. A. 2008. Buoyancy-dominated multiphase flow and its effect on geological sequestration of CO2. *SPE Journal,* 13**,** 447-454.

CADORET, T., MARION, D. & ZINSZNER, B. 1995. Influence of frequency and fluid distribution on elastic wave velocities in partially saturated limestones. *Journal of Geophysical Research: Solid Earth (1978–2012),* 100**,** 9789-9803.

CADORET, T., MAVKO, G. & ZINSZNER, B. 1998. Fluid distribution effect on sonic attenuation in partially saturated limestones. *Geophysics,* 63**,** 154-160.

CAIRNS, G., JAKUBOWICZ, H., LONERGAN, L. & MUGGERIDGE, A. 2012. Using time-lapse seismic monitoring to identify trapping mechanisms during CO2 sequestration. *International Journal of Greenhouse Gas Control,* 11**,** 316-325.

CAVANAGH, A. 2013. Benchmark Calibration and Prediction of the Sleipner CO2 Plume from 2006 to 2012. *Energy Procedia,* 37**,** 3529-3545.

CAVANAGH, A. & NAZARIAN, B. 2014. A new and extended Sleipner Benchmark model for CO2 storage simulations in the Utsira Formation. *Energy Procedia,* 63**,** 2831-2835.

CAVANAGH, A. J. & HASZELDINE, R. S. 2014. The Sleipner storage site: Capillary flow modeling of a layered CO2 plume requires fractured shale barriers within the Utsira Formation. *International Journal of Greenhouse Gas Control,* 21**,** 101-112.

CHADWICK, A., ARTS, R., BERNSTONE, C., MAY, F., THIBEAU, S. & ZWEIGEL, P. 2008. *Best Practice for the Storage of CO2 in Saline Aquifers-Observations and Guidelines from the SACS and CO2STORE projects*, British Geological Survey.

CHADWICK, A., ARTS, R., EIKEN, O., WILLIAMSON, P. & WILLIAMS, G. 2006a. Geophysical monitoring of the CO2 plume at Sleipner, North Sea. *Advances in the geological storage of carbon dioxide***,** 303-314.

CHADWICK, A., NOY, D., LINDEBERG, E., ARTS, R., EIKEN, O. & WILLIAMS, G. 2006b. Calibrating reservoir performance with time-lapse seismic monitoring and flow simulations of the Sleipner CO2 plume. *Energy Procedia*.

CHADWICK, R., ARTS, R., BENTHAM, M., EIKEN, O., HOLLOWAY, S., KIRBY, G., PEARCE, J., WILLIAMSON, J. & ZWEIGEL, P. 2009. Review of monitoring issues and technologies associated with the long-term underground storage of carbon dioxide. *Geological Society, London, Special Publications,* 313**,** 257-275.

CHADWICK, R., ARTS, R. & EIKEN, O. 2005. 4D seismic quantification of a growing CO2 plume at Sleipner, North Sea. *Geological Society, London, Petroleum Geology Conference series,* 6**,** 1385-1399.

CHADWICK, R., ARTS, R., EIKEN, O., KIRBY, G., LINDEBERG, E. & ZWEIGEL, P. 2004. 4D seismic imaging of an injected CO2 plume at the Sleipner Field, central North Sea. *Geological Society of London*.

CHADWICK, R. & NOY, D. 2010. History-matching flow simulations and time-lapse seismic data from the Sleipner CO2 plume. *Geological Society, London, Petroleum Geology Conference series,* 7**,** 1171-1182.

CHADWICK, R. A., MARCHANT, B. P. & WILLIAMS, G. A. 2014. CO2 storage monitoring: leakage detection and measurement in subsurface volumes from 3D seismic data at Sleipner. *Energy Procedia,* 63**,** 4224-4239.

CHRISTENSEN, N., SHERLOCK, D. & DODDS, K. 2006. Monitoring CO2 injection with cross-hole electrical resistivity tomography. *Exploration Geophysics,* 37**,** 44-49.

CLASS, H., EBIGBO, A., HELMIG, R., DAHLE, H., NORDBOTTEN, J., CELIA, M., AUDIGANE, P., DARCIS, M., ENNIS-KING, J., FAN, Y., FLEMISCH, B., GASDA, S., JIN, M., KRUG, S., LABREGERE, D., NADERI BENI, A., PAWAR, R., SBAI, A., THOMAS, S., TRENTY, L. & WEI, L. 2009. A benchmark study on problems related to CO2 storage in geologic formations. *Computational Geosciences,* 13**,** 409-434.

CONSTABLE, S. & SRNKA, L. J. 2007. An introduction to marine controlled-source electromagnetic methods for hydrocarbon exploration. *Geophysics,* 72**,** WA3-WA12.

COOK, P. 2012. *Clean energy, climate and carbon*, CSIRO PUBLISHING.

DAKE, L. P. 1983. *Fundamentals of reservoir engineering*, Elsevier.

DOMENICO, S. 1976. Effect of brine-gas mixture on velocity in an unconsolidated sand reservoir. *Geophysics,* 41**,** 882-894.

DRAKENGREN, T. 2008. PGS CSEM.

DUAN, Z. & SUN, R. 2003. An improved model calculating CO2 solubility in pure water and aqueous NaCl solutions from 273 to 533 K and from 0 to 2000 bar. *Chemical Geology,* 193**,** 257-271.

DUNLAP, H., GARROUCH, A. & SHARMA, M. M. 1991. Effects of wettability, pore geometry, and stress on electrical conduction in fluid-saturated rocks. *The Log Analyst,* 32.

DUTTA, N. C. & ODÉ, H. 1979a. Attenuation and dispersion of compressional waves in fluid-filled porous rocks with partial gas saturation (White model)—Part I: Biot theory. *Geophysics,* 44**,** 1777-1788.

DUTTA, N. C. & ODÉ, H. 1979b. Attenuation and dispersion of compressional waves in fluid-filled porous rocks with partial gas saturation (White model)—Part II: Results. *Geophysics,* 44**,** 1789-1805.

DVORKIN, J., GUTIERREZ, M. A. & GRANA, D. 2014. *Seismic reflections of rock properties*, Cambridge University Press.

DVORKIN, J. & NUR, A. 1996. Elasticity of high-porosity sandstones: Theory for two North Sea data sets. *Geophysics,* 61**,** 1363-1370.

DVORKIN, J. & NUR, A. 1998. Acoustic signatures of patchy saturation. *International Journal of Solids and Structures,* 35**,** 4803-4810.

EC 2009. Directive 2009/31/EC of the European Parliament and of the Council of 23 April 2009 on the Geological Storage of Carbon Dioxide. *European Commission, Brussels*.

EDWARDS, R. N. 1997. On the resource evaluation of marine gas hydrate deposits using sea-floor transient electric dipole-dipole methods. *Geophysics,* 62**,** 63-74.

EID, R., ZIOLKOWSKI, A., NAYLOR, M. & PICKUP, G. 2014. The Detectability of Free-phase Migrating CO2: A Rock Physics and Seismic Modelling Feasibility Study. *Energy Procedia,* 63**,** 4449-4458.

EID, R., ZIOLKOWSKI, A., NAYLOR, M. & PICKUP, G. 2015a. Seismic monitoring of CO2 plume growth, evolution and migration in a heterogeneous reservoir: Role, impact and importance of patchy saturation. *International Journal of Greenhouse Gas Control,* 43**,** 70-81.

EID, R., ZIOLKOWSKI, A., NAYLOR, M. & PICKUP, G. 2015b. Seismic Plume Evolution in a Heterogeneous Sandstone Reservoir: Role and Impact of Patchy CO2 Saturation. *77th EAGE Conference and Exhibition 2015.*

ELLIS, M. & SINHA, M. 2010. The Potential of Controlled Source Electromagnetic Surveying In CO2 Storage Monitoring. Society of Exploration Geophysicists.

EVANS, B. J., COCKER, J. & UROSEVIC, M. 1996. Recording Seismic Reflections Beneath High Velocity Layers. Society of Exploration Geophysicists.

FERGUSON, R. J. & MARGRAVE, G. F. 2005. Planned seismic imaging using explicit one-way operators. *Geophysics,* 70**,** S101-S109.

GASPERIKOVA, E. & HOVERSTEN, G. M. 2005. Geophysical Techniques for Monitoring CO2 Movement During Sequestration. California Energy Commission.

GASSMANN, F. 1951. *Über die elastizität poröser medien*, Inst. für Geophysik an der ETH.

GCCSI 2012. The global status of CCS. *Canberra, Australia*.

GHANBARI, S., AL-ZAABI, Y., PICKUP, G., MACKAY, E., GOZALPOUR, F. & TODD, A. 2006. Simulation of CO2 storage in saline aquifers. *Chemical Engineering Research and Design,* 84**,** 764-775.

GREGORY, A. 1976. Fluid saturation effects on dynamic elastic properties of sedimentary rocks. *Geophysics,* 41**,** 895-921.

GRUDE, S., LANDRØ, M. & OSDAL, B. 2013. Time-lapse pressure–saturation discrimination for CO2 storage at the Snøhvit field. *International Journal of Greenhouse Gas Control,* 19**,** 369-378.

GRUDE, S., LANDRØ, M., WHITE, J. C. & TORSÆTER, O. 2014. CO2 saturation and thickness predictions in the Tubåen Fm., Snøhvit field, from analytical solution and time-lapse seismic data. *International Journal of Greenhouse Gas Control,* 29**,** 248-255.

HACIKOYLU, P., DVORKIN, J. & MAVKO, G. 2006. Resistivity-velocity transforms revisited. *The Leading Edge,* 25**,** 1006-1009.

HAN, B. 1998. A comparison of four depth-migration methods. *68th Ann. Internat. Mtg., Soc. Expl. Geophys*.

HAN, D. & BATZLE, M. L. 2004. Gassmann's equation and fluid-saturation effects on seismic velocities. *Geophysics,* 69**,** 398-405.

HANSEN, O., GILDING, D., NAZARIAN, B., OSDAL, B., RINGROSE, P., KRISTOFFERSEN, J.-B., EIKEN, O. & HANSEN, H. 2013. Snøhvit: the history of injecting and storing 1 Mt CO 2 in the Fluvial Tubåen Fm. *Energy Procedia,* 37**,** 3565-3573.

HANTSCHEL, T. & KAUERAUF, A. I. 2009. *Fundamentals of basin and petroleum systems modeling*, Springer.

HEINEMANN, N., WILKINSON, M., PICKUP, G. E., HASZELDINE, R. S. & CUTLER, N. A. 2012. CO2 storage in the offshore UK Bunter Sandstone Formation. *International Journal of Greenhouse Gas Control,* 6**,** 210-219.

HILL, R. 1963. Elastic properties of reinforced solids: Some theoretical principles. *Journal of the Mechanics and Physics of Solids,* 11**,** 357-372.

HOLLOWAY, S., VINCENT, C. J., BENTHAM, M. S. & KIRK, K. L. 2006. Top-down and bottom-up estimates of CO2 storage capacity in the United Kingdom sector of the southern North Sea basin. *Environmental Geosciences,* 13**,** 71-84.

IEA 2011. World Energy Outlook. *OECD/IEA France*.

IEAGHG 2015. Review of Offshore Monitoring for CCS projects. 2015/02 ed.

IPCC 2005. IPCC special report on carbon dioxide capture and storage. *In:* METZ, B., DAVIDSON, O., DE CONINCK, H., LOOS, M. & MEYER, L. (eds.). Intergovernmental Panel on Climate Change, Geneva (Switzerland). Working Group III.

IPCC 2007. Climate Change 2007: Synthesis Report. Contribution of Working Groups I, II and III to the Fourth Assessment Report of the Intergovernmental Panel on Climate Change. *In:* PACHAURI, R. & REISINGER, A. (eds.) *Intergovernmental Panel on Climate Change.*

IPCC 2013. Climate Change 2013: The Physical Science Basis. *In:* STOCKER, T. F., QIN, D., PLATTNER, G.-K., TIGNOR, M., ALLEN, S. K., BOSCHUNG, J., NAUELS, A., XIA, Y., BEX, V. & MIDGLEY, P. M. (eds.) *Intergovernmental Panel on Climate Change*. Cambridge, United Kingdom: Cambridge University Press.

IVANDIC, M., JUHLIN, C., LÜTH, S., BERGMANN, P., KASHUBIN, A., SOPHER, D., IVANOVA, A., BAUMANN, G. & HENNINGES, J. 2015. Geophysical monitoring at the Ketzin pilot site for CO2 storage: New insights into the plume evolution. *International Journal of Greenhouse Gas Control,* 32**,** 90-105.

IVANDIC, M., YANG, C., LÜTH, S., COSMA, C. & JUHLIN, C. 2012. Time-lapse analysis of sparse 3D seismic data from the CO2 storage pilot site at Ketzin, Germany. *Journal of Applied Geophysics,* 84**,** 14-28.

JAFARGANDOMI, A. & CURTIS, A. 2011. Detectability of petrophysical properties of subsurface CO2-saturated aquifer reservoirs using surface geophysical methods. *The Leading Edge,* 30**,** 1112-1121.

JENKINS, C. R., COOK, P. J., ENNIS-KING, J., UNDERSHULTZ, J., BOREHAM, C., DANCE, T., DE CARITAT, P., ETHERIDGE, D. M., FREIFELD, B. M. & HORTLE, A. 2012. Safe storage and effective monitoring of CO2 in depleted gas fields. *Proceedings of the National Academy of Sciences,* 109**,** E35-E41.

JOHNSON, D. L. 2001. Theory of frequency dependent acoustics in patchy-saturated porous media. *Journal of the Acoustical Society of America,* 110**,** 682-694.

KANG, S., SEOL, S. J. & BYUN, J. 2012. A feasibility study of CO2 sequestration monitoring using the mCSEM method at a deep brine aquifer in a shallow sea. *Geophysics,* 77**,** E117-E126.

KAZEMEINI, S. H., JUHLIN, C. & FOMEL, S. 2010. Monitoring CO2 response on surface seismic data; a rock physics and seismic modeling feasibility study at the CO2 sequestration site, Ketzin, Germany. *Journal of Applied Geophysics,* 71**,** 109-124.

KEY, K. 2012. Is the fast Hankel transform faster than quadrature? *Geophysics,* 77**,** F21-F30.

KIESSLING, D., SCHMIDT-HATTENBERGER, C., SCHUETT, H., SCHILLING, F., KRUEGER, K., SCHOEBEL, B., DANCKWARDT, E. & KUMMEROW, J. 2010. Geoelectrical methods for monitoring geological CO2 storage: First results from cross-hole and surface–downhole measurements from the CO2SINK test site at Ketzin (Germany). *International Journal of Greenhouse Gas Control,* 4**,** 816-826.

KNIGHT, R., DVORKIN, J. & NUR, A. 1998. Acoustic signatures of partial saturation. *Geophysics,* 63**,** 132-138.

KNIGHT, R. & NOLEN-HOEKSEMA, R. 1990. A laboratory study of the dependence of elastic wave velocities on pore scale fluid distribution. *Geophysical Research Letters,* 17**,** 1529-1532.

LEBEDEV, M., TOMS-STEWART, J., CLENNELL, B., PERVUKHINA, M., SHULAKOVA, V., PATERSON, L., MÜLLER, T. M., GUREVICH, B. & WENZLAU, F. 2009. Direct laboratory observation of patchy saturation and its effects on ultrasonic velocities. *The Leading Edge,* 28**,** 24-27.

LEI, X. & XUE, Z. 2009. Ultrasonic velocity and attenuation during CO2 injection into water-saturated porous sandstone: Measurements using difference seismic tomography. *Physics of the Earth and Planetary Interiors,* 176**,** 224-234.

LESLIE, D. M. & EVANS, B. J. 1999. The Effects of High-velocity Layering On Seismic Wave Propagation. Society of Exploration Geophysicists.

LIEN, M. & MANNSETH, T. 2008. Sensitivity study of marine CSEM data for reservoir production monitoring. *Geophysics,* 73**,** F151-F163.

LOPES, S., LEBEDEV, M., MÜLLER, T. M., CLENNELL, M. B. & GUREVICH, B. 2014. Forced imbibition into a limestone: measuring P-wave velocity and water saturation dependence on injection rate. *Geophysical Prospecting,* 62**,** 1126-1142.

LUMLEY, D. 2010. 4D seismic monitoring of CO2 sequestration. *The Leading Edge,* 29**,** 150-155.

MARGRAVE, G. F. 2003. Numerical Methods of Exploration Seismology with Algorithms in MATLAB. *Calgary: Department of Geology and Geophysics, The University of Calgary*.

MARION, D. P. 1990. *Acoustical, mechanical, and transport properties of sediments and granular materials*, Stanford University, Department of Geophysics.

MAVKO, G. & MUKERJI, T. 1995. Seismic pore space compressibility and Gassmann's relation. *Geophysics,* 60**,** 1743-1749.

MAVKO, G. & MUKERJI, T. 1998. Bounds on low-frequency seismic velocities in partially saturated rocks. *Geophysics,* 63**,** 918-924.

MAVKO, G., MUKERJI, T. & DVORKIN, J. 2009. *The rock physics handbook: Tools for seismic analysis of porous media*, Cambridge University Press.

MINDLIN, R. D. 1949. Compliance of Elastic Bodies in Contact. *Journal of Applied Mechanics,* 16**,** 259-268.

MUKHOPADHYAY, P. K., MALLICK, S., PADHI, A. & ALVARADO, V. 2010. Time-lapse Monitoring Carbon Sequestrated Brine Aquifers- a Feasibility Study. Society of Exploration Geophysicists.

MÜLLER, T. M., GUREVICH, B. & LEBEDEV, M. 2010. Seismic wave attenuation and dispersion resulting from wave-induced flow in porous rocks—A review. *Geophysics,* 75**,** 75A147-75A164.

MURPHY, W. F. 1982. *Effects of microstructure and pore fluids on the acoustic properties of granular sedimentary materials.* Stanford University, Department of Geophysics.

NADER, R., SAMSON, C. & WHITE, D. 2012. Effectiveness of Seismic Detection Modelling for CO 2 Migration Scenarios Near the Aquistore CO 2 Injection Site, Estevan, Saskatchewan, Canada. *2012 SEG Annual Meeting*.

NIVEN, R. K. 2006. Force stability of pore-scale fluid bridges and ganglia in axisymmetric and non-axisymmetric configurations. *Journal of Petroleum Science and Engineering,* 52**,** 1-18.

NJIEKAK, G., SCHMITT, D. R., YAM, H. & KOFMAN, R. S. 2013. CO2 rock physics as part of the Weyburn-Midale geological storage project. *International Journal of Greenhouse Gas Control,* 16, Supplement 1**,** S118-S133.

NUR, A., MAVKO, G., DVORKIN, J. & GALMUDI, D. 1998. Critical porosity: A key to relating physical properties to porosity in rocks. *The Leading Edge,* 17**,** 357-362.

ORANGE, A., KEY, K. & CONSTABLE, S. 2009. The feasibility of reservoir monitoring using time-lapse marine CSEM. *Geophysics,* 74**,** F21-F29.

OSPAR 2007. OSPAR Guidelines for Risk Assessment and Management of Storage of CO2 Streams in Geological Formations.

PADHI, A., MALLICK, S., BEHZADI, H. & ALVARADO, V. 2014. Efficient modeling of seismic signature of patchy saturation for time lapse monitoring of carbon sequestrated deep saline reservoirs. *Applied Energy,* 114**,** 445-455.

PARK, J., FAWAD, M., VIKEN, I., AKER, E. & BJØRNARÅ, T. I. 2013. CSEM Sensitivity Study for Sleipner CO2-injection Monitoring. *Energy Procedia,* 37**,** 4199-4206.

PEARCE, J. 2005. *Technology Status Review: Monitoring Technologies for the Geological Storage of CO2*, DTI.

PERMEDIA 2014. BOS, Version 5.1. *Halliburton, Ottawa, Ontario*.

PEVZNER, R., UROSEVIC, M., CASPERI, E., GALVIN, R. J., MADADI, M., DANCE, T., SHULAKOVA, V., GUREVICH, B., TCHEVERDA, V. & CINAR, Y. 2013. Feasibility of time-lapse seismic methodology for monitoring the injection of small quantities of CO2 into a saline formation, CO2CRC Otway Project. . *Energy Procedia*.

PURNELL, G. W. 1992. Imaging beneath a high-velocity layer using converted waves. *Geophysics,* 57**,** 1444-1452.

RAMIREZ, A. L., NEWMARK, R. L. & DAILY, W. D. 2003. Monitoring carbon dioxide floods using electrical resistance tomography (ERT): Sensitivity studies. *Journal of Environmental and Engineering Geophysics,* 8**,** 187.

REUSS, A. 1929. Berechnung der Fließgrenze von Mischkristallen auf Grund der Plastizitätsbedingung für Einkristalle. *ZAMM-Journal of Applied Mathematics and Mechanics/Zeitschrift für Angewandte Mathematik und Mechanik,* 9**,** 49-58.

REYNOLDS, J. M. 2011. *An introduction to applied and environmental geophysics*, Wiley.

RIETSCH, E. 2010. SeisLab for MatLab, MATLAB Software for the Analysis of Seismic and Well-Log Data. A Tutorial.

RINGROSE, P. & BENTLEY, M. 2015. *Reservoir model design*, Springer.

SAADATPOOR, E., BRYANT, S. L. & SEPEHRNOORI, K. 2010. New trapping mechanism in carbon sequestration. *Transport in Porous Media,* 82**,** 3-17.

SENGUPTA, M. & MAVKO, G. 2003. Impact of flow-simulation parameters on saturation scales and seismic velocity. *Geophysics,* 68**,** 1267-1280.

SI, W., DI, B. & WEI, J. 2015. Seismic response variation of tight gas sand for uniform and patchy saturation patterns. *Journal of Applied Geophysics,* 116**,** 167-172.

SILIN, D., PATZEK, T. W. & BENSON, S. M. 2009. A one-dimensional model of vertical gas plume migration through a heterogeneous porous medium. *International Journal of Greenhouse Gas Control,* 3**,** 300-310.

SINGH, V. P., CAVANAGH, A., HANSEN, H., NAZARIAN, B., IDING, M. & RINGROSE, P. S. 2010. Reservoir Modeling of CO2 Plume Behavior Calibrated Against Monitoring Data From Sleipner, Norway. *Society of Petroleum Engineers*.

SMITH, T. M., SONDERGELD, C. H. & RAI, C. S. 2003. Gassmann fluid substitutions: A tutorial. *Geophysics,* 68**,** 430-440.

SMITH, W. O., FOOTE, P. D. & BUSANG, P. F. 1929. Packing of Homogeneous Spheres. *Physical Review,* 34**,** 1271-1274.

TAYLOR, C. & JULLIARD, F. 2013. An Introduction to Source Modelling and Wavelet Analysis Nucleus+.

TIAB, D. & DONALDSON, E. C. 2011. *Petrophysics: theory and practice of measuring reservoir rock and fluid transport properties*, Gulf professional publishing.

TOMS, J., MÜLLER, T., CIZ, R. & GUREVICH, B. 2006. Comparative review of theoretical models for elastic wave attenuation and dispersion in partially saturated rocks. *Soil Dynamics and Earthquake Engineering,* 26**,** 548-565.

UM, E. S. & ALUMBAUGH, D. L. 2007. On the physics of the marine controlled-source electromagnetic method. *Geophysics,* 72**,** WA13-WA26.

UROSEVIC, M., PEVZNER, R., KEPIC, A., WISMAN, P., SHULAKOVA, V. & SHARMA, S. 2010. Time-lapse seismic monitoring of CO 2 injection into a depleted gas reservoir—Naylor Field, Australia. *The Leading Edge,* 29**,** 164-169.

VOIGT, W. 1928. Lehrbuch der Kristallphysik, Teubner, Leipzig, 1928; A. Reuss. *Z. Angew. Math. Mech,* 9**,** 49.

WADSWORTH, J. 1960. Experimental examination of local processes in packed beds of homogeneous spheres. *Nat. Res. Council of Canada, Mech. Eng.*

WANDLER, A. V., DAVIS, T. L. & SINGH, P. K. 2012. An experimental and modeling study on the response to varying pore pressure and reservoir fluids in the Morrow A Sandstone. *International Journal of Geophysics,* 2012.

WANG, Z. 2001. Fundamentals of seismic rock physics. *Geophysics,* 66**,** 398-412.

WHITE, D. 2009. Monitoring CO 2 storage during EOR at the Weyburn-Midale Field. *The Leading Edge,* 28**,** 838-842.

WHITE, D. 2013a. Seismic characterization and time-lapse imaging during seven years of CO2 flood in the Weyburn field, Saskatchewan, Canada.

International Journal of Greenhouse Gas Control, 16, Supplement 1**,** S78-S94.

WHITE, D., BURROWES, G., DAVIS, T., HAJNAL, Z., HIRSCHE, K., HUTCHEON, I., MAJER, E., ROSTRON, B. & WHITTAKER, S. 2004. Greenhouse gas sequestration in abandoned oil reservoirs: The International Energy Agency Weyburn pilot project. *GSA today,* 14**,** 4-11.

WHITE, D. J. 2013b. Toward quantitative CO2 storage estimates from time-lapse 3D seismic travel times: An example from the IEA GHG Weyburn–Midale CO2 monitoring and storage project. *International Journal of Greenhouse Gas Control,* 16, Supplement 1**,** S95-S102.

WHITE, J. 1975. Computed seismic speeds and attenuation in rocks with partial gas saturation. *Geophysics,* 40**,** 224-232.

WILLIAMS, J. D. O., JIN, M., BENTHAM, M., PICKUP, G. E., HANNIS, S. D. & MACKAY, E. J. 2013. Modelling carbon dioxide storage within closed structures in the UK Bunter Sandstone Formation. *International Journal of Greenhouse Gas Control,* 18**,** 38-50.

WILSON, M. & MONEA, M. 2004. IEA GHG Weyburn CO2 monitoring & storage project. Summary report 2000-2004.

WINSAUER, W. O., SHEARIN JR, H., MASSON, P. & WILLIAMS, M. 1952. Resistivity of brine-saturated sands in relation to pore geometry. *AAPG bulletin,* 36**,** 253-277.

WRIGHT, D., ZIOLKOWSKI, A. & HOBBS, B. 2002. Hydrocarbon detection and monitoring with a multicomponent transient electromagnetic (MTEM) survey. *The Leading Edge,* 21**,** 852-864.

WYLLIE, M. & ROSE, W. D. 1950. Some theoretical considerations related to the quantitative evaluation of the physical characteristics of reservoir rock from electrical log data. *Journal of Petroleum Technology,* 2**,** 105-118.

XU, S. & WHITE, R. E. 1995. A new velocity model for clay-sand mixtu res1. *Geophysical Prospecting,* 43**,** 91-118.

ZIOLKOWSKI, A. 2007. Developments in the transient electromagnetic method. *First break,* 25.

ZIOLKOWSKI, A., HOBBS, B. & WRIGHT, D. 2007. Multitransient electromagnetic demonstration survey in France. *Geophysics,* 72**,** F197-F209.

ZIOLKOWSKI, A., PARR, R., WRIGHT, D., NOCKLES, V., LIMOND, C., MORRIS, E. & LINFOOT, J. 2010. Multi-transient electromagnetic repeatability experiment over the North Sea Harding field. *Geophysical Prospecting,* 58**,** 1159-1176.

ZIOLKOWSKI, A. & WRIGHT, D. 2007. Removal of the Air Wave In Shallow Marine Transient EM Data. Society of Exploration Geophysicists.

ZIOLKOWSKI, A., WRIGHT, D. & MATTSSON, J. 2011. Comparison of pseudo-random binary sequence and square-wave transient controlled-source

electromagnetic data over the Peon gas discovery, Norway. *Geophysical Prospecting,* 59**,** 1114-1131.

ZWEIGEL, P., ARTS, R., LOTHE, A. E. & LINDEBERG, E. B. 2004. Reservoir geology of the Utsira Formation at the first industrial-scale underground CO2 storage site (Sleipner area, North Sea). *Geological Society, London, Special Publications,* 233**,** 165-180.